

**Reactive transport modeling in geomechanically dynamic coal mine
systems - Numerical approaches to characterize subsurface mine
water interactions**

Inauguraldissertation

zur

Erlangung des akademischen Grades eines

Doktor der Naturwissenschaften (Dr. rer. nat.)

an der

Mathematisch-Naturwissenschaftliche Fakultät

der

Universität Greifswald

Vorgelegt von

Diego Alexander Bedoya Gonzalez, M.Sc.

Geboren am 18.02.1992

In Bogota, Kolumbien

Greifswald im Januar 2023

Dekan: Prof. Dr. Gerald Kerth

Erstgutachterin: Prof. Dr. Maria-Theresia Schafmeister

Zweitgutachterin: Assoc.-Prof. Dr. Sylke Hilberg

Drittgutachter: Prof. Dr. Georg H. E. Wieber

Viertgutachter: Prof. Dr. Steffen Birk

Tag der Promotion: 23. Juni 2023

"The earth, the air, the land, and the water are not an inheritance from our forefathers but on loan from our children. So, we have to handover to them at least as it was handed over to us."

Mahatma Gandhi (1869 - 1948)

Table of Contents

List of Figures	vii
List of Tables	xv
List of Symbols and Abbreviations	xvii
Abstract	1
Zusammenfassung	3
Chapter 1: Introduction	1
1.1 Bedrock response to intensive mining operations	1
1.2 Potential impacts on groundwater due to sequence disruptions.....	5
1.3 Modeling post mining setups	10
1.4 Scope and main research topics	14
1.5 Statement of own contribution to the manuscripts.....	19
1.6 References	21
Chapter 2: A Petrographic Investigation of the Carboniferous Sequence from the Ibbenbüren Mine: Tracing the Origin of the Coal Mine Drainage	31
Chapter 3: A dual-continuum model (TOUGH2) for characterizing flow and discharge in a mechanically disrupted sandstone overburden	55
Chapter 4: A multiple interactive continua model (MINC) to simulate reactive mass transport in a post-mining coal zone: A case study of the Ibbenbüren Westfield	77
Chapter 5: Geochemistry of coal mine drainage, groundwater, and brines from the Ibbenbüren mine, Germany: a coupled elemental- isotopic approach	117
Chapter 6: Conclusion	131
6.1 Future work	132
6.2 References	134
Eigenständigkeitserklärung	135
Curriculum Vitae	137
List of publications	140
Acknowledgments	143

List of Figures

Chapter 1

Fig. 1	Schematic profile and conceptual understanding of processes and modifications occurring in the overburden after high-recovery mining methods. Modified after Bai and Tu (2019) and David et al. (2017).	6
Fig. 2	Impacts on water availability generated by the reduction of phreatic levels due to development of subsidence-induced fracture zones along the overburden.	11
Fig. 3	Typical temporal variation in mine water ion concentration observed during and after the rebound process. The 'first flush ' leads to a peak in concentrations after dissolving precipitates in mine voids, followed by a rapid decline that reaches an eventual steady. Modified after Younger (1997) and Merritt and Power (2022)...	13
Fig. 4	Distributive approaches for modeling fractured rocks. Modified after Kordilla (2014).	16
Fig. 5	Location map of the Ibbenbüren Westfield. The Carboniferous block is enclosed by regional faults structures, which are effective hydrogeological boundaries for the coalfield. Chapters 2, 3 and 4 present similar location figures that detail the geologic and hydrogeological situation of the area.	19

Chapter 2

Fig. 1	Geographic and geological maps of the studied area. The polygons enclosed by the thick black line in the digital elevation image additionally illustrate the location of the other two Carboniferous blocks in the surrounding area. The A-A' line denotes the position of the cross-section in Figure 2. Modified after [10,35,36].	38
Fig. 2	Geological cross-section of the Ibbenbüren Westfield (cross-section line A-A' in Figure 1). The cross-section is vertically exaggerated 5x to better detail the shallow overburden structure and current hydrogeological situation. Modified after [39].	39
Fig. 3	Stratigraphic columns of the two core-samples recovered in the area. The sketch includes lithology and location of the samples analyzed in this paper. Cl = clay, Slt = silt, Sd = sand (v.f: very fine, f: fine, m: medium, c: coarse, v.c.: very coarse), Grv = gravel.	40
Fig. 4	Types of breakups encountered during the core logging. (a) Longitudinal and (b) cross-sectional images of joint networks, displaying limited alteration zones. In both sections iron (oxide-) hydroxides hold the rock pieces together hindering	

fluid flow. (c) Sub-vertical fracture showing clear influence in the weathering state of the sandstone interval. (d) Cracked sandstone interval with a sub-vertical fracture potentially associated with the exploitation of the Dickenberg coal seam, 4 m below it (this structure can be tracked on the core BK15 for approx. 5m). 42

Fig. 5 Photomicrographs of the main components found in the rock sequence. (a) Plastic lithic fragments, muscovite flakes and booklet crystals of kaolinite-group minerals squeezed among quartz and chert grains. The authigenic origin of the kaolinite-group minerals is interpreted from the pseudo-hexagonal form of the pore space. (b) Oxidation of a coal lithic fragment within conglomeratic sandstone interval. (c) Unaltered cluster of microcrystalline pyrite associated with a sedimentary lithic fragment. (d) Weathered thin section with iron (oxide-) hydroxides precipitating around and on the matrix and rock components. (e) Weathered cluster of microcrystalline pyrite completely transformed to iron (oxide-) hydroxide (holo-pseudomorph). (f) SEM image of prismatic barite crystals in a pore space. Lf = lithic fragment, Ms = muscovite, Kln = kaolinite-group minerals, Qz = quartz, Py = pyrite, Ill = illite, Ser = sericite, Fe ox. = iron (oxide-) hydroxides, PPL = plane polarized light, XPL = cross polarized light, SEM = scanning electron microscope. 43

Fig. 6 Diagnostic peaks of quartz, pyrite, kaolinite and dickite for samples IW1 uw and IW18 uw. 44

Fig. 7 Rock matrix components. (a) Altered pseudomatrix squeezed among quartz and chert grains. (b) Authigenic clayey matrix found in the sample. Illite fibers stand out from their bright interference colors around the loose aggregates of kaolinite-group minerals, while sericite is frequently observed on the surface of sedimentary lithic fragments. (c,d) Illite and kaolinite-group minerals with their respective EDS signals. Alt Pm = altered pseudomatrix, Qz = quartz, Kln = kaolinite-group minerals, Ill = illite, Ser = sericite, PPL = plane polarized light, XPL = cross polarized light, SEM = scanning electron microscope. 45

Fig. 8 Overview of the rock porosity. (a) Open straight-line contact between two quartz grains developing primary porosity. (b) Secondary microporosity highlighted by the speckled, pale blue color of the resin. (c) Thin section of a weathered interval displaying clogging of primary and secondary microporosity. (d) Iron (oxide-) hydroxides pore-lining, reducing and blocking the connection between pore spaces. Qz = quartz, Kln = kaolinite-group minerals, PPL = plane polarized light. 46

Fig. 9 Elemental composition of analyzed rock samples. Potassium and magnesium do not vary between weathered and unweathered zones, indicating low influence of water-rock interaction on aluminosilicate dissolution. Correlation of Zn, Pb and Ni indicates coprecipitation/sorption with secondary iron (oxide) hydroxide. 47

Chapter 3

Fig. 1 Schematic profile and conceptual understanding of groundwater flow in postmining fractured overburdens (modified after David et al. 2017 and Bai and Tu 2019). 57

Fig. 2 Maps showing the location of the Ibbenbüren coal-mining district. The dashed-line square in the digital elevation map encloses the study area further depicted in Fig. 3 (modified after Bedoya-Gonzalez et al. 2021a). 59

Fig. 3 Geological map and cross-section showing the hydrogeological boundaries and Dickenberg adit. The A–A’ line in the map denotes the position of the cross-section, which is vertically exaggerated 5× to better detail the shallow overburden structure (modified after Bedoya-Gonzalez et al. 2021a). 60

Fig. 4 Constructed grid for the DC Model. Recharge is applied directly onto the weathered blocks while an open boundary condition is set along the adit element. For each block colored in orange, the mesh is divided into two continua (fracture and porous media) with the same physical location. 62

Fig. 5 Comparison between the measured and simulated discharge of the Dickenberg adit. The graphs show: **a)** the best fit obtained during the calibration process for the year 2008; and **b)** the discharge signal obtained from the validation process for the year 2017. Both simulated discharge signals were obtained by summing the water flux of the matrix and fractured continua at the lower boundary of the model. 65

Fig. 6 Temporal and spatial distribution of the total fluid exchange and water saturation. **a)** Total daily exchange between the two continua for the whole system (positive values represent exchange from the fractures to the matrix while negative values from the matrix to the fractures). **b)** Spatial variation of the total water exchange between the first and last fractured sandstone layers. ... 65

Fig. 7 Change in water saturation and fluid exchange between the two continua at two temporal points. Water exchange is given in m³/day, while the variation in water saturation is measured with respect to the initial water content at the time the daily variable recharge is applied (i.e., the water saturation at the end of the 100-year long-term simulation). 66

Fig. 8 Nash-Sutcliffe efficiency criterion (NSE) of the model for the calibration and validation periods. Solid lines indicate the 1:1 slope between the observed and measured data. 67

Fig. 9 Variations of the calibrated discharge signal obtained during the sensitivity analysis. The most sensitive parameters include: **a)** height of the fractured zone; **b)** permeability of the sandstone layers; **c)** permeability of the fractured

continuum; and d the α parameter of the van Genuchten-Mualem function for the fractured continuum. 69

Fig. 10 Types of parameter codependences observed during the sensitivity analysis. **a–b)** Shows nonlinear dependency between two sensitive parameters, **c)** shows linear dependency with just one sensitive parameter, and **d)** shows both parameters being insensitive. 70

Chapter 4

Fig. 1 Location of the Ibbenbüren coal-mining district. The dashed-line square in the digital elevation map encloses the study area further depicted in Fig. 2 (from Bedoya-Gonzalez et al. 2022). 81

Fig. 2 Geological map and cross-section showing the hydrogeological boundaries and Dickenberg adit. The A–A' line in the map denotes the position of the cross-section, which is vertically exaggerated 5× to better detail the shallow overburden structure (from Bedoya-Gonzalez et al. 2022). 82

Fig. 3 Constructed grid for the shallow overburden of the Ibbenbüren Westfield. Recharge is applied directly onto the weathered blocks. For each block colored in orange, the mesh is divided into five continua with the same physical location: one for fracture (Fr) and four for the matrix media (Mn). 84

Fig. 4 Schematic representation of the 5-Stages simulation performed in this study. 89

Fig. 5 Comparison of the measured and simulated discharges of the Dickenberg adit for the years 2016 and 2017. DCM: dual continuum model, MINC: Multiple Interactive Continua model, α = alpha parameter for the fractured continuum. ... 89

Fig. 6 Water saturation in one of the model columns (Consider for subsequent column graphs that layers G, K and L correspond to shales). 90

Fig. 7 Distribution of chloride ion over time. **a)** Discharged evolution of the ion in the Dickenberg adit. **b)** Evolution and **c)** final state of the initial imposed chloride concentration in one of the model's representative columns. 91

Fig. 8 Pyrite –related ions concentrations over time. **a)** Discharged evolution for iron and sulfate ions in the Dickenberg adit. **b)** Evolution and **c)** final state of pyrite dissolution in one of the model's columns. Distribution of **d)** gaseous oxygen and **e)** precipitated iron hydroxides for one of the model's columns after 50 years of simulation. 92

Fig. 9 Evolution and distribution of hydrogen ion in the model during the 50 years simulation. **a)** pH values of the discharged water and **b)** kaolinite dissolution patterns observed in one model's columns. 93

Fig. 10	Behaviour of one artificial tracer and sulfate ion during the capillary-gravity equilibrium. a) Total amount of suctioned tracer. Migration pattern of the suctioned tracer in one model's column for b) the actual heterogeneous overburden of the Westfield and c) for a hypothetical homogeneous overburden composed of sandstones. d) Sulfate ion concentration before and after capillary suction in one model's column for the actual heterogeneous overburden.	94
Fig. 11	Post rebound evolution of the artificial tracer within the system. a) Simulated concentration discharges in the Dickenberg adit. b) Final concentration in one of the model columns for the actual heterogeneous overburden.	95
Fig. 12	Post rebound evolution of the system. Measured and simulated concentration discharges in the Dickenberg adit for a) sulfate, and b) iron. c) Comparison of the iron hydroxides precipitated in one of the model columns when including (or not) oxygen in the lower boundary.	96
Fig. 13	Simulated and measured seasonal variations of a) chloride, b) sulfate, and c) iron.	97
Fig. 14	Comparison between MINC and DC model setup for a) sulfate discharge evolution, and b) pyrite oxidation in one of the model's columns.	98
Fig. 15	Comparison among scenarios with 1 (benchmark), 2 and 3 fracture densities for a) sulfate discharge evolution, b) pyrite oxidation and c) iron hydroxide precipitation in one of the model's columns.	99
Fig. 16	Comparison between the benchmark setup and scenarios with variable mineral reactive surface area and kinetic rates for a) sulfate discharge evolution and b) pyrite oxidation in one of the model's columns. Log k in mol m ⁻² s ⁻¹	100
Fig. 17	Comparison of sulfate discharges for scenarios with varying amounts of pyrite in waste rock deposits. The graph shows concentrations recorded at the base of the waste rock deposits (markers only) and in the Dickenberg adit, where water from the entire area is collected (solid lines with markers).	100
Fig. 18	Comparison among the benchmark and subscenarios with heterogeneous and variable pyrite amounts for a) sulfate discharge evolution, b) pyrite oxidation and c) iron hydroxide precipitation in one of the model's column.	101

Chapter 5

- Fig. 1 Location of the Ibbenbüren coalfield. The Carboniferous blocks of the coalfield are divided by faults along the Bockradener Graben. Mining in the Westfield closed in 1979, whereas mining in the Eastfield continued until December 2018. The red line denotes the position of the cross section in Fig. 11. Modified after European Digital Elevation Model (EU-DEM), version 1.1. (For interpretation

	of the references to color in this figure legend, the reader is referred to the Web version of this article.).	119
Fig. 2	Chloride concentration [mol/kg] versus ionic strength. Increasing salinity is accompanied by an increasing percentage of sodium chloride in total salinity. The black line represents a pure NaCl (1:1) solution. Solutions plotting above this line indicate a higher fraction of divalent ions contributing to total salinity...	121
Fig. 3	Ternary plots showing the relative molar proportion of main cations (Mg^{2+} , Ca^{2+} , and Na^+) (a) , and main anions (SO_4^{2-} , Cl^- , and HCO_3^-) (b)	122
Fig. 4	Molar Na/Cl (a) , Cl/Br (b) , Cl/K (c) , and Cl/Li (d) ratios versus Cl concentration [mol/kg]. Seawater composition after Millero et al. (2008); Lithium concentration taken from Riley and Tongudai (1964); Evolution of the respective molar ratio during seawater evaporation until saturation of carnallite is reached for comparison (blue line). (For interpretation of the references to color in this figure legend, the reader is referred to the Web version of this article.).	122
Fig. 5	Lithium concentration versus potassium concentration [mol/kg].	123
Fig. 6	$\delta^{18}O$ versus δ^2H values (‰; VSMOW). The blue line denotes the Global Meteoric Waterline (GMWL) after Craig (1961). The grey line denotes the Local Meteoric Waterline (LMWL) of the nearest station (Bad Salzufflen) obtained from the IAE/WMO global network of isotopes in precipitation (GNIP) database Stumpp et al. (2014). Light grey crosses are annual average values of the station from 1978 to 2011, plotted for reference. The red dotted line shows the hypothetical trend during mixing of solution IBB-E 3 with seawater. (For interpretation of the references to color in this figure legend, the reader is referred to the Web version of this article.).	124
Fig. 7	Tritium units (TU) versus depth in meters. Within the uncertainty, Tritium was present down to the lowest level, indicating the presence of some modern water throughout the mine. Samples IBB-E 3 and IBB-E 4 from the lowest level show TU values below the detection limit (<0.6 TU). Tritium was not analyzed in all samples (see Table S1 (Supplementary Material)).	124
Fig. 8	$\delta^{34}S$ versus $\delta^{18}O$ (‰; VCDT) values of dissolved sulfate. The area between the dashed grey lines indicates the possible pathways of isotopic evolution during bacterial sulfate reduction (BSR), starting from sample IBB-E-14; slopes are derived from Brunner et al. (2005). The isotopic trend during conservative mixing is indicated for endmember IBB-E-3 (highest $\delta^{34}S$, highest ionic strength) with IBB-E-14 (pyrite oxidation, high sulfate). $\delta^{34}S$ range for middle Triassic to upper Jurassic evaporates from Müller et al. (1966), the range of $\delta^{18}O$ is based on Claypool et al. (1980).	125

Fig. 9	$\delta^{34}\text{S}$ versus dissolved sulfate (a) and $\delta^{34}\text{S}$ versus chloride [mol/kg] (b) . The area between the dashed grey lines denotes isotopic enrichment (ϵ) during bacterial sulfate reduction (BSR). The slopes are derived from Fritz et al. (1989). Endmember mixing is plotted for solution IBB-E 3 with IBB-E 14 (high sulfate), and for IBB-E 3 with IBB-E 11 (low sulfate).	126
Fig. 10	$^{87}\text{Sr}/^{86}\text{Sr}$ isotope ratio versus chloride [mol/kg] (a) , and $^{87}\text{Sr}/^{86}\text{Sr}$ ratio versus δD (‰, VSMOW) (b) in the deep mine water. The correlation indicates a contribution of isotopically heavy connate water to the mine water chemistry. ...	127
Fig. 11	Schematic cross section through the Ibbenbüren Eastfield including a conceptual hydrogeochemical model, depicting the origin and evolution of mine drainage, groundwater, and brines in the mine. Modified after Drozdowski (1985).	127

List of Tables

Chapter 1

Table 1	Fracture height predictions extracted from peer-review papers. M is mined height and n the number of consecutive mined seams.	8
---------	--	---

Chapter 2

Chapter 3

Table 1	Hydraulic parameters used in the model. Numbers outside the parentheses indicate the values that provided the best discharge agreement during the calibration process.	64
Table 2	Maximum RMSE for individual and pairs of parameters obtained during the sensitivity analyses for the year 2008. Parameters with RMSE values less than 1,360 m ³ /day are considered insensitive. Ss sandstone, Shl shale, Wth weathered layer, Frac fractured continuum, – combination not evaluated.	68

Chapter 4

Table 1	Calibrated hydraulic parameters used in the MINC model. Modified after Bedoya et al. (2022).	85
Table 2	Composition of the initial and boundary waters (in mg/L) employed in the model.	86
Table 3	Chemical properties of the primary mineral assemblage assigned to the overburden. Thermodynamic parameters (log K) are taken from the Japan Atomic Energy Agency (JAEA).	87
Table 4	Specifications of the different flow, transport and reaction parameters applied to each case scenario.	97
Table SI1	Relationship between the recharge calculated by the Geological Survey of North Rhine-Westphalia and the applied recharge in this study. Daily inputs are obtained by multiplying the daily precipitation by the percentages assigned for each month. Calculated using the data from Herrmann et al. (2014).	113
Table SI2	Monthly chemical composition of the imposed rainwater for the year 2016 and 2017 during the stage 5. Concentrations are given in mg/L. Calculated using the data from Herrmann et al. (2006).	114

Table SI3 Random distribution of pyrite per sandstone layer within the overburden in each of the 3 sub-scenarios modeled in the case scenario n°4. 115

Chapter 5

List of Symbols and Abbreviations

Common throughout the Thesis

Symbol/Abbreviation	Meaning / Description
SSE	South-southeast (one of the eight "half-winds" of a compass direction)
SSW	South-southwest
NNE	North-northeast
NNW	North-northwest
m a.s.l. / m asl.	Meters above the sea level
mD	Millidarcy (unit of permeability equivalent to $9.87 \times 10^{-13} \text{ m}^2$)
pH	Hydrogen potential in a solution. $\text{pH} = -\log([\text{H}^+])$
(aq), (g), (s)	Appended as subscripts at the end of chemical formulas, indicate that the material is dissolved in water, is a gas, or is a solid, respectively

Chapter 2

Symbol/Abbreviation	Meaning / Description
BK14a, BK15	Drilling Boreholes from which core samples were obtained.
PPL	Plane polarized light (microscopy)
XPL	Cross polarized light (microscopy)
SEM	Scanning electron microscope
EDS	Energy-dispersive X-ray spectroscopy
XRD	X-ray Powder Diffraction
ppm	Parts per million
Qz	Quartz
Py	Pyrite
Lf	Lithic fragment

Ms	Muscovite
Kln	Kaolinite-group mineral
Ilt	Illite
Ser	sericite
Fe ox.	Iron (oxide-)hydroxides
Alt Pm	altered pseudomatrix

Chapters 3 and 4

Symbol/Abbreviation	Meaning / Description
TOUGH2/ TOUGHREACT	Employed modeling code names. It stands for T ransport O f U nsaturated G roundwater and H eat.
EPM	Equivalent porous medium (approach or model).
DC	Dual-continuum (approach or model - DCM).
MINC	Multiple interactive continua (approach or model).
1D, 2D, 3D	One, two or three dimensions, respectively.
DEM	Digital elevation model.
ESM	Electronic supplementary material.
LANUV NRW	Landesamt für Natur, Umwelt und Verbraucherschutz Nordrhein-Westfalen (Regional Office for Nature, Environment and Consumer Protection North Rhine-Westphalia).
JAEA	Japan Atomic Energy Agency.
NSE	Nash-Sutcliffe efficiency criterion.
RMSE	Root mean square error.
<i>Ss</i>	Sandstone.
<i>Shl</i>	Shale.
<i>Wth</i>	Weathered layer.
<i>Fract</i>	Fractured continuum.

N/A	Not Applicable.
Re	Reynolds number (dimensionless).
ρ_w	Water density (kg/m ³).
μ_w	Water viscosity (Pa·s).
g	Gravity acceleration (m/s ²).
Φ	Porosity (m ³ /m ³).
θ	Specific volumetric water content (m ³ /m ³).
m, f	(As subscripts) matrix and fractured continua, respectively.
c	(As subscript) either continuum domain.
a	(As subscript) Interface between the fractured and matrix continua in one block.
K	(Upper case) Hydraulic conductivity (m/s).
K_{u-f}	(Upper case) Hydraulic conductivity (m/s) at the horizontal interface between the undisturbed layer (u subscript) and fractured continuum (f subscript).
k	(Lower case) Absolute permeability (m ²).
h	Hydraulic head (m).
Γ_{ex}	Scaled exchange term between the fractured and matrix continua (m/s).
$k_{rw\ c}$	(Lower case) relative permeability coefficient of the continuum (dimensionless), which varies from 0 to 1. For saturated media k_{rw} is equal to 1, while under unsaturated conditions, the coefficient varies according to several factors described by the van Genuchten-Mualem parametric model.
P_c^*	Capillary pressure (Pa).
Se c	Effective saturation of the continuum (dimensionless).
θ_r / S_{lr}	Residual volumetric water content (m ³ /m ³).
α	Alfa parameter of the van Genuchten-Mualem equation (1/m), corresponding approximately to the inverse of the air-entry value

n, m	Empirical fitting parameters associated with the pore distribution for the van Genuchten-Mualem parametric model (both dimensionless). $m = 1 - (1/n)$ and varies from 0 to 1.
α^*	Exchange coefficient (1/s), which depends on the size and shape of the mesh elements. Parameter used to calculate the Γ_{ex} term.
β	Geometry grid factor (dimensionless) used to calculate the α^* term. This value is 3 for rectangular blocks and 15 for spheres.
γ_w	Scaling coefficient (dimensionless) used to calculate the α^* term. It is usually set to 0.4.
$\text{Log } K$	Logarithm of the equilibrium constant for chemical reactions.
ν_{ji}, ν_{js}	Stoichiometric reaction coefficients for liquid and solid phase, respectively.
A_j, A_i	Aqueous primary and secondary species, respectively.
M_s	Mineral species.
ϵ_c	Volume fraction of a continuum (m^3/m^3).
Ψ_j	Total concentration of the solute j (mol/kg).
Ω_j	Total flux of the solute j ($\text{m}^3/\text{s} \cdot \text{m}^2$).
I_s	Kinetic reaction rate of a solid phase (the unit depends on the reaction order).
A_{ex}	Interface between fracture and matrix continua (m^2).
A_s	Specific reactive surface area of the solid phase (m^2/m^3 medium)
τ	Tortuosity (dimensionless).
D	Diffusion coefficient (m^2/s).
C_i, C_j	Concentration of the i th secondary species derived from the concentration of the primary specie C_j .
γ_i, γ_j	Thermodynamic activity coefficients of the primary and secondary species, respectively.
Q_s	Kinetic mineral saturation ratio (dimensionless).
P	Partial gas pressure (bar).

f	Fugacity coefficient (dimensionless). It is assumed equal to one for atmospheric pressure when the gaseous phase behaves like an ideal mixture.
d_{mf}	Distance between the nodes of the fractured and matrix continua (m).

Chapter 5

Symbol/Abbreviation	Meaning / Description
δ	Delta notation. It expresses the variation of an isotopic ratio of an element (R) relative to the isotopic ratio of a standard (R_{std}). $\delta = \left(\frac{R - R_{std}}{R_{std}} \right) * 1000$ The result is expressed in terms of per mil (parts per thousand, ‰).
VCDT	Vienna-Canyon Diablo Troilite (Isotopic standard for sulfate).
VSMOW	Vienna Standard Mean Ocean Water (Isotopic Standard for oxygen and hydrogen).
ICP-OES	Inductively coupled plasma - optical emission spectrometry.
MC-ICP-MS	Multicollector inductively coupled plasma mass spectrometer.
WS-CRDs	Wavelength-scanned cavity ring-down spectroscopy.
IRMS	Isotope-ratio mass spectrometry.
SD	Standard deviation.
IBB-E 1 to IBB-E 16	Groundwater samples from the Ibbenbüren Eastfield coalfield (Germany).
IBB-W1	Groundwater sample from the Ibbenbüren Westfield coalfield (Germany).
SGW 1 to SGW 6	Shallow groundwater samples from the surroundings of the Ibbenbüren Eastfield coalfield (Germany).
BBH 1 to BBH 4	Groundwater samples from Triassic formations used for the thermal spa in the city of Bad Bentheim (Germany).
BE 1	Groundwater sample from the North German Basin close to the city of Bad Essen (Germany).
WK 1 and WM 1	Groundwater samples from Cretaceous formations of the Northern border of the Münsterland Basin, in city of Bad Rothenfelde (Germany).
SGG 1	Groundwater sample from the Saline Gottesgabe saltworks in the city of Rheine (Germany).
D_{K^+} , D_{Br^-}	Distribution coefficient of potassium and Bromide (subscripts). It is defined as the concentration of solute in a

	solvent (halite) divided by the concentration of solute in the aqueous phase (brine).
GMWL	Global Meteoric Waterline (Global annual average relationship between hydrogen and oxygen isotope ratios in natural meteoric waters).
LMWL	Local Meteoric Waterline (measured at Bad Salzufen, Germany).
IAE/WMO	The International Atomic Energy Agency / The World Meteorological Organization.
GNIP	The Global Network of Isotopes in Precipitation.
TU	Tritium units (1TU = 1 atom of tritium per 10^{18} atoms of hydrogen).
d-excess	Deuterium-excess (^2H isotope).
δD	Isotopic ratio of Deuterium (^2H isotope).
ϵ	Isotope enrichment factor (the ratio between the isotopic abundance of an isotope for a material and the natural abundance of that isotope).
BSR	Bacterial sulfate reduction.

Abstract

Underground hard coal mining operations irreversibly disrupt the pre-existing mechanical equilibrium of the geological media. The employment of high-recovery methods modifies the stress field of the sedimentary sequence, generating movement and faulting of the rock layers above and below mined seams. These new fracture zones do affect the original conditions of the hydrogeological system by modifying flow pathways and increasing the permeability of the rock sequence. Moreover, the surface area of rock exposed to air and water is increased, conditioning the water-rock interaction. Despite this rather clear conceptualization, flow and reactive transport processes in fractured overburdens are rarely modeled simultaneously. Discrete setups that consider fractures and porous matrix require extensive characterization of both media, which is impractical for regional case studies. As a result, most post-mining models explicitly ignore fracture structures by employing the equivalent porous approach or even both media with lumped parameter models. However, omitting either medium represents a delicate simplification, considering that mining-related fractures control the rate and direction of water flow within moderately permeable but relatively highly porous rock sequences.

In this dissertation, the specific contribution of fractured and matrix continua to the transient discharge and water quality of a post-mining coal zone is quantified and evaluated. For this purpose, dual and multiple interacting continua models are employed to simulate fluid flow and reactive mass transport in fractured and variable water-saturated rock sequences. The effectiveness of the models is evaluated by simulating the origin, generation and transport of acid mine drainage (i.e., water with elevated concentrations of hydrogen, iron, sulfate and chloride) within the shallow overburden of the Ibbenbüren Westfield. Compared to other coal districts in Germany, this area is strongly delimited by the local geology and topography, resulting in a well-defined hydrogeological system to test the models. Petrographic and chemical analyses performed on core samples from the area show the strong influence of mining-derived fractures on the water-rock interaction within the Carboniferous sequence. The presence of oxidized pyrite along with amorphous iron hydroxide phases in weathering fronts on both sides of the fractures demonstrates the exchange of solutes and gases between the fractured and the porous matrix media.

Based on the previous evidence, the TOUGHREACT software is employed to characterize flow and reactive transport processes in the Westfield. However, each of the two processes is simulated at separate stages to have more control in the adjustment of sensitive parameters for which little information is available. For the flow component, a dual continuum model, with

Richard's equations is used to characterize the unsaturated water flow in both fractured and matrix media. Under this approach, the model adequately reproduces the bimodal flow behavior of the discharges measured in the mine drainage for the years 2008 and 2017. Simulation results show how the fractured continuum generates intense discharge events during the winter months while the rock matrix controls smooth discharge limbs in summer, when water is slowly released back to the fractures. With the flow component calibrated, the second part of the study incorporates the geochemical processes into the model based on actual data from the rock samples. Their simulation requires extending the two-continuum setup to a multiple continua model with five nested block strings: one for the fractures and four for the rock matrix. This further subdivision prevents under-representations of kinetic reactions with short equilibrium length scales and numerical instabilities due to lack of chemical and flow gradients. As a result, the new multiple continua model provides good agreement with respect to long- and short-term concentrations and discharge trends measured in the mine drainage. The flow of oxygen and meteoric water through the fractured continuum leads to a high and steady release of hydrogen, iron and sulfate ions derived from pyrite oxidation in the matrix continua closest to the fractures. Moreover, high chloride concentrations result from the mixing and gradual release of relatively immobile solutes in the matrix as they interact with percolating water in the fracture. Both findings are equally congruent with the reactive pyrite oxidation and iron hydroxide precipitation fronts identified in the fractured core samples.

In the end, the multiple continua models, the simulation procedure and the results of the benchmark and sensitivity analysis scenarios developed for the Westfield pave the way for the application of the approach in other mining zones. The first candidate emerges in the Ibbenbüren Eastfield, where a coupled elemental-isotopic approach included in this thesis has confirmed that water-conducting fracture zones are primary elements for solute generation and transport in the first 300 meters of the overburden. In the latter case, calibration and verification of the models can be complemented with measurements of $\delta^{34}\text{S}$ in sulfates and $\delta^{18}\text{O}$, $\delta^2\text{H}$, and Tritium in water.

Zusammenfassung

Der untertägige Steinkohlenbergbau stört irreversibel das zuvor bestehende mechanische Gleichgewicht des geologischen Untergrunds. Der Einsatz produktiver Abbaumethoden verändert das Spannungsfeld der sedimentären Sequenz und erzeugt Bewegungen und Verwerfungen in den Gesteinsschichten über und unter den abgebauten Flözen. Neu erzeugte Klüftzonen wirken sich auf die ursprünglichen Bedingungen des hydrogeologischen Systems aus, indem sie die Fließwege verändern und die Durchlässigkeit der Gesteinssequenz erhöhen. Zudem wird die Kontaktfläche des Gesteins erhöht, was die Wechselwirkung zwischen Wasser, Luft und Gestein beeinflusst. Trotz dieser Konzeptualisierung werden Fließ- und reaktive Transportprozesse in geklüfteten Deckschichten selten gleichzeitig modelliert. Diskrete Ansätze, die sowohl Klüfte und poröse Matrix berücksichtigen, erfordern eine umfassende Charakterisierung beider Medien, was für regionale Fallstudien unrealistisch ist. Daher ignorieren die meisten nachbergbaulichen Grund-/Grubenwassermodelle explizite Klüftstrukturen, indem sie diese mittels einem äquivalenten porösen Ansatz oder gar beide Medien mit pauschaler Parametrisierung darstellen. Die Nichtbeachtung eines der beiden geologischen Medien stellt jedoch eine kritische Vereinfachung dar, wenn man bedenkt, dass bergbaubedingte Risse die Geschwindigkeit und Richtung des Wasserflusses in mäßig durchlässigen, aber hochporösen Gesteinsschichten steuern.

In dieser Dissertation wird der spezifische Beitrag von Klüft- und Matrixkontinua zum instationären Abfluss und zur Wasserqualität einer Kohle-Nachbergbauzone quantifiziert und bewertet. Zu diesem Zweck werden Doppel- und multiple interagierende Kontinua-Modelle verwendet, um den Wasserfluss und den reaktiven Massentransport in geklüfteten und variabel wassergesättigten Gesteinssequenzen zu simulieren. Die Effektivität der Modelle wird anhand der Simulation des Entstehungsprozesses, des Auftretens und des Transports von saurem Grubenwasser (d.h. Wasser mit erhöhten Konzentrationen von Wasserstoff, Eisen, Sulfat und Chlorid) innerhalb des flachen Deckgebirges des Ibbenbürener Westfeldes bewertet. Im Vergleich zu anderen Kohlerevieren in Deutschland ist dieses Gebiet durch die örtliche Geologie und Topographie räumlich begrenzt, so dass ein gut definiertes hydrogeologisches System zum Testen der Modelle vorliegt. Petrographische und chemische Analysen von Bohrproben aus dem Gebiet zeigen einen starken Einfluss von bergbaubedingten Klüften auf die Wasser-Gesteins-Interaktion innerhalb der Karbonabfolge. Das Vorhandensein von oxidiertem Pyrit zusammen mit amorphen Eisenhydroxidphasen in Verwitterungsfronten auf beiden Seiten der Klüfte zeigt den Austausch von gelösten Stoffen und Gasen zwischen den Klüften und der porösen Matrix.

Auf der Grundlage der bisherigen Erkenntnisse wird die Software TOUGHREACT eingesetzt, um die Strömungs- und reaktiven Transportprozesse im Westfeld zu charakterisieren. Jeder der beiden Prozesse wird jedoch in getrennten Phasen simuliert, um eine bessere Kontrolle bei der Anpassung empfindlicher Parameter zu haben, für die nur wenige Informationen verfügbar sind. Für die Strömungskomponente wurde ein doppeltes Kontinuumsmodell mit den Richards-Gleichungen verwendet, um den ungesättigten Wasserfluss sowohl in geklüfteten als auch in Matrix-Medien zu charakterisieren. Mit diesem Ansatz gibt das Modell das bimodale Fließverhalten der in den Jahren 2008 und 2017 in der Grubenentwässerung gemessenen Abflüsse adäquat wieder. Die Simulationsergebnisse zeigen, wie das geklüftete Kontinuum während der Wintermonate intensive Abflussereignisse erzeugt, während die Gesteinsmatrix im Sommer, wenn das Wasser langsam in die Klüfte zurückfließt, glatte Abflussganglinien generiert. Nachdem die Strömungskomponente kalibriert wurde, werden im zweiten Teil der Studie die geochemischen Prozesse in das Modell integriert, die auf gemessenen Daten aus den Gesteinsproben basieren. Ihre Simulation erfordert die Erweiterung des Zwei-Kontinuum-Aufbaus zu einem Multi-Kontinuum-Modell mit fünf verschachtelten Modellblöcken: einen für die Klüfte und vier für die Gesteinsmatrix. Diese Unterteilung verhindert die Unterrepräsentation von kinetischen Reaktionen mit kurzen Gleichgewichtslängen sowie numerische Instabilitäten aufgrund fehlender chemischer und/oder Strömungsgradienten. Im Ergebnis liefert das neue Multi-Kontinuum-Modell eine gute Übereinstimmung sowohl der lang- als auch der kurzfristigen Konzentrationen und Abflusstrends, die in der Grubenentwässerung gemessen wurden. Der Fluss von Sauerstoff und meteorischem Wasser durch das Kluftkontinuum führt zu einer hohen und stetigen Freisetzung von Wasserstoff-, Eisen- und Sulfationen, die aus der Pyritoxidation in den den Klüften am nächsten liegenden Matrixkontinua stammen. Darüber hinaus ergeben sich hohe Chloridkonzentrationen aus der Vermischung und allmählichen Freisetzung von relativ unbeweglichen gelösten Stoffen in der Matrix, die mit dem im Kluftbereich versickernden Wasser interagieren. Beide Ergebnisse stimmen mit den reaktiven Pyrit-Oxidations- und Eisenhydroxid-Ausfällungsfronten überein, die in den Bohrproben aus den Brüchen identifiziert wurden.

Schließlich ebnet die Multi-Kontinuum-Modelle, das Simulationsverfahren und die Ergebnisse der für das Westfeld entwickelten Benchmark- und Sensitivitätsanalyse-Szenarien den Weg für die Anwendung des Modellansatzes in anderen Abbaugebieten. Zuvorderst für das Ibbenbürener Ostfeld, wo ein in dieser Arbeit enthaltener gekoppelter elementar-isotopischer Ansatz bestätigt hat, dass wasserführende Kluftzonen primäre Elemente für die Bildung und den Transport gelöster Stoffe in den ersten 300 Metern des Deckgebirges sind. Im letzteren Fall kann die Kalibrierung und Verifizierung der Modelle durch Messungen von $\delta^{34}\text{S}$ in Sulfaten und $\delta^{18}\text{O}$, $\delta^2\text{H}$ und Tritium in Wasser vervollständigt werden.

Chapter 1: Introduction

1.1 Bedrock response to intensive mining operations

Underground coal mining operations tend to modify the pre-existing equilibrium conditions of the geological media (Kim et al. 1997). Coal removal redistributes the stress state in the surrounding rocks, leading to a series of mechanical effects that include movement, deformation and failure of bedrocks above and below the seam (Palchik 2003). The effects appear to be even more pronounced with the employment of intensive methods such as longwall or high-extraction room and pillar (Newman et al. 2017). In longwall mining, lengthy rectangular blocks (panels) are extracted in a single continuous operation using an automated cutting head that moves parallel to the coal face. When this happens, the work area is protected by a hydraulic roof support system. The latter, however, is moved as the mining front advances, causing the roof to collapse behind the operation line (Majdi et al. 2012; Cutler and Morris 2015). On the other hand, Room and pillar mining partially mine the coal seams, leaving intact large pillars to support the overlying bedrocks during the mine life. However, towards the end of the operations, miners systematically remove many of the pillars to obtain as much of the resource as possible, causing the roof to collapse behind them (Di Gianfrancesco 2017)

The collapse of the roof in either case causes temporally and permanent changes on the nature of the overburden structure and groundwater bodies. However, the magnitude and intensity of the disruptions are not only influenced by mining factors, but also by geological features such as thickness, lithology, geological structures, mechanical properties and in-situ stress state of the rock sequence (Meng et al. 2016). Over time, scholars have used these factors to characterize the zones into which the overburden is subdivided, usually known as caved, fractured and deformation zone (**Fig. 1**) (Palchik 2003; Zhang et al. 2018a; Bai and Tu 2019; Liu et al. 2019). The caved zone encompasses the highly fragmented area formed after the overburden fall to the mine floor, breaking the rock mass into irregular shapes of various sizes. A fractured zone is developed immediately above the caved zone, where the bedrocks break into blocks by both horizontal and through-going sub-vertical fractures. This bidirectional distribution of the fractures consequently creates a highly permeable fracture zone: while sub-vertical fractures dominate the vertical flow through the overburden, horizontal fractures areally connect the disrupted zone (Zhang et al. 2018c). Lastly, the overburden ends with a continuous deformation zone, where the layers bend without the development of major fractures.

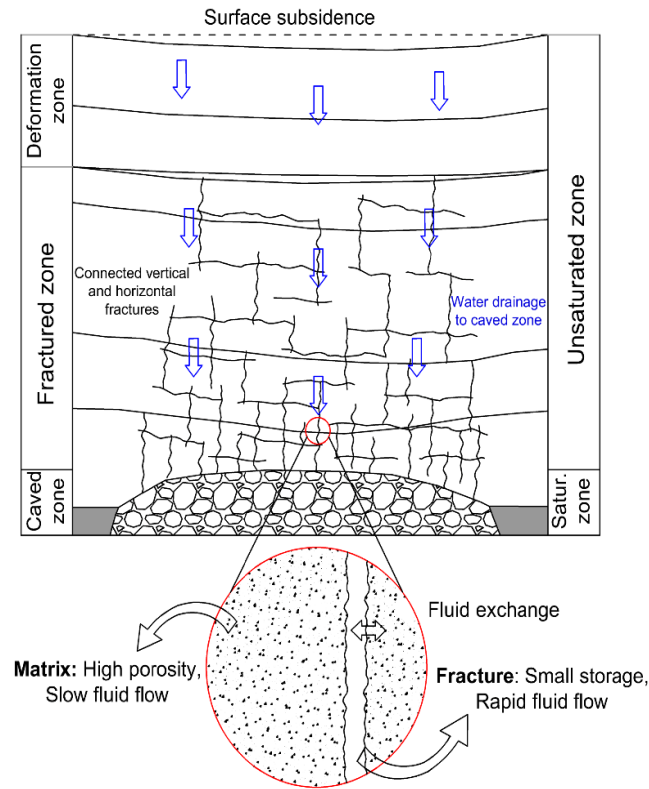


Fig. 1 Schematic profile and conceptual understanding of processes and modifications occurring in the overburden after high-recovery mining methods. Modified after Bai and Tu (2019) and David et al. (2017).

Out of the three zones, caved and water-conducting fracture zones have received the most attention given the threats of flooding and contaminant transport they pose to mining operations and the environment. Their hydrodynamic characterization is carried out with numerical and physical models, as well as empirical relationships that use parameters collected from field methods such as drill core analysis, remote sensing, fluid loss measurements, slug tests and geophysical loggings, among others. On the one hand, caved zones exhibit very high porosity and permeability values that allow the accumulation of large quantities of gas and water coming from the adjacent rock strata (Yang et al. 2018; Zhang et al. 2019; Mark 2021). Their vertical extension, however, is limited and depends mainly on the thickness of the coal seam and the strength and stratigraphy of the roof strata. Among the most conservative caving heights are those reported by Singh and Kendorski (1981), who calculated values from 3 to 6 times the thickness of the mined coalbed. Similarly, Zhang et al. (2011) determined caved zone extensions in the range of 5 to 6 times the mining height base on groundwater drawdown measurements and presence of surface cracks in the Shendong Coalfield, China. Longer extensions are reported by Karmis et al. (1983), with heights around 12 times the thickness of the exploited coal seam. This height was determined analyzing subsidence data measured in

longwall systems in the Appalachian coalfield, United States. Finally, Palchik (2002) found that caved zones in abandoned mines in Donetsk (Ukraine) could reach 4 to 11 times the thickness of the mined coal seam in places where overburden rocks are weak and porous. Thus, the collapse nature, high porosity and limited extent make it understandable that much of the research about the caved zone deals with calculating ground subsidence, doing mine planning of the overlying layers or detecting gas accumulations for its exploitation or spontaneous combustion prevention.

Fractured zones, on the other hand, represent major water and gas flow channels along the overburden, reason why many studies have focused on characterizing their extension and transport capacity. For instance, Gao et al. (2014) investigated rock fracturing due to stress and deformation changes in the rock mass surrounding the mining panels. Their numerical simulation on shear and tensile fracture propagation in a Ruhr coalfield showed horizontal extensions of 60 m in front of the extraction face and up to 80-90 m behind it. Later, Bai and Tu (2019) delved into the processes that generate tensile failure in bedrock above longwall mining, which led them to calculate development of vertical joints with openings in the range of 0.01 to 0.001 m. Complementary, Zhang et al. (2018b) used physical models to demonstrate higher density of inter-strata (i.e., vertical) fractures in areas above panel edges, marking these regions as the most suitable for coal methane extraction although without suggesting permeability or density values.

Regarding vertical dimensions, many studies have developed regression statistics and lithological constants to establish simple mathematical relationships to calculate heights of mining-derived fracture zones (see **Table 1**). For example, Booth and Spande (1992) examined the response of potentiometric levels and hydraulic properties caused by longwall mining in a 220-m-thick overburden in the southern Illinois coal basin. Pumping and packer tests yielded one order of magnitude increase in hydraulic conductivity for shale and sandstone layers 20 to 60 m above the mining face. Palchik (2003) determined heights of interconnected fractures zones between 19 and 41 times the thickness of the mined seam after measuring gas emission in wells located at different depths within the mining overburden. On their side, Majdi et al. (2012) presented five mathematical approaches to estimate extensions of distressed zones (fractured and caved zone combined). By analyzing mining free spaces and geometric dependencies of the strata during overburden movement, the authors calculate heights in the range of 6.5 to 46.5 times the mined thickness. Some other authors have tried to separate the hydraulically linked fractured zone from the overall disturbed zone. In this line, Guo et al. (2012) calculated cross-strata fracturing zone heights between 2 and 14 times the mined

thickness from groundwater pressure changes in the overburden. Qu et al. (2015) reduced this height to a range of 7 to 10 times the mining thickness, considering an overburden strength classification and the presence of competent strata (e.g., cemented) within the stratigraphic sequence. Finally, Zha et al. (2020) partially validated the empirical formula currently used in Chinese mining engineering for shallow operations. By using analogous physical models, the authors obtained heights around 20 times the mined seam for compressive strength regimes below 20 MPa. Apart from the cited literature, notable outlines of other empirical fracture/caving height formulas can be found in Bai & Tu (2019), Majdi et al. (2012) and Qu et al. (2015). Moreover, textbooks by Galvin (2016) and Peng (2021) are suggested for further detail of the technique, mechanical theory and field investigations associated with longwall mining.

Table 1 Fracture height predictions extracted from peer-review papers. M is mined height and n the number of consecutive mined seams.

Reference	Fractured zone height	Finding method
Booth and Spande (1992)	20 to 60 times the mined height.	Potentiometric drawdown measurements at a longwall mine with a 220 m overburden thickness located in the southern Illinois coal basin, USA.
Palchik (2003)	19 to 41 times the mining height.	Gas emission measurements in wells above coal mine faces located at depths of 280-420 m, Torezko-Snezhnyanskaya mining area, Ukraine.
Karacan and Goodman (2009)	6 - 22 times the mined height.	Change in overburden permeability values measured in gob gas ventholes within an 82-122 m thick coal mine overburden, in the northern Appalachian Basin, USA.
Zhang et al. (2011)	10 to 11 times the mining height.	Water table drawdown, surface cracks and ground subsidence measurements from boreholes and surface surveys in a 55 m thick mining overburden in the Shendong coal basin, China.
Majdi et al. (2012)	6.5 to 46.5 the mined height.	Five mathematical models that considers: <ul style="list-style-type: none"> - Geometry-independent factors: sequence compaction when accommodating the free space left by mining. - Geometry factors: geometric figures (parabola, vertical ellipse and triangle) whose base edge is the mined panel width. All five models are independent of depth, lithology, and location.

Reference	Fractured zone height	Finding method
Guo et al. (2012)	2 to 14 times the mined height	Measurements of groundwater pressure changes along a 700 m thick overburden of a coal mine in Anhui Province, China.
Qu et al. (2015)	7 to 10 times the mined height	Overburden strength classification based on lithological features and presence of key strata (e.g., cemented sandstones or shales) within non-particular rock sequence or depth.
Guo et al. (2019)	$H = 39.83 \ln(M) - 1.85$	Analogy experiments of a medium-hard lithologic array that emulates the 175 m thick overburden of the Gequan coal mine, Hebei Province, China.
Zha et al. (2020)	$H = \frac{100M}{5.1n + 5.2} + 5.1$	Analogous physical models that validate the employment of an empirical formula for weak overburdens (i.e., compressive strength less than 20 MPa) in Chinese coal mines.

1.2 Potential impacts on groundwater due to sequence disruptions

1.2.1 Integrity and flow conditions

Impacts on water quantity and quality following mining operations require careful assessment, even when some of these changes persist for centuries or millennia after mine closure (Wolkersdorfer 2006). Much of the concern arises from the modification of piezometric levels in aquifers (e.g. Walker 1988; Booth 2002, 2006; Newman et al. 2017; Zhang and López 2019). Development of subsidence-induced fractures along the overburden tend to reduce groundwater levels (**Fig. 2**), potentially causing serious environmental effects such as (ERMITE-Consortium et al. 2004):

- Depletion of water supply or irrigation wells, leading to an increase in the pumping head
- Drying up of springs and wells
- Land subsidence, either due to compaction of fine-grained sediments or the collapse of voids in karstic terrains; and
- Decreased flows in streams, wetlands, and lakes due to presence of compressive and tensile cracks at the waterbeds.

Specifically, groundwater drawdowns are attributed to three mechanisms acting over different time spans: 1) creation of fracture porosity, 2) direct water drainage via permeable fractures, and 3) transmitted drawdown. The first mechanism is usually related to an early and rapid

lowering of the water table due to sudden groundwater drainage into the newly created fracture spaces (Booth 2007). However, since fracture porosity is only a small proportion of the total overburden porosity, the decline phenomenon often stabilizes after a few weeks. As for the drawdown magnitude, this would depend on whether it is a confined or free aquifer. The volume of water released from storage with respect to the change in potential is equivalent to pore drainage for unconfined aquifers (i.e., specific yield), whereas for confined aquifers it depends on the elastic compressibility of the rock skeleton (i.e., storativity) (Booth 2002). Therefore, the enormous differences in magnitude between these two parameters cause the decrease in water table to vary widely. For example, an unconfined aquifer of 1m^2 area, specific yield of 0.1 and a fracture opening of 0.01m would have a head drop equal to 0.1m, while the same array would show a drawdown of 100 m if it were a confined aquifer with a storativity of 1×10^{-4} . In the latter case, the piezometric level drops very rapidly, potentially changing the condition of the aquifer from confined to unconfined in the event that fractures create a connection with the atmosphere.

Diversely, the increase of the vertical permeability of the sequence due to the fractured zones has a significant and permanent impact on the hydrogeological system. (Booth 2002). This second mechanism creates sharp changes in both hydraulic gradients and groundwater flow directions given the moderate permeability of many coal-bearing rock sequences (Morin and Hutt 2001; Wolkersdorfer 2006; Younger 2006). For example, new fracture zones cause higher infiltration rates of meteoric water into the sequence (i.e., groundwater recharge), drainage of aquifers and aquitards around the mined seam, or water-inrush into the tunnels, which is one of the most common and dangerous hazards in mining operations (Wang et al. 2012; Li et al. 2013; Li 2016). As for the degree of influence, this is given by specific fracture characteristics such as opening, frequency, direction, filling, smoothness and interconnectivity of one fracture with another. However, detailed delineation of these features for all relevant fractures surrounding a mine is beyond current technology and economics (Morin and Hutt 2001). This difficulty has led many studies to evaluate the response of the fracture network as a whole and not just individual structure. For instance, the employment of field or empirical methods in shallow rock sequences (e.g., pumping tests before and after mining, mathematical functions constructed from precipitation data, and measurements of surface streams losses) have revealed permeability increases of one to three orders of magnitude as a result of fracture zones (Zhang et al. 2018b; Lu et al. 2022).

The third mechanism corresponds to a horizontal propagation of the groundwater drawdown in rocks with relatively high transmissions. In such sequences, water withdrawal at the mine face

generates horizontal replenishment from further distances, developing an elongated cone of depression that may exit the mining area. For example, Booth (2002) reports groundwater depressions of 20 m in areas within 400 m horizontal distance of longwall operations in sandy coal mine sequences in Jefferson County (USA). However, this mechanism seems to be quite specific to certain locations, as there are numerous studies showing its absence as a consequence of the low transmissivity of coal-bearing sequences (e.g., Walker 1988; Booth and Spande 1992; Kay and Somer 2006; Bukowski and Bukowska 2012; Xu et al. 2018).

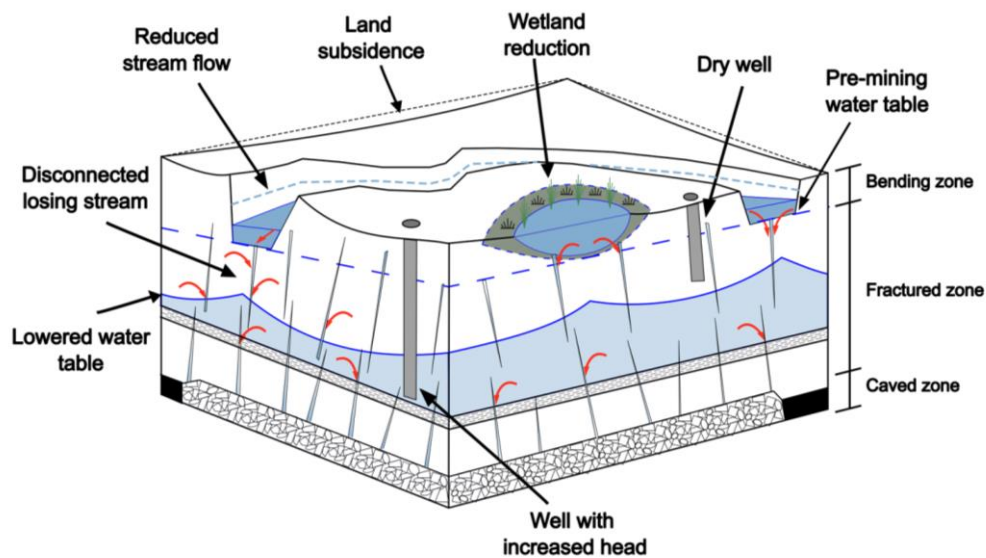


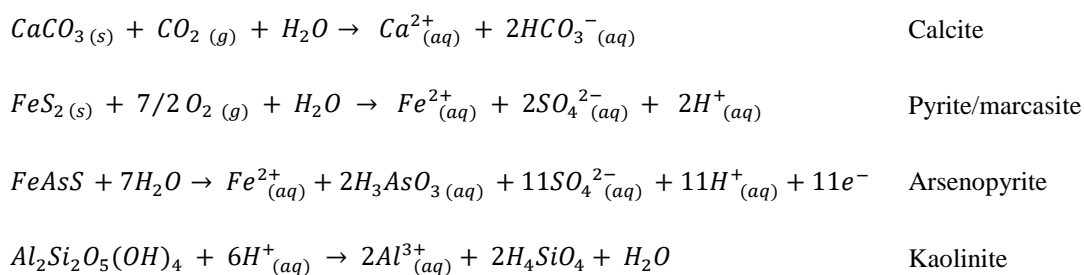
Fig. 2 Impacts on water availability generated by the reduction of phreatic levels due to development of subsidence-induced fracture zones along the overburden.

1.2.2 Geochemical conditions

Several studies have described how modifications of hydrogeological systems due to mine subsidence lead to changes in groundwater chemistry. On the one hand, increased water seepage from overlying and surrounding units causes its transport and mixing with pre-existing waters along the rock sequence. Whether this mixing causes a deterioration or an improvement in quality would depend on the chemistry of water from the recharging source (Booth and Bertsch 1999; ERMITE-Consortium et al. 2004). One example is what Pauvlik and Esling (1987) discovered on water samples of a glacial-alluvial aquitard in the Illinois basin. Prior to longwall mining, the aquitard showed consistent compositions of brackish and sulfate water. However, once mining began, chemical parameters exhibited seasonal fluctuations, which the authors linked to the application of agricultural fertilizers during the growing season. Therefore, longwall coal mining must have generated fractures that extended to the surface, allowing the input and transport of fertilizers to the aquitard. In the same Illinois basin, Booth and Bertsch

(1999) found that the development of a fracture zone increased rainwater percolation, causing a decrease in the sodium, chloride and sulfate contents of the water contained in shale layers above the mining panels. At the same time, they identified an enrichment of sulfate loads in the water of an underlying sandstone, which would evidence downward leakage from the shale caused by the fracture zone.

Alternatively, mining can affect the geochemistry of the overburden by promoting the weathering of minerals locked in the rocks. The newly created fracture network above the mining panels act as conduits for fluid flow, allowing water and air to interact with the freshly exposed material (Booth 2002). This process has been reported to be much more pronounced in shallow bedrocks, where groundwater drawdown enhances chemical reactions with the atmosphere oxygen (ERMITE-Consortium et al. 2004). Chemical reactions typically include dissolution of carbonates, precipitation of metal oxides/hydroxides, oxidation of sulfide minerals and acid dissolution of aluminosilicate minerals (Jankowski and Spies 2007). For example, sulfide minerals such as pyrite/marcasite (FeS_2), sphalerite (ZnS), galena (PbS), chalcopyrite ($CuFeS_2$), millerite (NiS) and arsenopyrite ($FeAsS$) weather from dissolved oxygen in water, releasing sulfate (SO_4^{2-}), their constituent metal cations and hydrogen into aqueous solutions (ERMITE-Consortium et al. 2004). Subsequently, the increased acidity favors the dissolution of clay minerals like kaolinite, muscovite, smectite and chlorite, releasing aluminum to the aqueous medium (Cama and Ganor 2015). The result of the overall process is the formation of a metalliferous leachate, typically known as acid mine drainage, which has the potential to adversely affect water, soil, flora and fauna elements (Semenkov et al. 2022). Some examples of the aforementioned dissolution reactions are presented below (Banks 2003):



In terms of concentration, dissolved metal loads in groundwater depend on the precipitation of secondary phases. Solid materials such as hydroxysulfates and amorphous ferric hydroxides can trap large proportion of the cations. Examples of these products include gypsum [$CaSO_4 \cdot 2H_2O$], melanterite [$FeSO_4 \cdot 7H_2O$], Coquimite [$Fe_2(SO_4)_3 \cdot 9H_2O$], Alunite [$KAl_3(SO_4)_2(OH)_6$], schwertmannite [$Fe^{III}_{16}O_{16}(OH)_{10}(SO_4)_3 \cdot 10H_2O$] and ferrihydrite [$Fe^{III}HO_8 \cdot 4H_2O$] among others. The degree of immobilization of the ions in these solid

phases can be appreciated by comparing molar concentrations. Generally, mine waters have sulfate molar concentrations ten or more times higher than those of the metals, which causes a sharp contrast with the 1:1 correspondence of the mineral formulas. However, despite trapping, the fraction that remains in solution is often sufficient to generate toxic effects in receiving waters and lands (ERMITE-Consortium et al. 2004).

It should be noted that seasonal fluctuations in the hydrodynamic and geochemical conditions of the mining system can lead to dissolution of solid phases and remobilization of trapped metals. Probably the most critical case occurs after mine closure, when pumping ceases and the water table rebounds to pre-mining levels. The rising water dissolves the highly soluble efflorescent salts and hydroxides accumulated over decades in mine buildings, flushing them out at concentrations several times higher than those observed during mining (Younger 1997; Gzyl and Banks 2007). This process, also known as first flush, results in environmentally aggressive waters, with very low pH and high sulfate and metal loads (**Fig. 3**). Over time, these high concentrations decrease exponentially until reaching levels close to the natural values observed in the surrounding aquifers (Younger 2000; Mugova and Wolkersdorfer 2022). The reason is the depletion of sulfate hydroxides together with the poor sulfide oxidation in the saturated zone. In the long term, significant ion production can only keep occurring in fractured strata that are permanently or temporarily (e.g., only in summer and autumn) above the water table (Younger 2002).

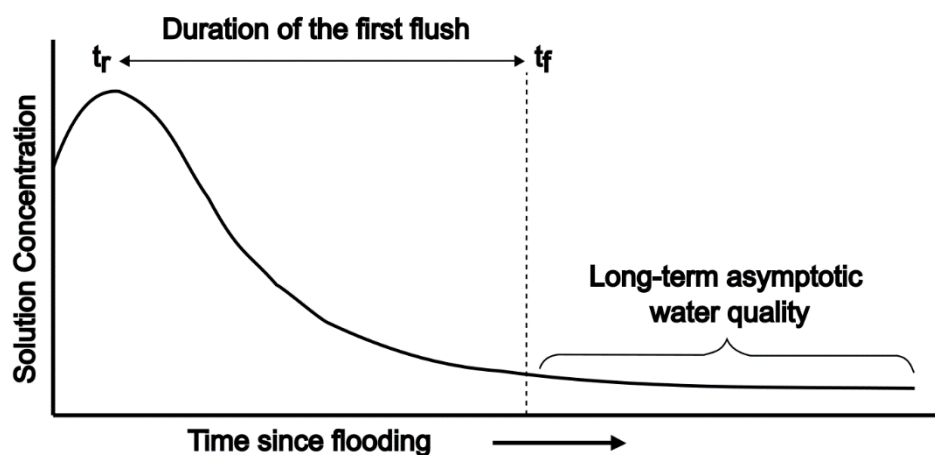


Fig. 3 Typical temporal variation in mine water ion concentration observed during and after the rebound process. The 'first flush' leads to a peak in concentrations after dissolving precipitates in mine voids, followed by a rapid decline that reaches an eventual steady. Modified after Younger (1997) and Merritt and Power (2022)

1.3 Modeling post mining setups

Most of the hydrogeological models employed for coal mining areas can be divided into global or distributive numerical models (Wolkersdorfer 2006; Kovács and Sauter 2007; Newman 2018). Analytical models have also been built, but their application is outdated, limited and highly disputed due to the complicated configuration of real underground mines (Wolkersdorfer 2006). The latter are used to solve problems involving uniform porous aquifers, with simple homogeneous geometry and under isothermal conditions. This section describes the generalities and principles of the two most used modeling approaches, without going into specifics on how they work, since most of them are adapted to particular requirements.

1.3.1 Global models

Global models, also called lumped parameter models or black box models, are single or multiple entity systems, designed to lump inflow, storage, and outflow processes into empirical mathematical functions (Younger 2006). The latter are able to reflect spatial patterns and time-dependent discharges only with the analysis of time series, thus ignoring the dynamics of groundwater flow in the system (Kordilla et al. 2012). Therefore, this type of analysis makes the approach especially useful for areas with little knowledge of the involved physical or chemical properties (Wolkersdorfer 2006). On the downside, lumping the system response into global factors makes the application of these models very difficult and misleading for characterizing heterogeneous sequences. For example, Maloszewski and Zuber (1996) show how the average age of a degradable tracer in a strongly stratified sequence can either give ages that only represent the upper, more active part of the system or show tracer-free waters due to heavy retention losses. In particular, two types of global models can be distinguished: single event and time series models (Jeannin and Sauter 1998)

Single event models deal with the global hydraulic response of the system to a unique recharge event. For this purpose, the storage and flow times of the input water are adjusted with simple or complex cascades of reservoirs (Kovács and Sauter 2007). Therefore, these models emerge as a volume balance method that requires hydraulic elements such as mine drives, drainages and faults to interconnect the boxes and adjust the final water balance in each compartment (DMT GmbH & Co. KG 2011). There are other type of models that provide a semi-quantitative relationship between the global flow and some hydraulic parameters, as well as the inclusion of reservoir geometric properties (Kovács and Sauter 2007). In those cases, there is a partial understanding and characterization of the system, so it is more appropriate to refer to them as "gray box models" rather than "black box models".

Time series analysis, on the other hand, evaluates the system response to a set of rainfall events by applying statistical techniques such as multivariate regression, curve fitting algorithms, parameter fitting packages, polynomial spline curves, Fourier series, wavelets, NURBS (non-uniform rational B-spline) or neural networks (Vermeulen et al. 2004). The basic principle is to compare a time series with itself in order to identify distinctive or concordant features, mainly cyclic variations, that are not visible in a standard hydrograph (Jeannin and Sauter 1998). Since the method is solely based on statistics, it fails to provide information on the physical functioning of the systems, being useful mainly for determining past trends or future predictions. In addition, each adjustment process is valid only for one site. An example of this approach is developed by Chen et al. (2002), who used cross correlation calculation, Fourier series, moving averaging and normal probability paper plot to correlate precipitation events and air temperatures with water levels recorded in more than 80 wells in an aquifer of southern Manitoba, Canada. Other examples of time series analysis are described by Sherwood and Younger 1994; Adams and Younger 2001; Banks 2001; Hoang et al. 2004; Wolkersdorfer 2006; and Westermann et al. 2018.

1.3.2 Numerical distributive models

Distributive models use numerical analysis to evaluate spatial and temporal variations in the physicochemical properties of hydrogeological systems (Galvin 2016). To do so, the heterogeneous media is discretized into subunits, with their own geometry, hydraulic parameters and boundary conditions (Kovács and Sauter 2007). Discretization can be carried out using either the Finite Difference Method (FDM) or the Finite Element Method (FEM) according to the selected numerical code (e.g., MODFLOW, TOUGH2, COMSOL and pFLOTRAN use finite differences while FEFLOW uses finite element). The distinction between one or the other lies in the way the flow domain is partitioned and, thus, the solution of the conservation equations (Kovács and Sauter 2007; Strack 2017). On the one hand, FDM subdivides the model domain into rectangular cells, which allows solving the partial derivatives by means of simple differences between a given number of adjacent nodes located at the corners or in the center of each cell. For its part, FEM subdivides the model domain into a triangular and/or quadrangular finite element network, facilitating the discretization of irregular elements. By having variable geometries, the approximation of the differential operators is analytical, and involves integral quantities for each element. Detailed information on the conservation equations for each method can be found in the textbooks of Wang and Anderson 1982; Zhang and Bennett 1995; and Strack 2017, while comprehensive comparisons between the two have

been addressed by van Genuchten 1982; Gray 1984; Celia et al. 1990; and Simpson and Clement 2003.

Within the distributed models, three approaches have been widely used to treat and discretize the heterogeneous media (**Fig. 4**): equivalent porous medium, dual or multiple continuum media and discrete fracture networks (Hartmann et al. 2014). In the first two, heterogeneities are averaged and treated in terms of effective parameters, while the third includes them as single or multiple entities, with their own distinct values. Among the three, most of the coal mine modeling has been carried out with the equivalent porous approach given its low discretization complexity and minimal changes in hydraulic parameters between adjacent units of similar size (e.g., Long et al. 1982; Bai and Elsworth 1993; Xiao et al. 1999; Vincenzi et al. 2010; Hu and Walsh 2021). The basic assumption underlying these models is that the disrupted rock sequence behaves as a porous continuum, with a hydraulic response lying somewhere in between the fracture network and the matrix medium (Kim et al. 1997; Younger 2006). Single parameters for the entire model (e.g., one porosity or one permeability value) are assigned based on average values obtained from field tests. Therefore, this approach does not adequately account for the hydraulic behavior of a medium without a very high fracture density (Long et al. 1982). In such a case, there is an oversimplification of one of the mediums' contribution, since field tests are performed either in the bulk material or close to a fracture structure (i.e., the measured flow is not generalized but happens only in certain parts of the model) (Hu and Walsh 2021).

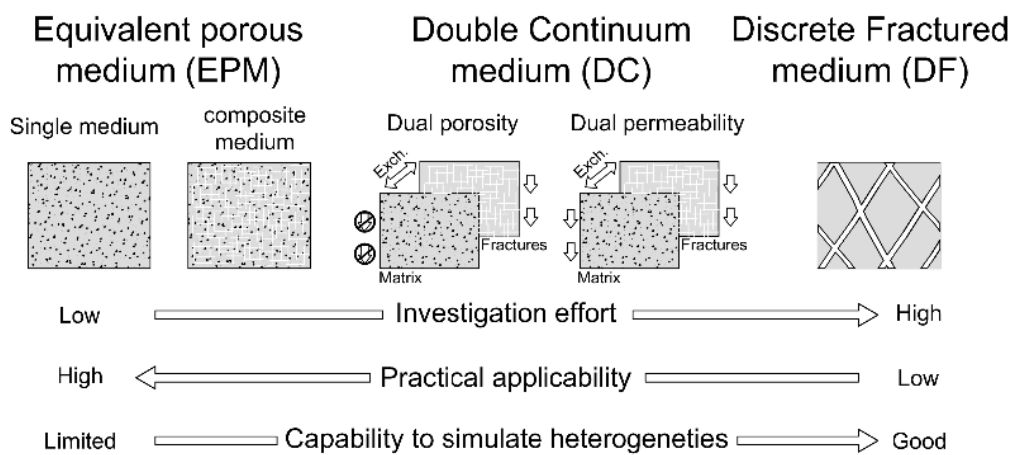


Fig. 4 Distributive approaches for modeling fractured rocks. Modified after Kordilla (2014)

In contrast, discrete fracture networks models (DFNs) focus on explicitly representing fractures as the only components responsible for the global flow. The approach treats each element as a semi-confined aquifer, being necessary to assign them separate values of transmissivity and storativity, as well as geometric parameters such as orientation, size, position, aperture, and

shape (La Touche and Cottrell 2017). The difficulty of obtaining detailed measurement of these features in the field, however, creates an inherent constraint when building deterministic DFN models. For example, while fracture orientation can be estimated from downhole measurements, aperture and continuity are always uncertain in three dimensions. These limitations have led to the employment of stochastic distribution methods (e.g., uniform, normal, normal, lognormal, Fisher or Elliptical Fisher) to randomly locate fractures in space (Dershowitz and Einstein 1988; Lei et al. 2017). It is important to note that stochastic models are computationally complex to perform and require an in-depth statistical treatment to validate the results (Rouleau and Gale 1987; Younes et al. 2020; Drouin et al. 2021). Additionally, model results are more likely to be unrealistic if the assumptions are simple (Fielding et al. 2011). Up to now, stochastic DFN models have been constructed in coal mining to simulate deformation structures from mass removal, being sporadically complemented with flow and transport components (e.g., Grenon et al. 2014; Katsaga et al. 2015; Lorig et al. 2015). Other DFN models have been built for nuclear waste repositories (e.g., Follin et al. 2014; Hadgu et al. 2017), unconventional hydrocarbon exploitation (e.g., Wei et al. 2019; Yaghoubi 2019) and CO₂ storage (e.g., Wang et al. 2019; Zhang et al. 2021).

Finally, the dual or multiple continuum approach represents a middle ground in modeling fractured sequences by considering them as two interacting, overlapping continua with different flow, transport, and storage parameters. Its way of addressing fractures as a single network of average characteristics acting in parallel to the porous medium solved the inability of equivalent porous models to account for both components and the difficulties of obtaining detailed information to build discrete fracture models. The interaction between the two continua is achieved by a mass transfer function determined by the size and shape of the blocks, as well as by their local difference in pressure and/or temperature potentials (Pruess and Narasimhan 1985; Beyer and Mohrlök 2006). Dual continuum models have been widely employed to solve diverse energetically and environmental topics, including heat transfer in fractured geothermal formations (e.g., Pruess and Narasimhan 1985; Hao et al. 2013), hydrocarbons production in hydraulically fractured shale and tight gas reservoirs (e.g., Kasiri and Bashiri 2011; Wu et al. 2011; Azom and Javadpour 2012), infiltration of water and nutrients into heterogeneous structured soils (e.g., Dohnal et al. 2007; Dušek et al. 2013) and simulation of saturated and unsaturated flow in karstified aquifers (e.g., Sauter 1992; Kordilla et al. 2012). In this sense, the poor record of the approach in coal mining is incomprehensible given its relative success in simulating flow and transport in fractured heterogeneous sequences. One of the few examples is developed by Guo et al. (2009) who coupled a mechanical model with a dual porosity setup

to describe and forecast water inflow and gas emission from two underground coal mines in Australia. Comparisons of numerical predictions with mine measurements demonstrated the capability of this approach to accurately predict fluxes in the fractured sequences above the longwall panels. Other examples have been directed at assessing methane release from coal beds in response to brittle deformation (e.g., Liu and Rutqvist 2010; Chen et al. 2019).

1.4 Scope and main research topics

The present dissertation focuses on establishing a dual and multiple continua models that can simulate fluid flow and reactive transport of contaminants through the water-conducting fractured zone resulting from longwall coal mining. The high fracture density as a byproduct of mining makes it possible to group them into a continuum with unique characteristics that reflect the hydraulic response of the entire network when modeled (Palchik 2003; Pruess et al. 2012; Bai and Tu 2019). This would address the difficulty of obtaining detailed information to construct discrete fracture setups and the inability of equivalent porous and lumped parameter models to account for fracture zones within a porous medium. In this regard, one of the main objectives of using the multiple continuum approach is to discover the extent to which the interaction of fluids with porous and fracture media is significant to the quantity and quality of water in post-mining zones. Additionally, I explore the ability of the approach to simulate phenomena such as hydrodynamic dispersion and mine water rebound, including characterization of the imbibition process.

This thesis takes the Ibbenbüren Westfield mine, located in northwest Germany, as a study case for constructing and evaluating the model (**Fig. 5**). Compared to other coal districts in the country, the Ibbenbüren's Carboniferous sequence is strongly delimited by geology and local topography, being expressed as an island-shaped hill (Bässler 1970). There, room and pillar was the dominant mining method until the 1940s, when operations were intensified using longwall technology (Rinder et al. 2020). In 1979 mining ceased, allowing groundwater to rebound over the next three years to a level of 65 m a.s.l. (Klinger et al. 2019). Until today the same water table is maintained by the Dickenberg adit, a drainage located about 60 m below ground surface, but 10 m higher than the surrounding plains (< 55 m a.s.l.). The higher level makes percolated precipitation the only groundwater input of the mine drainage, ruling out influences from surrounding Mesozoic and Quaternary aquifers. Therefore, this work focuses on the interaction of rainwater with porous units in the unsaturated zone (i.e., the first 60 meters) as the primarily responsible for the volume and chemistry of discharged mine water.

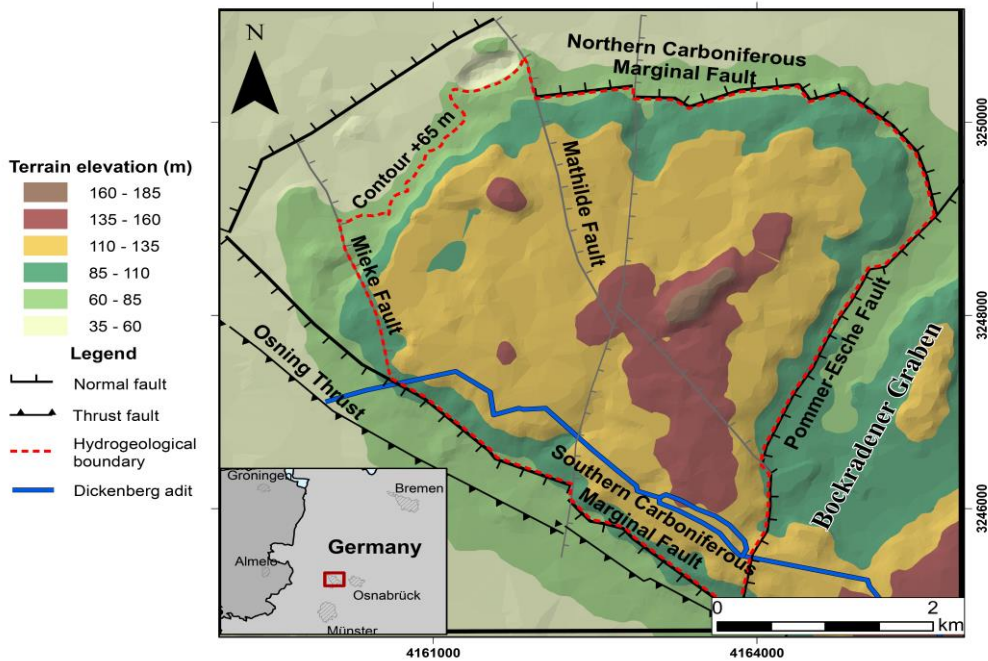


Fig. 5 Location map of the Ibbenbüren Westfield. The Carboniferous block is enclosed by regional faults structures, which are effective hydrogeological boundaries for the coalfield. Chapters 2, 3 and 4 present similar location figures that detail the geologic and hydrogeological situation of the area.

Besides the clear topographic and hydrogeological delineation, the area has the advantage of owing recent data from water samplings and core drilling campaigns. These data are used throughout the thesis to conceptualize, build and calibrate the numerical model. However, it should be noted that the objective is not simply to reproduce and verify the observations, but rather to understand the relative contribution of both elements (i.e., fracture and matrix) in the evolution of the flow and transport regimes in the area. The topics and questions addressed to achieve this objective are developed through three peer-reviewed publications included in this cumulative dissertation. A fourth article addressing water-rock interaction in the adjacent and deeper Carboniferous sequence of the Ibbenbüren Eastfield is also included. Specificities of each of the four publications are summarized below.

1.4.1 Article 1: A Petrographic Investigation of the Carboniferous Sequence from the Ibbenbüren Mine: Tracing the Origin of the Coal Mine Drainage.

This first paper examines the spatial distribution of water-rock interactions in the fractured overburden of the Westfield and their potential influence on the elevated chloride, iron and sulfate contents recorded in the discharged water. As the Westfield phreatic level is above the surrounding Quaternary plains, the chemical signature of the discharge water must be influenced by the interaction of percolating rainwater with the unsaturated rock sequence. However, many studies over time have described both low permeability and reduced porosity

values for the Carboniferous block (e.g., Bässler 1970; Wüstefeld et al. 2017; Becker et al. 2017, 2019; Klinger et al. 2019). This clearly limits access to the reactive minerals and solutes contained in the matrix, which are the potential source of the high ion concentrations.

Our hypothesis is that water-rock interaction has been greatly enhanced by decades of longwall mining in the Dickenberg coal seam, located about 60 m below ground surface. These operations may have generated vertical brittle deformations (i.e., fractures) that increase hydraulic conductivity and alter groundwater flow paths in the shallow overburden. The percolating water harnesses these water-conducting fractured zones to interact with the minerals and solutes present in the rock matrix. To test the hypothesis, we combine several analytical techniques to characterize the Westfield Carboniferous sequence from two full-diameter core samples recovered in the area. The study includes the identification and analysis of mineralogical components and rock structures that support recent bedrock alterations (e.g., authigenic, reactive or altered mineral phases, fractures, and morphological features) and that, in turn, may relate to mechanisms governing the chemical signature of coal mine drainage. Particular attention is given to the distribution of both sulfide mineral alteration and iron hydroxides precipitation throughout the fractured sandstones. This article forms Chapter two of this thesis and was published in the special issue *Geochemistry and Mineralogy of Coal-Bearing Rocks* of the journal *Minerals*.

1.4.2 Article 2: A dual-continuum model (TOUGH2) for characterizing flow and discharge in a mechanically disrupted sandstone overburden.

With the first article, we showed the occurring interplay between the fractured and matrix media in the Westfield. For example, the presence of alteration fronts on both sides of open fractures confirms water and oxygen exchange between the newly opened structures and the overburden. These results were the key point that allowed us to conceptualize the flow component of the area, which can also be applicable to other mining zones. In general, fluid flow in post-mining overburden can be described by four processes: (1) meteoric water infiltration into the first meters of soil and disaggregated rock, (2) percolation through an undisturbed zone, (3) groundwater flow in sub-vertical fracture networks, and (4) flow and groundwater storage in the porous matrix. However, as the latter two processes take place in the same physical space (i.e., water-conducting fractured zone), they are rarely modeled simultaneously given the extensive characterization required for both media. As discussed earlier in the introduction, most post-mining models explicitly ignore fracture structures by employing the equivalent porous medium (EPM) approach or even both media with lumped parameter models.

The purpose of the second paper is to characterize fluid flow in the water-conducting fractured zone of the Ibbenbüren Westfield using the Dual Continuum (DC) approach. The latter allows us to quantify the contribution that both fractures and matrix elements have on the volumes of discharged water throughout the year. Based on hydrographs of the area, we hypothesize that the fractured zone behaves similar to a karst system, where discharge peaks reveal the response of conduits to large recharge events, while recession limbs are the result of water flow in the matrix blocks (e.g., see Sauter 1992; Bonacci 1993; Kordilla et al. 2012). To test this idea, the TOUGH2 software (by Lawrence Berkeley National Laboratory) is employed in this paper to simulate the fractured and unsaturated overburden of the Westfield. The model is calibrated using daily discharges recorded throughout 2008, and then validated with discharge data from 2017. Moreover, the study includes a sensitivity analysis that helps to reduce the ambiguity of the results, while giving an idea of those variables that can be set within a reasonable range without affecting the model's efficiency. This article constitutes the third chapter of the present thesis and was published in *Hydrogeology* journal.

1.4.3 Article 3: A multiple interactive continua model (MINC) to simulate reactive mass transport in a post-mining coal zone: A case study of the Ibbenbüren Westfield.

The promising results of chapter three led us to extend the flow setup to a model that includes conservative solute transport along with kinetic and equilibrium geochemical reactions. The goal of such a model is to identify and reproduce both long- and short-term formation, movement, and deposition of contaminants in the Westfield since the mining onset. We also study the temporal and spatial evolution of brine dilution, pyrite oxidation and iron hydroxide precipitation, all processes inferred from the analysis of drill cores in the first article. These reactions, promoted by the movement of water and oxygen in the fractures, would be responsible for the generation of acid mine drainage and, therefore, for the high concentrations of sulfate, iron, chloride, and other dissolved metals measured in the Dickenberg adit.

In this third paper, the software TOUGHREACT is employed to set up a 2D multiple interactive continuum model of the unsaturated overburden of the Westfield. The model's geochemical component includes dissolution, precipitation and dilution processes related to iron-, sulfate- and chloride-bearing minerals and solutions. The simulation is performed through a 5-stage process that addresses variable initial and boundary conditions resulting from system modification due to variable mining phases. As for the setup, we extend the two-element dual continuum approach, used for the flow component, to a model with a one-element fractured continuum and four nested blocks for the matrix continuum, each located at a variable distance

from the fracture. This new configuration allows accounting for reaction fronts across matrix blocks, showing the geochemical variations of both rocks and groundwater over time. For example, reactive minerals and solutes closer to fractures would interact readily with oxygen and water percolating through them during the early years of mining. However, over time this interaction would tend to reduce as the materials near the fracture are depleted, causing the water to penetrate further into the matrix to interact with fresh rocks. The increase in the number of continua also validates the use of the approach to simulate fractured media by solving the block size constraint when simulating diffusive flow across the fracture-matrix interface. This latter is one of the limitations commonly raised against the dual continuum method (e.g., Lichtner 2000; Iraola et al. 2019). This article represents Chapter 4 and was presented for review in the journal *Mine Water and the Environment* at the time of the thesis submission.

1.4.4 Article 4: Geochemistry of coal mine drainage, groundwater, and brines from the Ibbenbüren mine, Germany: A coupled elemental-isotopic approach.

At the Ibbenbüren Eastfield, much of the public attention has focused on the characterization and management of the mine drainage since its closure, in December 2018. However, water quantity and quality at this mine are slightly different from those measured at the Westfield due to variations in geological and mining conditions. On the one hand, the Carboniferous sequences of the West- and East-field are separated by a graben structure that generates stratigraphic differences of up to 500 meters in favor of the latter (i.e., a more complete sequence). Also, the Eastfield block has less fault segmentation, resulting in greater horizontal continuity of the sedimentary layers. These two factors prompted longwall mining to depths down to -1500 m a.s.l., potentially modifying several hydrogeological units within the Carboniferous block. Therefore, this paper, led by Thomas Rinder, applies a coupled elemental-isotopic approach to identify the origin of extracted mine drainage, groundwater, and brines in the Eastfield.

Specifically, isotope ratios $^{34}\text{S}/^{32}\text{S}$ and $^{18}\text{O}/^{16}\text{O}$ in sulfate, $^{18}\text{O}/^{16}\text{O}$ and $^2\text{H}/^1\text{H}$ in H_2O , and $^{87}\text{Sr}/^{86}\text{Sr}$ in dissolved Sr are used to elucidate the origin of solutes found at different depths within the mine. Analysis of these isotopic systems allows us to develop a conceptual fluid and mass transport model that should vary as a function of depth. Unlike Westfield, water-conducting fracture zones at Eastfield are unlikely to be the main flow paths along the 1500 meters of mined block due to their closure by lithostatic pressure (Wang et al. 2016a, b). Thus, we aim to determine up to what depth these fracture zones influence the composition of the mine drainage with shallow fluids. We also look for evidence of other elements or phenomena

that can transport formation, deep and surface waters or other solutes from outside the block to the mine drainage. This paper represents the fifth chapter of this thesis and was published in the journal *Applied Geochemistry*.

1.5 Statement of own contribution to the manuscripts

1. **Bedoya-Gonzalez, D.**, Hilberg, S., Redhammer, G. & Rinder, T. (2021) A Petrographic Investigation of the Carboniferous Sequence from the Ibbenbüren Mine: Tracing the Origin of the Coal Mine Drainage. *Minerals*, 11, 1–19. <https://doi.org/10.3390/min11050483>

As a first author, I wrote the manuscript, conceived and planned the experiments, prepared and described the thin sections from the core samples, analyzed the samples with polarized and scanning electron microscopes and prepared all figures and tables. Sylke Hilberg supervised the project and supported the author throughout the manuscript creation process with valuable comments and discussions. Günther Redhammer prepared the samples and performed the X-ray diffraction measurements, providing valuable comments to their analysis. Thomas Rinder conceived and planned the experiments, drafted sections of the manuscript and interpreted the X-ray diffraction data. All authors discussed the results and commented on the manuscript.

2. **Bedoya-Gonzalez, D.**, Kessler, T., Rinder, T., & Schafmeister, M.T. (2022) A dual-continuum model (TOUGH2) for characterizing flow and discharge in a mechanically disrupted sandstone overburden. *Hydrogeol J.*, 30, 1717–1736. <https://doi.org/10.1007/s10040-022-02507-3>

As a first author, I wrote the manuscript, conceptualized and created the model, researched and scrubbed the employed data, performed the numerical simulations and prepared all figures and tables. Timo Kessler and Thomas Rinder verified the conceptual model and contributed to the interpretation of the results. Maria-Theresia Schafmeister commented and helped with the sensitivity analysis, supervised the project and supported the first author throughout the manuscript creation process with critical feedback. All authors discussed the results and commented on the manuscript.

3. **Bedoya-Gonzalez, D.**, Kessler, T., Rinder, T., Hilberg, S., Szabó-Krausz, Z., & Schafmeister, M.T. [Subm.] A multiple interactive continua model (MINC) to simulate reactive mass transport in a post-mining coal zone: A case study of the Ibbenbüren Westfield. *Mine Water and the Environment J.*

As a first author, I wrote the manuscript, researched and adapted the approach theory, conceptualized and created the model, designed the simulation methodology; scrubbed the employed data, performed the numerical simulations and prepared all figures and tables. Timo Kessler verified the conceptual model and helped with the construction of the transport component of the model. Thomas Rinder and Zsuzsanna Szabó-Krausz contributed with the construction of the chemical component of the model, including the formulation of the chemical reactions, equilibrium and kinetic constants. Sylke Hilberg and Maria-Theresia Schafmeister checked the basis of the model, supervised the project and supported the first author throughout the manuscript creation process with critical feedback and discussions. All authors discussed the results and commented on the manuscript.

4. Rinder, T., Dietzel, M., Stammeier, J.A., Leis, A., **Bedoya-González, D.**, & Hilberg, S. (2020) Geochemistry of coal mine drainage, groundwater, and brines from the Ibbenbüren mine, Germany: a coupled elemental- isotopic approach. *Appl Geochemistry J.*, 121, 104693. <https://doi.org/10.1016/j.apgeochem.2020.104693>

I contributed and commented on the construction of the conceptual transport model from the data analysis and helped with the preparation of the figures. Thomas Rinder conceived the original idea, wrote the manuscript, carried out the sampling, designed and performed the experiments, analyzed the results, prepared the tables and figures. Martin Dietzel and Sylke Hilberg supported the first author throughout the manuscript creation process with valuable comments and discussions. Jessica Stammeier and Albrecht Leis prepared and performed the isotopic analyses on the water samples in addition to assisting the first author with the analysis of the results. All authors discussed the results and commented on the manuscript.

Diego Alexander Bedoya Gonzalez

I confirm the author contribution statements.

Greifswald, _____
(date) Prof. Dr. Maria-Theresia Schafmeister

1.6 References

- Adams R, Younger PL (2001) A strategy for modeling ground water rebound in abandoned deep mine systems. *Ground Water* 39:249–261. <https://doi.org/10.1111/j.1745-6584.2001.tb02306.x>
- Azom PN, Javadpour F (2012) Dual-Continuum Modeling of Shale and Tight Gas Reservoirs. Paper presented at the SPE Annual Technical Conference and Exhibition, San Antonio, Texas, USA. *Soc Pet Eng*. <https://doi.org/10.2118/159584-MS>
- Bai M, Elsworth D (1993) Transient poroelastic response of equivalent porous media over a mining panel. *Eng Geol* 35:49–64. [https://doi.org/10.1016/0013-7952\(93\)90069-O](https://doi.org/10.1016/0013-7952(93)90069-O)
- Bai Q, Tu S (2019) A general review on longwall mining-induced fractures in near-face regions. *Geofluids* 2019:22. <https://doi.org/10.1155/2019/3089292>
- Banks D (2003) Geochemical processes controlling minewater pollution. In: Prokop G, Younger P, Roehl KE (eds) *Groundwater management in mining areas*. Umweltbundesamt GmbH, Pécs, Hungary, June 23-27, 2003, pp 17–44
- Banks D (2001) A variable-Volume, head-dependnt mine water fillig model. *Ground Water* 39:362–365. <https://doi.org/10.1111/j.1745-6584.2001.tb02319.x>
- Bässler R (1970) Hydrogeologische, chemische und Isotopen - Untersuchungen der Grubenwässer im Ibbenbürener Steinkohlenrevier. *Z deutsch geol Ges* 209–286. <https://doi.org/10.1127/zdgg/120/1970/209>
- Becker I, Busch B, Koehrer B, et al (2019) Reservoir Quality Evolution of Upper Carboniferous (Westphalian) Tight Gas Sandstones, Lower Saxony Basin, Nw Germany. *J Pet Geol* 42:371–392. <https://doi.org/10.1111/jpg.12742>
- Becker I, Wüstefeld P, Koehrer B, et al (2017) Porosity and permeability variations in a tight gas sandstone reservoir analogue, Westphalian D, Lower Saxony basin, NW Germany: influence of depositional setting and diagenesis. *J Pet Geol* 40:363–389. <https://doi.org/10.1111/jpg.12685>
- Beyer M, Mohrlök U (2006) Parameter estimation for a double continuum transport model for fractured porous media. In: *Proceedings of ModelCARE'*. IAHS Publ. 304, 2006., The Hague, The Netherlands, June 2005, pp 80–86
- Bonacci O (1993) Karst springs hydrographs as indicators of karst aquifers. *Hydrol Sci J* 38:51–62. <https://doi.org/10.1080/02626669309492639>
- Booth CJ (2006) Groundwater as an environmental constraint of longwall coal mining. *Environ Geol* 49:796–803. <https://doi.org/10.1007/s00254-006-0173-9>
- Booth CJ (2002) The effects of longwall coal mining on overlying aquifers. *Geol Soc Spec Publ* 198:17–45. <https://doi.org/10.1144/GSL.SP.2002.198.01.02>
- Booth CJ (2007) Confined-unconfined changes above longwall coal mining due to increases in fracture porosity. *Environ Eng Geosci* 13:355–367. <https://doi.org/10.2113/gseegeosci.13.4.355>
- Booth CJ, Bertsch LP (1999) Groundwater geochemistry in shallow aquifers above longwall mines in Illinois, USA. *Hydrogeol J* 7:561–575. <https://doi.org/10.1007/s100400050229>
- Booth CJ, Spande ED (1992) Potentiometric and Aquifer Property Changes Above Subsiding

- Longwall Mine Panels, Illinois Basin Coalfield. *Groundwater* 30:362–368. <https://doi.org/10.1111/j.1745-6584.1992.tb02004.x>
- Bukowski P, Bukowska M (2012) Changes of some of the mechanical properties of rocks and rock mass in conditions of mining exploitation and mine workings flooding. *AGH J Min Geoengin* 36:57–67
- Cama J, Ganor J (2015) Dissolution Kinetics of Clay Minerals. In: Tournassat C, Steefel CI, Bourg IC, Bergaya F (eds) *Developments in Clay Science*, 1st edn. Elsevier, pp 101–153
- Celia MA, Bouloutas ET, Zarba RL (1990) A general mass-conservative numerical solution for the unsaturated flow equation. *Water Resour Res* 26:1483–1496. <https://doi.org/10.1029/WR026i007p01483>
- Chen M, Hosking LJ, Sandford RJ, Thomas HR (2019) Dual porosity modelling of the coupled mechanical response of coal to gas flow and adsorption. *Int J Coal Geol* 205:115–125. <https://doi.org/10.1016/j.coal.2019.01.009>
- Chen Z, Grasby SE, Osadetz KG (2002) Predicting average annual groundwater levels from climatic variables: An empirical model. *J Hydrol* 260:102–117. [https://doi.org/10.1016/S0022-1694\(01\)00606-0](https://doi.org/10.1016/S0022-1694(01)00606-0)
- Cutler JC, Morris C (2015) *Dictionary of Energy*, 2nd edn. Elsevier, Amsterdam, Netherlands
- David K, Timms WA, Barbour SL, Mitra R (2017) Tracking changes in the specific storage of overburden rock during longwall coal mining. *J Hydrol* 553:304–320. <https://doi.org/10.1016/j.jhydrol.2017.07.057>
- Dershowitz WS, Einstein HH (1988) Characterizing rock joint geometry with joint system models. *Rock Mech Rock Eng* 21:21–51. <https://doi.org/10.1007/BF01019674>
- Di Gianfrancesco A (2017) Worldwide overview and trend for clean and efficient use of coal. In: Di Gianfrancesco A (ed) *Materials for Ultra-Supercritical and Advanced Ultra-Supercritical Power Plants*. Woodhead Publishing, pp 643–687
- DMT GmbH & Co. KG (2011) *BoxModel Concept: ReacFlow3D - Modelling of the flow of mine water and groundwater, mass and heat transport*. Essen, Germany
- Dohnal M, Dusek J, Vogel T, et al (2007) Dual-continuum modeling of dye tracer infiltration into soil with biopores. In: *Proceedings Bioclimatology and natural hazards International Scientific Conference*. Poľana nad Detvou, Slovakia, September 17 - 20, 2007.
- Drouin G, Fahs M, Droz B, et al (2021) Pollutant Dissipation at the Sediment-Water Interface: A Robust Discrete Continuum Numerical Model and Recirculating Laboratory Experiments. *Water Resour Res* 57:1–16. <https://doi.org/10.1029/2020WR028932>
- Dušek J, Lichner Ľ, Tomáš V, Štekauerová V (2013) Transport of iodide in structured soil under spring barley during irrigation experiment analyzed using dual-continuum model. *Biologia (Bratisl)* 68:1094–1098. <https://doi.org/https://doi.org/10.2478/s11756-013-0249-4>
- ERMITE-Consortium, Younger PL, Wolkersdorfer C (2004) Mining Impacts on the Fresh Water Environment: Technical and Managerial Guidelines for Catchment-Focused Remediation. *Mine Water Environ* 23:s2–s80. <https://doi.org/https://doi.org/10.1007/s10230-004-0028-0>
- Fielding M, Nott DJ, Liong SY (2011) Efficient MCMC schemes for computationally expensive posterior distributions. *Technometrics* 53:16–28. <https://doi.org/10.1198/TECH.2010.09195>

- Follin S, Hartley L, Rhén I, et al (2014) Une méthodologie pour établir les paramètres du modèle hydrogéologique d'un réseau de fractures discrètes dans une roche cristalline peu fracturée, illustrée d'après les données du site de stockage de déchets nucléaires haute activité projeté à Forsmark, . *Hydrogeol J* 22:313–331. <https://doi.org/10.1007/s10040-013-1080-2>
- Galvin JM (2016) *Ground Engineering - Principles and Practices for Underground Coal Mining*, 1st edn. Springer Cham, Switzerland
- Gao F, Stead D, Coggan J (2014) Evaluation of coal longwall caving characteristics using an innovative UDEC Trigon approach. *Comput Geotech* 55:448–460. <https://doi.org/10.1016/j.compgeo.2013.09.020>
- Gray W (1984) Comparison of Finite Difference and Finite Element Methods. In: *Fundamentals of Transport Phenomena in Porous Media*, NATO Advanced Science Institutes Series. Martinus Nijhoff Publishers, The Netherlands, pp 899–952
- Grenon M, Bruneau G, Kapinga Kalala I (2014) Quantifying the impact of small variations in fracture geometric characteristics on peak rock mass properties at a mining project using a coupled DFN-DEM approach. *Comput Geotech* 58:47–55. <https://doi.org/10.1016/j.compgeo.2014.01.010>
- Guo H, Adhikary DP, Craig MS (2009) Simulation of mine water inflow and gas emission during longwall mining. *Rock Mech Rock Eng* 42:25–51. <https://doi.org/10.1007/s00603-008-0168-9>
- Guo H, Yuan L, Shen B, et al (2012) Mining-induced strata stress changes, fractures and gas flow dynamics in multi-seam longwall mining. *Int J Rock Mech Min Sci* 54:129–139. <https://doi.org/10.1016/j.ijrmms.2012.05.023>
- Guo W, Zhao G, Lou G, Wang S (2019) Height of fractured zone inside overlying strata under high-intensity mining in China. *Int J Min Sci Technol* 29:45–49. <https://doi.org/10.1016/j.ijmst.2018.11.012>
- Gzyl G, Banks D (2007) Verification of the “first flush” phenomenon in mine water from coal mines in the Upper Silesian Coal Basin, Poland. *J Contam Hydrol* 92:66–86. <https://doi.org/10.1016/j.jconhyd.2006.12.001>
- Hadgu T, Karra S, Kalinina E, et al (2017) A comparative study of discrete fracture network and equivalent continuum models for simulating flow and transport in the far field of a hypothetical nuclear waste repository in crystalline host rock. *J Hydrol* 553:59–70. <https://doi.org/10.1016/j.jhydrol.2017.07.046>
- Hao Y, Fu P, Carrigan CR (2013) Application of a dual-continuum model for simulation of fluid flow and heat transfer in fractured geothermal reservoirs. In: *Proceedings, 38th Workshop On Geothermal Reservoir Engineering*, vol SGP-TR-198. Stanford University, Stanford, California. 11-13 February 2013, pp 462–469
- Hartmann A, Goldscheider N, Wagener T, et al (2014) Karst water resources in a changing world: Review of hydrological modeling approaches. *Rev Geophys Rev* 218–242. <https://doi.org/10.1002/2013RG000443>
- Hoang DL, Trinh VG, Dang DN (2004) Modeling of groundwater flow by black box models and environmental isotopes. *Commun Phys* 14:221–226
- Hu R, Walsh SDC (2021) Effective continuum approximations for permeability in brown-coal and other large-scale fractured media. *Geosci* 11:.

<https://doi.org/10.3390/geosciences11120511>

- Iraola A, Trincherio P, Karra S, Molinero J (2019) Assessing dual continuum method for multicomponent reactive transport. *Comput Geosci* 130:11–19. <https://doi.org/10.1016/j.cageo.2019.05.007>
- Jankowski J, Spies B (2007) Impact of longwall mining on surface water-groundwater interactions and changes in chemical composition of creek water. In: Ribeiro L, Chambel A, Condesso de Melo MT (eds) *Proceedings of the XXXV IAH Congress: Groundwater and Ecosystems*. International Association of Hydrogeologists, Lisbon, Portugal, 17-21 September, 2007, pp 144–154
- Jeannin P-Y, Sauter M (1998) Analysis of karst hydrodynamic behaviour using global approaches: a review. *Bull d'hydrogéologie* 16:31–48. <https://doi.org/PNR61>
- Karacan Ö, Goodman G (2009) Hydraulic conductivity changes and influencing factors in longwall overburden determined by slug tests in gob gas ventholes. *Int J Rock Mech Min Sci* 46:1162–1174. <https://doi.org/10.1016/j.ijrmms.2009.02.005>
- Karmis M, Triplett T, Haycocks C, Goodman G (1983) Mining subsidence and its prediction in an Appalachian coalfield. In: *Rock Mechanics: Theory, Experiment, Practice. Proc. 24th US Symp. Rock Mechanics*. Balkema, Rotterdam, 20–23 June 1983, Texas, USA., pp 665–675
- Kasiri N, Bashiri A (2011) Status of Dual-Continuum Models for Naturally Fractured Reservoir Simulation. *Pet Sci Technol* 29:1236–1248. <https://doi.org/10.1080/10916460903515557>
- Katsaga T, Riahi A, DeGagne DO, et al (2015) Hydraulic fracturing operations in mining: Conceptual approach and DFN modeling example. *Trans Institutions Min Metall Sect A Min Technol* 124:255–266. <https://doi.org/10.1179/1743286315Y.0000000022>
- Kay D, Somer B De (2006) Impacts of Longwall Mining to Rivers and Cliffs in the Southern Coalfield. In: Aziz N, Kininmonth B (eds) *Proceedings of the 2006 Coal Operators' Conference*. Wollongong, Australia, 6-7 July 2006, pp 327–336
- Kim JM, Parizek RR, Elsworth D (1997) Evaluation of fully-coupled strata deformation and groundwater flow in response to longwall mining. *Int J Rock Mech Min Sci* 34:1187–1199. [https://doi.org/10.1016/S1365-1609\(97\)80070-6](https://doi.org/10.1016/S1365-1609(97)80070-6)
- Klinger C, Rüterkamp P, Eckart M (2019) Abschlussbetriebsplan des Steinkohlenbergwerks Ibbenbüren Anlage 17 - Prognose zur optimierten Wasserannahme nach Stilllegung des Steinkohlenbergwerkes Ibbenbüren (Ostfeld). (Final operating plan of the Ibbenbüren hard coal mine Annex 17 - Forecast for optimized water intake after closure of the Ibbenbüren hard coal mine (Ostfeld)). Essen, Germany
- Kordilla J (2014) Flow and transport in saturated and unsaturated fractured porous media: Development of particle-based modeling approaches (Doctoral dissertation). Faculty of Geoscience and Geography, Georg-August-Universität Göttingen
- Kordilla J, Sauter M, Reimann T, Geyer T (2012) Simulation of saturated and unsaturated flow in karst systems at catchment scale using a double continuum approach. *Hydrol Earth Syst Sci* 16:3909–3923. <https://doi.org/10.5194/hess-16-3909-2012>
- Kovács A, Sauter M (2007) Modelling karst hydrodynamics. In: Goldscheider N, Drew D (eds) *Methods in Karst Hydrogeology*. Taylor & Francis, London, pp 201–222
- La Touche GD, Cottrell M (2017) The Application of Discrete Fracture Network Models to

- Mine Groundwater Studies. In: Wolkersdorfer C, Sartz L, Sillanpää M, Häkkinen A (eds) Proceedings of the 13th International Mine Water Association Congress. 25-30 June 2017, Lappeenranta, Finland, pp 548–555
- Lei Q, Latham JP, Tsang CF (2017) The use of discrete fracture networks for modelling coupled geomechanical and hydrological behaviour of fractured rocks. *Comput Geotech* 85:151–176. <https://doi.org/10.1016/j.compgeo.2016.12.024>
- Li T, Mei T, Sun X, et al (2013) A study on a water-inrush incident at Laohutai coalmine. *Int J Rock Mech Min Sci* 59:151–159. <https://doi.org/10.1016/j.ijrmms.2012.12.002>
- Li Y (2016) Groundwater system for the periods of pre- and post-longwall mining over thin overburden. *Int J Mining, Reclam Environ* 30:295–311. <https://doi.org/10.1080/17480930.2015.1044595>
- Lichtner PC (2000) Critique of dual continuum formulations of multicomponent reactive transport in fractured porous media. In: Faybishenko B, Witherspoon PA, Benson S (eds) *Dynamics of Fluids in Fractured Rock, Volume 122*. The American Geophysical Union, pp 281–298
- Liu HH, Rutqvist J (2010) A new coal-permeability model: Internal swelling stress and fracture-matrix interaction. *Transp Porous Media* 82:157–171. <https://doi.org/10.1007/s11242-009-9442-x>
- Liu Y, Liu Q meng, Li W ping, et al (2019) Height of water-conducting fractured zone in coal mining in the soil–rock composite structure overburdens. *Environ Earth Sci* 78:242–255. <https://doi.org/10.1007/s12665-019-8239-7>
- Long JCS, Remer JS, Wilson CR, Witherspoon PA (1982) Porous media equivalents for networks of discontinuous fractures. *Water Resour Res* 18:645–658. <https://doi.org/10.1029/WR018i003p00645>
- Lorig LJ, Darcel C, Damjanac B, et al (2015) Application of discrete fracture networks in mining and civil geomechanics. *Trans Institutions Min Metall Sect A Min Technol* 124:239–254. <https://doi.org/10.1179/1743286315Y.00000000021>
- Lu S, Li M, Ma Y, et al (2022) Permeability changes in mining-damaged coal: A review of mathematical models. *J Nat Gas Sci Eng* 106:104739. <https://doi.org/10.1016/j.jngse.2022.104739>
- Majdi A, Hassani FP, Nasiri MY (2012) Prediction of the height of distressed zone above the mined panel roof in longwall coal mining. *Int J Coal Geol* 98:62–72. <https://doi.org/10.1016/j.coal.2012.04.005>
- Mark C (2021) An updated empirical model for ground control in U.S. multiseam coal mines. *Int J Min Sci Technol* 31:163–174. <https://doi.org/10.1016/j.ijmst.2020.12.024>
- Meng Z, Shi X, Li G (2016) Deformation, failure and permeability of coal-bearing strata during longwall mining. *Eng Geol* 208:69–80. <https://doi.org/10.1016/j.enggeo.2016.04.029>
- Merritt P, Power C (2022) Assessing the long-term evolution of mine water quality in abandoned underground mine workings using first-flush based models. *Sci Total Environ* 846:157390. <https://doi.org/10.1016/j.scitotenv.2022.157390>
- Morin K, Hutt N (2001) *Environmental geochemistry of minesite drainage: practical theory and case studies*, Digital ed. MDAG Publishing, Vancouver, British Columbia, Canada
- Mugova E, Wolkersdorfer C (2022) Density stratification and double-diffusive convection in

- mine pools of flooded underground mines – A review. *Water Res* 214:118033. <https://doi.org/10.1016/j.watres.2021.118033>
- Newman C, Agioutantis Z, Boede Jimenez Leon G (2017) Assessment of potential impacts to surface and subsurface water bodies due to longwall mining. *Int J Min Sci Technol* 27:57–64. <https://doi.org/10.1016/j.ijmst.2016.11.016>
- Newman CP (2018) Guidance for hydrogeologic groundwater flow modeling at mine sites. Nevada Division of Environmental Protection. Carson City, Nevada, USA
- Palchik V (2003) Formation of fractured zones in overburden due to longwall mining. *Environ Geol* 44:28–38. <https://doi.org/10.1007/s00254-002-0732-7>
- Palchik V (2002) Influence of physical characteristics of weak rock mass on height of caved zone over abandoned subsurface coal mines. *Environ Geol* 42:92–101. <https://doi.org/10.1007/s00254-002-0542-y>
- Pauvlik CM, Esling SP (1987) The effects of longwall mining subsidence on the groundwater conditions of a shallow unconfined aquitard in southern Illinois. In: Proceedings 1987 Natl Symp on Mining, hydrology, sedimentology and reclamation. Springfield, Illinois, USA, pp 189–196
- Peng SS (2020) Longwall Mining, 3rd edn. CRC Press/Balkema, Leiden, The Netherlands
- Pruess K, Narasimhan TN (1985) A practical method for modeling fluid and heat flow in fractured porous media. *Soc Pet Eng J* 25:14–26. <https://doi.org/doi:10.2118/10509-PA>
- Pruess K, Oldenburg C, Moridis G (2012) TOUGH2 user's guide , version 2. Earth Sciences Division, Lawrence Berkeley National Laboratory, University of California, Berkeley, California, USA
- Qu Q, Xu J, Wu R, et al (2015) Three-zone characterisation of coupled strata and gas behaviour in multi-seam mining. *Int J Rock Mech Min Sci* 78:91–98. <https://doi.org/10.1016/j.ijrmms.2015.04.018>
- Rinder T, Dietzel M, Stammeier JA, et al (2020) Geochemistry of coal mine drainage, groundwater, and brines from the Ibbenbüren mine, Germany: A coupled elemental-isotopic approach. *Appl Geochemistry* 121:104693. <https://doi.org/10.1016/j.apgeochem.2020.104693>
- Rouleau A, Gale JE (1987) Stochastic discrete fracture simulation of groundwater flow into an underground excavation in granite. *Int J Rock Mech Min Sci* 24:99–112. [https://doi.org/10.1016/0148-9062\(87\)91929-2](https://doi.org/10.1016/0148-9062(87)91929-2)
- Sauter M (1992) Quantification and forecasting of regional groundwater flow and transport in a karst aquifer (Gallusquelle, Malm, SW. Germany) (Doctoral dissertation). Geowissenschaftliche Fakultät, Universität Tübingen
- Semenkov I, Sharapova A, Lednev S, et al (2022) Geochemical Partitioning of Heavy Metals and Metalloids in the Ecosystems of Abandoned Mine Sites: A Case Study within the Moscow Brown Coal Basin. *Water (Switzerland)* 14:. <https://doi.org/10.3390/w14010113>
- Sherwood JM, Younger PL (1994) Modelling groundwater rebound after coalfield closure: An example from County Durham, United Kingdom. In: Reddish DJ (ed) Proceedings of the 5th International Minewater Congress. 18-23 September 1994; Nottingham, UK, pp 769–777
- Simpson MJ, Clement TP (2003) Comparison of finite difference and finite element solutions

- to the variably saturated flow equation. *J Hydrol* 270:49–64.
[https://doi.org/10.1016/S0022-1694\(02\)00294-9](https://doi.org/10.1016/S0022-1694(02)00294-9)
- Singh MM, Kendorski FS (1981) Strata disturbance prediction for mining beneath surface water and waste impoundments. In: *Proceedings of the 1st Conference on Ground Control in Mining*. 27–29 July 1981, Morgantown, West Virginia, USA, pp 76–89
- Strack O (2017) *Finite Differences and Finite Elements*. In: *Analytical Groundwater Mechanics*, 1st edn. Cambridge University Press., Cambridge, UK, pp 403–422
- van Genuchten MT (1982) A comparison of numerical solutions of the one-dimensional unsaturated–saturated flow and mass transport equations. *Adv Water Resour* 5:46–55.
[https://doi.org/https://doi.org/10.1016/0309-1708\(82\)90028-8](https://doi.org/https://doi.org/10.1016/0309-1708(82)90028-8)
- Vermeulen PTM, Heemink AW, Te Stroet CBM (2004) Reduced models for linear groundwater flow models using empirical orthogonal functions. *Adv Water Resour* 27:57–69. <https://doi.org/10.1016/j.advwatres.2003.09.008>
- Vincenzi V, Piccinini L, Gargini A, Sapigni M (2010) Parametric and numerical modelling tools to forecast hydrogeological impacts of a tunnel. *Acque Sotter J Groundw* 1:135–154.
<https://doi.org/10.7343/as-2022-558>
- Walker JS (1988) Case study of the effects of longwall mining induced subsidence on shallow ground water sources in the Northern Appalachian coalfield. United States Department of The Interior, Bureau of Mines. Pittsburgh, PA, USA
- Wang HF, Anderson MP (1982) *Introduction to groundwater modeling: finite difference and finite element methods.*, 1st edn. Academia Press INC., San Francisco, USA
- Wang W, Jiang T, Faybishenko B, et al (2016a) Closure of Fracture Due to Cover Stress Re-establishment After Coal Mining. *Geotech Geol Eng* 34:1525–1537.
<https://doi.org/10.1007/s10706-016-0059-x>
- Wang WX, Sui WH, Faybishenko B, Stringfellow WT (2016b) Permeability variations within mining-induced fractured rock mass and its influence on groundwater inrush. *Environ Earth Sci* 75:1–15. <https://doi.org/10.1007/s12665-015-5064-5>
- Wang Y, Li T, Chen Y, Ma G (2019) Numerical analysis of heat mining and geological carbon sequestration in supercritical CO₂ circulating enhanced geothermal systems inlaid with complex discrete fracture networks. *Energy* 173:92–108.
<https://doi.org/10.1016/j.energy.2019.02.055>
- Wang Y, Yang W, Li M, Liu X (2012) Risk assessment of floor water inrush in coal mines based on secondary fuzzy comprehensive evaluation. *Int J Rock Mech Min Sci* 52:50–55.
<https://doi.org/10.1016/j.ijrmms.2012.03.006>
- Wei M, Duan Y, Dong M, et al (2019) Transient Production Decline Behavior Analysis for a Multi-Fractured Horizontal Well With Discrete Fracture Networks in Shale Gas Reservoirs. *J Porous Media* 22:343–361. <https://doi.org/10.1615/jpormedia.2019028982>
- Westermann S, Rudakov D, Melchers C (2018) Analytical assessment of mine water rebound. Case study Ruhr coal basin. In: *Proceedings of the International Scientific and Technical Forum of Mining Engineers*. 10-13 October 2018, Dnipro, Ukraine, pp 204–212
- Wolkersdorfer C (2006) *Water Management at Abandoned Flooded Underground Mines*, 1st edn. Springer, Freiberg, Sachsen, Germany
- Wu Y-S, Di Y, Kang Z, Fakcharoenphol P (2011) A multiple-continuum model for simulating

- single-phase and multiphase flow in naturally fractured vuggy reservoirs. *J Pet Sci Eng* 78:13–22. <https://doi.org/10.1016/j.petrol.2011.05.004>
- Wüstefeld P, Hilse U, Koehrer B, et al (2017) Critical evaluation of an Upper Carboniferous tight gas sandstone reservoir analog: Diagenesis and petrophysical aspects. *Mar Pet Geol* 86:689–710. <https://doi.org/10.1016/J.MARPETGEO.2017.05.034>
- Xiao YX, Lee CF, Wang SJ (1999) Assessment of an equivalent porous medium for coupled stress and fluid flow in fractured rock. *Int J Rock Mech Min Sci* 36:871–881. [https://doi.org/10.1016/s0148-9062\(99\)00060-1](https://doi.org/10.1016/s0148-9062(99)00060-1)
- Xu K, Dai G, Duan Z, Xue X (2018) Hydrogeochemical Evolution of an Ordovician Limestone Aquifer Influenced by Coal Mining: A Case Study in the Hancheng Mining Area, China. *Mine Water Environ* 37:238–248. <https://doi.org/10.1007/s10230-018-0519-z>
- Yaghoubi A (2019) Hydraulic fracturing modeling using a discrete fracture network in the Barnett Shale. *Int J Rock Mech Min Sci* 119:98–108. <https://doi.org/10.1016/j.ijrmms.2019.01.015>
- Yang X, Sasaki K, Zhang X, Sugai Y (2018) Permeability estimate of underground long-wall goaf from P-wave velocity and attenuation by lab-scale experiment on crushed rock samples. *J Appl Geophys* 159:785–794. <https://doi.org/10.1016/j.jappgeo.2018.09.009>
- Younes A, Fahs M, Ataie-Ashtiani B, Simmons CT (2020) Effect of distance-dependent dispersivity on density-driven flow in porous media. *J Hydrol* 589:. <https://doi.org/10.1016/j.jhydrol.2020.125204>
- Younger PL (1997) The longevity of minewater pollution: a basis for decision-making. *Sci Total Environ* 194–195:457–466. [https://doi.org/10.1016/S0048-9697\(96\)05383-1](https://doi.org/10.1016/S0048-9697(96)05383-1)
- Younger PL (2006) *Groundwater in the Environment: An Introduction*, 1st edn. Blackwell Publishing, Newcastle, UK
- Younger PL (2000) Predicting temporal changes in total iron concentrations in groundwaters flowing from abandoned deep mines: A first approximation. *J Contam Hydrol* 44:47–69. [https://doi.org/10.1016/S0169-7722\(00\)00090-5](https://doi.org/10.1016/S0169-7722(00)00090-5)
- Younger PL (2002) Mine water pollution from Kernow to Kwazulu-Natal: Geochemical remedial options and their selection in practice. *Geosci South-West Engl (Proc Usher Soc)* 10:255–266
- Zha H, Liu W, Liu Q (2020) Physical Simulation of the Water-Conducting Fracture Zone of Weak Roofs in Shallow Seam Mining Based on a Self-Designed Hydromechanical Coupling Experiment System. *Geofluids* 2020:. <https://doi.org/10.1155/2020/2586349>
- Zhang C, Tu S, Zhao YX (2019) Compaction characteristics of the caving zone in a longwall goaf: a review. *Environ Earth Sci* 78:1–20. <https://doi.org/10.1007/s12665-018-8037-7>
- Zhang D, Fan G, Ma L, Wang X (2011) Aquifer protection during longwall mining of shallow coal seams: A case study in the Shendong Coalfield of China. *Int J Coal Geol* 86:190–196. <https://doi.org/10.1016/j.coal.2011.01.006>
- Zhang D, Sui W, Liu J (2018a) Overburden Failure Associated with Mining Coal Seams in Close Proximity in Ascending and Descending Sequences Under a Large Water Body. *Mine Water Environ* 37:322–335. <https://doi.org/10.1007/s10230-017-0502-0>
- Zhang Q, López DL (2019) Use of Time Series Analysis to Evaluate the Impacts of Underground Mining on the Hydraulic Properties of Groundwater of Dysart Woods, Ohio.

Mine Water Environ 38:566–580. <https://doi.org/10.1007/s10230-019-00619-z>

Zhang R, Cheng Y, Zhou H, et al (2018b) New insights into the permeability-increasing area of overlying coal seams disturbed by the mining of coal. *J Nat Gas Sci Eng* 49:352–364. <https://doi.org/10.1016/j.jngse.2017.11.031>

Zhang R han, Wu J fa, Zhao Y long, et al (2021) Numerical simulation of the feasibility of supercritical CO₂ storage and enhanced shale gas recovery considering complex fracture networks. *J Pet Sci Eng* 204:108671. <https://doi.org/10.1016/j.petrol.2021.108671>

Zhang X, Ghabraie B, Ren G, Tu M (2018c) Strata movement and fracture propagation characteristics due to sequential extraction of multiseam longwall panels. *Adv Civ Eng* 2018:. <https://doi.org/10.1155/2018/4802075>

Zheng C, Bennett GD (1995) *Applied Contaminant Transport Modeling: Theory and Practice*, 2nd edn. Wiley-Interscience, New York, NY, USA

Zuber A, Maloszewski P (2008) Lumped parameter models (IAEA-TCS--32/F). International Atomic Energy Agency (IAEA): 5-36

Chapter 2: A Petrographic Investigation of the Carboniferous Sequence from the Ibbenbüren Mine: Tracing the Origin of the Coal Mine Drainage

Bedoya-Gonzalez, D.^{1,2}, Hilberg, S.¹, Redhammert, G.³, & Rinder, T.¹

¹ Department of Geography and Geology, University of Salzburg, Hellbrunner Str. 34, 5020 Salzburg, Austria.

² Institute for Geography and Geology, University of Greifswald, Friedrich-Ludwig-Jahn Str. 17a, 17487 Greifswald, Germany.



³ Department of Chemistry and Physics of Materials, University of Salzburg, Jakob-Haringer-Straße 2, 5020 Salzburg, Austria.

Published in: Minerals (2021), Vol. 11, 483.

<https://doi.org/10.3390/min11050483>

Article

A Petrographic Investigation of the Carboniferous Sequence from the Ibbenbüren Mine: Tracing the Origin of the Coal Mine Drainage

Diego Bedoya-Gonzalez ^{1,2,*} , Sylke Hilberg ¹, Günther Redhammer ³  and Thomas Rinder ¹

¹ Department of Geography and Geology, University of Salzburg, Hellbrunner Str. 34, 5020 Salzburg, Austria; sylke.hilberg@sbg.ac.at (S.H.); Thomas.rinder@sbg.ac.at (T.R.)

² Institute for Geography and Geology, University of Greifswald, Friedrich-Ludwig-Jahn Str. 17a, 17487 Greifswald, Germany

³ Department of Chemistry and Physics of Materials, University of Salzburg, Jakob-Haringer-Straße 2, 5020 Salzburg, Austria; guenther.redhammer@sbg.ac.at

* Correspondence: diegoalexander.bedoyagonzalez@sbg.ac.at; Tel.: +43-662-8044-5495

Abstract: The mine drainage of the Ibbenbüren anthracite coal mine is characterized by exceptionally high concentrations of dissolved iron and sulfate. The elevated position of the coal field with respect to the surrounding area makes the neighboring sediments an unlikely source of these elements. Accordingly, it has been hypothesized that interaction between infiltrating rainwater and the fractured overburden is a key process governing the mine drainage chemistry. To test this hypothesis, two full-diameter core samples drilled above the discharging adit of the coal mine were investigated. The methodology combined several analytical techniques to identify and characterize traces of water–rock interaction related to both diagenesis and relatively recent weathering processes along open fractures. The coupled appearance of kaolinite-dickite-illite minerals in weathered and unweathered rock sections was clearly connected to the burial history of the Carboniferous sequence. In contrast, the formation of iron (oxide-) hydroxides together with the presence of oxidized pyrite in weathering profiles along both sides of the fractures was positively related to the geochemical footprint of the coal mine drainage. Thus, open fractures, possibly originated from mining activities, may play a significant role in the drainage chemistry, especially considering the rather poor hydraulic conditions of the overburden.

Keywords: mine drainage; Ibbenbüren anthracite coal mine; Carboniferous sequence; water–rock interaction; geochemistry



Citation: Bedoya-Gonzalez, D.; Hilberg, S.; Redhammer, G.; Rinder, T. A Petrographic Investigation of the Carboniferous Sequence from the Ibbenbüren Mine: Tracing the Origin of the Coal Mine Drainage. *Minerals* **2021**, *11*, 483. <https://doi.org/10.3390/min11050483>

Academic Editors: Monika J. Fabiańska, Magdalena Misz-Kennan and Justyna Ciesielczuk

Received: 31 March 2021
Accepted: 28 April 2021
Published: 30 April 2021

Publisher's Note: MDPI stays neutral with regard to jurisdictional claims in published maps and institutional affiliations.



Copyright: © 2021 by the authors. Licensee MDPI, Basel, Switzerland. This article is an open access article distributed under the terms and conditions of the Creative Commons Attribution (CC BY) license (<https://creativecommons.org/licenses/by/4.0/>).

1. Introduction

In December 2018, hard coal mining in Germany came to its end when collieries in Ibbenbüren and Prosper Haniel ceased to operate [1–3]. However, with the end of mining activities the need for mitigation of environmental impacts still continues [4,5]. Amongst others, management of mineralized mine drainage remains a considerable challenge in many places [6–13]. The problem begins as soon as operations start, but may continue for centuries after mine closures [14–16].

Mining exposes large surfaces of coal and coal-bearing rocks to air, water and microorganisms. The oxidation of reducing agents in these layers (e.g., iron sulfides and organic matter) generates acidic conditions with exceptionally elevated concentrations of sulfate, iron and manganese ions [17]. Trace elements present in the lattice of the minerals, such as Co, Cu, As, Pb, Ni, Se, U and Zn, can also be released at levels that are harmful to aquatic and terrestrial organisms [6,9,18,19]. These products may be sorbed and coprecipitated by buffering minerals, resulting in their partial reduction [18,20]. If there are no such buffers, the referred products may be flushed from the system either rapidly or potentially long

into the future [21]. Consequently, the drainage quality of each mine site depends on its particular structure and (hydro-) geological conditions.

Historically, the drainage of Ibbenbüren Westfield has displayed high iron (100–1000 mg/L) and sulfate (1000–5000 mg/L) contents [22,23]. Even after its closure and subsequent flooding in 1979, the mine drainage has continued to bear high loads of total dissolved solids and metals [10]. A comprehensive clarification of this mineralization, which is the highest reported for European hard coal mines, requires an approach that considers geological, hydrological and mining conditions. The Ibbenbüren Westfield represents an isolated mountain range, topographically elevated with respect to the foreland. Accordingly, it has been hypothesized that the actual chemical signature of the drainage is influenced by the interaction of percolating rainwater with sulfur-bearing rock layers above the adit. This water–rock interaction could be favored by decades of mining activities, which generate strains (i.e., deformations) derived from the redistribution, concentration, reorientation and release of stress [24]. Large vertical strains result in fracture structures that modify the hydrogeological system, increasing their hydraulic conductivity and altering the groundwater flow paths [25–29]. The percolating water can then harness these water-conducting fracture zones to interact with the rock sequence. To test this hypothesis, the present study combines several analytical techniques to characterize the Carboniferous sequence within two full-diameter core samples recovered from the Ibbenbüren Westfield. Particular attention is given to components and structures (e.g., authigenic, reactive or altered mineral phases, fractures, and morphological features) that allow identification of the mechanisms governing the chemical signature of the coal mine drainage.

2. Site Description

2.1. Geological Setting

The Ibbenbüren Carboniferous crustal block represents the largest outcrop of Paleozoic coal-bearing rocks in northwest Germany. Similar Carboniferous island-like blocks can be found in Hüggel [30] and Piesberg [31] hills, a few kilometers to the east (Figure 1). Based on tectonic studies, all three blocks have been linked to the Ruhr district, about 90 km to the south of Ibbenbüren. There, the Carboniferous sequence dips north under the Mesozoic rocks of the Münsterland basin, emerging in the study area due to the inversion of the Osning fault in the Upper Cretaceous [32,33]. At that time, the block was subject to compressive strength produced by dextral movements. This generated a crustal uplifting of about 2 km compared to the Triassic and Jurassic foreland, currently under the Quaternary deposits [32]. Consistently, the Carboniferous sequence developed an island-like appearance, being limited on all its sides by marginal faults that follow the NNW–SSE Osning thrust axis (Figure 1) [34].

Antithetic faults created during the tectonic inversion also divide the Carboniferous block into 2 NNE–SSW striking horst structures separated by the Bockradener graben [23]. Horst structures were named East- and Westfield for mining purposes (Figure 1). An additional boundary between the Westfield and Bockradener graben was also defined at the Pommer–Esche fault, where the rock sequence exhibits vertical displacements from 210 to 500 meters [34]. Finally, several local faults further segment the Westfield into small blocks, promoting the infiltration of meteoric water (Figure 1).

2.2. Stratigraphy

Rock layers in the study area were deposited during the higher Westphalian C and lower Westphalian D stages [30,37]. The sequence is composed of an alternating pattern of sandstone and conglomerate layers (approx. 80%), with few mudstone levels (20%) wherein 81 coal seams are included [34]. On top of this, thin Quaternary sediments sparsely cover the sequence, as well as two localized waste rock deposits, which do not extend more than 0.5 km². Because of the low dip angle (<10°) and fairly constant nature of the rocks, coal seams offer good reference levels when comparing the stratigraphic sequence

at various locations into the field [23]. However, parallelization between areas is often uncertain due to strong facies changes at large-scales.

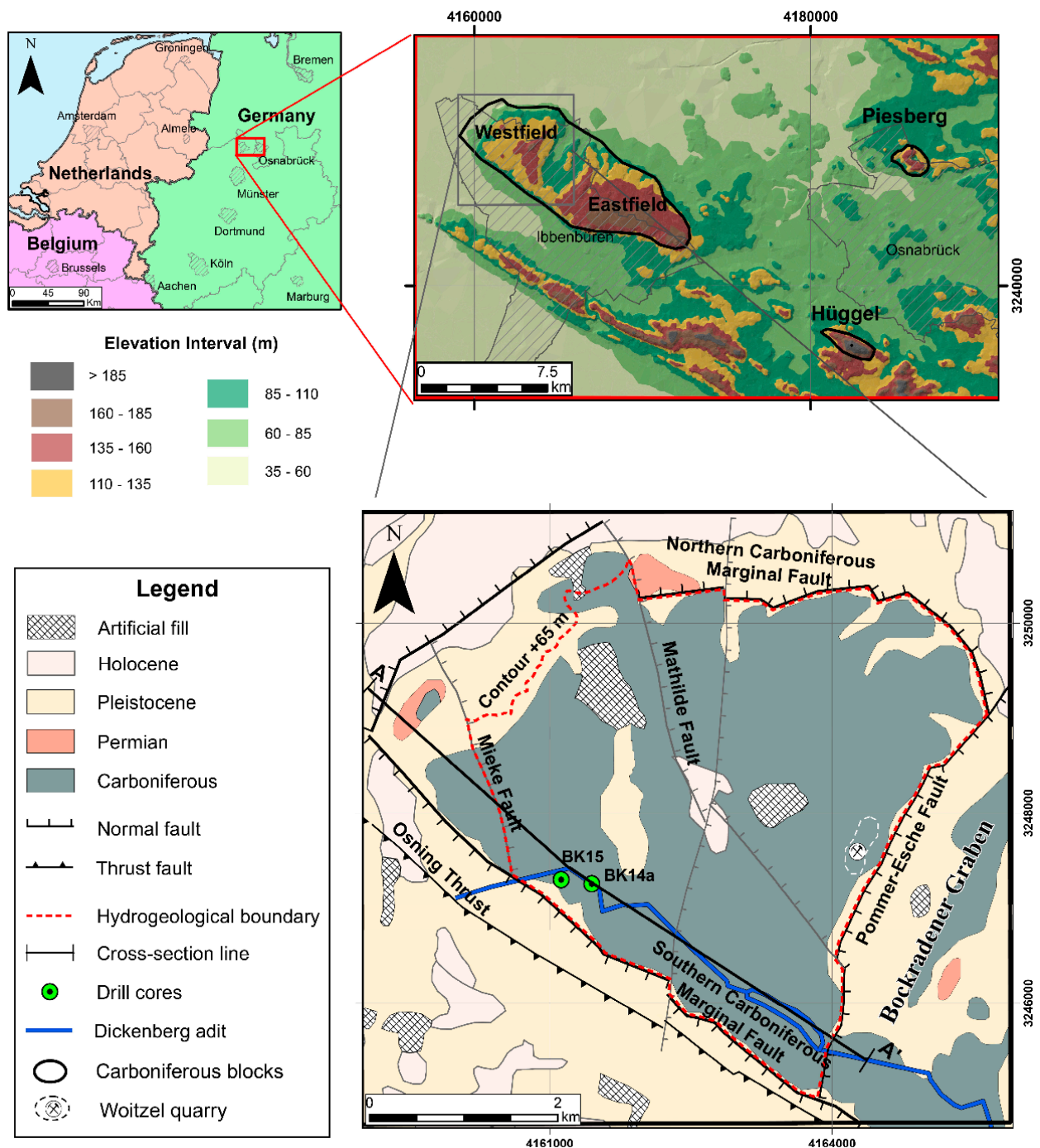


Figure 1. Geographic and geological maps of the studied area. The polygons enclosed by the thick black line in the digital elevation image additionally illustrate the location of the other two Carboniferous blocks in the surrounding area. The A-A' line denotes the position of the cross-section in Figure 2. Modified after [10,35,36].

2.3. Hydrogeological Conditions

Mining in the Westfield stopped in June 1979, with excavations as deep as 600 m below the ground level [22]. After closure, the dewatering system was progressively shut down, allowing groundwater to bounce back. As a result, the area was flooded under control up to an elevation of around 65 m a.s.l., where the groundwater reaches the Dickenberg adit

(Figure 2) [38]. Nowadays, this level is still regulated by direct connections between the adit and the Dickenberg coal seam [22].

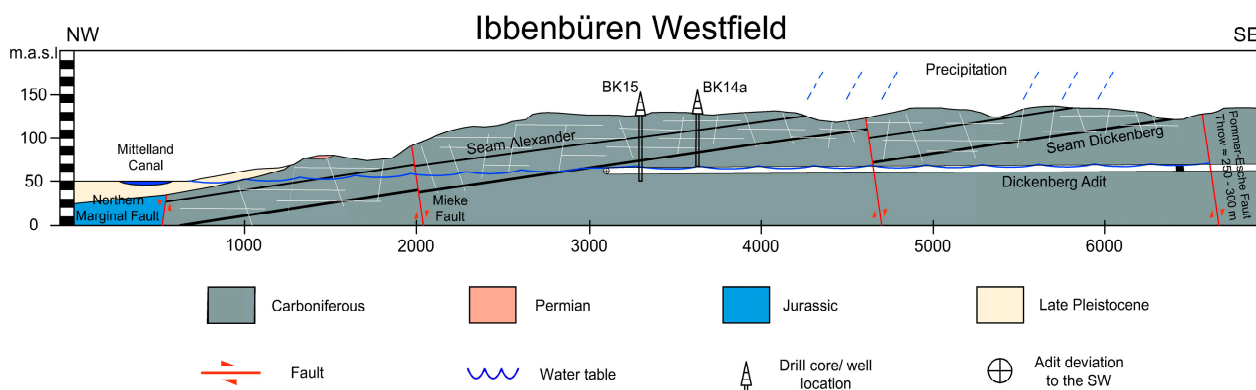


Figure 2. Geological cross-section of the Ibbenbüren Westfield (cross-section line A-A' in Figure 1). The cross-section is vertically exaggerated 5x to better detail the shallow overburden structure and current hydrogeological situation. Modified after [39].

As the phreatic level of the former coalfield is above the foreland surface (<55 m a.s.l.), precipitation turns into the unique source of groundwater recharge. The thin and sparse Quaternary sediments offer neither storage capacity nor resistance for meteoric water to percolate. Likewise, percolation may be promoted by water-conducting fracture zones as Lotze et al. [23] and Bässler [34] suggested. Both authors observed a direct correlation between seasonal precipitation events and the amount of discharged mine water. Additionally, both authors described a sharp drop in the groundwater table for the whole Westfield when mining was active. The development of a continuous cone of depression rules out the presence of a free aquifer on top of the sequence while confirming a direct connection between the surface and underground works. The actual discharge of the adit, therefore, depends on the amount of meteoric water that percolates through the overburden enclosed by the northern and southern Carboniferous marginal faults, Mieke Fault and Pommer-Esche Fault. Furthermore, groundwater can only be extracted from areas higher than the Dickenberg adit, turning the terrain contour +65 m into an additional hydrogeological limit (Figure 1).

3. Materials and Methods

Full-diameter rock samples (i.e., 4 inches diameter) from two drill cores were evaluated in this study. The samples were obtained from a drilling campaign for the construction of a new drainage adit in Ibbenbüren, where boreholes BK14a and BK15 were the only ones drilled on the Westfield. In total, more than 130 m of rock samples, with an approximately stratigraphic representation of 80 m, were recovered (Figure 3). From these, 22 intervals were picked for further investigation including mineralogy, rock structures and alteration zones. The selected intervals included at least two samples of each lithology identified on the drill cores. These were chosen with a depth spacing as regular as possible to homogeneously cover the whole sequence. Additionally, intervals with the presence of reactive, unstable or altered mineral phases (e.g., pyrite, carbonates and (oxide-) hydroxides) as well as with permeable features such as fractures were also selected.

Detailed petrographic characterization was carried out on 22 thin sections of the selected intervals. Descriptions were performed with a LEITZ laborlux 12 polarized microscope with magnifications between 2.5 and 40×. Although all slides were carefully examined, only six sections of the most frequent rock intervals with both altered and pristine zones were selected to perform detailed point-counting analysis, as described by the Gazzi–Dickinson method (e.g., see [40]). For each thin section, 300 points were counted using a maximum of 1 mm grid spacing covering the entire slide. This amount

of counts yielded statistically reliable values for all parameters, reasserting the textural and compositional classification of overburden rocks. Grain size and sorting analysis was performed by measuring the long axis of at least 100 grains per thin section. Petrographic descriptions were complemented with the analysis of two thin sections under a Zeiss Ultra Plus 55 field emission scanning electron microscope (SEM). Measurements were carried out with an accelerating voltage of 15 kV and a working distance of approximately 10 mm. The dispersive X-ray spectrometer system mounted in the SEM was further used to identify unknown accessories and clay minerals.

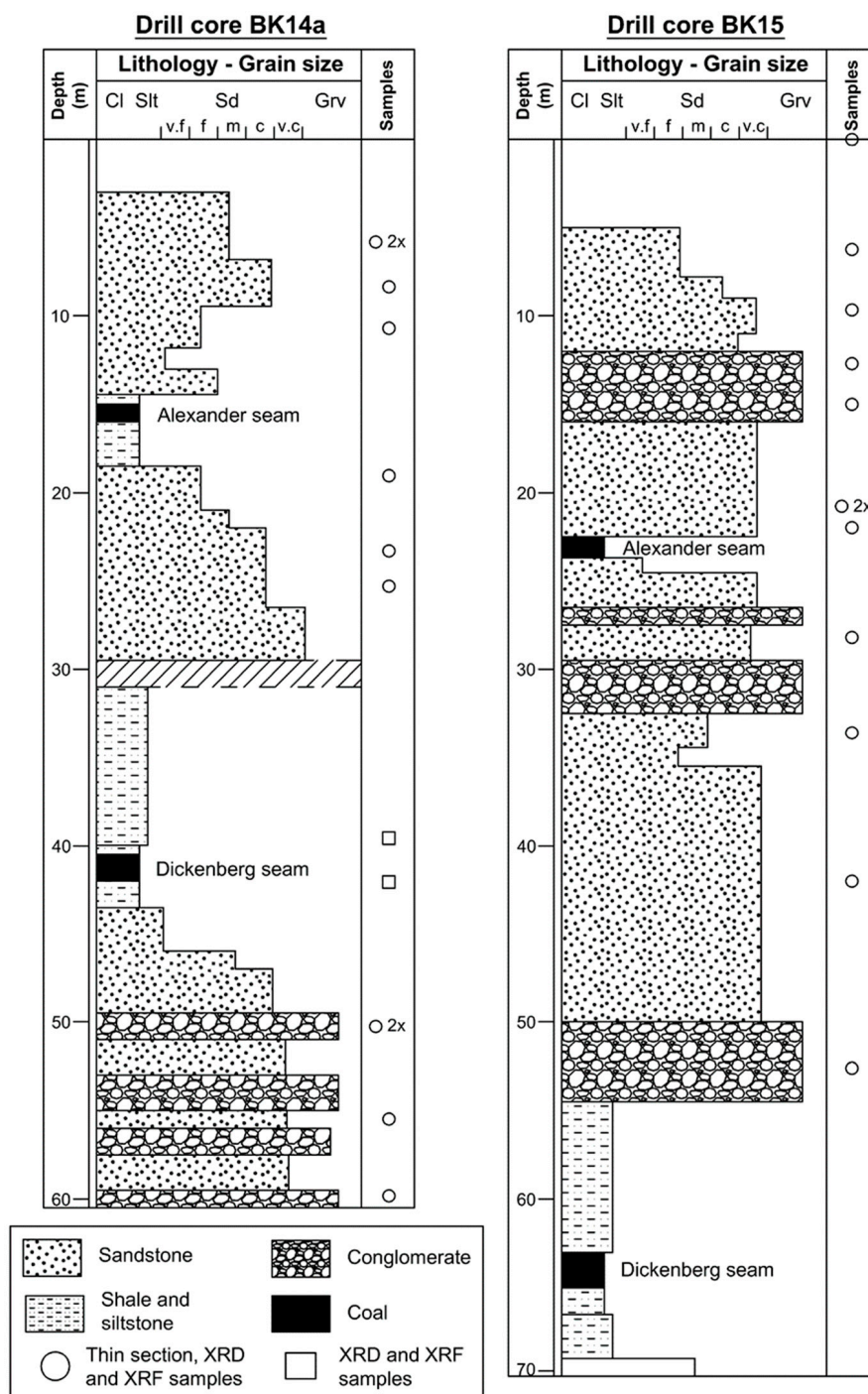


Figure 3. Stratigraphic columns of the two core-samples recovered in the area. The sketch includes lithology and location of the samples analyzed in this paper. Cl = clay, Slt = silt, Sd = sand (v.f: very fine, f: fine, m: medium, c: coarse, v.c.: very coarse), Grv = gravel.

Mineralogical composition of the rocks was determined by powder X-ray diffraction (PXRD) on 34 samples. The measurements were collected in coupled Theta–Theta mode on a Bruker D8 Advance diffractometer (Bruker AXS, Karlsruhe, Germany), being equipped with a fast-solid-state Lynxeye detector and an automatic sample changer. Data acquisition was performed using $\text{CuK}\alpha_{1,2}$ radiation between 10° and 90° 2θ , with a step size of 0.015° , integration time of 1 s, with the divergence slit and the anti-scatter-slits opened at 0.3° and 4° , respectively. A primary and secondary side 2.5° Soller slit was used to minimize axial divergence, and the detector window opening angle was chosen as 2.93° .

Finally, the elemental composition of selected weathered and unweathered rock samples ($n = 34$) was analyzed with “S4 Pioneer” X-ray Fluorescence microscopy (Bruker AXS). This device is equipped with a 4 kW X-ray tube, whereby the main elements were measured with reduced power. The counting times were chosen in such a way that the double standard deviation for SiO_2 and Al_2O_3 was below 1% (relative) and below 5% (relative) for those elements that contained 1–10%. At low concentrations (<10 ppm) the measurement error is typically 1–3 ppm. At concentrations around 1000 ppm, the errors are maximum 50 ppm, but with many trace elements, they are significantly lower.

4. Results

4.1. Core Logging

4.1.1. Lithology

The most frequent lithology in the drill cores corresponds to greyish hard sandstone layers, medium-to-coarse-grained and moderately sorted. Layers are homogeneously composed of quartz, sedimentary lithic fragments (mostly chert, mudstones and coal), muscovite, and variable pyrite amounts. Rocks do not present cement, but a clayey matrix produces a dense hard packing with apparent low porosity (Figure 3). Sedimentary features include massive and cross-bedding structures, with local variations to conglomeratic lenses. Some intervals show reddish tones associated with precipitation of iron (oxide-) hydroxides near fracture structures.

Interspersed with the sandstones, clast-supported pebble conglomerates appear in the sequence (Figure 3). These are massive and poorly sorted rocks, with normal gradation to very coarse-grained sandstones of similar composition as described above. Lastly, few levels of dark-gray mudstone and remnants of two coal seams were found in both drill cores (Figure 3). According to a personal communication of the RAG Company, these two coal samples belong to Alexander and Dickenberg seams. By taking them as guides, a significant textural fluctuation is observed laterally (Figure 3). For instance, in between the two coal seams, lithology varies from fine-to-medium-grained on the core BK14a to very-coarse and conglomeratic on the core BK15.

4.1.2. Joints and Fractures

Rock breakups were grouped into joints and fractures according to their influence on the integrity and alteration state of the samples. Other parameters such as strike, inclination or dip direction were not evaluated due to lack of on-site information and sample orientation.

Joints correspond to short and relatively planar cracks, easily traceable by their narrow alteration zones. They display millimeter-scale tensional offsets and reddish-brown altered fringes of up to 0.5 cm at each side of their planes (Figure 4b). Secondary iron hydroxides commonly close the open spaces, cementing the divided fragments (Figure 4a). However, no other sealing element associated with the mineralogical composition of the rock, such as quartz veins or clay smears, was observed.

Fractures, on the other hand, are open structures that segment the core samples into two or more pieces. Weathering fronts with precipitated iron (oxide-) hydroxides are consistently related to them, changing the rocks' optical properties according to their distance from the fractures (Figure 4c). Rock sections close to fracture planes develop more intense and hard reddish-brown crusts in comparison with further areas. In general, these

alteration zones extend for several centimeters on both sides of the planes, comprising even the whole core interval in coarser lithologies (Figure 4c,d, respectively).

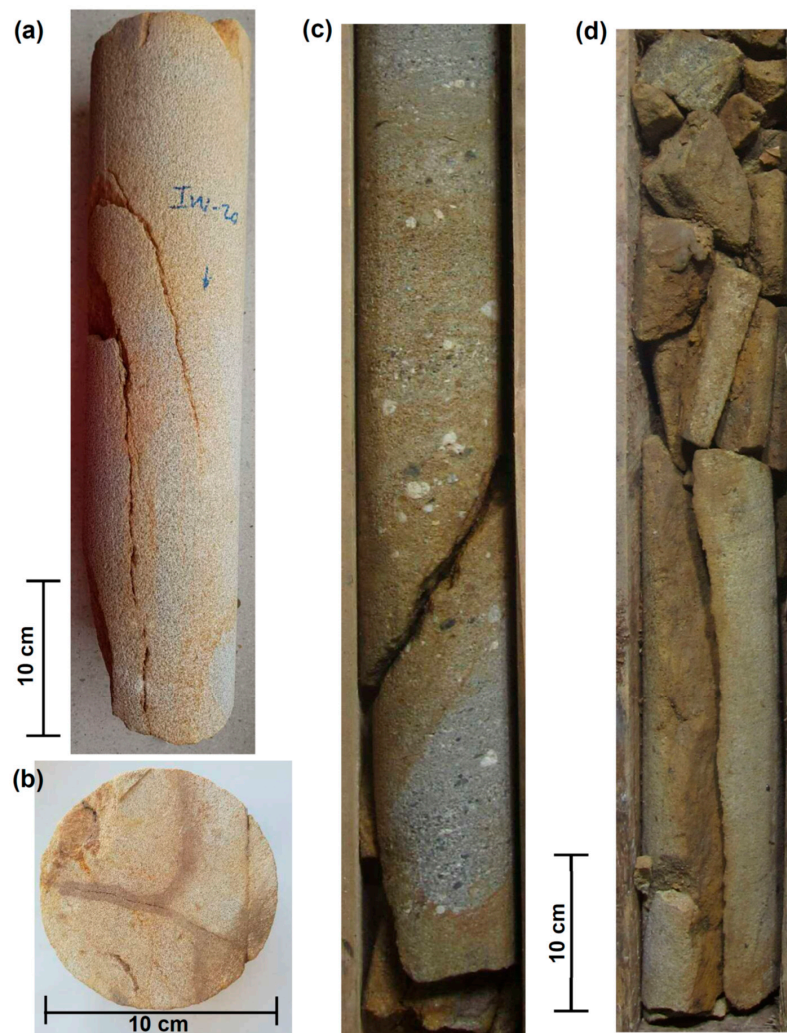


Figure 4. Types of breakups encountered during the core logging. (a) Longitudinal and (b) cross-sectional images of joint networks, displaying limited alteration zones. In both sections iron (oxide-) hydroxides hold the rock pieces together hindering fluid flow. (c) Sub-vertical fracture showing clear influence in the weathering state of the sandstone interval. (d) Cracked sandstone interval with a sub-vertical fracture potentially associated with the exploitation of the Dickenberg coal seam, 4 m below it (this structure can be tracked on the core BK15 for approx. 5 m).

4.2. Petrography

Sandstones display high proportions of detrital quartz, with little evidence of overgrowth or sutured contacts. Most of the lithic fragments correspond to chert and ductile mudstones partially altered to sericite (Figure 5a). Additionally, lenses and high amounts of coal fragments appear in several layers, some of which exhibit oxidation signs on the surrounding matrix (Figure 5b). Detrital muscovite and ductile lithics are frequently affected by compaction, being incorporated into the primary pore spaces as pseudomatrix (Figure 5a). Unaltered feldspars are extremely rare, although their initial presence is interpreted from the development of pseudohexagonal stacks of kaolinite-group minerals. Pyrite occurs as clusters of very fine sand and silt crystals (i.e., microcrystalline pyrite) usually associated with sedimentary lithic fragments and rarely as frame macrocrystals (Figure 5c). Finally, iron (oxide-) hydroxides are found coating and covering lithoclast surfaces in fractured core intervals (Figure 5d).

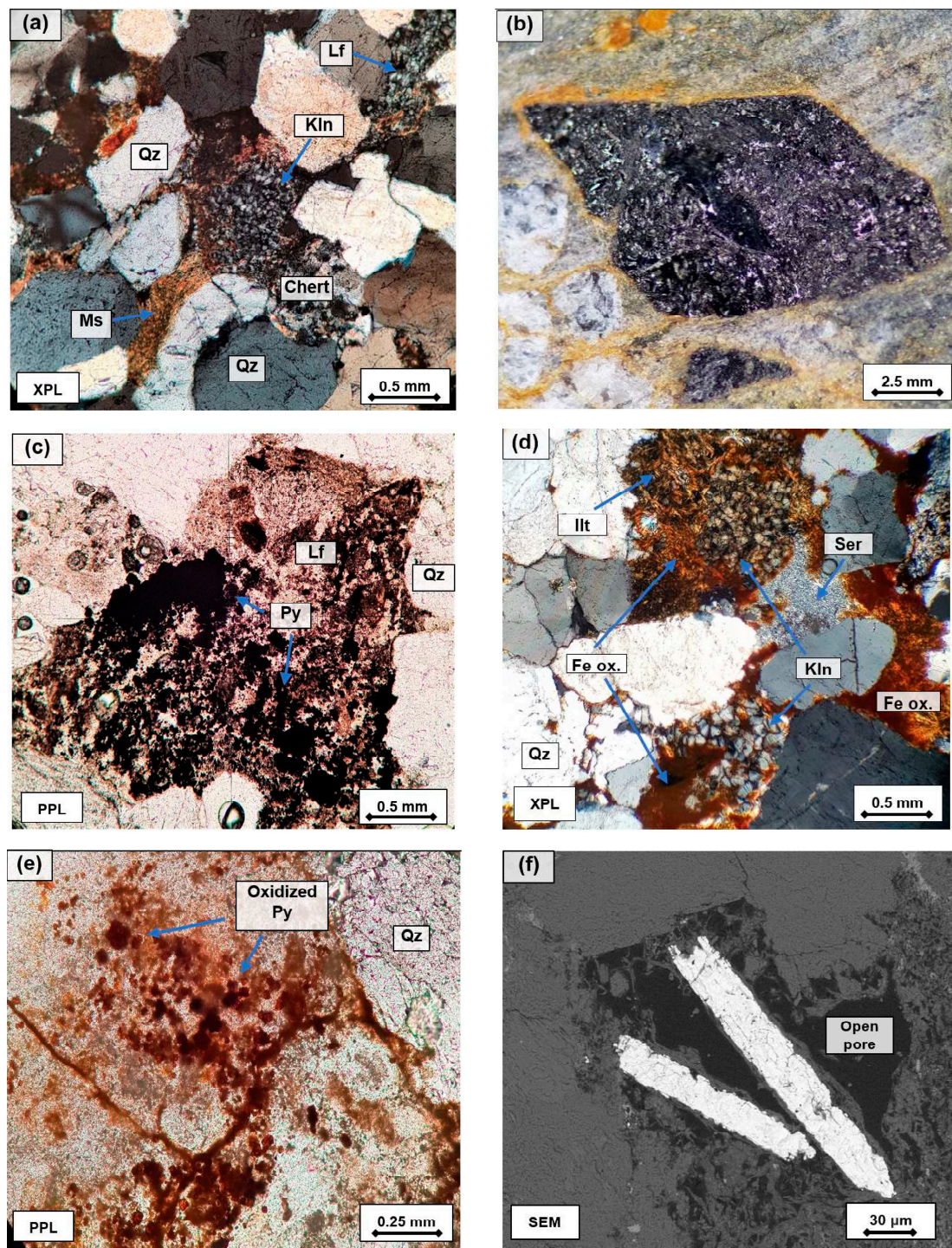


Figure 5. Photomicrographs of the main components found in the rock sequence. (a) Plastic lithic fragments, muscovite flakes and booklet crystals of kaolinite-group minerals squeezed among quartz and chert grains. The authigenic origin of the kaolinite-group minerals is interpreted from the pseudo-hexagonal form of the pore space. (b) Oxidation of a coal lithic fragment within conglomeratic sandstone interval. (c) Unaltered cluster of microcrystalline pyrite associated with a sedimentary lithic fragment. (d) Weathered thin section with iron (oxide-) hydroxides precipitating around and on the matrix and rock components. (e) Weathered cluster of microcrystalline pyrite completely transformed to iron (oxide-) hydroxide (holo-pseudomorph). (f) SEM image of prismatic barite crystals in a pore space. Lf = lithic fragment, Ms = muscovite, Kln = kaolinite-group minerals, Qz = quartz, Py = pyrite, Ill = illite, Ser = sericite, Fe ox. = iron (oxide-) hydroxides, PPL = plane polarized light, XPL = cross polarized light, SEM = scanning electron microscope.

Based on point counting, sandstones can be classified as medium-grained sublithic arenites with some variations to coarse-grained lithic arenites. Both lithologies present granoblastic texture with gradational and parallel-oriented structures. Samples exhibit textural maturity, expressed in moderately sorted frameworks, with sub-rounded and moderate spherical grains. In general, normalized mineralogical compositions display 58% mono- and polycrystalline quartz grains, 20% lithic fragments and 12% authigenic clay minerals (kaolinite-group minerals and illite). Minor constituents include 3% muscovite, <2% alkali feldspar and 5% microcrystalline pyrite. However, this latter figure may have been overestimated due to the dark opaque nature of a range of thin section components (mudstone, coal particles and iron oxides). Within weathered rock zones, up to 5% of iron (oxide-) hydroxides are additionally present. These appear as a massive solid phase, darkening the frame and clay matrix minerals of the samples (Figure 5d). Pellicular rims of (oxide-) hydroxides can also be spotted around pyrite and coal particles, evolving in some cases into full crystal replacement (holo-pseudomorphism—Figure 5e). Lastly, SEM and EDS images reveal trace quantities of barite and heavy clay-size particles, enriched in strontium, lead and rare earth elements (i.e., lanthanum, cerium and neodymium). These were rarely encountered in the primary porosity of the rock, alongside the clayey matrix (Figure 5f).

Under the XRD, both weathered and unweathered rocks did not show significant mineralogical differences. As an exception, pyrite was only identified in selected unweathered samples. Diagnostic peaks of kaolinite group minerals reveal the presence of both kaolinite and dickite in the samples (Figure 6).

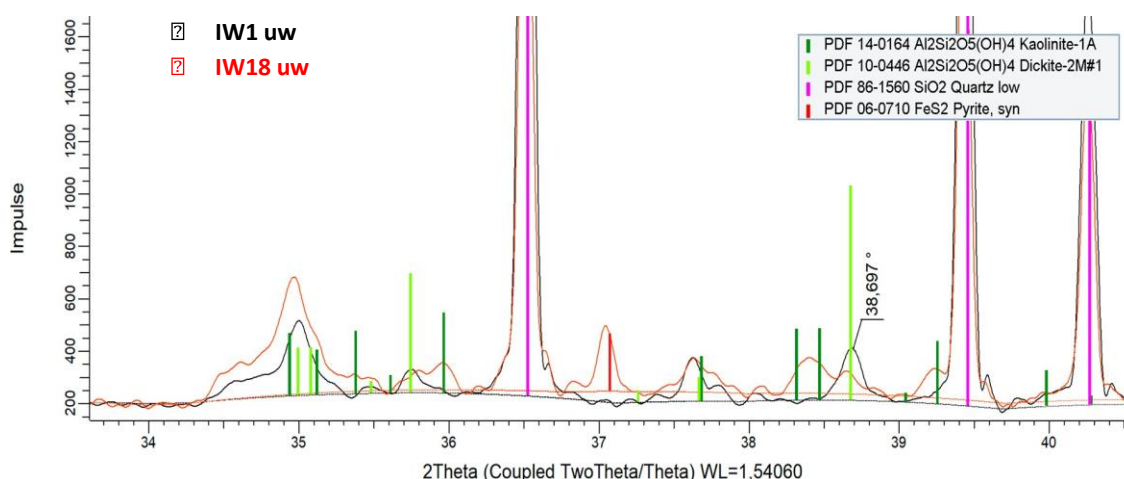


Figure 6. Diagnostic peaks of quartz, pyrite, kaolinite and dickite for samples IW1 uw and IW18 uw.

4.2.1. Rock Matrix

The matrix is predominantly composed of lithic fragments (pseudomatrix) and authigenic clayey minerals. The pseudomatrix corresponds to ductile mudstone and fine-grained lithic fragments, with significant alteration to sericite (Figure 7a). The criteria for classifying them as pseudomatrix implies that individual fragments are hardly distinguishable, but their deformation is still visible through flow structures (e.g., see [41]). Other lithics like coal and chert remain undeformed taking part of the rocks' frame.

Most of the clayey matrix occurs as stacks of face-to-face plates and booklet crystals of kaolinite-group minerals. The pseudo-hexagonal shape of these aggregates suggests that they were formed from the alteration process of detrital feldspars. Additionally, elongate, filamentous and hairy crystals of illite are also observed on the top and edges of these minerals. The bright interference colors on plain-colored booklet-shaped crystals show their illitization to some extent. To rule out illite pseudomorphism and, therefore, complete replacement of the kaolinite-group minerals, the coexistence of both minerals

was investigated through SEM and EDS. Results validate the partial illitization of the sample, confirming the consistency between the characteristic habit of the minerals and their chemical composition (Figure 7b–d).

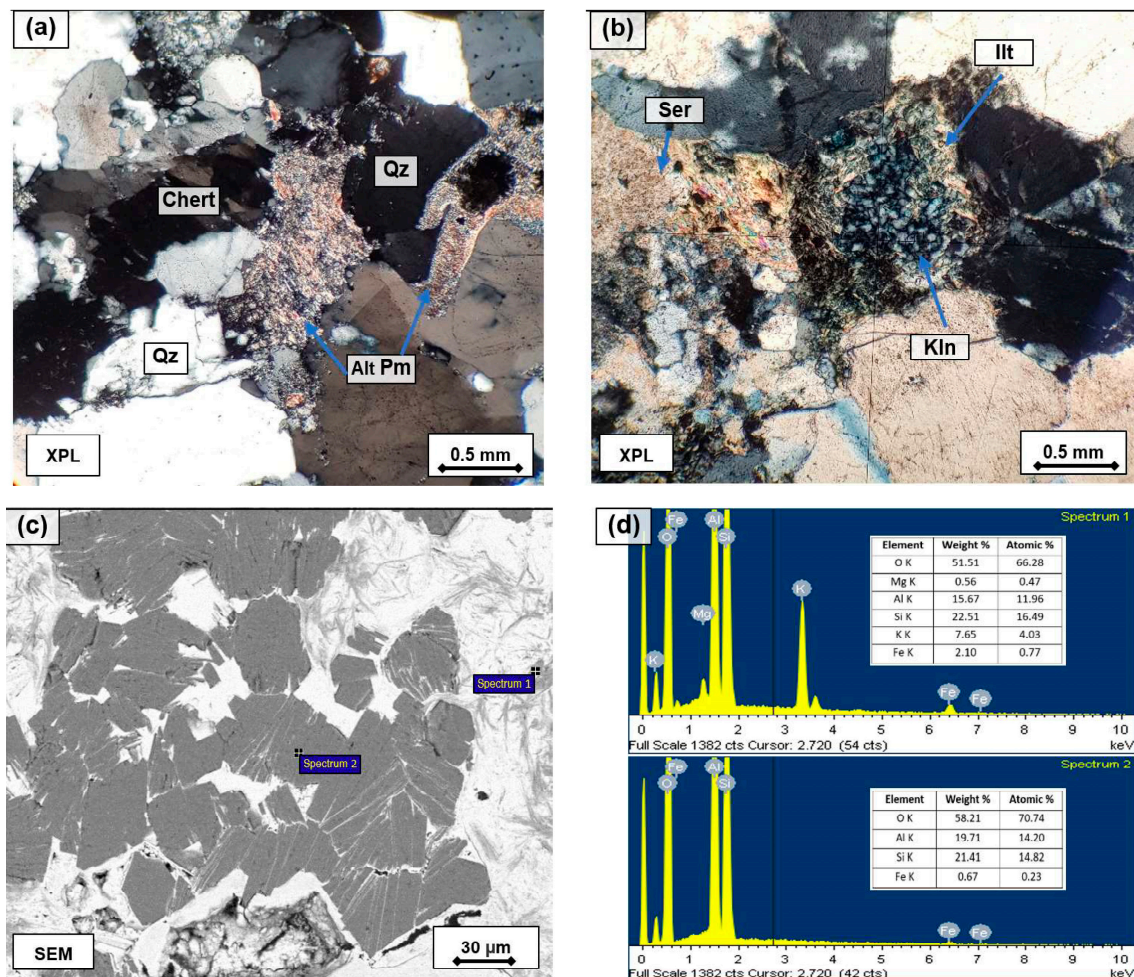


Figure 7. Rock matrix components. (a) Altered pseudomatrix squeezed among quartz and chert grains. (b) Authigenic clayey matrix found in the sample. Illite fibers stand out from their bright interference colors around the loose aggregates of kaolinite-group minerals, while sericite is frequently observed on the surface of sedimentary lithic fragments. (c,d) Illite and kaolinite-group minerals with their respective EDS signals. Alt Pm = altered pseudomatrix, Qz = quartz, Kln = kaolinite-group minerals, Ill = illite, Ser = sericite, PPL = plane polarized light, XPL = cross polarized light, SEM = scanning electron microscope.

4.2.2. Porosity and Permeability

The visual porosity of the analyzed thin sections is between 8 and 11%. Core samples are characterized by moderately sorted sediments and straight-line contacts, with few sutured or point junctions among the sub-rounded grains (Figure 8a). This type of arrangement creates intergranular pore spaces that can be either free or matrix-filled. In the area, most of the samples exhibit a significant percentage of clayey matrix (15%) that, together with the sorting grade of the rocks, results in the rather low porosity. Moreover, primary porosity is reduced by the formation of pseudomatrix, which represents around 10% of the total rock volume.

In addition to the counted primary porosity, secondary microporosity was also identified within the stack of booklet crystals of the kaolinite-group minerals. This feature, widely discussed in petroleum engineering papers (e.g., see [42]), was highlighted by the blue-dye epoxy used in the samples (Figure 8b). Although no percentage was determined,

it may contribute largely to the total porosity considering the extensive development of kaolinite-group minerals in the rocks. This idea is supported by Wüstefeld et al. [31] who performed visual and helium pycnometry measurements on sandstone outcrops in Piesberg. Discrepancies of about 4% between both techniques were attributed to the development of microporosity in authigenic clay minerals, only detectable by helium pycnometry. As the two rock sequences are comparable in terms of age, composition and burial history, a similar effect in the studied samples can be assumed (i.e., porosity values around 15%).

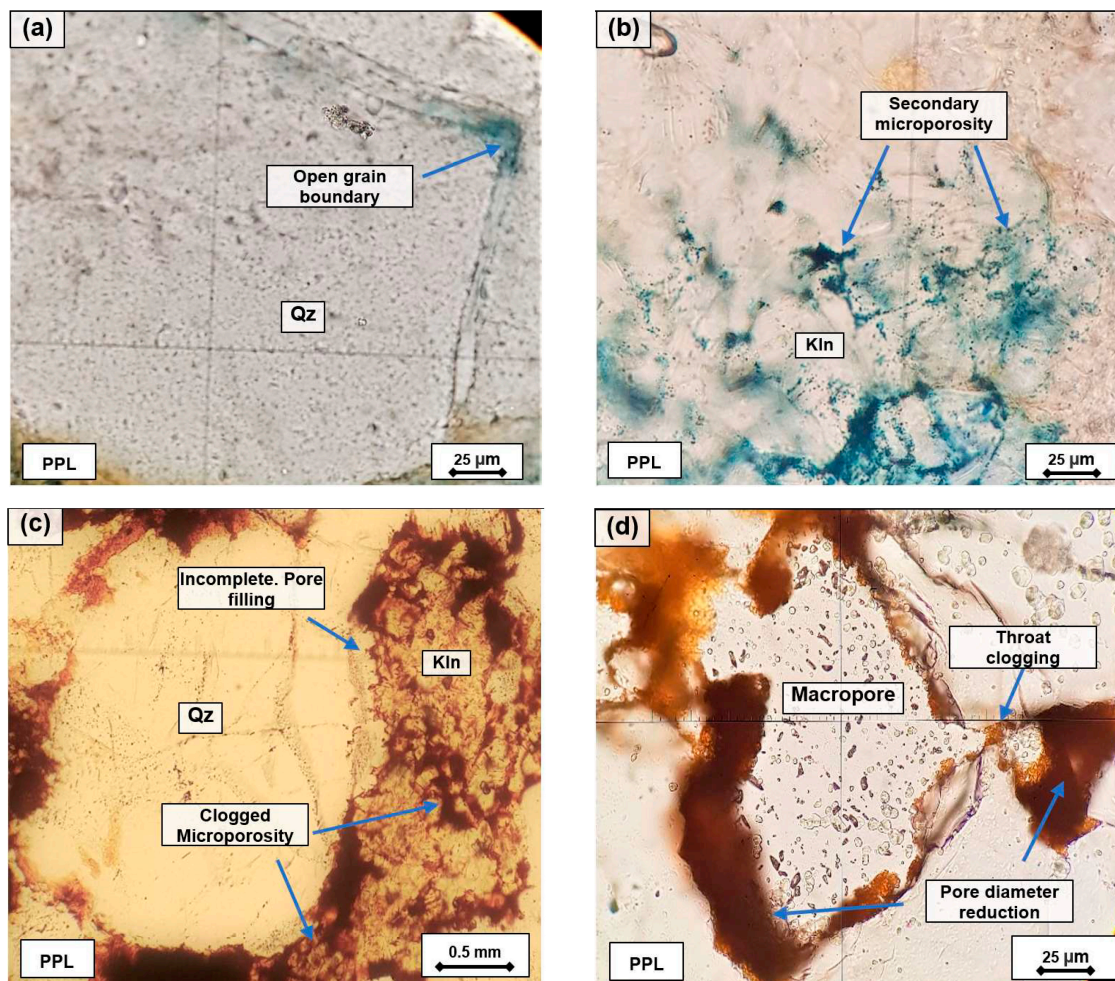


Figure 8. Overview of the rock porosity. (a) Open straight-line contact between two quartz grains developing primary porosity. (b) Secondary microporosity highlighted by the speckled, pale blue color of the resin. (c) Thin section of a weathered interval displaying clogging of primary and secondary microporosity. (d) Iron (oxide-) hydroxides pore-lining, reducing and blocking the connection between pore spaces. Qz = quartz, Kln = kaolinite-group minerals, PPL = plane polarized light.

Finally, low permeability values are expected for the studied overburden. Reduction of the rock porosity by ductile fragments tends to disconnect the free pathways of the bedrocks. Likewise, iron (oxide-) hydroxides frequently precipitate on the clayey minerals and pore throats, potentially reducing the connection between adjacent free spaces (Figure 8c,d).

4.3. Elemental Rock Composition

The chemical composition of the selected rock samples is shown in Table S1 of the supplementary files. Generally, the elemental composition of both weathered and un-weathered sections resembles the results from the petrological investigation. Iron content

increases in the reddish weathered rock zones with respect to the unweathered zones (Figure 9a). In contrast, aluminium content does not vary in between sections, indicating only minor importance of secondary Al-bearing (oxide-) hydroxides in the weathered rock zones. In addition, both alkaline and earth alkaline elements are correlated to Al content, indicating their siliciclastic origin. Potassium and magnesium do not vary significantly between weathered and unweathered rock zones (Figure 9b,c). Nickel, zinc and, to a lesser extent, lead (Figure 9d–f) are correlated with secondary iron phases, indicating co-precipitation and sorption. In principle, sulfide minerals in the Carboniferous sequence are potential sources of those metals. Moreover, it has been suggested that they migrated vertically into the Carboniferous sandstones when the area was still covered by shale, halite, limestone and conglomerate layers of Permian (Zechstein) age [23]. However, the recent influence of these Zechstein remnants that were dragged up by the south and north marginal faults has been discarded by isotopic studies carried out by Rinder et al. [10] in the Ibbenbüren Eastfield.

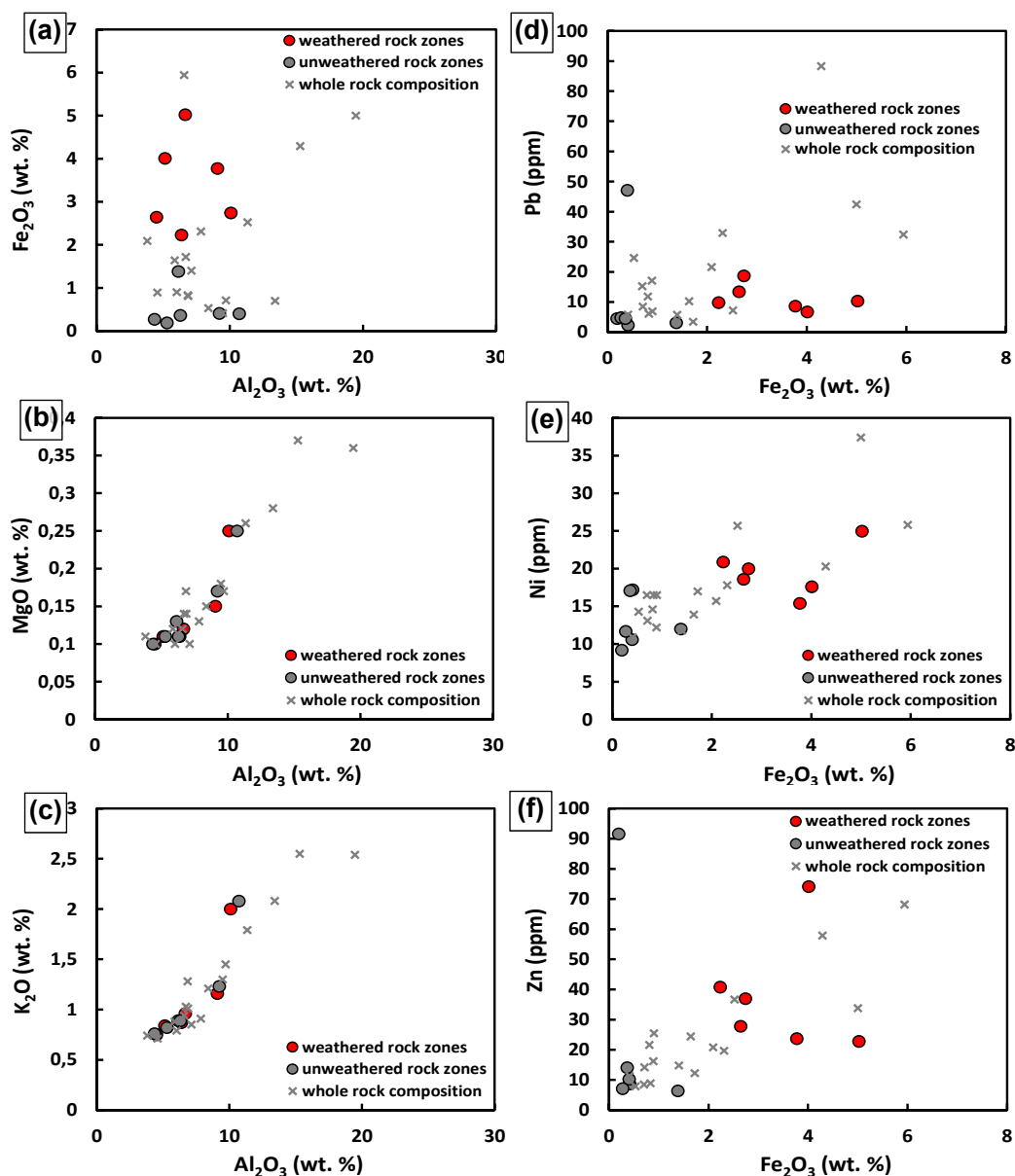


Figure 9. Elemental composition of analyzed rock samples. Potassium and magnesium do not vary between weathered and unweathered zones, indicating low influence of water–rock interaction on aluminosilicate dissolution. Correlation of Zn, Pb and Ni indicates coprecipitation/sorption with secondary iron (oxide-) hydroxides.

5. Discussion

The studied sequence corresponds to a fining-upwards array of multi-story sand bodies with intercalated coal seams. According to Becker et al. [30,37], the short horizontal gradation of the sandstones is a consequence of a braided to meandering fluvial environment. This does not modify the mineralogical composition of the rocks but their proportions.

Based on the distribution of mineral transformations, two types of water–rock interaction are distinguished. On one hand, kaolinite, dickite, illite and sericite are present in all the analyzed sections, being related to similar alteration processes over the whole Westfield. On the other hand, iron (oxide-) hydroxides display variable spatial distribution at large scale, being linked to weathering processes near fracture elements. Considering the poor hydraulic properties of the rocks, mineral arrangements may also allow discrimination between diagenetic alteration processes and “recent” weathering events.

5.1. Kaolinite, Dickite, Illite and Sericite Formation

Relatively constant amounts of kaolinite, dickite, illite and sericite were found in the samples of both drill cores. Mineral habits suggest their formation from alteration processes of feldspars and lithic grains. However, no significant difference was recognized on their distribution between weathered reddish zones and grayish pristine rock sections. Therefore, water–rock interaction under the current conditions of the area had little influence on the rock matrix.

Feldspar kaolinitization occurs in areas with humid and mild climates, constantly flushed with meteoric or low-pH waters [43]. Even though these conditions existed in the studied area, low permeability of shales, coal and tight sandstones provide a sufficient seal against regional weathering. Bässler [34], for example, estimated permeabilities below 1 millidarcy (mD) for shallow coal roof sandstones in Ibbenbüren. In addition, Becker et al. [30] used more than 30 sandstone samples from the Woitzel quarry (see Figure 1) to calculate an average permeability of 0.05 mD at confining pressures of 1 MPa (≈ 30 m depth). From these low values, it is highly unlikely that recent water–rock interaction generates the widespread distribution of kaolinite in the overburden. Feldspar kaolinitization could then occurred during an early diagenetic stage. According to Wüstefeld et al. [31], a warm climate controlled the Eodiagenesis of the German northwestern Carboniferous sequence. During this stage, mechanical compaction reorganized most of the feldspar fragments into the pore spaces, letting them interact with the rock fluids. This interaction resulted in grain dissolution with subsequent kaolinite precipitation. Nowadays, feldspar kaolinitization is irrelevant due to the low proportion of remaining feldspars.

In addition to kaolinite, dickite was identified in the sandstone matrix. “Dickitization” has been reported at temperatures above 130 °C at a depth of approximately 3.2 km in the Norwegian shelf [44]. Similarly, the transformation of kaolinite to dickite has been prescribed to depths below 3.3 km by Beaufort et al. [45], linking this formation to the time of deep burial.

Illite appears as a secondary phase mainly formed from the alteration of kaolinite and dickite. Time, pressure, pore fluid composition and hydrothermal activity are important factors in the mineral formation [46,47]. Illitization is a diagenetic process that takes place over long timespans, at intermediate burial depth, with temperatures and pressures around 100 °C and 100 MPa (>3 km depth) [30,48,49]. Since samples only cover the first 80 m of the shallowest overburden, illitization had to happen probably during the mesogenetic realm, when the deep burial of the sedimentary sequence began [31,50]. A similar explanation is proposed for sericite formation, which requires the rock to interact with moderately acidic fluids at high temperatures, usually associated with deep burial conditions [51]. Under such conditions, water is tightly bound to the primary porosity. Ions that are liberated from the primary minerals diffuse slowly and migrate over short distances before being incorporated into the secondary minerals.

The preservation of kaolinite and dickite alongside illite may point to the limited availability of potassium-bearing solutions in the Ibbenbüren sandstones [49]. However,

the transformation of kaolinite into dickite through a coupled dissolution–precipitation process suggests that pore waters were available when the relevant temperatures for illitization were present [44]. In addition, potassium-rich pore waters have been reported within the carboniferous sandstones from the Ibbenbüren coalfield [10]. Considering that dickite is a thermodynamically stable mineral in a range of environmental conditions [52], a kinetic control due to a relatively short timespan at depths with relevant pressure and temperature could explain the coexistence of kaolinite and dickite. Similarly, this could also explain the incomplete illitization of both mineral phases.

Interestingly, the partial illitization of kaolinite observed in the samples would show a different burial record from that described in Becker et al. [30]. Here, the author separated the diagenetic history of the Ibbenbüren Carboniferous block from that of Hügge and Piesberg based on the complete replacement of illite during the earliest burial phase. Again, this points to the relatively strong heterogeneity of sandstone reservoirs at small scales, which make the extrapolation of core logging a challenging process.

5.2. (Oxide-) Hydroxide Formation

The lower Westphalian D sequence has been interpreted to be deposited under humid conditions, with almost no presence of opaque or iron oxide minerals [53]. This feature is contrary to the relatively high percentage of (oxide-) hydroxides encountered in fractured intervals. However, deposits of weathering origin can be distinguished from those of detrital origin by careful observation of thin sections. Iron (oxide-) hydroxides that originate from transport as solutions show a tendency to nucleate and grow perpendicular to the walls of the pore system, whereas those that come from the transport of detrital material exhibit a tendency to be layered or deposited among the frame minerals of the rock [54].

Within the thin section, iron (oxide-) hydroxides show perpendicular growing around the pore walls. Their development in the fracture vicinity rules out a regional oxidative process during the diagenesis, whilst their absence in unfractured samples discards a syndepositional origin. Thus, local weathering of Fe-bearing minerals prompted by fractures may be the origin of the iron (oxide-) hydroxides in the area. This can be evidenced, for example, from the alteration state of pyrite clusters. While fresh brass-yellow pyrite appears in complete core samples, holopseudomorphism and pellicular rims of (oxide-) hydroxides are developed around the crystals of the fractured segments.

5.2.1. Fe Source in the Rocks

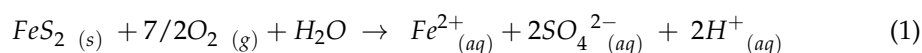
Pyrite is the only Fe-bearing reactive mineral identified in the rock samples. The mineral occurs as clusters of microcrystals usually associated with sedimentary lithic fragments and rarely as frame macro-crystals. Development of microcrystals represents higher reactive surface areas, which is a key parameter for the oxidation rate [55]. Moreover, fine-grained marcasite and pyrite crystals are expected to be present in lenses and coal fragments within the sandstones. This consideration is supported by Lotze et al. [23], who blamed the high pyrite content in some coal seams as one of the elements in charge of generating mineralized drainage in the Ibbenbüren Westfield.

5.2.2. Influence of Fractures in the Oxidation-Precipitation System of the Westfield

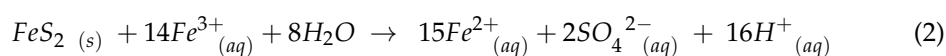
Fractures may strongly influence the water–rock interaction in the tight Carboniferous sequence. These structures broadly segment core samples into several pieces, developing weathering fronts at both sides of their planes. Contrarily, joints develop black oxide cements on their surface, leaving almost no open spaces for water to flow. Although the exact nature of fractures is unknown, some are expected to be related to former mining activities. The absence of healing elements (as occurred with the joints) and the partial alteration of rock volumes around them, may be interpreted as indicators of their recent origin.

Underground coal mining operations tend to change the stress state of the rocks, generating horizontal and sub-vertical fracture networks above and below the mined seams [28]. This bidirectional distribution creates a highly permeable zone that dominates the global

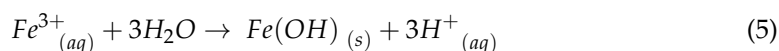
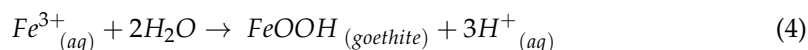
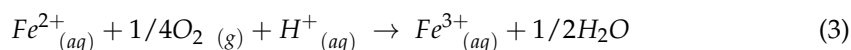
vertical water flow [28]. Locally, fluid can be horizontally exchanged between fractures and porous rocks by pressure and chemical differences [56]. As a result, water propagates rapidly through the fractures, while slowly invading the tight matrix blocks [57–60]. In such a system water can interact with iron-bearing minerals within the overburden. Oxidized pyrite and iron (oxide-) hydroxides in weathering profiles along both sides of the macro-fractures are the result of this interaction. Thus, when meteoric (oxygenated) water flows from the fracture into the sandstones, pyrite oxidation would proceed according to Reaction (1) [61]:



This process additionally releases trace elements included within the mineral lattice (e.g., Se, As, Cd and Zn). Alternatively, oxidation can proceed according to the following reaction:



After pyrite oxidizes, amorphous iron (oxide-) hydroxides can be formed through the oxidation of $Fe^{2+}_{(aq)}$ to $Fe^{3+}_{(aq)}$ (Reaction (3)). Subsequently, $Fe^{3+}_{(aq)}$ can either precipitate as goethite, which is the thermodynamic stable phase at pH values 2.5–5.5 (Reaction (4)), or as ferrihydrite, stable at pH values >5.5 (Reaction (5)) [61]:



For deep unsaturated zones, Reactions (3) to (5) would be limited by the small amount of oxygen left by pyrite oxidation (Reaction (1)). As a result, $Fe^{2+}_{(aq)}$, $SO_4^{2-}_{(aq)}$ and $H^+_{(aq)}$ are released to the fractures when water potential is high in the porous medium (reverse flow). It is also expected that ion freight decreases over time due to pore clogging and grain coating by iron (oxide-) hydroxides. In the end, the whole oxidation–precipitation process is repeated for each rainy event, which replenishes the dissolved oxygen in the medium.

However, the observed features in the weathering profiles along both sides of fractures are not enough to generate the high iron and sulfate content of the discharge water. The textural fluctuations between core samples together with the variable percentages of reactive components among layers (pyrite and coal particles) generate a significant uncertainty. For instance, the relatively high total iron content in weathered samples is not balanced by pyrite-bound iron in the unweathered samples. This points either to the migration and transport of fluid through larger distances within the porous medium (i.e., the outflow of formation water from the porous sandstones after the induction of fractures) or to the origin of those elements from outside of the sampled sandstones. In the latter case, origin of iron-rich waters, infiltrated from the previous Permian (Zechstein) cover, would be a possible source. However, no evidence of Permian influence on formation waters was found in the deep Ibbenbüren mine [10]. Either way, it is unlikely that modern interaction between percolating rain water and the evaluated rock section in this study is the primary source of the dissolved iron and sulfate in the mine drainage. This in turn points to the heterogeneity within the overburden, with large amounts of pyrite in localized areas and/or the dissolution of secondary sulfur-bearing minerals from the mine shafts [62].

6. Conclusions

Traces of water–rock interaction were assigned to two different categories. Illite, kaolinite and dickite are evenly distributed among the matrix of the weathered and unweathered rock zones and are related to the diagenesis history of the area. On the other hand, the

presence of iron (oxide-) hydroxides along the fractures is linked to the dissolution of pyrite. However, relatively high iron contents in the weathered zone face relatively low pyrite contents in the unweathered rocks. The low porosity and permeability of the analyzed samples exclude deep percolation of infiltrated rainwater into the rocks. Accordingly, the high contents of iron (oxide-) hydroxides may be the result of outflowing formation water, within a relatively short timespan after the opening of the fractures. Alternatively, pyrite dissolution from outside of the analyzed core samples is also possible. The latter points to the heterogeneity observed within the sedimentary sequence and the challenge of upscaling observations from drill cores to complete rock sequences.

Supplementary Materials: The following are available online at <https://www.mdpi.com/article/10.3390/min11050483/s1>, Table S1: The chemical composition of the selected rock samples.

Author Contributions: Conceptualization, D.B.-G. and T.R.; methodology, D.B.-G. and T.R.; investigation, D.B.-G., T.R. and G.R.; writing—original draft preparation, D.B.-G. and T.R.; writing—review and editing, D.B.-G., T.R. and S.H.; funding acquisition, S.H. All authors have read and agreed to the published version of the manuscript.

Funding: This work was financially supported by the Forum Bergbau und Wasser—FBW.

Acknowledgments: The authors would like to thank Manfred Bernroider for assistance with the petrographic investigation. Bastian Nippert (from Spang Ingenieurgesellschaft für Bauwesen, Geologie und Umwelttechnik mbH) is thanked for providing the core samples for the studied area. Natasa Ostermann is thanked for her help in the preparation of the thin sections. The authors would also like to acknowledge the facilities and the scientific assistance of the staff at the Department of Chemistry and Physics of Materials at the University of Salzburg, especially David Schiller and Fritz Finger for RFA Analyses and Gregor Zickler for his help with the SEM. We thank everybody from RAG Anthrazit Ibbenbüren for facilitating sampling and providing important insights into mine details. The academic editors and three anonymous reviewers are thanked for their help to improve this manuscript.

Conflicts of Interest: The authors declare that they have no known competing financial interests or personal relationships that could have appeared to influence the work reported in this paper.

References

1. Kretschmann, J. Post-Mining—A Holistic Approach. *Min. Metall. Explor.* **2020**, *37*, 1401–1409. [[CrossRef](#)]
2. Kretschmann, J. Sustainability-orientated post-mining in Germany. *Eurasian Min.* **2017**, 33–38. [[CrossRef](#)]
3. Oei, P.Y.; Brauers, H.; Herpich, P. Lessons from Germany's hard coal mining phase-out: Policies and transition from 1950 to 2018. *Clim. Policy* **2020**, *20*, 963–979. [[CrossRef](#)]
4. Kretschmann, J.; Efremenkov, A.B.; Khoreshok, A.A. From Mining to Post-Mining: The Sustainable Development Strategy of the German Hard Coal Mining Industry. *IOP Conf. Ser. Earth Environ. Sci.* **2017**, *50*, 012024. [[CrossRef](#)]
5. Kessler, T.; Mugova, E.; Jasnowski-Peters, H.; Rinder, T.; Stemke, M.; Wolkersdorfer, C.; Hilberg, S.; Melchers, C.; Struckmeier, W.; Wieber, G.; et al. Grundwasser in ehemaligen deutschen Steinkohlenrevieren—Ein wissenschaftlicher Blickwinkel auf Grubenflutungen. *Grundwasser* **2020**, *25*, 259–272. [[CrossRef](#)]
6. Cravotta, C.A. Dissolved metals and associated constituents in abandoned coal-mine discharges, Pennsylvania, USA. Part 1: Constituent quantities and correlations. *Appl. Geochem.* **2008**, *23*, 166–202. [[CrossRef](#)]
7. Cravotta, C.A.; Brady, K. Priority pollutants and associated constituents in untreated and treated discharges from coal mining or processing facilities in Pennsylvania, USA. *Appl. Geochem.* **2015**, *62*, 108–130. [[CrossRef](#)]
8. Morin, K.A.; Hutt, N.M. *Environmental Geochemistry of Minesite Drainage: Practical Theory and Case Studies*; MDAG Publishing: Vancouver, BC, Canada, 2001; ISBN 0968203914.
9. Nordstrom, D.K. Mine waters: Acidic to circumneutral. *Elements* **2011**, *7*, 393–398. [[CrossRef](#)]
10. Rinder, T.; Dietzel, M.; Stammeier, J.A.; Leis, A.; Bedoya-González, D.; Hilberg, S. Geochemistry of coal mine drainage, groundwater, and brines from the Ibbenbüren mine, Germany: A coupled elemental-isotopic approach. *Appl. Geochem.* **2020**, *121*, 104693. [[CrossRef](#)]
11. Wolkersdorfer, C.; Bowell, R. Contemporary reviews of mine water studies in Europe, Part. *Mine Water Environ.* **2004**, *23*, 162–182. [[CrossRef](#)]
12. Younger, P.L.; Wolkerdorfer, C.H.; Bowell, R.J.; Diels, L. Partnership for acid drainage remediation in Europe (PADRE): Building a better future founded on research and best practice. In *Proceedings of the 7th International Conference on Acid Rock Drainage (ICARD)*, St. Louis, MO, USA, 26–30 March 2006; American Society of Mining and Reclamation: Lexington, KY, USA, 2006; Volume 3, pp. 2571–2574. [[CrossRef](#)]

13. Gombert, P.; Sracek, O.; Koukouzas, N.; Gzyl, G.; Valladares, S.T.; Fraczek, R.; Klinger, C.; Bauerek, A.; Areces, J.E.Á.; Chamberlain, S.; et al. An Overview of Priority Pollutants in Selected Coal Mine Discharges in Europe. *Mine Water Environ.* **2018**, *38*, 16–23. [[CrossRef](#)]
14. Johnson, D.B.; Hallberg, K.B. Acid mine drainage remediation options: A review. *Sci. Total Environ.* **2005**, *338*, 3–14. [[CrossRef](#)] [[PubMed](#)]
15. Qureshi, A.; Maurice, C.; Öhlander, B. Potential of coal mine waste rock for generating acid mine drainage. *J. Geochem. Explor.* **2016**, *160*, 44–54. [[CrossRef](#)]
16. Johnson, D.B. Chemical and microbiological characteristics of mineral spoils and drainage waters at abandoned coal and metal mines. *Water Air Soil Pollut. Focus* **2003**, *3*, 47–66. [[CrossRef](#)]
17. Xu, T.; White, S.P.; Pruess, K.; Brimhall, G.H. Modeling of pyrite oxidation in saturated and unsaturated subsurface flow systems. *Transp. Porous Media* **2000**, *39*, 25–56. [[CrossRef](#)]
18. Banks, D.; Younger, P.L.; Arnesen, R.T.; Iversen, E.R.; Banks, S.B. Mine-water chemistry: The good, the bad and the ugly. *Environ. Geol.* **1997**, *32*, 157–174. [[CrossRef](#)]
19. Blowes, D.W.; Ptacek, C.J.; Jambor, J.L.; Weisener, C.G. The Geochemistry of Acid Mine Drainage. *Treatise Geochem.* **2003**, *9*, 149–204.
20. Akcil, A.; Koldas, S. Acid Mine Drainage (AMD): Causes, treatment and case studies. *J. Clean. Prod.* **2006**, *14*, 1139–1145. [[CrossRef](#)]
21. Younger, P.L.; Robins, N.S. *Challenges in the Characterization and Prediction of the Hydrogeology and Geochemistry of Mined Ground*; Special Publications; Geological Society of London: London, UK, 2002; Volume 198, pp. 1–16. [[CrossRef](#)]
22. DMT GmbH & Co. KG. *Abschlussbetriebsplan des Steinkohlenbergwerks Ibbenbüren Anlage 17—Prognose zur optimierten Wasserannahme nach Stilllegung des Steinkohlenbergwerkes Ibbenbüren (Ostfeld)*; RAG Anthrazit Ibbenbüren GmbH: Essen, Germany, 2019; 104p.
23. Lotze, F.; Semmler, W.; Kötter, K.; Mausolf, F. *Hydrogeologie des Westteils der Ibbenbürener Karbonscholle*; Springer Fachmedien Wiesbaden GmbH: Wiesbaden, Germany, 1962; ISBN 9783663006657.
24. David, K.; Timms, W.A.; Barbour, S.L.; Mitra, R. Tracking changes in the specific storage of overburden rock during longwall coal mining. *J. Hydrol.* **2017**, *553*, 304–320. [[CrossRef](#)]
25. Liu, Y.; Liu, Q.M.; Li, W.P.; Li, T.; He, J.H. Height of water-conducting fractured zone in coal mining in the soil–rock composite structure overburdens. *Environ. Earth Sci.* **2019**, *78*, 242–255. [[CrossRef](#)]
26. Majdi, A.; Hassani, F.P.; Nasiri, M.Y. Prediction of the height of distressed zone above the mined panel roof in longwall coal mining. *Int. J. Coal Geol.* **2012**, *98*, 62–72. [[CrossRef](#)]
27. Qu, Q.; Xu, J.; Wu, R.; Qin, W.; Hu, G. Three-zone characterisation of coupled strata and gas behaviour in multi-seam mining. *Int. J. Rock Mech. Min. Sci.* **2015**, *78*, 91–98. [[CrossRef](#)]
28. Zhang, X.; Ghabraie, B.; Ren, G.; Tu, M. Strata movement and fracture propagation characteristics due to sequential extraction of multiseam longwall panels. *Adv. Civ. Eng.* **2018**. [[CrossRef](#)]
29. Newman, C.; Agioutantis, Z.; Boede Jimenez Leon, G. Assessment of potential impacts to surface and subsurface water bodies due to longwall mining. *Int. J. Min. Sci. Technol.* **2017**, *27*, 57–64. [[CrossRef](#)]
30. Becker, I.; Wüstefeld, P.; Koehrer, B.; Felder, M.; Hilgers, C. Porosity and permeability variations in a tight gas sandstone reservoir analogue, Westphalian D, Lower Saxony basin, NW Germany: Influence of depositional setting and diagenesis. *J. Pet. Geol.* **2017**, *40*, 363–389. [[CrossRef](#)]
31. Wüstefeld, P.; Hilse, U.; Koehrer, B.; Adelman, D.; Hilgers, C. Critical evaluation of an Upper Carboniferous tight gas sandstone reservoir analog: Diagenesis and petrophysical aspects. *Mar. Pet. Geol.* **2017**, *86*, 689–710. [[CrossRef](#)]
32. Drozdzewski, G.; Dölling, M. *Elemente der Osning-Störungzone (NW-Deutschland)—Leitstrukturen einer Blattverschiebungszone*. In *Scriptum online 7*; Geologischer Dienst Nordrhein-Westfalen: Krefeld, Germany, 2018.
33. Bruns, B.; Littke, R. Lithological dependency and anisotropy of vitrinite reflectance in high rank sedimentary rocks of the Ibbenbüren area, NW-Germany: Implications for the tectonic and thermal evolution of the Lower Saxony Basin. *Int. J. Coal Geol.* **2015**, *137*, 124–135. [[CrossRef](#)]
34. Bässler, R. Hydrogeologische, chemische und Isotopen—Untersuchungen der Grubenwässer im Ibbenbürener Steinkohlenrevier. *Z. Deutsch. Geol. Ges.* **1970**, 209–286. [[CrossRef](#)]
35. Coldewey, W.G.; Wesche, D. Hydrologie und Hydrogeologie der Ibbenbürener Karbon-Scholle. In *Scriptum Online 14*; Geologischer Dienst Nordrhein-Westfalen: Krefeld, Germany, 2020; pp. 1–10. Available online: https://www.gd.nrw.de/zip/scriptumonline-14_2020-07.pdf (accessed on 28 April 2021).
36. Bundesamt für Kartographie und Geodäsie, (BKG). Shapefile of Administrative Boundaries (WGS84). 2011. Available online: https://www.zensus2011.de/EN/Media/Background_material/Background_material_node.html (accessed on 23 April 2021).
37. Becker, I.; Busch, B.; Koehrer, B.; Adelman, D.; Hilgers, C. Reservoir Quality Evolution of Upper Carboniferous (Westphalian) Tight Gas Sandstones, Lower Saxony Basin, Nw Germany. *J. Pet. Geol.* **2019**, *42*, 371–392. [[CrossRef](#)]
38. Rudakov, D.V.; Coldewey, W.G.; Goerke-Mallet, P. Modeling the Inflow and Discharge from Underground Structures within the Abandoned Hardcoal Mining Area of West Field (Ibbenbüren). In *An Interdisciplinary Response to Mine Water Challenges, Proceedings of the 12th International Mine Water Association Congress (IMWA), Xuzhou, China, 18–22 August 2014*; Sui, W., Sun, Y., Wang, C., Eds.; China University of Mining and Technology: Xuzhou, China, 2014; pp. 699–705.

39. Drozdowski, G. Tiefentektonik der Ibbenbürener Karbon-Scholle. In *Beiträge zur Tiefentektonik westdeutscher Steinkohlenlagerstätten*; Geologisches Landesamt Nordrhein Krefeld: Krefeld, Germany, 1985; pp. 189–216.
40. Ingersoll, R.V.; Bullard, T.F.; Ford, R.L.; Grimm, J.P.; Pickle, J.D.; Sares, S.W. The effect of grain size on detrital modes: A test of the Gazzi-Dickinson point-counting method (Holocene, sand, New Mexico, USA). *J. Sediment. Petrol.* **1984**, *54*, 103–116.
41. Bertier, P.; Swennen, R.; Lagrou, D.; Laenen, B.E.N.; Kempes, R. Palaeo-climate controlled diagenesis of the Westphalian C & D fluvial sandstones in the Campine Basin (north-east Belgium). *Sedimentology* **2008**, *55*, 1375–1417.
42. Nagy, K.L.; Blum, A.E.; Lasaga, A.C. Kaolinite precipitation and dissolution: Effects on porosity and permeability. *Am. Assoc. Pet. Geol. Bull.* **1989**, *73*.
43. Pierini, C.; Mizusaki, A.M.P.; Scherer, C.M.S.; Alves, D.B. Integrated stratigraphic and geochemical study of the Santa Maria and Caturrita formations (Triassic of the Paraná Basin), southern Brazil. *J. S. Am. Earth Sci.* **2002**, *15*, 669–681. [[CrossRef](#)]
44. Ehrenberg, S.N.; Aagaard, P.; Wilson, M.J.; Fraser, A.R.; Duthie, D.M.L. Depth-Dependent Transformation of Kaolinite to Dickite in Sandstones of the Norwegian Continental Shelf. *Clay Miner.* **1993**, *28*, 325–352. [[CrossRef](#)]
45. Beaufort, D.; Cassagnabere, A.; Petit, S.; Lanson, B.; Berger, G.; Lacharpagne, J.C.; Johansen, H. Kaolinite-to-dickite reaction in sandstone reservoirs. *Clay Miner.* **1998**, *33*, 297–316. [[CrossRef](#)]
46. Huggett, J.M. Clays and Their Diagenesis. In *Encyclopedia of Geology*; Selley, R.C., Cocks, L.R., Plimer, I., Eds.; Elsevier Ltd.: London, UK, 2005; pp. 62–70.
47. Huang, W. The Formation of Illitic Clays from Kaolinite in KOH Solution from 225 °C to 350 °C. *Clays Clay Miner.* **1993**, *41*, 645–654.
48. Mantovani, M.; Becerro, A.I. Illitization of kaolinite: The effect of pressure on the reaction rate. *Clays Clay Miner.* **2010**, *58*, 766–771. [[CrossRef](#)]
49. Thyne, G.; Boudreau, B.P.; Ramm, M.; Midtbø, R.E. Simulation of potassium feldspar dissolution and illitization in the Statfjord Formation, North Sea. *Am. Assoc. Pet. Geol. Bull.* **2001**, *85*, 621–635. [[CrossRef](#)]
50. Galán, E.; Ferrell, R.E. *Genesis of Clay Minerals*; Developments in Clay Science, Elsevier Ltd.: Oxford, UK, 2013; Volume 5, pp. 83–126. ISBN 9780080982588. [[CrossRef](#)]
51. Que, M.; Allen, A.R. Sericitization of plagioclase in the Rosses Granite Complex, Co. Donegal, Ireland. *Mineral. Mag.* **1996**, *60*, 927–936. [[CrossRef](#)]
52. Zotov, A.; Mukhamet-Galeev, A.; Schott, J. An experimental study of kaolinite and dickite relative stability at 150–300 degrees C and the thermodynamic properties of dickite. *Am. Mineral.* **1998**, *83*, 516–524. [[CrossRef](#)]
53. Besly, B.M.; Burley, S.D.; Turner, P. The late Carboniferous “Barren Red Bed” play of the Silver Pit area, southern north sea. *Pet. Geol. Conf. Proc.* **1993**, *4*, 727–740. [[CrossRef](#)]
54. Delvigne, J.E. *Atlas of Micromorphology of Mineral Alteration and Weathering*; Special Publication; Martin, R.F., Ed.; Mineralogical Association of Canada: Quebec City, QC, Canada, 1998; ISBN 0921294433.
55. Chandra, A.P.; Gerson, A.R. The mechanisms of pyrite oxidation and leaching: A fundamental perspective. *Surf. Sci. Rep.* **2010**, *65*, 293–315. [[CrossRef](#)]
56. Pruess, K.; Narasimhan, T.N. A practical method for modeling fluid and heat flow in fractured porous media. *Soc. Pet. Eng. J.* **1985**, *25*, 14–26. [[CrossRef](#)]
57. Hao, Y.; Fu, P.; Carrigan, C.R. Application of a dual-continuum model for simulation of fluid flow and heat transfer in fractured geothermal reservoirs. In *Proceedings of the 38th Workshop on Geothermal Reservoir Engineering*; SGP-TR-198; Stanford University: Stanford, CA, USA, 2013; pp. 462–469.
58. Kordilla, J.; Sauter, M.; Reimann, T.; Geyer, T. Simulation of saturated and unsaturated flow in karst systems at catchment scale using a double continuum approach. *Hydrol. Earth Syst. Sci.* **2012**, *16*, 3909–3923. [[CrossRef](#)]
59. Kovács, A.; Sauter, M. Modelling karst hydrodynamics. In *Methods in Karst Hydrogeology*; Goldscheider, N., Drew, D., Eds.; Taylor & Francis: London, UK, 2007; pp. 201–222. ISBN 6087858393.
60. Sauter, M. *Quantification and Forecasting of Regional Groundwater Flow and Transport in a Karst Aquifer (Gallusquelle, Malm, SW. Germany)*; Geowissenschaftliche Fakultät: Jena, Germany, 1992.
61. Nordstrom, D.K.; Blowes, D.W.; Ptacek, C.J. Hydrogeochemistry and microbiology of mine drainage: An update. *Appl. Geochem.* **2015**, *57*, 3–16. [[CrossRef](#)]
62. Hammarstrom, J.M.; Seal, R.R.; Meier, A.L.; Kornfeld, J.M. Secondary sulfate minerals associated with acid drainage in the eastern US: Recycling of metals and acidity in surficial environments. *Chem. Geol.* **2005**, *215*, 407–431. [[CrossRef](#)]

Chapter 3: A dual-continuum model (TOUGH2) for characterizing flow and discharge in a mechanically disrupted sandstone overburden

Bedoya-Gonzalez, D.^{1,2}, Kessler, T.², Rinder, T.¹, & Schafmeister, M.T.²

¹ Department of Geography and Geology, University of Salzburg, Hellbrunner Str. 34, 5020 Salzburg, Austria.

² Institute for Geography and Geology, University of Greifswald, Friedrich-Ludwig-Jahn Str. 17a, 17487 Greifswald, Germany.

Published in: Hydrogeology Journal (2022), Vol. 30, pages 1717–1736.

<https://doi.org/10.1007/s10040-022-02507-3>



A dual-continuum model (TOUGH2) for characterizing flow and discharge in a mechanically disrupted sandstone overburden

Diego Bedoya-Gonzalez^{1,2}  · Timo Kessler¹ · Thomas Rinder² · Maria-Theresia Schafmeister¹

Received: 16 December 2021 / Accepted: 12 June 2022
© The Author(s) 2022

Abstract

Underground hard coal mining usually disrupts the mechanical equilibrium of rock sequences, creating fractures within minor permeable rocks. The present study employs a dual-continuum model to assess how both fractured and porous sandstone media influence the percolation process in postmining setups. To test the approach, the software TOUGH2 was employed to simulate laminar fluid flow in the unsaturated zone of the Ibbenbüren Westfield mining area. Compared to other coal mining districts in Germany, this area is delineated by the topography and local geology, leading to a well-defined hydrogeological framework. Results reveal good agreement between the calculated and measured mine water discharge for the years 2008 and 2017. The constructed model was capable of reproducing the bimodal flow behavior of the adit by coupling a permeable fractured continuum with a low-conductivity rock matrix. While flow from the fractured continuum results in intense discharge events during winter months, the rock matrix determines a smooth discharge limb in summer. The study also evaluates the influence of individual and combined model parameters affecting the simulated curve. A detailed sensitivity analysis displayed the absolute and relative permeability function parameters of both continua among the most susceptible variables. However, a strong a priori knowledge of the value ranges for the matrix continuum helps to reduce the model ambiguity. This allowed for calibration of some of the fractured medium parameters for which sparse or variable data were available. However, the inclusion of the transport component and acquisition of more site-specific data is recommended to reduce their uncertainty.

Keywords Dual-continuum model · Fractured rocks · Coal mining · TOUGH2 · Germany

Introduction

Underground hard coal mining operations irreversibly disrupt the preexisting mechanical equilibrium of the geological media (Kim et al. 1997; Newman et al. 2017). The employment of high-recovery methods redistributes, concentrates and reorientates the stress state of the bedrock above the mined seams (Palchik 2003; Meng et al. 2016; David et al. 2017). Conceptually, coal mine overburden can be subdivided into caved, fractured and deformation zones (Fig. 1), according to their response to the disruptions

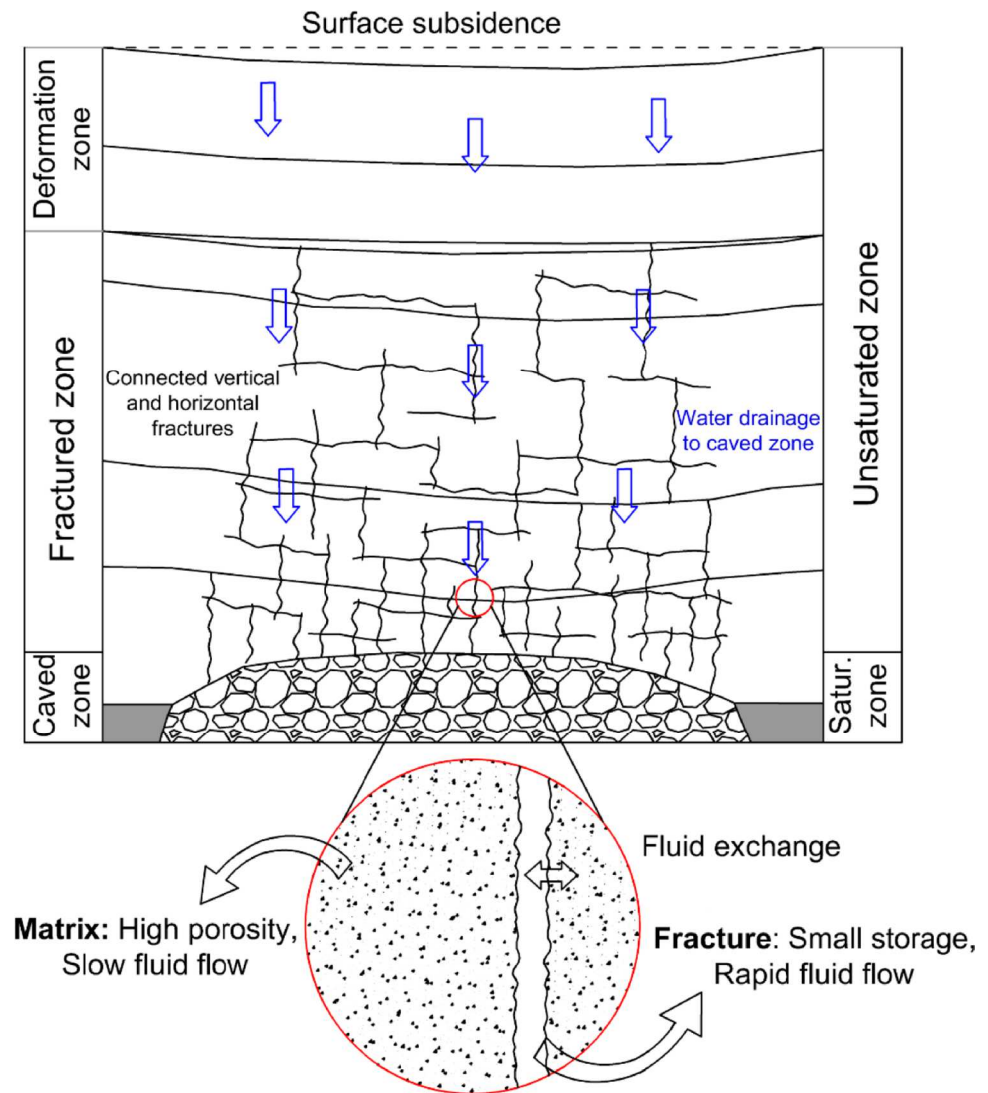
(Palchik 2003; Zhang et al. 2018a; Bai and Tu 2019; Liu et al. 2019). The caved zone encompasses the highly fragmented area formed after the overburden falls to the mine level. Above it, horizontal and subvertical fractures break the bedrock, developing a fractured zone, whereas towards the top of the rock sequence, layers of higher plasticity create a deformation zone, dampening the movement of the underlying sequence. These overburden deformations also modify the hydrogeological setting of mined areas. Induced fractures, for instance, alter the flow paths of percolating groundwater while increasing the hydraulic conductivity of the rocks (Qu et al. 2015; Zhang et al. 2018b; Liu et al. 2019; Qiao et al. 2019). In addition, subsidence related to the deformation zone may change surface hydrological networks, increasing or decreasing the water balance of the mined area and changing the water level in the aquifers (Kelleher et al. 1991; Blodgett and Kuipers 2002). Accordingly, fluid flow in postmining overburdens can be described by four processes: (1) meteoric water infiltration into the

✉ Diego Bedoya-Gonzalez
diegoalexander.bedoyagonzalez@sbg.ac.at

¹ Institute for Geography and Geology, University of Greifswald, Friedrich-Ludwig-Jahn Str. 17a, 17487 Greifswald, Germany

² Department of Geography and Geology, University of Salzburg, Hellbrunner Str. 34, 5020 Salzburg, Austria

Fig. 1 Schematic profile and conceptual understanding of groundwater flow in postmining fractured overburdens (modified after David et al. 2017 and Bai and Tu 2019)



first meters of soil and disaggregated rock, (2) percolation through an undisturbed zone, (3) groundwater flow in sub-vertical fracture networks, and (4) flow and groundwater storage in the porous matrix (Fig. 1). However, as the latter two processes take place in the same physical space, they are rarely modeled simultaneously. The simulation of a discrete setup that considers fractures and porous matrix requires extensive characterization of both media (Ghasemizadeh et al. 2012; Hao et al. 2013). This results in models with poor real-field practicability and lots of uncertainties due to the high demand for restricted-access data, especially those related to fracture size, spacing, orientation and transmissivity distributions (Kovács and Sauter 2007; Koohbor et al. 2019). Addressing the influence of such uncertainties and, therefore, their effect on the models' predictive capability is a complex task that requires the use of probability distribution methods such as Monte Carlo or polynomial chaos (Rouleau and Gale 1987; Younes et al. 2020; Drouin et al.

2021; Guo et al. 2021). In the presence of a large number of variables, the model requires a significant amount of simulations to cover the range of parameters, being computationally robust and expensive. Furthermore, if poor parameters and constraints are introduced into the model, poor results will be obtained (Fielding et al. 2011). All this has led most postmining models to explicitly ignore fracture structures by employing the equivalent porous medium (EPM) approach or even both media with lumped parameter models (e.g., see Adams and Younger 2001; Banks 2001; Vincenzi et al. 2010). Notwithstanding that both approaches have been successfully applied in case studies, they exhibit notable drawbacks when describing the fast component of the fractured system (Kim et al. 1997; Rapantova et al. 2007).

The present study proposes the dual-continuum (DC) approach as a potential tool to include fracture and matrix flow in minewater models. The DC approach was first proposed by Barenblatt et al. (1960) to describe fluid seepage

in fissured rocks without treating the subsurface as a single porous medium. The approach overcomes the difficulties of obtaining detailed information for constructing discrete models by handling fractures as a network of averaged characteristics. Thus, fractures and porous media are considered as two overlapping and interacting continua, with different flow, transport and storage parameters. The interaction between the two is achieved through a mass transfer function determined by the size and shape of the blocks, as well as their local difference in pressure, temperature and chemical potentials (Pruess and Narasimhan 1985; Beyer and Mohrlok 2006; Aguilar-López et al. 2020). Over time, the DC approach has been adapted for numerous subsurface processes, including oil recovery, geothermal energy, nuclear waste repositories, and CO₂ sequestration (e.g., see Kasiri and Bashiri 2011; Wu et al. 2011; Azom and Javadpour 2012; Hao et al. 2013). However, it has been particularly suited for the simulation of diffusive flow and rapid drainage processes in two-dimensional (2D) karst aquifers (Sauter 1992; Kovács and Sauter 2007; Kordilla et al. 2012; Dal Soglio et al. 2020).

Here, the software package TOUGH2 is employed to test the applicability of the DC approach in mining-derived flow regimes characterized by induced fractures within porous units. For this purpose, the well-defined hydrogeological system of the Ibbenbüren Westfield in north-west Germany is selected. Although the area was mined for decades within sharp topographic and geologic boundaries, only a few hydrogeological models have been published. By the time the Westfield mine was active, reports were limited to pointing out fluid flow through a fractured sequence due to low measured permeabilities, below 1 mD (e.g., see Lotze et al. 1962; Bäessler 1970). The first reference to a numerical model appeared for the mine closure plan in 1979, where water rebound was calculated using boxes to accommodate the water within empty spaces left by mining. However, this model was questioned some time after, as the rebound occurred 2 years later than predicted (Klinger et al. 2019). Some of the reasons given for the delay were the disregard of water-bearing fractures along with the imbibition process of unsaturated permeable units. Most recently, Rudakov et al. (2014) presented a lumped parameter model to simulate the temporal distribution of the mine water discharge as a factor of the precipitation. This model, however, shows deviations of up to 40% in summer months for heavy precipitation events. Lastly, Coldewey et al. (2018) developed an equivalent continuous model with a fixed recharge boundary to replicate the measured phreatic points around Westfield. This fit was achieved by setting rock permeabilities around 1×10^{-12} m², which are values three orders of magnitude above the maximums reported in the literature. With this hindsight in mind, the present DC model configures a breakthrough in the application of flow modeling by considering and

quantifying the specific contribution of fractured and matrix continua to the final transient mine discharge signal of the entire coal basin. Likewise, the study further evaluates the effect of individual and combined hydraulic parameters of the overburden. This sensitivity analysis reduces the model ambiguity by elucidating the importance and dependence of such variables. The study outcomes aim to pave the way for the application of the approach in other postmining scenarios, whilst being an important step towards the simulation of more complex processes such as contaminant migration or groundwater rebound.

Materials and methods

Geological setting

The Ibbenbüren coal-mining district is located in the northern part of North Rhine-Westphalia, north-west Germany (Fig. 2). Centuries-old mining industry was founded here on the exploitation of anthracitic coal seams encountered in a Carboniferous crustal block (Drozdowski and Dölling 2018; Rinder et al. 2020). The coal-bearing sequence was brought to the surface by a compression event during the Upper Cretaceous, which produced a crustal uplifting of about 2 km compared to the Triassic and Jurassic foreland, currently under the Quaternary. (Drozdowski 1985; Drozdowski and Dölling 2018). This process created an island-like shape hill, with marginal faults limiting all its sides (Figs. 2 and 3). Compression forces also created antithetic faults that divided the block into two NNE–SSW striking horst structures separated by the Bockradenergraben. The latter represents a stratigraphic discontinuity of more than 250 m in relation to the rock sequence contained in the horst structures. (Lotze et al. 1962; Bäessler 1970). For mining purposes, the two horst structures were named Eastfield and Westfield.

Lithology of the Westfield is well known based on geological documentation of mining activities. Rocks were deposited during the higher Westphalian C and lower Westphalian D stages, reaching a total thickness of more than 1,500 m (Blowes and Jambor 1990; Wüstefeld et al. 2017; Becker et al. 2019). The subhorizontal sequence follows an alternating pattern of sandstone and conglomerate layers, with sporadic presence of shales, wherein 81 coal seams are embedded (Lotze et al. 1962; Bäessler 1970). This pattern is equally observed in the shallow overburden, where a fining-upwards array of sublithic sandstone layers (approx. 80%) appears interspersed with dark-gray shales (20%) and remnants of two coal seams (Bedoya-Gonzalez et al. 2021a). On the surface, thin Quaternary sediments and a few anthropogenic waste rock deposits occasionally cover the Carboniferous rocks.

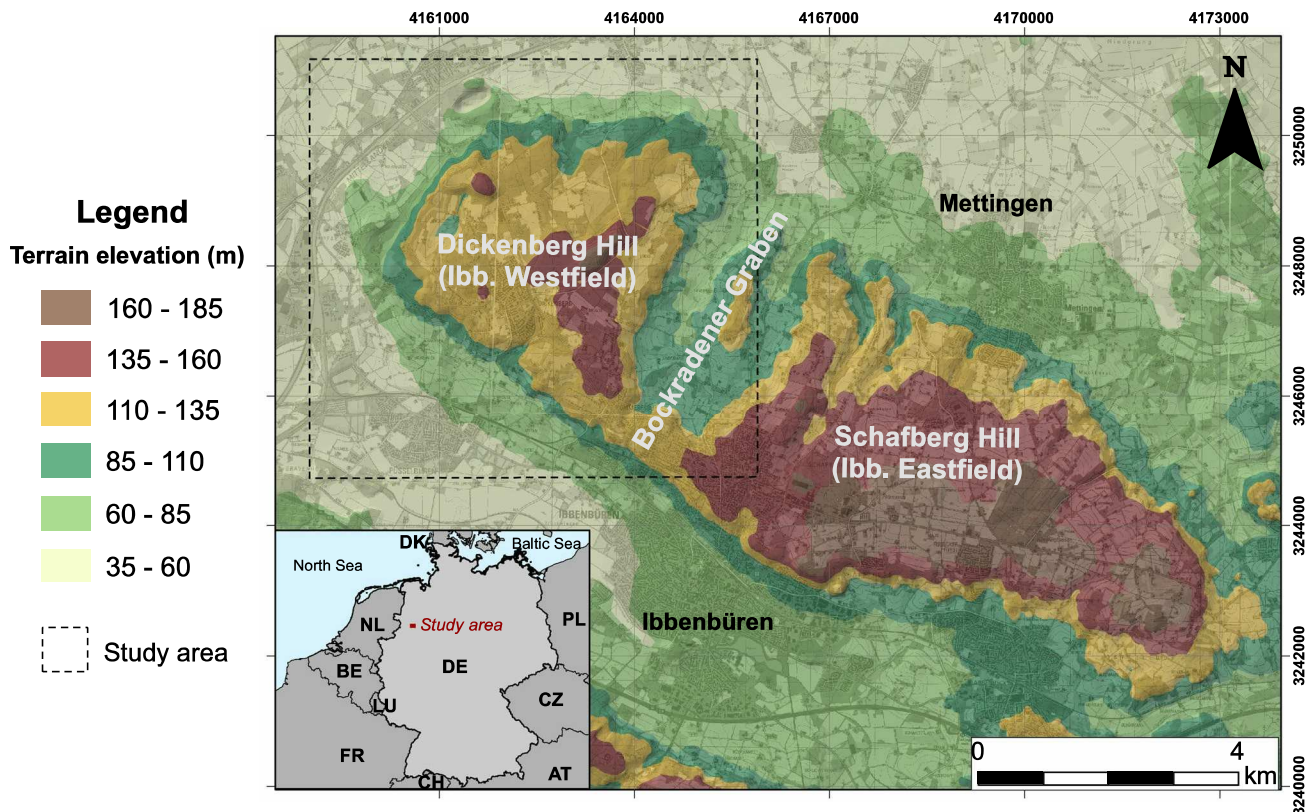


Fig. 2 Maps showing the location of the Ibbenbüren coal-mining district. The dashed-line square in the digital elevation map encloses the study area further depicted in Fig. 3 (modified after Bedoya-Gonzalez et al. 2021a)

Hydrogeological setting

Mining operations on the Westfield stopped in June 1979, with excavations as deep as 600 m below ground level (Klinger et al. 2019). After its closure, the area experienced controlled flooding up to 65 m above sea level (asl; Rudakov et al. 2014; Bedoya-Gonzalez et al. 2021b). At this elevation, groundwater reached an underground tunnel known as Dickenberg adit that runs along the southern edge of the field. Hydraulic connection from the Bockradener Graben to the adit is prevented with artificial underground dams. This generates the Dickenberg adit to drain the water from most of the Westfield, maintaining the phreatic level at 65 m asl. This includes the area enclosed by the Northern and Southern Carboniferous Marginal faults, Mieke Fault and Pommer-Esche Fault (Fig. 3), which represent effective hydrogeological boundaries (Rudakov et al. 2014; Coldewey et al. 2018). Furthermore, groundwater can be extracted only in areas higher than the Dickenberg adit, turning the terrain contour +65 m into an additional hydrogeological limit.

Since the phreatic level of the former coalfield is above the foreland surface (<55 m asl), percolated precipitation becomes the only groundwater input. The Geological Survey of North Rhine-Westphalia has calculated the groundwater

recharge of the area as a percentage of the precipitation using a water budget model that considers seasonality, soil type, land use and vegetation (Herrmann et al. 2014). Outcomes show an intensive groundwater recharge in winter, with a maximum in December and January, where it can reach 40–80 mm/month. In November, February and March, the monthly sums of groundwater recharge are around 30–40% lower than the previous period. April and May represent transition months where significantly more water is evaporated due to the beginning of the vegetation period. During summer months, recharge drops to almost zero, reaching a maximum multiyear average of 10 mm/month. Finally significant recharge is observed again in October. In conclusion, the Westfield can be conceived as a well-defined closed system, where the discharge at the Dickenberg adit depends on the temporal distribution of the recharge and the percolation dynamics through the unsaturated fractured overburden.

The dual-continuum approach

This study implements TOUGH2 code (by Lawrence Berkeley National Laboratory) to formulate a dual-continuum model of the fractured and unsaturated overburden of the Ibbenbüren Westfield. The numerical solution of the

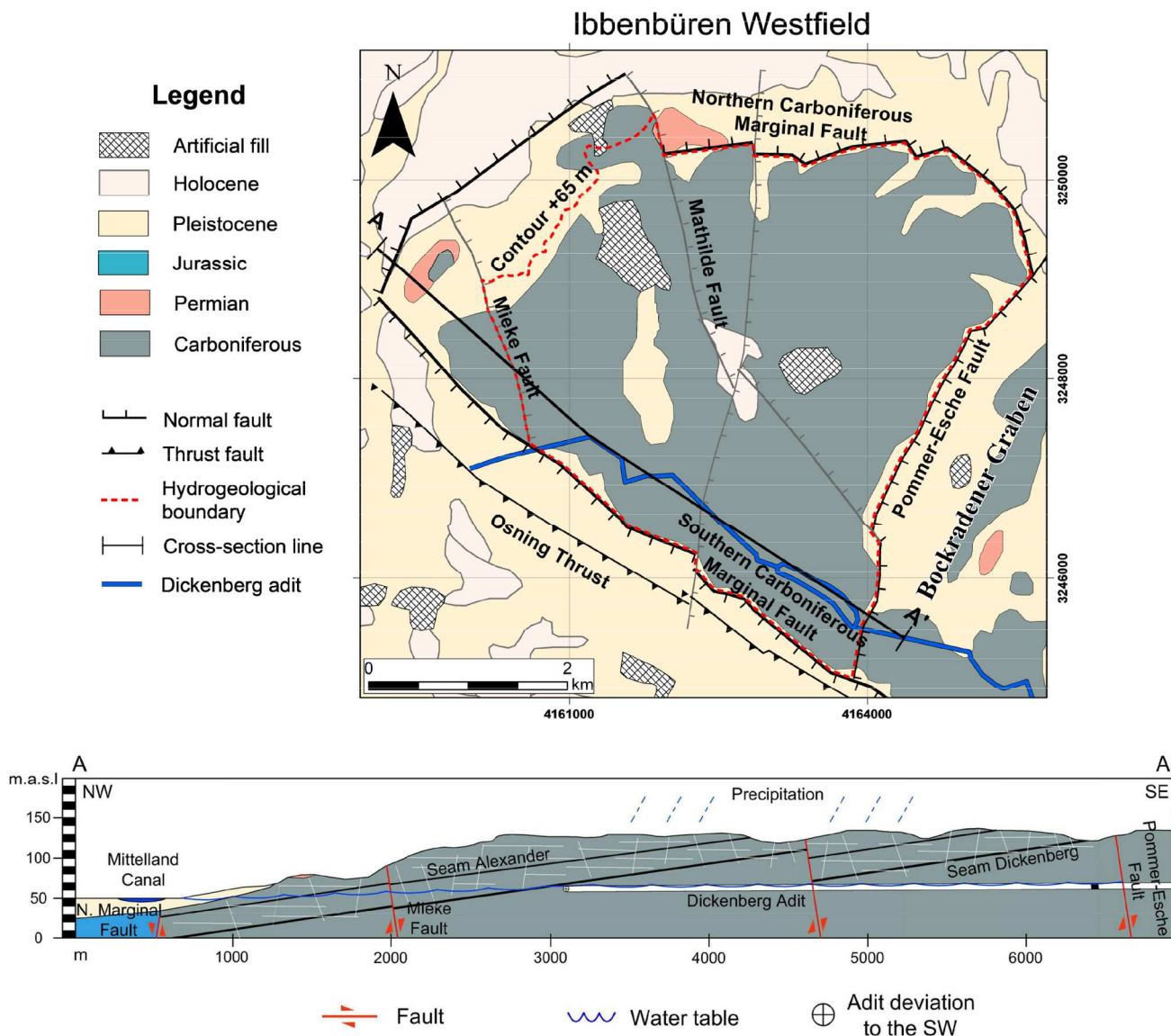


Fig. 3 Geological map and cross-section showing the hydrogeological boundaries and Dickenberg adit. The A–A' line in the map denotes the position of the cross-section, which is vertically exagger-

ated 5× to better detail the shallow overburden structure (modified after Bedoya-Gonzalez et al. 2021a)

software employs space discretization with integral finite differences and fully implicit first-order finite differences in time (Xu et al. 2000). Modeling scenarios include isothermal flow conditions, with air and water as the two phase components. The model requires the software to simultaneously solve two sets of flow equations at the same node: one for the porous medium and the other for the fracture network (Pruess and Narasimhan 1985). Here, the fractured system is represented as a porous medium by considering laminar flow through a network of small conduits. This assumption also accounts for the presence of undisturbed porous layers above the fractured medium as described for mining models. If water inflow at the interface with the fractured continuum

is greatly dependent on the hydraulic conductivity of the overlying layers, the Reynolds number (Re) for such continuum (Eq. 1) would most likely be below 10, allowing turbulent flow to be neglected (Bear 1972):

$$Re = \frac{\rho_w K_{u-f} d}{\mu_w} \tag{1}$$

where ρ_w is the water density (kg/m³), K_{u-f} is the hydraulic conductivity (m/s) at the interface between the undisturbed layer and fractured continuum, μ_w the water viscosity (Pa s), and d is a representative length dimension for the porous medium (m), commonly taken as a mean grain diameter.

Following this approach, the computational burden is reduced to solving a pair of Darcian flow equations rather than coupling, for example, a numerical Darcian solution to a Navier-Stokes equation (Chen et al. 2012; Aguilar-López et al. 2020). For an unsaturated system, flow can be described by two Richards equations (Richards 1931), coupled by a scaled exchange term (Γ_{ex}) that considers the interaction between both media (Gerke and van Genuchten 1993):

$$\frac{\partial}{\partial t} \theta_m = \nabla(K_m \nabla h_m) + \Gamma_{ex} \quad (2)$$

$$\frac{\partial}{\partial t} \theta_f = \nabla(K_f \nabla h_f) + \Gamma_{ex} \quad (3)$$

where the subscripts m and f indicate matrix and fractured continua respectively (hereafter replaced by the subscript c for space saving reasons since the equations for each continuum look the same), θ is the specific volumetric water content (m^3/m^3) defined as the product between the porosity (-) and water saturation (m^3/m^3), h is the hydraulic head (m) and K is the hydraulic conductivity (m/s). K in turn can be obtained from Eq. (4) (Pruess et al. 2012):

$$K_c = k_c k_{rwc} \frac{\rho_w g}{\mu_w} \quad (4)$$

where g is the gravity acceleration (m/s^2), k_c the absolute permeability (m^2) and k_{rwc} a relative permeability coefficient (-) directly related with the water saturation of each medium. For saturated media k_{rwc} is equal to 1, while under unsaturated conditions, the coefficient varies according to a number of factors described by the van Genuchten-Mualem parametric model (Mualem 1976; van Genuchten 1980):

$$k_{rwc} = S_{ec}^{0.5} \left[1 - \left(1 - S_{ec}^{1/m_c} \right)^{m_c} \right]^2 \quad (5)$$

$$S_{ec} = \left[1 + \left(|\alpha_c h| \right)^{n_c} \right]^{-m_c} = \frac{\theta_c - \theta_{rc}}{1 - \theta_{rc}} \quad (6)$$

with S_{ec} being the effective saturation (-), θ_{rc} the residual volumetric water content (m^3/m^3), α_c a scaling fitting parameter (1/m), and n_c and m_c fitting parameters associated with the pore distribution. Finally, the exchange term (Γ_{ex}) in the Eqs. (2) and (3) can be defined as (Gerke and van Genuchten 1993):

$$\Gamma_{ex} = K_a \alpha^* (h_f - h_m) \quad (7)$$

where K_a is the hydraulic conductivity at the interface (m/s), $(h_f - h_m)$ is the head difference between the two media (m)

and α^* is the exchange coefficient (1/s), which depends on the size and shape of the mesh elements according to:

$$\alpha^* = \frac{\beta \gamma_w}{a^2} \quad (8)$$

In Eq. (8), β is a geometry grid factor (3 for rectangular blocks, 15 for spheres), a is the distance between the center of a matrix block and the adjacent fracture and γ_w is a dimensionless scaling coefficient usually set to 0.4 (Pruess 1983; Gerke and van Genuchten 1993; Gerke et al. 2007; Kordilla et al. 2012)

Model calibration, efficiency and sensitivity analysis

The required parameters for fractured and matrix continua are manually calibrated using daily discharges recorded throughout the year 2008. The process is carried out through a trial-and-error scheme in which the simulated signal is visually adjusted with respect to the measured discharge. It starts with the adjustment of known parameters, including the permeabilities and porosities of the rocks, followed by the unsaturated properties of the porous units and hydraulic properties of the fractured continuum (usually reported in the literature and mining reports), and ending with the setting of the unsaturated parameters of the fractured continuum that have the lowest degree of knowledge. Once calibrated, the quality of the obtained parameters are validated using the measured discharges of the year 2017. Thereafter, the Nash-Sutcliffe efficiency (NSE) criterion is used to quantify the predictive power of the model for simulating the water discharge of the calibration and validation periods. This is a normalized coefficient that determines the relative magnitude of the residual variance compared to the measured data variance. NSE indicates how well the plot of observed versus simulated data fits the 1:1 line (Moriassi et al. 2015). While NSE equal to one represents a perfect match of the simulated to the observed data, values equal or lower than zero indicate that the model predictions are as accurate as the mean of the observed data. Thus, NSE is a convenient tool to evaluate the ability of a model to predict observations in long-term continuous simulations by comparing its effectiveness with respect to its mean value (Gupta et al. 2009).

A sensitivity analysis is additionally performed to determine those variables that can be set over a reasonable range, without affecting the efficiency of the model. The process is conducted by changing individual parameters of each continuum to at least four different points along the entire range of values. Although simple, this method appropriately quantifies the factors influencing the distributed regional model, maintaining narrow and reasonable control of the outcomes of interest with relatively few simulations (e.g., see Herman

et al. 2013; Rakovec et al. 2014; Devak and Dhanya 2017). Here, the lower and upper limits of each parameter are set on the maximum and minimum measured values present in the literature. The impact of the parameters is evaluated by calculating the root mean square error (RMSE) of the computed outflows compared to the calibrated discharge signal of the year 2008. The RMSE metric is preferred over the NSE in this step to overcome the known weaknesses of the latter in identifying differences in timing and magnitude of peak flows and shape of recession curves (e.g., see Krause et al. 2005; Pushpalatha et al. 2012; Moriasi et al. 2015). The calibrated signal of the year 2008 is also employed to facilitate interpretation regarding the best obtained adjustment, while preventing the computed RMSE values from being affected by outliers of measured daily discharges. Finally, interrelations between factors are evaluated with a codependency analysis, changing in pairs all the modeled parameters across the predetermined ranges.

Results

Model setup

Geometry and grid construction

The conceptualization of the modeled area is depicted in Fig. 4. Its design and dimensions are constructed according to the limits previously described in the hydrogeological section and illustrated in Fig. 3. The 3D system is discretized into vertical columns of $100 \times 100 \text{ m}^2$ base and variable height to represent the concave topography of the Westfield. The columns' height decreases about 5 m per column according to the average thickness of the rock layers. This size considers actual measurements made on core samples of the shallow overburden in the study area (Bedoya-Gonzalez et al. 2021a). The total number of columns for each height interval is, then, normalized by intersecting the

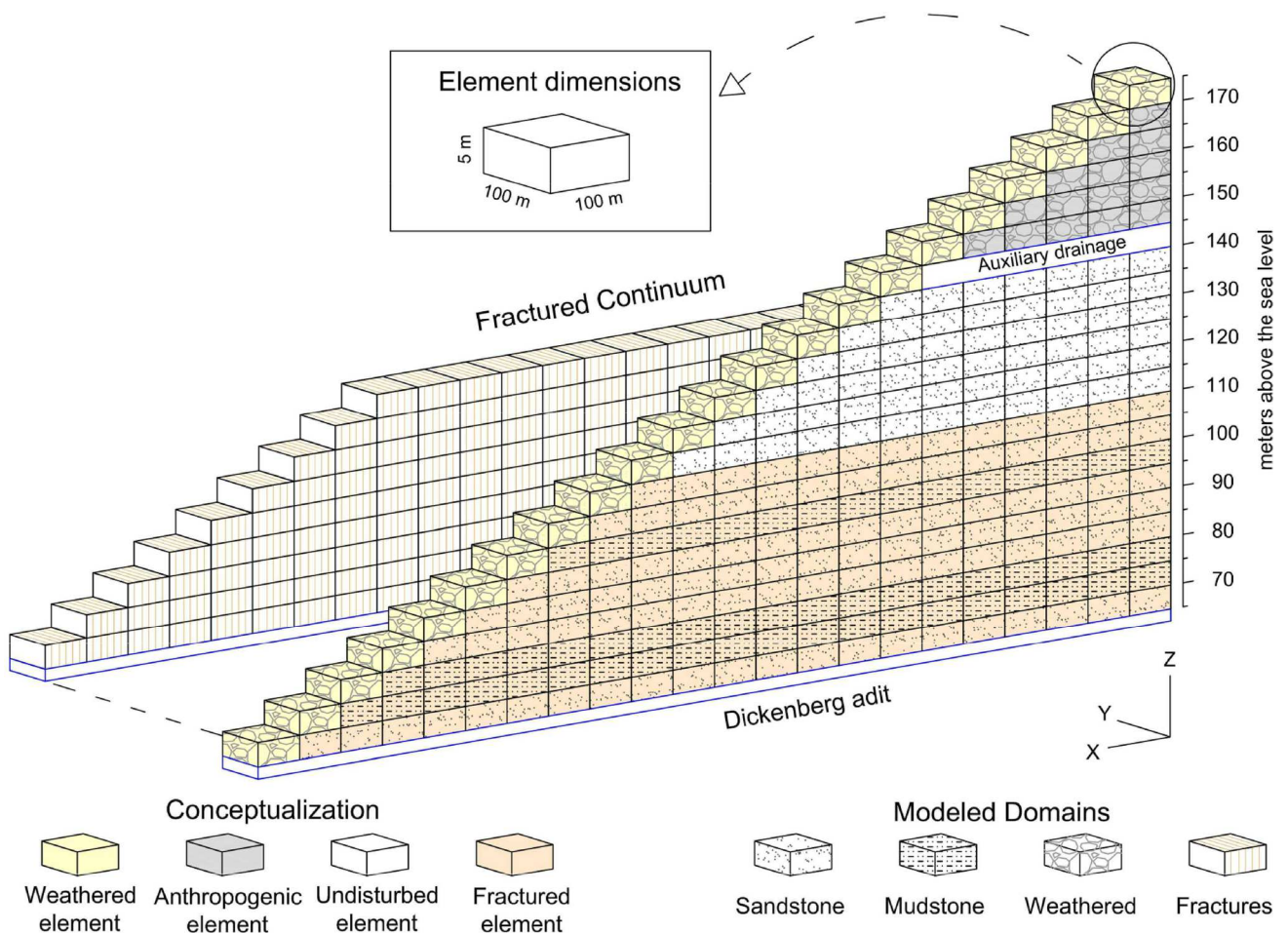


Fig. 4 Constructed grid for the DC Model. Recharge is applied directly onto the weathered blocks while an open boundary condition is set along the adit element. For each block colored in orange, the

mesh is divided into two continua (fracture and porous media) with the same physical location

digital elevation model (DEM) of the Westfield with the base boundary (i.e., 65 m asl). Finer horizontal discretizations of the columns are neglected since the model only computes gravity-driven vertical flow. Moreover, TOUGH2 requires fracturing information (i.e., spacing, number of sets, and shape of matrix blocks) and not block size to set the nodes location for calculating the driving pressure gradient at the matrix/fracture interface.

The average measured thickness of the layers is also used to subdivide the grid into blocks of 5-m vertical spacing (Fig. 4). Further vertical refinement is not implemented considering the rather homogeneous sequence, which is discretized into three lithologies, with predominance of sandstones (more than 80%). More layers would slightly modify the permeability of the columns due to minor saturation differences within the smaller blocks, but at higher computational cost. Like the thickness, horizontal layers are assigned within the columns maintaining the lithological proportions and stratigraphic position described in Bedoya-Gonzalez et al. (2021a). Exceptions are weathered intervals within the uppermost 5 m of each column and zones above 140 m, which correspond to anthropogenic rock deposits assigned to the weathered rock domain. Mining-induced fractures were estimated to extend up to 45 m above the uppermost mined seam, i.e. above the Dickenberg adit. This estimation is based on mathematical relationships between thickness of the excavated area and thickness of the overburden as previously established in Palchik (2003), Bai and Tu (2019), Guo et al. (2019) and Zha et al. (2020). However, additional grids with heights of 30 and 40 m are created to assess alternative values derived from these models. In any case, the base of the weathering zone turns into the uppermost limit of the fractured continuum. This causes the splitting not to extend to the first element of each column, even if the thickness of the overburden is less than the assumed height. Finally, the fracture density (i.e., number of vertical fractures per grid block) is assumed to be equal to 10, resulting in a total exchange area of 10,000 m² between both continua. As there is no study to the authors' knowledge that gives an approximation to this value, grid cells with 5 and 20 fractures per block are also constructed for the sensitivity analysis of the parameter.

Boundary and initial conditions

The lateral sides of each column are defined as no flow boundaries while the lower boundary is set to allow free drainage under gravity force. A specified flux boundary is set at the top of each column (i.e., in the weathered blocks) to account for diffuse recharge (Fig. 4). The amount of flux at the top is based on the recharge model developed by the Geological Survey of North Rhine-Westphalia (see section 'Hydrogeological setting'). To account for weather

variability, daily precipitation measurements are normalized with respect to the precipitation values used in the recharge model. Precipitation above the coalfield is calculated using the arithmetic mean values of daily events measured at the two closer meteorological stations, Mettingen and Laggenbeck, for the years 2007 to 2017 (data provided by the LANUV NRW). As a result, recharge imposed on the model intrinsically considers the influence of the climatic and physical characteristics of the area, varying daily according to the precipitation events—Table S1 in the electronic supplementary material (ESM).

Under unsaturated conditions, TOUGH2 requires water saturation as the initial condition for each grid element. Here, saturation values are computed from a long-term simulation that starts with the residual water content of each lithology (see the following section). First, constant recharge of 240 mm/year, equivalent to the long-term average groundwater recharge in northwest Germany (BGR 2021), is assigned over 100 years (approximate time from mine opening to 2008). Daily recharge values for the years 2007 and 2008 are then applied to ensure the seasonal variability of the water storage during the model calibration. Finally, daily inputs are continuously applied for another 9 years to maintain the temporal variability for the model validation in 2017.

Parameterization

Parameters used in the model are listed in Table 1. These values were extensively searched in the literature and assigned according to the characteristics of the matrix and fractured continua (Freeze and Cherry 1979; Kordilla et al. 2012; Parajuli et al. 2017; Coldewey et al. 2018; Bedoya-Gonzalez et al. 2021a). For model calibration and sensitivity analysis, parameters are varied within reasonable data ranges consistent with known field conditions (values in parentheses Table 1). Since there are no documented values for the hydraulic properties at the interfaces, these are set equal to the harmonic mean between the two continua. This forces the local exchange to be dominated by the lower conductive domain (i.e., the matrix), which might be closer to reality (Ray et al. 2004; Song et al. 2018; Aguilar-López et al. 2020). Specific storage coefficients for both media are neglected since the model faces unsaturated conditions and water release by compression is irrelevant.

Given that parameters of the van Genuchten-Mualem function have been developed for porous media, values assigned to fractured continuum have questionable physical meaning (e.g., see Sauter 1992; Kordilla et al. 2012). Here, these parameters are allocated to recreate the expected hydrological response of a highly permeable medium. Total porosity is set to 0.99 for the software to assume open fractures without solid elements, as identified

Table 1 Hydraulic parameters used in the model. Numbers outside the parentheses indicate the values that provided the best discharge agreement during the calibration process

Lithology	Permeability (m ²)	Eff. porosity (-)	Van Genuchten-Mualem parameters ^{a,b}		
			θ_r (m ³ /m ³)	α (m ⁻¹)	m (-)
Sandstone	5×10^{-14} ($1 \times 10^{-13} - 1 \times 10^{-15}$) ^c	0.10 (0.08–0.15) ^d	0.30 (0.25–0.40)	0.07 (0.5–0.05)	0.35 (0.5–0.3)
Shale	1×10^{-17} ($1 \times 10^{-16} - 1 \times 10^{-18}$) ^e	0.05 ^c	0.65	0.04	0.22
Weathered interval	5×10^{-13} ($1 \times 10^{-12} - 1 \times 10^{-14}$) ^c	0.15 (0.1–0.2) ^c	0.2 (0.05–0.40)	0.3 (1–0.01)	0.65 (0.5–0.7)
Fractured continuum	5×10^{-11} ($1 \times 10^{-8} - 1 \times 10^{-14}$)	0.99 (0.5–0.99) ^d	0.05	0.3 (0.1–5)	0.8 (0.5–0.8)

^aKordilla et al. (2012)^bParajuli et al. (2017)^cColdewey et al. (2018)^dBedoya-Gonzalez et al. (2021a)^eFreeze and Cherry (1979).

by Bedoya et al. 2021 in core samples of the study area. However, the influence of a solid phase within the fractured continuum (e.g., sediment mixing flow, clay smear or cement) is also considered within the sensitivity analysis by reducing the open porosity down to 50%. The residual water content (θ_r) is fixed at 0.05 to allow the continuum to transmit water during dry periods. If this value was zero, the relative permeability would nullify the exchange with the matrix, generating numerical insufficiencies. The small amount of water saturation acquires physical meaning, for example, if a process such as gravity-driven film flow on the fracture walls was to be considered (Tokunaga and Wan 1997; Kordilla et al. 2012). Finally, the parameters m and α also reproduce the behavior of a large-pored material (e.g., gravel) that will saturate and transmit water rapidly during rainfall events. However, α parameter needs to be adjusted during the calibration process.

Calibration and validation of the model

The parameterization within the model was calibrated using daily discharges recorded throughout 2008 and subsequently validated with data of 2017. Fluid flow was simulated in the vertical component of each column, allowing lateral exchanges between fractured and porous media. The total discharge of the study area was obtained by summing the water flux of the two continua at the lower boundary of every column (i.e., at 65 m asl). This is equivalent to a dual permeability model, in which the global flow occurs in both continua. In the case where columns are covered by waste rock deposits, discharge measurements were made around 140 m asl, considering that an auxiliary drainage directs the water from these deposits towards the Dickenberg adit (B. Nippert, RAG GmbH, personal communication, 2019).

Figure 5a shows the measured and simulated discharge volumes of the Dickenberg adit for the year 2008. The graphed curve corresponds to the best match using the values listed outside the parentheses in Table 1. Model calibration was accomplished by fitting the observed and simulated discharge curves through a trial and error exercise that was performed in a series of more than 500 runs. Due to software limitations, it was not possible to perform, compare or supplement the calibration process with automatic inverse methods. Notwithstanding, manual calibration alone is expected to produce process-based (i.e., conceptually realistic) and reliable predictions from a clear understanding of the model structure (i.e., hydrological processes) and physical characteristics of the area (Ndiritu 2009; Arnold et al. 2012; Acero Triana et al. 2019). To prove it, the model reliability was validated for another 12-month period using the discharge of the year 2017 (Fig. 5b). Both, calibration and validation processes used variable time stepping. The initial time step was set at 100 s being systematically doubled if convergence occurred within the first four iterations up to a maximum of 1 day. Conversely, time step was reduced in multiples of 4 if the system exceeded 8 Newton-Raphson iterations to solve the connected equations. At the end the discharge was computed on a daily basis to compare the simulated signal with the measured data in the Dickenberg adit.

Modeling results also describe the temporal and spatial interaction between the fractured and matrix continua. For instance, the initial response of the system to a strong precipitation event in winter is a significant water transfer from the fractures to the matrix (Fig. 6a). However, much of this water returns to the fractures during spring and summer months (negative exchange values), as water pressure in the matrix increases, especially at interfaces with shale layers. On the other hand, Fig. 6b displays the exchange rate at the first and last fractured sandstone layer during a high rainfall

Fig. 5 Comparison between the measured and simulated discharge of the Dickenberg adit. The graphs show: **a** the best fit obtained during the calibration process for the year 2008; and **b** the discharge signal obtained from the validation process for the year 2017. Both simulated discharge signals were obtained by summing the water flux of the matrix and fractured continua at the lower boundary of the model

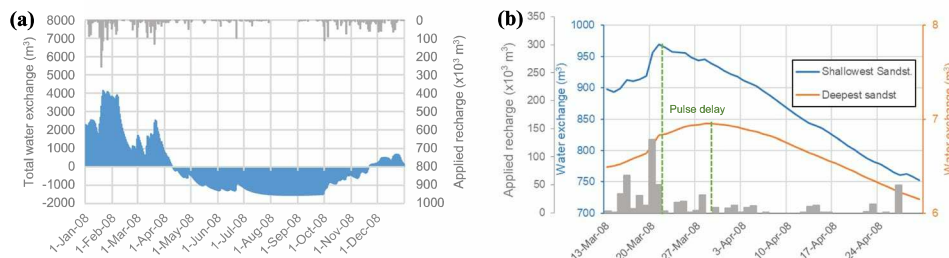
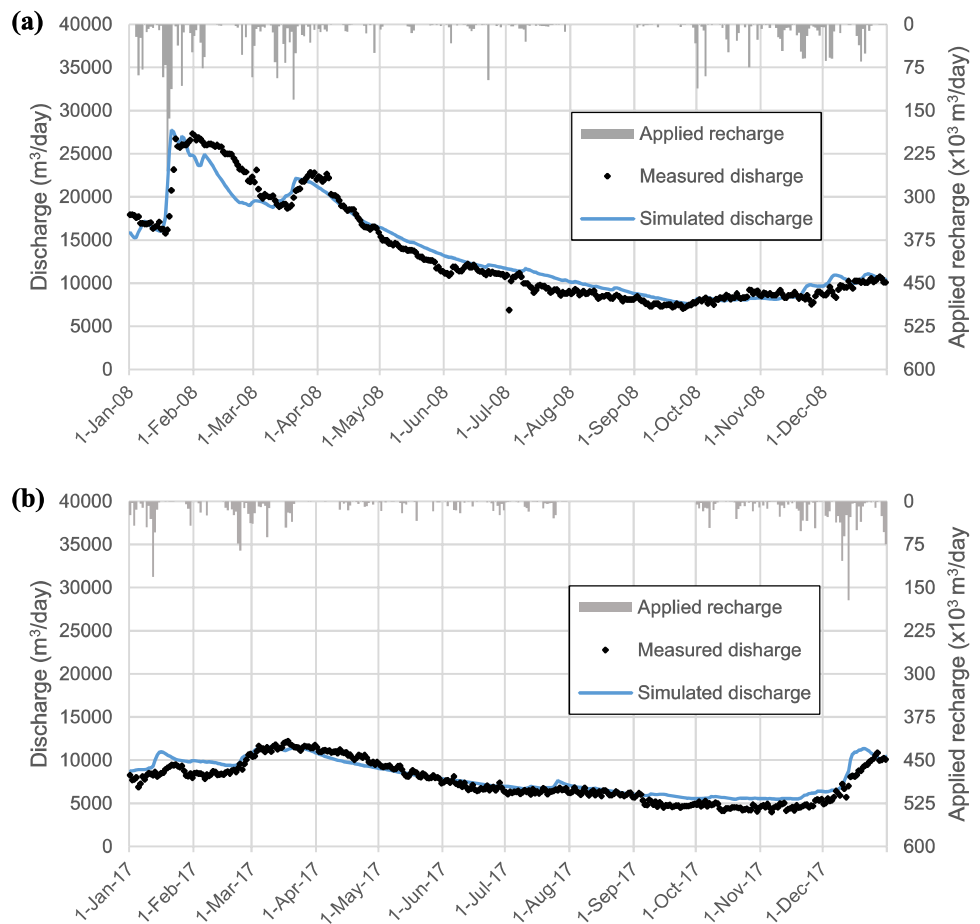


Fig. 6 Temporal and spatial distribution of the total fluid exchange and water saturation. **a** Total daily exchange between the two continua for the whole system (positive values represent exchange from

the fractures to the matrix while negative values from the matrix to the fractures). **b** Spatial variation of the total water exchange between the first and last fractured sandstone layers

period in March 2008. The delay of the inflow pulse to the matrix is associated to the pathway followed by the water within the fractured continuum and the storage capacity of the porous medium. Note that the exchanged water volume is much lower in the last layer because of its high saturation and spatial proximity to the water table. Besides, the exchange pulse shows a broader timeline in the last sandstone layer when compared to the first layer. This is considered a dispersive phenomenon which may be caused by

the difference in hydraulic properties between the two continua leading to variations in percolation velocities across the overburden. Lastly, Fig. 7 shows saturation variations due to water exchange between fractured and matrix continua for one of the columns. Results reveal that the fractured continuum saturated and desaturated faster and in higher percentages than the matrix medium, although the amount of water either gained or lost in the latter is much higher than in the fractured one. Figure 7 also summarizes how the

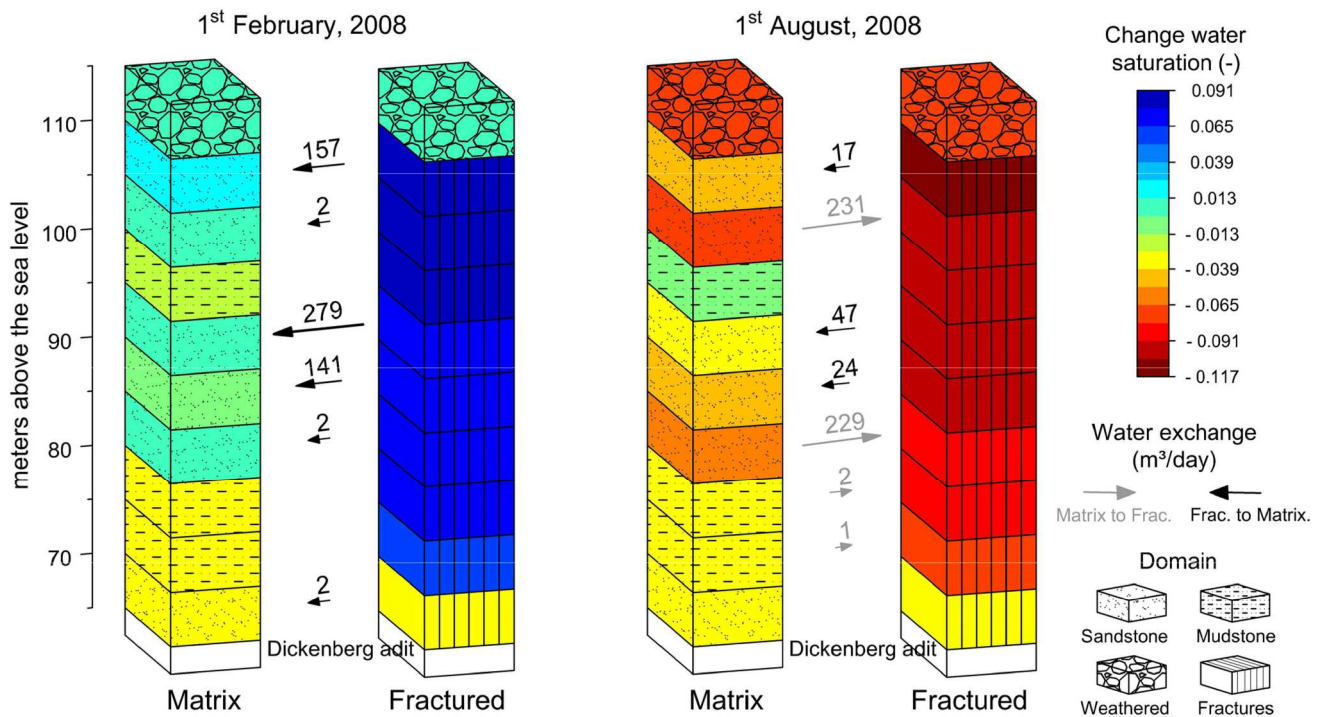


Fig. 7 Change in water saturation and fluid exchange between the two continua at two temporal points. Water exchange is given in m^3/day , while the variation in water saturation is measured with respect to the

initial water content at the time the daily variable recharge is applied (i.e., the water saturation at the end of the 100-year long-term simulation)

matrix absorbs water from the fracture in the winter, when saturation is higher, returning a large amount in the summer season due to pressure increase, especially at the interfaces with the shale layers. Despite this, the closest matrix blocks to the surface continue to absorb water coming from the unfractured sequence above them, preventing the fractures from easily discharging percolating rainwater into the adit during the drier months.

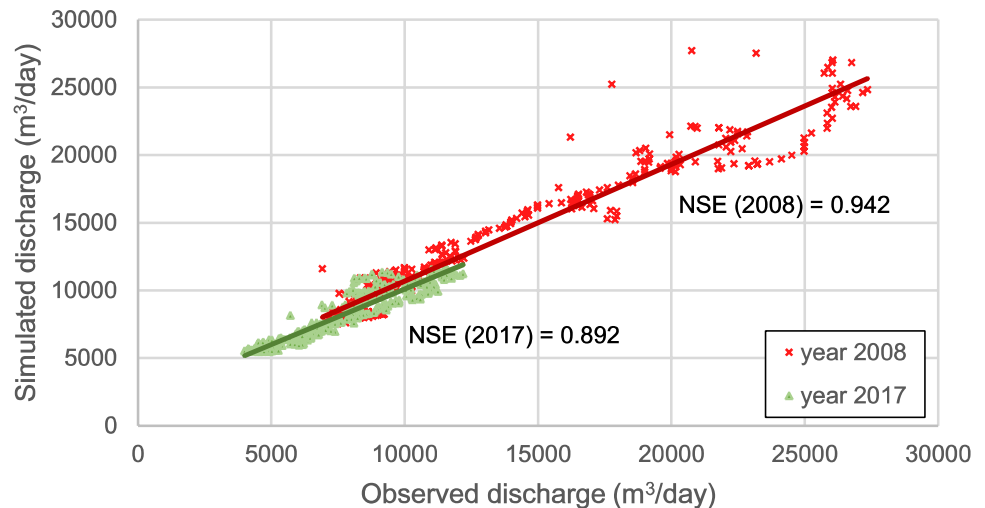
Model reliability and sensitive parameters

The simulated signals for calibration and validation periods display good visual agreement with the measured data. Results show few discrepancies in the discharge peaks for the winter months and a small signal advance in time, likely derived from the nonestimation of the rapid flow from the adit to the measurement point. The reliability of the model in fitting the measured discharges is further proven by NSE values close to one (Fig. 8). The largest discrepancies from the 1:1 trend line correspond mostly to an overestimation of the simulated discharge (values above the trend line in Fig. 8) derived from the aforementioned signal advance. The steep rising discharge limbs in winter derive significant differences between the measured and simulated values. For example, there is a difference of about $6,000 m^3$ between the two discharge signals at the end of January 2008, because

the peak of the simulated signal is reached 1 day earlier compared to the measured discharge. The simulated signal also presents underestimations in the discharge calculation associated with recession limbs in winter. However, differences between the two models are much smaller than those observed with the rising limb and are associated to punctuated events.

Table 2 provides an overview of all the field parameters required by the software as well as their sensitivity within the model. The range of values considered for each parameter matches those reported in Table 1, in addition to the variations of the fracture density and fractured zone height discussed in the section ‘Geometry and grid construction’. Here, parameters have been categorized as sensitive if the maximum dispersion of the data points around the regression line of the calibrated mean annual discharge is greater than 10%, which is equivalent to an RMSE of $1,360 m^3/day$ for the year 2008. As some parameters are likely to be insensitive when varied independently due to the complexity of the model, codependences are evaluated by varying two parameters at the same time. Thus, Table 2 also shows the highest RMSE discharge values for pairs of parameters with just one being sensitive (i.e., linear relationship) and pairs where both parameters are sensitive (i.e., nonlinear relationship). The analysis, however, neglects those recurrent insensitive and unrelated pairs of parameters associated

Fig. 8 Nash-Sutcliffe efficiency criterion (NSE) of the model for the calibration and validation periods. Solid lines indicate the 1:1 slope between the observed and measured data



with the model setup. For example, the influence of shale permeability when varied with respect to the porosity of the fractured continuum is considered redundant for two reasons: (1) fracture porosity minimally influences the already affected discharge signal by the fracture permeability (i.e., there is a linear relationship between the two parameters where only the fracture permeability influences the discharge) and (2) fluid exchange at interfaces was set up to depend largely on matrix permeability instead of fractured continuum permeability (see section ‘Parameterization’). As a result, the behavior and RMSE values are almost identical to those already reported for scenarios in which the shale permeability is varied along with the permeability of the fractured continuum.

Complementarily to Table 2, Fig. 9 displays the discharge curves of individual parameters with the highest sensitivity, while Fig. 10 shows the types of codependences that exist between some couples (all the codependences between parameters can be found in Fig. S1 of the ESM). From Fig. 9, it is observed that shorter water-conducting fractured zones (Fig. 9a) and higher sandstone permeabilities (Fig. 9b) broaden and enlarge the recession limbs, with up to 25% more water discharge. On the one hand, shorter fractures generate longer water residence times in the uppermost pristine layers, while higher sandstone permeability enhances the exchange from the fractured to the porous medium. Note that the exchange process between the two media is dominated by the permeability of the matrix (see ‘Parameterization’). This configuration causes strong discharge peaks in winter months when the sandstone permeability is reduced (Fig. 9b), as well as minimal signal differences after increasing the fracture permeability (Fig. 9c). The insensitivity of the model to higher fracture permeability is also related to the placement of a weathered layer on top of the columns, which acts as a buffer for the amount of precipitation that infiltrates into the continuum. On the other hand, lower

fracture permeability results in higher base flow discharges at the expense of decreased winter peaks (Fig. 9c). Observe that for the lowest value (i.e., $k_f = 1 \times 10^{-12} \text{ m}^2$), the fractured medium reaches a permeability similar to that of the porous medium, generating the closest scenario to an EPM model. Finally, it was observed that the alpha (α) parameter of the van Genuchten-Mualem function is directly related to the magnitude of the discharge (Fig. 9d). Higher values cause the fractured continuum to retain less water during the winter months, transmitting it more quickly and generating greater discharge.

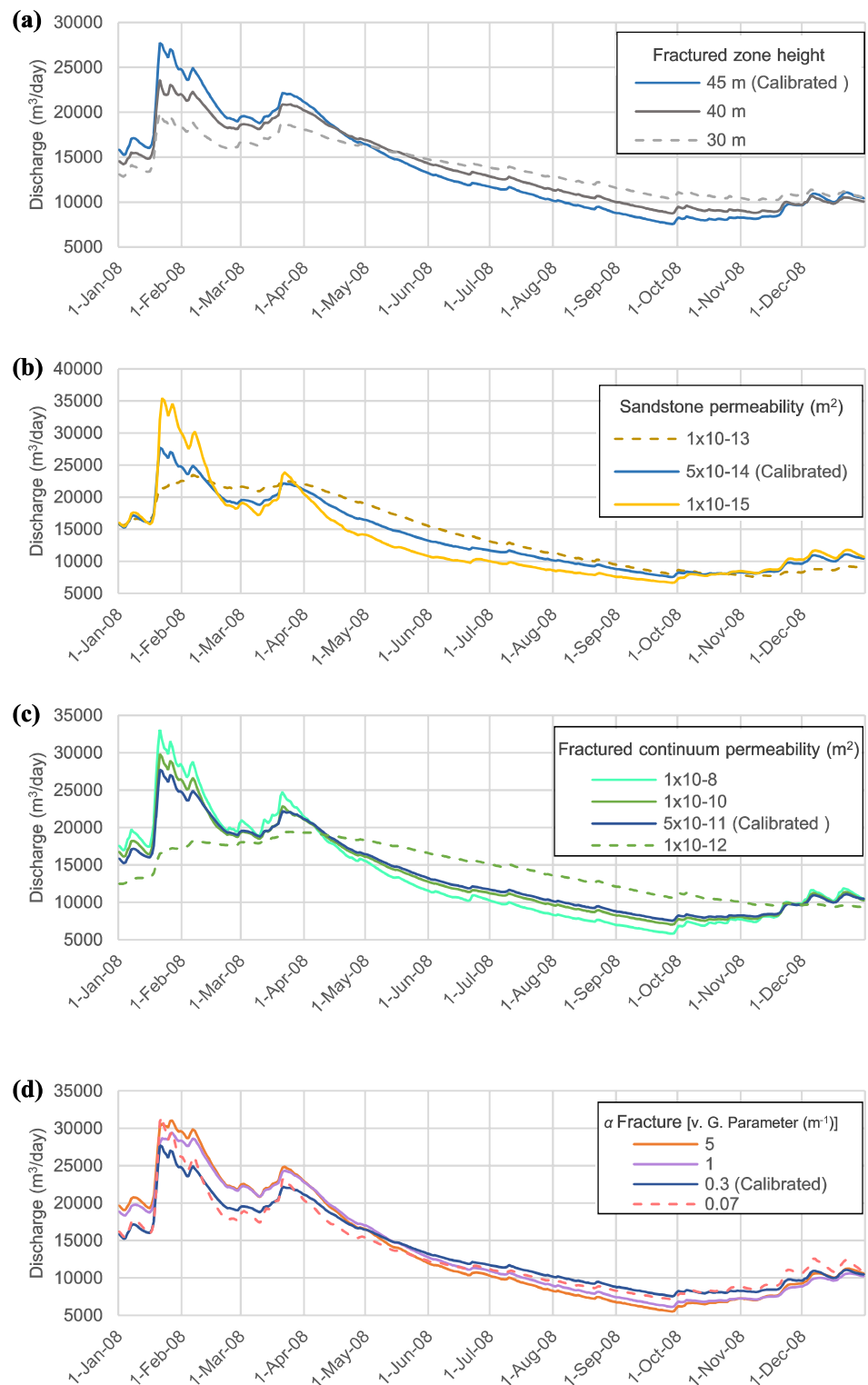
The analysis of codependences revealed 14 combinations in which both parameters were shown to be sensitive. For example, the simultaneous variation of sandstone permeability (k_s) and porosity (Φ_s) shows pronounced fluctuations, especially for low values (Fig. 10a). Whereas for the calibrated permeability (i.e., $k_s = 5 \times 10^{-14} \text{ m}^2$) Φ_s is insensitive; a k_s of one order of magnitude lower turns the porosity sensitive with a RMSE of around 2,500 m³/day for 8% and 1,400 m³/day for 15%. A more abrupt change is observed when varying the fracture alpha (α_f) parameter over the lower limit of the k_s (Fig. 10b). The lowest values of both parameters produce a minor sensitive combination, with a RMSE of about 1,500 m³/day. In contrast, the combination of the highest α_f with the lowest k_s increases the RMSE to almost 5,000 m³/day. It was also observed that the α_f exhibits mostly a linear relationship with almost all parameters evaluated. For example, Fig. 10c shows how the RMSE of the discharge varies widely as α_f increases without being affected by the residual water saturation of the fracture (θ_{rf}). Similar linear relationships are observed for couples that include k_s and k_f . Lastly, Fig. 10d illustrates how Φ_s and θ_{rs} are insensitive over the entire evaluated spectrum. Other recurrent insensitive variables are the van Genuchten m parameter of the porous layers, the permeability of the shales, the fracture continuum porosity (Φ_f), and the fracture density.

Table 2 Maximum RMSE for individual and pairs of parameters obtained during the sensitivity analyses for the year 2008. Parameters with RMSE values less than 1,360 m³/day are considered insensitive. *Ss* sandstone, *Shl* shale, *With* weathered layer, *Frac* fractured continuum, – combination not evaluated

Parameter	Lithology	Range	Single RMSE (m ³ /day)						Porosity (-)						van Genuchten-Mualem parameters																																	
			Low		High		Max RMSE (m ³ /day)	Ss	Shl	With	Frac	Ss	With	Frac	Ss	With	Frac	Ss	With	Frac	Ss	With	Frac																									
No. of fractures per block		30				1,229																																										
		20				1,058																																										
Fracture zone height (m)		5				684																																										
		40				867																																										
		30				2,814																																										
<i>k</i> (m ²)	<i>Ss</i>	1 × 10 ⁻¹⁵				1,996																																										
	<i>Shl</i>	1 × 10 ⁻¹⁸				63																																										
	<i>With</i>	5 × 10 ⁻¹⁴				1,135																																										
Porosity (-)	<i>Frac</i>	1 × 10 ⁻¹²				3,262																																										
	<i>Ss</i>	0.08				864																																										
	<i>With</i>	0.1				936																																										
	<i>Frac</i>	0.5				110																																										
	<i>Ss</i>	0.2				161																																										
θ_t (-)	<i>With</i>	0.05				676																																										
	<i>Frac</i>	0.05				497																																										
	<i>Ss</i>	0.05				838																																										
α (m ⁻¹)	<i>With</i>	0.07				3,334																																										
	<i>Frac</i>	0.07				2,085																																										
	<i>Ss</i>	0.3				627																																										
<i>m</i> (-)	<i>With</i>	0.5				399																																										
	<i>Frac</i>	0.5				1,189																																										
		0.5				1,189																																										

^aSensitive pairs of parameters with linear relationship
^bSensitive pairs of parameters with nonlinear dependency

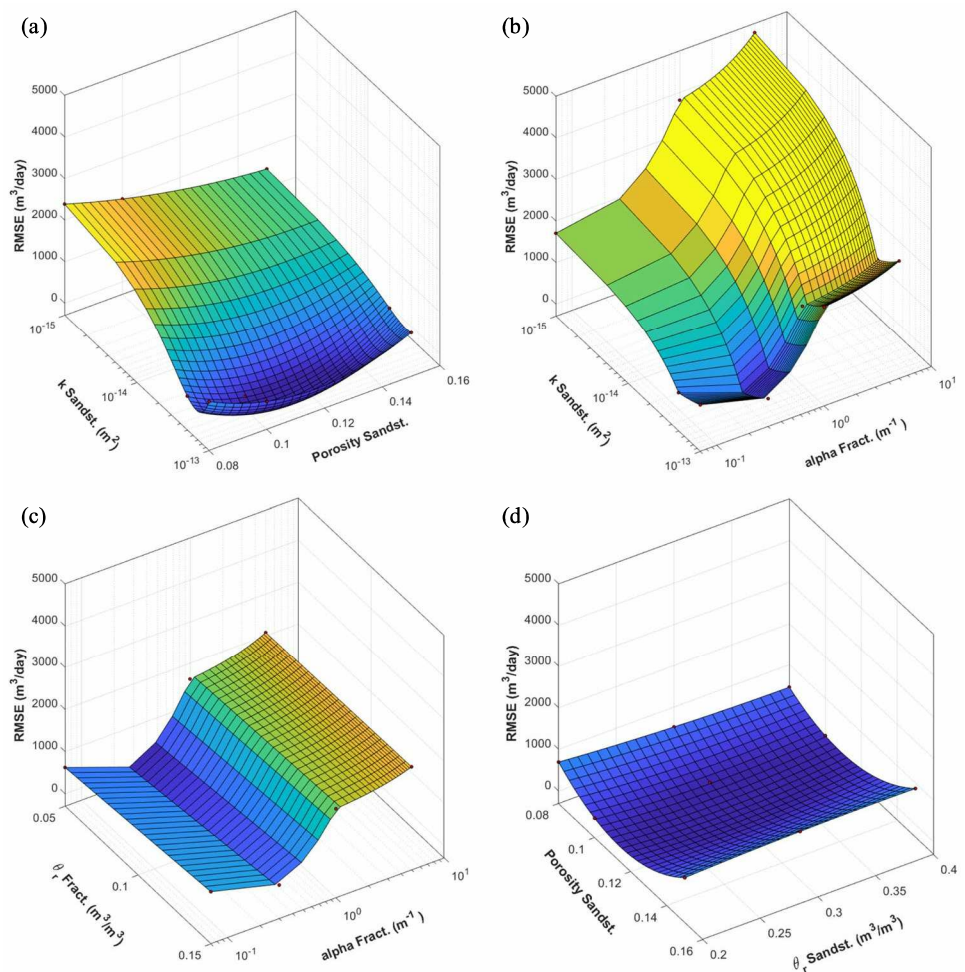
Fig. 9 Variations of the calibrated discharge signal obtained during the sensitivity analysis. The most sensitive parameters include: **a** height of the fractured zone; **b** permeability of the sandstone layers; **c** permeability of the fractured continuum; and **d** the α parameter of the van Genuchten-Mualem function for the fractured continuum



The behavior of the latter is surprising as higher densities generate larger exchange area between the two continua. The low permeability of the matrix seems to be a highly restrictive parameter in this model, maintaining the global discharge of the study area. This same trend would be partially

responsible for the low sensitivity of the fracture continuum porosity. The reduction of Φ_f leads to higher water saturation in the continuum, increasing its potential to the matrix. However, matrix tightness causes minimal variations in the amount of exchangeable water for any permeability assigned

Fig. 10 Types of parameter codependences observed during the sensitivity analysis. **a–b** Shows nonlinear dependency between two sensitive parameters, **c** shows linear dependency with just one sensitive parameter, and **d** shows both parameters being insensitive



to the sandstone layers (see Table 2). On the other hand, the increase in water saturation is not sufficient to increase the water flow and discharge within the fractured continuum. The small saturation changes are a consequence of the storage capacity and low transmissivity of the pristine rock layers above the fractured zone. As a result, the van Genuchten-Mualem parameters employed for the fractured continuum derives minimal variations of the relative permeability values. Fracture porosity would, however, play a more significant role in a reactive model in which the solid fraction interacts chemically with the percolating water.

Discussion

The good agreement between the measured and simulated discharge of the Ibbenbüren Westfield suggests that the dual-continuum approach is appropriate to characterize water movement through the heterogeneous and disrupted overburden of underground mines. The constructed model reproduces the bimodal behavior of the adit discharge taking

into account the rapid flow of a fractured continuum, the storage capacity of a matrix continuum and the water transfer between both media. It was not possible to model a comparable signal trend or magnitude by assigning similar hydraulic properties to both continua under the same water balance or overburden arrangement. The dashed lines in Fig. 9b,c show how the model averages the discharge of the adit when the permeabilities of both media are close to each other (i.e., the closest scenario to an EPM model). Neither the winter discharge peaks (discharge is underestimated) nor the recession during the summer months (discharge is overestimated) are correctly simulated, resulting in scenarios with the largest discrepancies compared to the measured data. This behavior could be one of the reasons why the average discharge of the adit was used to calibrate the most recent EPM model of the Westfield (Coldewey et al. 2018). In contrast, the simulated signal where the permeability of the fractured medium is significantly higher than the porous one (i.e., solid lines of the Fig. 9b,c) would support the convenience of the DC approach over an EPM. The importance of the fractured medium for the hydrology of the Westfield had, in fact, been previously

identified in mining reports. For instance, Lotze et al. (1962) and Bässler (1970) observed a direct correlation between seasonal precipitation and the amount of discharged water for works deeper than 200 m. Both authors also described a sharp drop in the water table for the whole field when mining was active. The development of a continuous cone of depression suggests a direct connection between the surface and underground works considering the low permeability of the sandstones, usually below $1 \times 10^{-12} \text{ m}^2$ (Bässler 1970; Wüstefeld et al. 2017; Becker et al. 2017). More recently, Bedoya-Gonzalez et al. (2021a) studied several drill core intervals segmented by subvertical fractures just above the Dickenberg coal seam. The presence of weathering fronts at both sides of the fracture planes together with the absence of healing elements suggest a recent origin probably linked with mining activities.

Simulations showed that the permeable fractured continuum dominates the flow system in the winter months, facilitating rapid responses after precipitation events. This behavior generates for example the two strong discharge peaks in February and March 2008 (Fig. 5a). For both events, the volume and subsequent recession limb were effectively simulated by the model, producing a good match with the measured data. The greatest model mismatch occurred in the length of the first discharge peak, which could not be fitted with the calibrated parameters. Initially, this inconsistency may be related to the type of precipitation. A similar factor could cause the slight discrepancies observed in the small peaks of January 2008 and 2017. It is worth noting that only liquid precipitation was considered when applying the daily recharge to the model. In the case of strong snowfall, recharge will be conditioned to the snowmelt over the following days and weeks, generating a delay in the discharge as well as long-lasting peaks during the melting period (Buttle 1989; Flerchinger et al. 1992; Eckhardt and Ulbrich 2003). If so, the recharge adopted for February 2008 was likely underestimated. A more detailed local water balance would be necessary to quantify this effect, as it is clear that the system reacts easily to recharge events due to the fractured continuum. Other reasons for the aforementioned discrepancies may include variations in the layer geometry, layer thickness or a more heterogeneous overburden, all of which were excluded during the model calibration.

Diversely, the regional recession limb of the discharge signal is influenced by the matrix flow as shown in Fig. 6a. During summer months the saturation of the fractured medium drops, increasing the relative potential of the matrix. The difference causes the water contained within the porous material to be slowly released back to the fractures and towards the adit. The continued desaturation of the system during these months increases the capillary pressure of the matrix sucking in fresh precipitation water. As a result, the system does not readily respond to precipitation events

in summer. This phenomenon may be also affected by the presence of large pores. Be reminded that this model approximates the fractured continuum as a porous medium with enhanced hydraulic properties, similar to a gravel bed. Under low saturation conditions, large pores behave more like a barrier where air cannot be easily displaced by new percolating water (Villagra-Mendoza and Horn 2018; Aguilar-López et al. 2020). Thus, the employment of the Richards equation for both continua is a common simplification that fits the study quite well when compared to other DC models. Simulations of karst systems, for example, often adjust boundary conditions to include the nonlaminar fast component of conduits (e.g., Kordilla et al. 2012; Dal Soglio et al. 2020). This issue seems to be related to the rapid percolation process of meteoric water through wide and continuous karst elements reaching the surface. Within coal mining areas, the occurrence of an undisturbed overburden above the fracture zone reduces the flow velocity of water entering into the fractures, favoring the application of a Darcian porous-media numerical solution for the entire system. Values from 0.0028 to 0.28 corroborate the laminar flow regime when calculating the Reynolds numbers (Eq. 1) at the upper interface of the fractured continuum with the sandstone layers and using their highest hydraulic conductivities (i.e., fully saturated conditions). Complementarily, the development of shorter, narrower and rougher walled fractures allows the fractured continuum to more closely resemble a porous medium, as it is affected by matrix potential and capillary forces (Liu and Bodvarsson 2001; Finsterle et al. 2003). This is added to the fact that change in fracture density along the vertical direction would lead to only part of the elements becoming active to water flow, increasing tortuosity and offsetting the potential fast component (Liu et al. 1998, 2003).

The sensitivity analysis proved major variation of the discharge curve when varying the permeability and van Genuchten-Mualem parameters of both continua; however, the model ambiguity was remarkably reduced by having a strong a priori knowledge of the parameters for the matrix continuum. The hydraulic properties of the sandstones were obtained from local investigations conducted at the Ibbenbüren Westfield. The mining framework was an advantage for the model setup since mining companies typically hold considerable amounts of geological information collected during the exploration and exploitation stages. There are other sensitive parameters though, with scarce reported values or minimal information about their measurement. One of them is the α parameter of the van Genuchten-Mualem function for the fractured continuum. Although many studies did use it to simulate unsaturated flow in DC and discrete models, only a few have explained its meaning for fracture networks and respected uncertainty for nonporous materials (e.g., Vogel et al. 2000; Liu et al. 2003; Colombo et al. 2013; Koohbor et al. 2020). In this study, all the parameters of the

van Genuchten-Mualem function were initially assigned to correspond to a permeable medium with large pore diameters; however, the α value had to be adjusted to a value similar of the sandstone layers to bring the system and adit discharge to a reasonable state. The adjustment was done after constraining many of the matrix parameters with real data. It would be useful to determine whether this calibrated α value has a physical meaning, i.e. whether or not it could be adapted for other model applications, or it is just a fitting factor. Fractured zone heights represent another sensitive feature that must be carefully set. The parameter value varies from site to site, depending on technical and geological factors such as mining depth, lithology, layer thickness and rock deformation (Meng et al. 2016). A more accurate characterization of each postmining overburden would help to improve the model outcomes. Lastly, even though fracture density was highlighted as an insensitive variable, its influence should not be neglected, especially when working with more permeable rock sequences or contaminant transport. Here, the number of fractures and their aperture were calculated using the cubic law and calibrated permeability. For example, if a grid cell of 1 m^3 contains a single set of fractures with permeability of $1 \times 10^{-10} \text{ m}^2$, the fractured continuum can be either depicted with 10 elements of $1.1 \times 10^{-5} \text{ m}$ aperture or 20 elements of $7.7 \times 10^{-6} \text{ m}$ aperture. The difference, then, lies in the contact surface between the two continua. For the second case the surface area is doubled compared to the first. This generates a significant increase in the volume of rock exposed to water and air due to fractures, which would greatly influence the generation and transport of contaminants. The inclusion of the latter would also help to evaluate the dispersive capability of the model, complementing what was observed in the infiltration pulses in Fig. 6b. The concept of hydrodynamic dispersion treated as a Fickian diffusion process is diminished in TOUGH2. However, a similar and more realistic process could be obtained by considering molecular diffusion together with flux dispersion due to mesh heterogeneities. The latter was apparently achieved in this model after considering various hydraulic and physical properties for each continuum.

Conclusions

The application of a dual-continuum model successfully reproduces the transient discharge of the Dickenberg adit in the Ibbenbüren Westfield. The good agreement between the calculated and measured signals for the years 2008 and 2017 was possible by coupling a high permeability fractured continuum with a low-conductivity matrix continuum. The unified water flow through the unsaturated overburden was simulated using two Richards equations, linked together with a scaled exchange term. Results show the fractured continuum

as the main factor responsible for strong and short discharge events during the months of heaviest precipitation, while flow within the matrix continuum greatly influences the smooth recession limb of the dry period. The direction and quantity of exchanged water between them follow pressure differences according to the dominant flow element in each season (i.e., mainly from the fracture to the matrix during winter months). The largest discrepancies in the results were associated with the regional recharge model used as input to the simulations. The lack of a more precise water balance that additionally includes, for example, the type of precipitation, altered the shape of some discharge peaks in winter due to the rapid reaction of the fractured medium.

Results of the sensitivity analysis for the Ibbenbüren Westfield showed the permeability and van Genuchten-Mualem α parameter as two of the most sensitive variables. However, a solid a priori knowledge of the study zone helped to restrict the ranges of porous media values, reducing the ambiguity of the model. This allowed fitting the fracture continuum α parameter during the calibration process, for which sparse data were available. The same served to fix the fractured zone height and fracture density variables. The construction and application of a similar adjustment process for others DC models (i.e., different coal mines) would be required to know whether the sensitive variables fitted here remain valid or change following variations in hydraulic parameters, layer heterogeneity or external recharge factors. In this sense, the existence of extensive databases in many coal mining areas would allow for relatively easy construction, calibration and confirmation processes. However, the acquisition of more site-specific data and the inclusion of the transport component would still be essential to reduce the uncertainty of the fractured continuum parameters. The transport component would in fact help to extend the analysis of the dispersion phenomenon obtained from the heterogeneity of the two continua when assessing the production and migration of contaminants. In contrast, the simulations of the study area showed little sensitivity to changing the porosity of the matrix continuum, as well as the m and n van Genuchten-Mualem parameters for both continua. Therefore, these variables can be fixed by reasonable estimates.

Supplementary Information The online version contains supplementary material available at <https://doi.org/10.1007/s10040-022-02507-3>.

Acknowledgements The authors would like to thank Professor Dr. Sylke Hilberg and Moritz Liebl at the Department of Geography and Geology, University of Salzburg, for their assistance and advice with the data management. We thank everybody from RAG Anthrazit Ibbenbüren for facilitating the discharge measurements and providing important insights into mine details. The Landesamt für Natur, Umwelt und Verbraucherschutz Nordrhein-Westfalen (LANUV) is thanked for supplying the precipitation data of the study area. We also thank the academic and technical editors as well as two anonymous reviewers for their comments and suggestions to improve the manuscript.

Funding Open access funding provided by Paris Lodron University of Salzburg. This work was financially supported by the Forum Bergbau und Wasser—FBW.

Declarations

Conflict of interest The authors declare no conflict of interest

Open Access This article is licensed under a Creative Commons Attribution 4.0 International License, which permits use, sharing, adaptation, distribution and reproduction in any medium or format, as long as you give appropriate credit to the original author(s) and the source, provide a link to the Creative Commons licence, and indicate if changes were made. The images or other third party material in this article are included in the article's Creative Commons licence, unless indicated otherwise in a credit line to the material. If material is not included in the article's Creative Commons licence and your intended use is not permitted by statutory regulation or exceeds the permitted use, you will need to obtain permission directly from the copyright holder. To view a copy of this licence, visit <http://creativecommons.org/licenses/by/4.0/>.

References

- Acero Triana JS, Chu ML, Guzman JA, Moriasi DN, Steiner JL (2019) Beyond model metrics: the perils of calibrating hydrologic models. *J Hydrol* 578:124032. <https://doi.org/10.1016/j.jhydrol.2019.124032>
- Adams R, Younger PL (2001) A strategy for modeling ground water rebound in abandoned deep mine systems. *Ground Water* 39:249–261. <https://doi.org/10.1111/j.1745-6584.2001.tb02306.x>
- Aguilar-López JP, Bogaard T, Gerke HH (2020) Dual-permeability model improvements for representation of preferential flow in fractured clays. *Water Resour Res* 56. <https://doi.org/10.1029/2020WR027304>
- Arnold JG, Moriasi DN, Gassman PW, Abbaspour KC, White MJ, Srinivasan R, Santhi C, Harmel RD, Van Griensven A, Van Liew MW, Kannan N, Jha MK (2012) SWAT: model use, calibration, and validation. *Trans ASABE* 55:1491–1508. <https://doi.org/10.13031/2013.42256>
- Azom PN, Javadpour F (2012) Dual-continuum modeling of shale and tight gas reservoirs. Paper presented at the SPE Annual Technical Conference and Exhibition, San Antonio, Texas, USA. *Soc Pet Eng*. <https://doi.org/10.2118/159584-MS>
- Bai Q, Tu S (2019) A general review on longwall mining-induced fractures in near-face regions. *Geofluids* 2019:22. <https://doi.org/10.1155/2019/3089292>
- Banks D (2001) A variable-volume, head-dependent mine water filling model. *Ground Water* 39:362–365. <https://doi.org/10.1111/j.1745-6584.2001.tb02319.x>
- Barenblatt GI, Zheltov IP, Kochina IN (1960) Basic concepts in the theory of seepage of homogeneous liquids in fissured rocks [strata]. *J Appl Math Mech* 24:1286–1303. [https://doi.org/10.1016/0021-8928\(60\)90107-6](https://doi.org/10.1016/0021-8928(60)90107-6)
- Bässler R (1970) Hydrogeologische, chemische und Isotopen: Untersuchungen der Grubenwässer im Ibbenbürener Steinkohlenrevier [Hydrogeological, chemical and isotopes: studies of mine water in the Ibbenbüren coalfield]. *Z deutsch geol Ges*. <https://doi.org/10.1127/zdgg/120/1970/209>
- Bear J (1972) Dynamics of fluids in porous media, 1st edn. Elsevier, New York, pp 125–129
- Becker I, Wüstefeld P, Koehrer B, Felder M, Hilgers C (2017) Porosity and permeability variations in a tight gas sandstone reservoir analogue, Westphalian D, Lower Saxony basin, NW Germany: influence of depositional setting and diagenesis. *J Pet Geol* 40:363–389. <https://doi.org/10.1111/jpg.12685>
- Becker I, Busch B, Koehrer B, Adelmann D, Hilgers C (2019) Reservoir quality evolution of upper Carboniferous (Westphalian) tight gas sandstones, Lower Saxony Basin, NW Germany. *J Pet Geol* 42:371–392. <https://doi.org/10.1111/jpg.12742>
- Bedoya-Gonzalez D, Hilberg S, Redhammer G, Rinder T (2021a) A petrographic investigation of the Carboniferous sequence from the Ibbenbüren Mine: tracing the origin of the coal mine drainage. *Minerals* 11:1–19. <https://doi.org/10.3390/min11050483>
- Bedoya-Gonzalez D, Kessler T, Schafmeister MT (2021b) Employment of a double continuum model to characterize groundwater flow in underground post-mining setups: case study of the Ibbenbüren Westfield. In: Stanley P, Wolkersdorfer C, Wolkersdorfer K (eds) Mine water management for future generations. Natural Resources Wales, The Coal Authority, Welsh Government, Cardiff University, Cardiff, Wales, pp 47–53
- Beyer M, Mohrlok U (2006) Parameter estimation for a double continuum transport model for fractured porous media. In: Proceedings of ModelCARE, The Hague, The Netherlands, 2005, IAHS Publ. 304, IAHS, Wallingford, UK, pp 80–86
- BGR (2021) Groundwater resources in Germany. In: Bundesanstalt für Geowissenschaften und Rohstoffe. https://www.deutsche-rohstoffagentur.de/EN/Themen/Wasser/grundwasser_deutschland_en.html. Accessed 1 December 2021
- Blodgett S, Kuipers JR (2002) Underground hard-rock mining: subsidence and hydrologic environmental impacts. Center for Science and Public Participation, Bozeman, MT
- Blowes DW, Jambor JL (1990) The pore-water geochemistry and the mineralogy of the vadose zone. *Appl Geochemistry* 5:327–346. [https://doi.org/10.1016/0883-2927\(90\)90008-S](https://doi.org/10.1016/0883-2927(90)90008-S)
- Buttle JM (1989) Soil moisture and groundwater responses to snowmelt on a drumlin sideslope. *J Hydrol* 105:335–355. [https://doi.org/10.1016/0022-1694\(89\)90112-1](https://doi.org/10.1016/0022-1694(89)90112-1)
- Chen N, Gunzburger M, Hu B, Wang X, Woodruff C (2012) Calibrating the exchange coefficient in the modified coupled continuum pipe-flow model for flows in karst aquifers. *J Hydrol* 414–415:294–301. <https://doi.org/10.1016/j.jhydrol.2011.11.001>
- Coldewey G, Hollenbeck I, Babilinski S (2018) Abschlussbetriebsplan des Steinkohlenbergwerks Ibbenbüren Anlage 16 - Auswirkungen des Grubenwasseranstiegs im Ostfeld des Bergwerkes Ibbenbüren der RAG Anthrazit Ibbenbüren GmbH [Final operating plan of the Ibbenbüren hard coal mine Annex 16: effects of the increase in mine water in the east field of the Ibbenbüren mine of RAG Anthrazit Ibbenbüren GmbH]. RAG Anthrazit Obbenbüren, Ibbenbüren, Germany
- Colombo L, Gattinoni P, Rizzo S, Scesi L (2013) Flow modelling of dual permeability systems: the case of the Vigolana Massif (Trento, Northern Italy). *WIT Trans Ecol Environ* 172:51–62. <https://doi.org/10.2495/RBM130051>
- Dal Soglio L, Danquigny C, Mazzilli N, Emblanch C, Massonnat G (2020) Modeling the matrix-conduit exchanges in both the epikarst and the transmission zone of karst systems. *Water (Switzerland)* 12:1–19. <https://doi.org/10.3390/w12113219>
- David K, Timms WA, Barbour SL, Mitra R (2017) Tracking changes in the specific storage of overburden rock during longwall coal mining. *J Hydrol* 553:304–320. <https://doi.org/10.1016/j.jhydrol.2017.07.057>
- Devak M, Dhanya CT (2017) Sensitivity analysis of hydrological models: review and way forward. *J Water Clim Chang* 8:557–575. <https://doi.org/10.2166/wcc.2017.149>
- Drouin G, Fahs M, Droz B, Younes A, Imfeld G, Payraudeau S (2021) Pollutant dissipation at the sediment–water interface: a robust discrete continuum numerical model and recirculating laboratory experiments. *Water Resour Res* 57:1–16. <https://doi.org/10.1029/2020WR028932>

- Drozdowski G (1985) Tiefentektonik der Ibbenbürener Karbon-Scholle [Depth tectonics of the Ibbenbüren Carboniferous coal floe]. In: Beiträge zur Tiefentektonik westdeutscher Steinkohlenlagerstätten [Contributions to the deep tectonics of West German coal deposits, 1st edn.] Geologisches Landesamt Nordrhein-Westfalen, Krefeld, Germany, pp 189–216
- Drozdowski G, Dölling M (2018) Elemente der Osning-Störungszone (NW-Deutschland): Leitstrukturen einer Blattverschiebungszone [Elements of the Osning Fault Zone (NW Germany): guiding structures of a foliation displacement zone]. Geologischer Dienst Nordrhein-Westfalen, Krefeld, Germany
- Eckhardt K, Ulbrich U (2003) Potential impacts of climate change on groundwater recharge and streamflow in a central European low mountain range. *J Hydrol* 284:244–252. <https://doi.org/10.1016/j.jhydrol.2003.08.005>
- Fielding M, Nott DJ, Liang SY (2011) Efficient MCMC schemes for computationally expensive posterior distributions. *Technometrics* 53:16–28. <https://doi.org/10.1198/TECH.2010.09195>
- Finsterle S, Ahlers CF, Trautz RC, Cook PJ (2003) Inverse and predictive modeling of seepage into underground openings. *J Contam Hydrol* 62–63:89–109. [https://doi.org/10.1016/S0169-7722\(02\)00174-2](https://doi.org/10.1016/S0169-7722(02)00174-2)
- Flerchinger GN, Cooley KR, Ralston DR (1992) Groundwater response to snowmelt in a mountainous watershed. *J Hydrol* 133:293–311. [https://doi.org/10.1016/0022-1694\(92\)90260-3](https://doi.org/10.1016/0022-1694(92)90260-3)
- Freeze R, Cherry JA (1979) Physical properties and principles. In: Brenn C, McNeily K (eds) *Groundwater*, 1st edn., vol 07632. Prentice-Hall, Englewood Cliffs, NJ, pp 14–79
- Gerke HH, van Genuchten MT (1993) Evaluation of a first-order water transfer term for variably saturated dual-porosity flow models. *Water Resour Res* 29:1225–1238. <https://doi.org/10.1029/92WR02467>
- Gerke HH, Dusek J, Vogel T, Khne JM (2007) Two-dimensional dual-permeability analyses of a bromide tracer experiment on a tile-drained field. *Vadose Zone J* 6:651–667. <https://doi.org/10.2136/vzj2007.0033>
- Ghasemzadeh R, Hellweger F, Butscher C, Padilla I, Vesper D, Field M, Alshawabkeh A (2012) Review: Groundwater flow and transport modeling of karst aquifers, with particular reference to the North Coast Limestone aquifer system of Puerto Rico. *Hydrogeol J* 20:1441–1461. <https://doi.org/10.1007/s10040-012-0897-4>
- Guo W, Zhao G, Lou G, Wang S (2019) Height of fractured zone inside overlying strata under high-intensity mining in China. *Int J Min Sci Technol* 29:45–49. <https://doi.org/10.1016/j.ijmst.2018.11.012>
- Guo L, Fahs M, Hoteit H, Gao R, Shao Q (2021) Uncertainty analysis of seepage-induced consolidation in a fractured porous medium. *Comput Model Eng Sci* 129:279–297. <https://doi.org/10.32604/cmescs.2021.016619>
- Gupta HV, Kling H, Yilmaz KK, Martinez GF (2009) Decomposition of the mean squared error and NSE performance criteria: implications for improving hydrological modelling. *J Hydrol* 377:80–91. <https://doi.org/10.1016/j.jhydrol.2009.08.003>
- Hao Y, Fu P, Carrigan CR (2013) Application of a dual-continuum model for simulation of fluid flow and heat transfer in fractured geothermal reservoirs. In: *Proceedings, 38th Workshop on Geothermal Reservoir Engineering*, vol SGP-TR-198. Stanford University, Stanford, CA, pp 462–469
- Herman JD, Kollat JB, Reed PM, Wagener T (2013) Technical Note: Method of Morris effectively reduces the computational demands of global sensitivity analysis for distributed watershed models. *Hydrol Earth Syst Sci* 17:2893–2903. <https://doi.org/10.5194/hess-17-2893-2013>
- Herrmann F, Chen S, Kunkel R, Wendland F (2014) Auswirkungen von Klimaänderungen auf das nachhaltig bewirtschaftbare Grundwasserangebot und den Bodenwasserhaushalt in Nordrhein-Westfalen [Effects of climate change on the sustainably manageable groundwater supply and the soil water balance in North Rhine-Westphalia]. Forschungszentrum Jülich, Jülich, Germany
- Kasiri N, Bashiri A (2011) Status of dual-continuum models for naturally fractured reservoir simulation. *Pet Sci Technol* 29:1236–1248. <https://doi.org/10.1080/10916460903515557>
- Kelleher JT, Van Roosendaal DJ, Mehnert BB, Brucher DF, Bauer RA (1991) Overburden deformation and hydrologic changes due to longwall coal mine subsidence on the Illinois Basin. In: *Proc 4th International Conference on Land Subsidence*. International Association of Hydrological Sciences, Houston, TX, pp 195–204
- Kim JM, Parizek RR, Elsworth D (1997) Evaluation of fully-coupled strata deformation and groundwater flow in response to longwall mining. *Int J Rock Mech Min Sci* 34:1187–1199. [https://doi.org/10.1016/S1365-1609\(97\)80070-6](https://doi.org/10.1016/S1365-1609(97)80070-6)
- Klinger C, Rüterkamp P, Eckart M (2019) Abschlussbetriebsplan des Steinkohlenbergwerks Ibbenbüren Anlage 17: Prognose zur optimierten Wasserannahme nach Stilllegung des Steinkohlenbergwerkes Ibbenbüren (Ostfeld) [Final operating plan of the Ibbenbüren Hard Coal Mine Annex 17: forecast for optimized water intake after closure of the Ibbenbüren hard coal mine (Ostfeld)]. DMT, Essen, Germany
- Koohbor B, Fahs M, Ataie-Ashtiani B, Belfort B, Simmons CT, Younes A (2019) Uncertainty analysis for seawater intrusion in fractured coastal aquifers: effects of fracture location, aperture, density and hydrodynamic parameters. *J Hydrol* 571:159–177. <https://doi.org/10.1016/j.jhydrol.2019.01.052>
- Koohbor B, Fahs M, Hoteit H, Doummar J, Younes A, Belfort B (2020) An advanced discrete fracture model for variably saturated flow in fractured porous media. *Adv Water Resour* 140:0–49. <https://doi.org/10.1016/j.advwatres.2020.103602>
- Kordilla J, Sauter M, Reimann T, Geyer T (2012) Simulation of saturated and unsaturated flow in karst systems at catchment scale using a double continuum approach. *Hydrol Earth Syst Sci* 16:3909–3923. <https://doi.org/10.5194/hess-16-3909-2012>
- Kovács A, Sauter M (2007) Modelling karst hydrodynamics. In: Goldscheider N, Drew D (eds) *Methods in karst hydrogeology*. Taylor and Francis, London, pp 201–222
- Krause P, Boyle DP, Bäse F (2005) Comparison of different efficiency criteria for hydrological model assessment. *Adv Geosci* 5:89–97. <https://doi.org/10.5194/adgeo-5-89-2005>
- Liu HH, Bodvarsson GS (2001) Constitutive relations for unsaturated flow in a fracture network. *J Hydrol* 252:116–125. [https://doi.org/10.1016/S0022-1694\(01\)00449-8](https://doi.org/10.1016/S0022-1694(01)00449-8)
- Liu HH, Doughty C, Bodvarsson GS (1998) An active fracture model for unsaturated flow and transport in fractured rocks. *Water Resour Res* 34:2633–2646. <https://doi.org/10.1029/98WR02040>
- Liu H-H, Zhang G, Bodvarsson GS (2003) The active fracture model: its relation to fractal flow patterns and an evaluation using field observations. *Vadose Zone J* 2:259. <https://doi.org/10.2136/vzj2003.0259>
- Liu Y, Meng LQ, Ping LW, Li T, Hui HJ (2019) Height of water-conducting fractured zone in coal mining in the soil-rock composite structure overburdens. *Environ Earth Sci* 78:242–255. <https://doi.org/10.1007/s12665-019-8239-7>
- Lotze F, Semmler W, Kötter K, Mausolf F (1962) *Hydrogeologie des Westteils der Ibbenbürener Karbonscholle (Hydrogeology of the western part of the Ibbenbüren Carboniferous floe, 1st edn.)* Springer Fachmedien, Wiesbaden, Germany
- Meng Z, Shi X, Li G (2016) Deformation, failure and permeability of coal-bearing strata during longwall mining. *Eng Geol* 208:69–80. <https://doi.org/10.1016/j.enggeo.2016.04.029>
- Moriasi DN, Gitau MW, Pai N, Daggupati P (2015) Hydrologic and water quality models: performance measures and evaluation criteria. *Trans ASABE* 58:1763–1785. <https://doi.org/10.13031/trans.58.10715>
- Mualem Y (1976) A new model for predicting the hydraulic conductivity of unsaturated porous media. *Water Resour Res* 12:513–522. <https://doi.org/10.1029/WR012i003p00513>

- Ndiritu J (2009) A comparison of automatic and manual calibration using the Pitman model. *Phys Chem Earth* 34:729–740. <https://doi.org/10.1016/j.pce.2009.06.002>
- Newman C, Agioutantis Z, Boede Jimenez Leon G (2017) Assessment of potential impacts to surface and subsurface water bodies due to longwall mining. *Int J Min Sci Technol* 27:57–64. <https://doi.org/10.1016/j.ijmst.2016.11.016>
- Palchik V (2003) Formation of fractured zones in overburden due to longwall mining. *Environ Geol* 44:28–38. <https://doi.org/10.1007/s00254-002-0732-7>
- Parajuli K, Sadeghi M, Jones S (2017) A binary mixing model for characterizing stony-soil water retention. *Agric For Meteorol* 244–245:1–8. <https://doi.org/10.1016/j.agrformet.2017.05.013>
- Pruess K (1983) GMINC: a mesh generator for flow simulations in fractured reservoirs. Lawrence Berkeley National Laboratory, University of California, Berkeley, CA. <https://doi.org/10.2172/6065621>
- Pruess K, Narasimhan TN (1985) A practical method for modeling fluid and heat flow in fractured porous media. *Soc Pet Eng J* 25:14–26. <https://doi.org/10.2118/10509-PA>
- Pruess K, Oldenburg C, Moridis G (2012) TOUGH2 user's guide, version 2. Earth Sciences Division, Lawrence Berkeley National Laboratory, Berkeley, CA
- Pushpalatha R, Perrin C, Le Moine N, Andréassian V (2012) A review of efficiency criteria suitable for evaluating low-flow simulations. *J Hydrol* 420–421:171–182. <https://doi.org/10.1016/j.jhydrol.2011.11.055>
- Qiao W, Li W, Zhang S, Niu Y (2019) Effects of coal mining on the evolution of groundwater hydrogeochemistry. *Hydrogeol J* 27:2245–2262. <https://doi.org/10.1007/s10040-019-01969-2>
- Qu Q, Xu J, Wu R, Qin W, Hu G (2015) Three-zone characterisation of coupled strata and gas behaviour in multi-seam mining. *Int J Rock Mech Min Sci* 78:91–98. <https://doi.org/10.1016/j.ijrmm.2015.04.018>
- Rakovec O, Hill MC, Clark MP, Weerts AH, Teuling AJ, Uijlenhoet R (2014) Distributed evaluation of local sensitivity analysis (DELSA), with application to hydrologic models. *Water Resour Res* 50:409–426. <https://doi.org/10.1002/2013WR014063>
- Rapantova N, Grmela A, Vojtek D, Halir J, Michalek B (2007) Ground water flow modelling applications in mining hydrogeology. *Mine Water Environ* 26:264–270. <https://doi.org/10.1007/s10230-007-0017-1>
- Ray C, Vogel T, Dusek J (2004) Modeling depth-variant and domain-specific sorption and biodegradation in dual-permeability media. *J Contam Hydrol* 70:63–87. <https://doi.org/10.1016/j.jconhyd.2003.08.009>
- Richards LA (1931) Capillary conduction of liquids through porous mediums. *Physics* 1:318–333. <https://doi.org/10.1063/1.1745010>
- Rinder T, Dietzel M, Stammeyer JA, Leis A, Bedoya-González D, Hilberg S (2020) Geochemistry of coal mine drainage, groundwater, and brines from the Ibbenbüren mine, Germany: a coupled elemental-isotopic approach. *Appl Geochemistry* 121:104693. <https://doi.org/10.1016/j.apgeochem.2020.104693>
- Rouleau A, Gale JE (1987) Stochastic discrete fracture simulation of groundwater flow into an underground excavation in granite. *Int J Rock Mech Min Sci* 24:99–112. [https://doi.org/10.1016/0148-9062\(87\)91929-2](https://doi.org/10.1016/0148-9062(87)91929-2)
- Rudakov D V, Coldewey WG, Goerke-Mallet P (2014) Modeling the inflow and discharge from underground structures within the abandoned hardcoal mining area of West Field (Ibbenbüren). In: Sui W, Sun Y, Wang C (ed) An interdisciplinary response to mine water challenges. 12th International Mine Water Association Congress (IMWA 2014). Xuzhou, China, 18–22 August 2014; pp 699–705
- Sauter M (1992) Quantification and forecasting of regional groundwater flow and transport in a karst aquifer (Gallusquelle, Malm, SW. Germany). Geowissenschaftliche Fakultät, Universität Tübingen, Tübingen, Germany
- Song L, Li J, Garg A, Mei G (2018) Experimental study on water exchange between crack and clay matrix. *Geomech Eng* 14:283–291. <https://doi.org/10.12989/gae.2018.14.3.283>
- Tokunaga TK, Wan J (1997) Water film flow along fracture surfaces of porous rock. *Water Resour Res* 33:1287–1295. <https://doi.org/10.1029/97WR00473>
- van Genuchten MT (1980) A closed-form equation for predicting the hydraulic conductivity of unsaturated soils. *Soil Sci Soc Am J* 44:892–898. <https://doi.org/10.2136/sssaj1980.03615995004400050002x>
- Villagra-Mendoza K, Horn R (2018) Effect of biochar on the unsaturated hydraulic conductivity of two amended soils. *Int Agrophysics* 32:373–378. <https://doi.org/10.1515/intag-2017-0025>
- Vincenzi V, Piccinini L, Gargini A, Sapigni M (2010) Parametric and numerical modelling tools to forecast hydrogeological impacts of a tunnel. *Acque Sotter J Groundw* 1:135–154. <https://doi.org/10.7343/as-2022-558>
- Vogel T, Gerke HH, Zhang R, van Genuchten MT (2000) Modeling flow and transport in a two-dimensional dual-permeability system with spatially variable hydraulic properties. *J Hydrol* 238:78–89. [https://doi.org/10.1016/S0022-1694\(00\)00327-9](https://doi.org/10.1016/S0022-1694(00)00327-9)
- Wu Y-S, Di Y, Kang Z, Fakcharoenphol P (2011) A multiple-continuum model for simulating single-phase and multiphase flow in naturally fractured vuggy reservoirs. *J Pet Sci Eng* 78:13–22. <https://doi.org/10.1016/j.petrol.2011.05.004>
- Wüstefeld P, Hilse U, Koehrer B, Adelmann D, Hilgers C (2017) Critical evaluation of an Upper Carboniferous tight gas sandstone reservoir analog: diagenesis and petrophysical aspects. *Mar Pet Geol* 86:689–710. <https://doi.org/10.1016/j.MARPETGEO.2017.05.034>
- Xu T, White SP, Pruess K, Brimhall GH (2000) Modeling of pyrite oxidation in saturated and unsaturated subsurface flow systems. *Transp Porous Media* 39:25–56. <https://doi.org/10.1023/A:1006518725360>
- Younes A, Fahs M, Ataie-Ashtiani B, Simmons CT (2020) Effect of distance-dependent dispersivity on density-driven flow in porous media. *J Hydrol* 589. <https://doi.org/10.1016/j.jhydrol.2020.125204>
- Zha H, Liu W, Liu Q (2020) Physical simulation of the water-conducting fracture zone of weak roofs in shallow seam mining based on a self-designed hydromechanical coupling experiment system. *Geofluids*. <https://doi.org/10.1155/2020/2586349>
- Zhang D, Sui W, Liu J (2018a) Overburden failure associated with mining coal seams in close proximity in ascending and descending sequences under a large water body. *Mine Water Environ* 37:322–335. <https://doi.org/10.1007/s10230-017-0502-0>
- Zhang Y, Cao S, Wan T, Wang J (2018b) Field measurement and mechanical analysis of height of the water flowing fracture zone in short-wall block backfill mining beneath the aquifer: a case study in China. *Geofluids*. <https://doi.org/10.1155/2018/7873682>

Publisher's note Springer Nature remains neutral with regard to jurisdictional claims in published maps and institutional affiliations.

Chapter 4: A multiple interactive continua model (MINC) to simulate reactive mass transport in a post-mining coal zone: A case study of the Ibbenbüren Westfield

Bedoya-Gonzalez, D.^{1,2}, Kessler, T.², Rinder, T.¹, Szabó-Krausz, Z.³, & Schafmeister, M.T.²

¹ Department of Environment & Biodiversity, University of Salzburg, Hellbrunner Str. 34, 5020 Salzburg, Austria.

² Institute for Geography and Geology, University of Greifswald, Friedrich-Ludwig-Jahn Str. 17a, 17487 Greifswald, Germany.

³ Lithosphere Fluid Research Lab and Centre of Environmental Sciences, Eötvös Loránd University, Pázmány 9 P.s. 1/C, 1117, Budapest, Hungary.

Submitted in: Mine Water and the Environment Journal (December 20th, 2022)

Mine Water and the Environment

A multiple interactive continua model (MINC) to simulate reactive mass transport in a post-mining coal zone: A case study of the Ibbenbüren Westfield.

--Manuscript Draft--

Manuscript Number:	MWEN-D-22-00207	
Full Title:	A multiple interactive continua model (MINC) to simulate reactive mass transport in a post-mining coal zone: A case study of the Ibbenbüren Westfield.	
Article Type:	Technical Article	
Corresponding Author:	Diego Bedoya-Gonzalez University of Greifswald: Universitat Greifswald Greifswald, Mecklenburg-Vorpommern GERMANY	
Corresponding Author Secondary Information:		
Corresponding Author's Institution:	University of Greifswald: Universitat Greifswald	
Corresponding Author's Secondary Institution:		
First Author:	Diego Bedoya-Gonzalez	
First Author Secondary Information:		
Order of Authors:	Diego Bedoya-Gonzalez	
	Timo Kessler	
	Thomas Rinder	
	Sylke Hilberg	
	Zsuzsanna Szabó-Krausz	
	Maria-Theresia Schafmeister	
Order of Authors Secondary Information:		
Funding Information:	Forum Bergbau und Wasser - FBW	M.Sc. Diego Bedoya-Gonzalez
Abstract:	<p>This paper tests the suitability of the multiple interactive continua approach (MINC) to simulate reactive mass transport in a disturbed post-mining coal zone. To the authors' knowledge, this approach has not been employed in such mining settings despite its relative success in other environmental fields. To this end, TOUGHREACT software is used to setup a MINC model of the unsaturated overburden of the Ibbenbüren Westfield. With it, we examined and evaluated water-rock interactions in both the fractured and porous continua as the main driver of elevated hydrogen, iron, sulfate and chloride concentrations in the coal mine groundwater. Long and seasonal geochemical signatures are obtained by formulating and applying a 5-stage modelling process that depicts the mining history of the area. Simulation results show a good agreement with respect to concentrations and discharge trends measured in the mine drainage. Oxygen and meteoric water flow through the fractured continuum leads to a high and steady release of hydrogen, iron and sulfate ions derived from pyrite oxidation in the matrix continua closest to the fractures. Likewise, high chloride concentrations would result from the mixing and gradual release of relatively immobile solutes in the matrix as they interact with percolating water in the fracture. In both cases the use of a multiple continua approach becomes essential to resolve sharp gradients for advection and faster kinetic reactions, while reducing the model's dependence on block size for diffusive transport at the fracturematrix interface. The model further allows to calculate and analyse the exchange and transport of solutes in the unsaturated overburden resulted from rebound and imbibition processes, something pioneering when compared to other models in the field.</p>	
Suggested Reviewers:		

Multiple interactive continua approach (MINC) to simulate reactive mass transport in a disturbed post-mining coal zone: A case study of the Ibbenbüren Westfield.

Diego Bedoya-Gonzalez^{1,2,*}, Timo Kessler¹, Thomas Rinder², Sylke Hilberg², Zsuzsanna Szabó-Krausz³, Maria-Theresia Schafmeister¹

¹ *Institute for Geography and Geology, University of Greifswald, Friedrich-Ludwig-Jahn Str. 17a, 17487, Greifswald, Germany.*

² *Department of Environment & Biodiversity, University of Salzburg, Hellbrunner Str. 34, 5020, Salzburg, Austria*

³ *Lithosphere Fluid Research Lab and Centre of Environmental Sciences, Eötvös Loránd University, Pázmány P.s. 1/C, 1117, Budapest, Hungary.*

Abstract

This paper tests the suitability of the multiple interactive continua approach (MINC) to simulate reactive mass transport in a disturbed post-mining coal zone. To the authors' knowledge, this approach has not been employed in such mining settings despite its relative success in other environmental fields. To this end, TOUGHREACT software is used to setup a MINC model of the unsaturated overburden of the Ibbenbüren Westfield. With it, we examined and evaluated water-rock interactions in both the fractured and porous continua as the main driver of elevated hydrogen, iron, sulfate and chloride concentrations in the coal mine groundwater. Long and seasonal geochemical signatures are obtained by formulating and applying a 5-stage modelling process that depicts the mining history of the area. Simulation results show a good agreement with respect to concentrations and discharge trends measured in the mine drainage. Oxygen and meteoric water flow through the fractured continuum leads to a high and steady release of hydrogen, iron and sulfate ions derived from pyrite oxidation in the matrix continua closest to the fractures. Likewise, high chloride concentrations would result from the mixing and gradual release of relatively immobile solutes in the matrix as they interact with percolating water in the fracture. In both cases the use of a multiple continua approach becomes essential to resolve sharp gradients for advection and faster kinetic reactions, while reducing the model's dependence on block size for diffusive transport at the fracture-matrix interface. The model further allows to calculate and analyse the exchange and transport of solutes in the unsaturated overburden resulted from rebound and imbibition processes, something pioneering when compared to other models in the field.

Keywords Reactive transport, TOUGHREACT, water-rock interaction, multiple interactive continua, pyrite oxidation, groundwater rebound.

Introduction

Environmental impacts generated by poor water quality from coal mining areas are well documented around the world (Banks et al. 1997; Nieto et al. 2007; Doumas et al. 2018; Wolkersdorfer et al. 2022a). Drainage of saline water contained into rock formations increases the concentration of chloride in freshwater bodies, causing quality detriment and toxicity to their communities (Turek 2004; Elphick et al. 2011; Timpano et al. 2015; Vöröš et al. 2021). Weathering of naturally occurring sulfide ores leads to the formation of acid mine drainage, which results in an abundance of iron and sulfate ions and the mobilization of toxic metals (Cravotta and Brady 2015; Gombert et al. 2018; Acharya and Kharel 2020; Zhang et al. 2021). The eventual precipitation of hydrous ferric oxides resulted from high iron contents tend to clog riverbeds, generating negative effects on the flora and fauna (McKnight and Feder 1984; MacCausland and McTammany 2007).

The drainage of the former anthracite coal mine in the Ibbenbüren Westfield is no exception to the aforementioned contaminants. Pumped mine waters from the field are acidic and characterized by high iron, sulfate and chloride content, frequently exceeding the threshold values considered harmful for freshwater ecosystems (Bässler 1970; Rinder et al. 2020). This situation has generated public interest in the long-term liabilities associated with the disposal of the mineralized water since the closure of the mine, in 1979. Increasing attention is being devoted not

only to avoid or mitigate the negative environmental effects, but also to recover and reuse resources deriving from the drainage (Simate and Ndlovu 2014; Moodley et al. 2018; Wolkersdorfer et al. 2022b). The latter is becoming increasingly important with the European Green Deal focusing on recycling as an important factor of the future economy. Either way, whether choosing the best treatment option or deciding on the possibilities of reuse the solid or aquatic resources, requires a long-term prognosis based on the correct characterization of the elements of the hydrogeological system.

The source and evolution of the contamination at Westfield, however, has been widely debated and partially characterized. Much of the attention has focused on identifying and dissolve efflorescent salts (i.e., by-products of pyrite oxidation) that may remain in tunnels and work faces. This works is done through box models which predict ion release from dissolution calculations of solid quantities already present in empty spaces, with little concern for the water-rock interactions that lead to their formation (e.g., see (Klinger et al. 2019)). In addition, the approach is not feasible to describe long-term production and high concentrations of dissolved iron and sulfate after mine flooding such as occurs in the study area. Alternatively, Bässler (1970) attributed the high ion levels to the continuous and homogeneous interaction of meteoric water with the solutes and minerals contained in the bedrocks. In such a case, the characterization of the geochemical interactions could resemble an equivalent porous medium model, commonly applied in coal mining areas. The latter represents an oversimplification of the medium since the moderate permeability of the coal overburden limits the flow and interaction of groundwater with the matrix components. In reality, the water-rock interaction would be more complex, being closely linked to the creation of fractured zones derived from mining.

The importance of considering both fractures and rock matrix has been corroborated by Bedoya-Gonzalez et al. (2022) who used a dual continuum model (DCM) to fit the transient discharge behaviour of the Ibbenbüren Westfield. Their results show the fractured continuum as the main responsible of the strong and short discharge events of the mine drainage during the months of heaviest precipitation, while flow within the matrix continuum greatly influences the smooth recession limb of the dry period. Regarding the geochemical component, development of conductive fracture networks results in new and extensive exposure of rock components to atmospheric conditions for weathering. This process has been reported to be much more pronounced in shallow aquifers above mined panels, where groundwater drawdown enhance chemical reactions with atmospheric oxygen and percolating meteoric water (Booth 2002; Younger and Wolkersdorfer 2004). Chemical reactions typically include dissolution of carbonate minerals, reductive dissolution of metal hydroxides and oxidation of sulfur minerals, which mobilize cations, anions and metals from rock strata (Jankowski and Spies 2007). Moreover, fractures become the main flow pathways, with advection being the main transport mechanism, whereas transport within the surrounding rock matrix is much slower, mainly driven by diffusion. The latter may lead to movement and mixing of pre-existing waters along the rock sequence. Whether this mixing causes a deterioration or an improvement in quality would depend on the chemistry of water from the recharging source (Booth and Bertsch 1999; Younger and Wolkersdorfer 2004).

The objective of this study is to evaluate the suitability of the multiple interactive continua (MINC) approach for the characterization of multispecies mass transport and a range of geochemical reactions in geomechanically disrupted coal mining areas. Typically, intensive coal mining generates a high density of fractures in the overburden that would allow them to be grouped within a continuum, assigning it common properties distinct from the surrounding porous units. Grouping all fractures as a separate continuum represents a significant advantage of the MINC approach over equivalent porous media models, which are generally unable to capture the duality characteristic behaviour of fractured systems. Moreover, The MINC approach requires less amount of data compared to a discrete fracture model, making it more practical. In order to test the approach, this study employs TOUGHREACT software to set up a 2D cross-sectional MINC model of the partially fractured and unsaturated overburden of the Ibbenbüren Westfield. The construction process extends the already calibrated DC model of the flow component to a model with five strings of nested continua: one for the fractures and four for the rock matrix. The further subdivision of the matrix enables to describe chemical and multispecies mass transport gradients within the matrix blocks during their long transient periods of interporosity flow (weeks and months). For the model assessment, this study simulates and compares the long-term and short-term contaminant formation, deposition and transport in the study area since the start of mining operations. For this purpose,

dissolution, precipitation and dilution processes related to iron, sulfate and chloride-bearing minerals and solutions are modelled using a 5-step process that emulates the mining history of the area.

Methods

Geological and hydrogeological setting

The study area is part of the Ibbenbüren mining district, located in north western Germany (Fig. 1). It is one of the two collieries that mined anthracitic coal from a Carboniferous crustal block. The latter was brought up to the surface by an inversion event of the Osning fault system during the Late Cretaceous (Drozdowski and Dölling 2018; Rinder et al. 2020). As a result, marginal faults with offset of up to 2000 m separated the Carboniferous sequence from the surrounding Triassic and Jurassic foreland, currently under the Quaternary (Fig. 2). Compression forces also created the antithetic faults that divided the block into two Horst structures (Dickenberg and Schafberg) separated by a NNE-SSW striking graben known as the Bockradener Graben (Fig. 2). For mining purposes, Schafberg and Dickenberg hills were named “Eastfield” and “Westfield”, respectively.

Westfield's lithology is well known based on geological documentation of mining activities. The rock sequence, deposited during the Upper Westphalian C and Lower Westphalian D phases, reaches a thickness of more than 1500 m (Wüstefeld et al. 2017; Becker et al. 2019). However, mining was concentrated at depths down to -170 m above sea level (a.s.l.) (Bässler 1970; Rinder et al. 2020). In this interval, the strata follows an alternating pattern of sublitic sandstone and conglomerate layers (ca. 80%), with sporadic presence of shales (20%) and coal seams (Lotze et al. 1962; Bedoya-Gonzalez et al. 2021a). On the surface, thin Quaternary sediments and few anthropogenic waste rock deposits of the same Carboniferous sandstones occasionally cover the rocks.

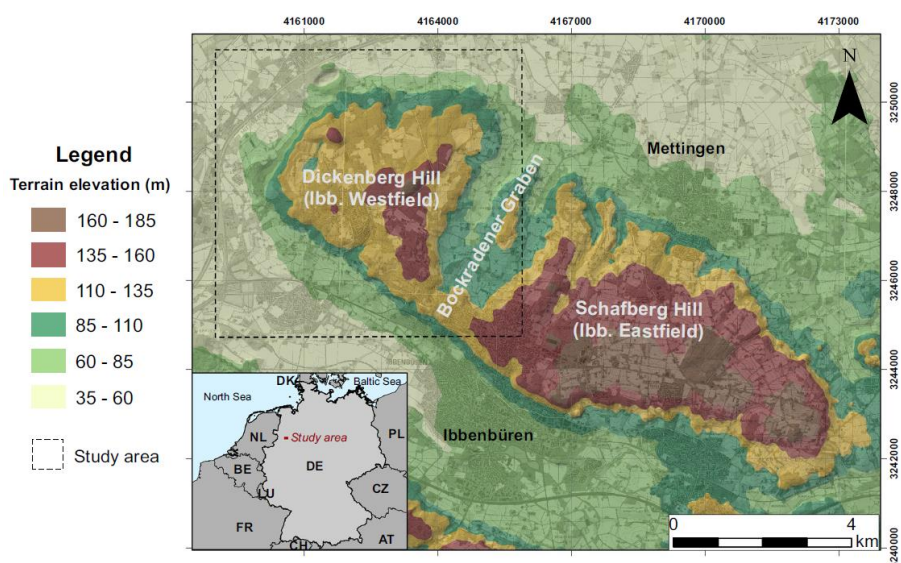


Fig. 1 Location of the Ibbenbüren coal-mining district. The dashed-line square in the digital elevation map encloses the study area further depicted in Fig. 2 (from Bedoya-Gonzalez et al. 2022)

During Westfield operation, mine dewatering was largely influenced by the seasonal rainfall pattern. About 90% of the extracted water ($10 \text{ m}^3/\text{min}$) agreed with the volume of infiltrated precipitation. Such a great amount was possible due to the absence of a Quaternary cover in the area along with the development of anthropogenic water-conducting fracture zone. The remainder water volume was hypothesized as inputs from the surrounding Mesozoic aquifers and formation water (Klinger et al. 2019). The latter would represent up to $2/3$ of the sandstone porosity volume, which ranges from 10 to 15% (Becker et al. 2017). Deep percolation of rainfall was also confirmed with the chemical composition of the pumped water. Samples extracted along the 200 m working depths in the Westfield were classified as Ca-Mg-Na-SO₄ type (Bässler 1970). This composition is markedly different from the Na-Cl water type identified in seams at -400 m.a.s.l. in the Eastfield (Rinder et al. 2020).

However, pumped waters at the westfield had pH values around 3 and unusually high concentrations of iron (100 - 1,000 mg/L) sulfate (1,000 - 3,000 mg/L) and chloride (up to 200 mg/L) whose origin was not very clear.

In 1979, the Westfield colliery closed and the dewatering system was progressively shut down. This caused groundwater to rebound over the next 4 years reaching a level of 65 m.a.s.l (i.e., an average depth of 60 meters below ground surface). At this depth, the Dickenberg adit passively collects all mine water, directing it to a sequence of settling ponds for its treatment (Rudakov et al. 2014; Bedoya-Gonzalez et al. 2021b). Initial geochemical signatures of the rebounded water in 1982 yielded discharges with iron concentrations up to 2,000 mg/L, sulfate up to 4,500 mg/L, and chloride up to 180 mg/L (Klinger et al. 2019). Six years later, iron and sulfate concentrations were significantly reduced to 500 and 2,800 mg/L respectively, while chloride remains constant. From 1988 to 2018 the concentration of the three ions slowly continued to decrease, reaching annual averages of 180 mg/L for iron, 1,800 mg/L for sulfate and 180 mg/L for chloride. Since the Dickenberg adit has imposed a water table that is above the ground surface of the surroundings (i.e., < 55 m.a.s.l.), quality and quantity of the discharged waters after the rebound depend only on the temporal distribution of the precipitation and the percolation dynamics through the unsaturated fractured overburden. This includes the area enclosed by the Northern and Southern Carboniferous Marginal faults, Mieke Fault and Pommer-Esche Fault (Fig. 2), which represent effective hydrogeological boundaries (Rudakov et al. 2014; Coldewey et al. 2018).

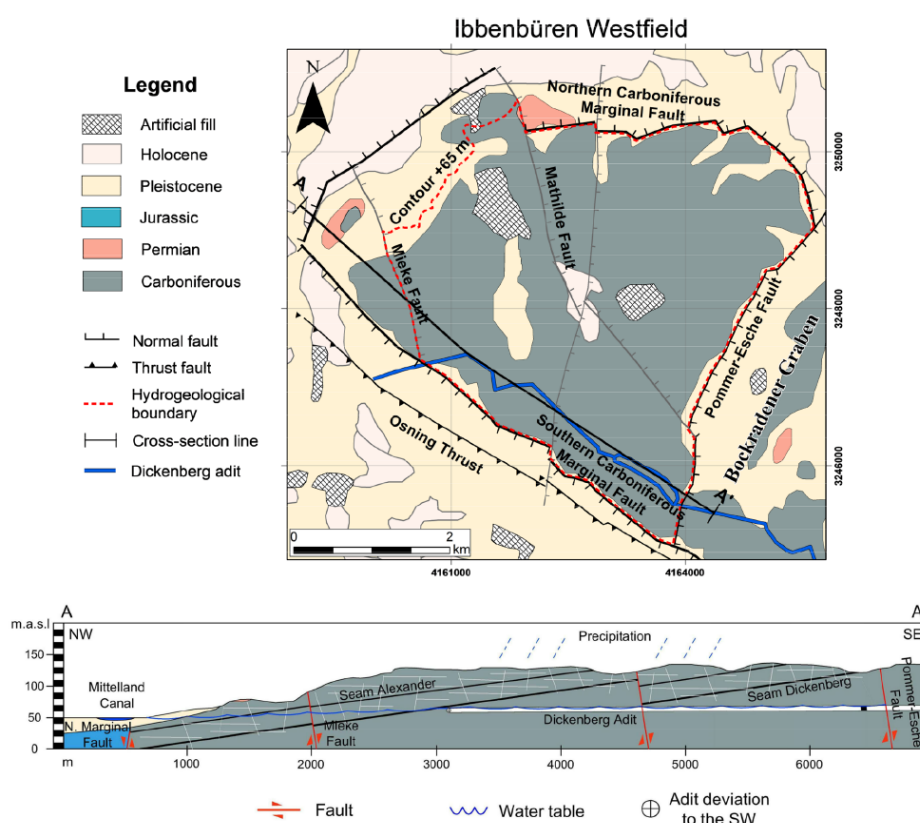
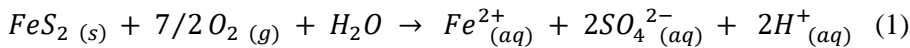


Fig. 2 Geological map and cross-section showing the hydrogeological boundaries and Dickenberg adit. The A–A' line in the map denotes the position of the cross-section, which is vertically exaggerated 5× to better detail the shallow overburden structure (from Bedoya-Gonzalez et al. 2022)

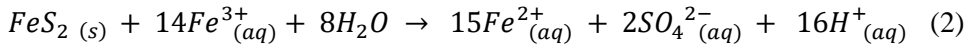
Geochemical processes

Of particular concern at the Westfield is the production of acid mine drainage, with high load of iron and sulfate ions. Consistent with that described by Bedoya-Gonzalez et al. (2021a) in rocks from the area, groundwater composition would result from oxidation of small pyrite amounts together with the dissolution of authigenic kaolinite embedded in the rock matrix. Both reaction would occur into sandstones layers, being promoted by the

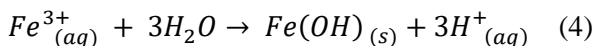
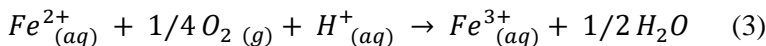
development of permeable sub-vertical fracture networks. The horizontal exchange of fluids from the fracture into the matrix would cause meteoric (oxygenated) water to interact with pyrite, oxidizing it:



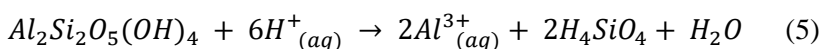
Reaction 1 produces one mole of $Fe^{2+}_{(aq)}$, two moles of $SO_4^{2-}_{(aq)}$ and two moles of $H^+_{(aq)}$ for every mole of pyrite (Blowes and Ptacek 2015). Alternatively, oxidation can proceed according to the following reaction:



Commonly, reaction 2 is reported to be faster than reaction 1. Rate constants of pyrite oxidation by O_2 range from 1×10^{-9} to 5×10^{-10} mol m^{-2} s^{-1} , while those by $Fe^{3+}_{(aq)}$ range from 1×10^{-8} to 9.6×10^{-9} mol m^{-2} s^{-1} (Williamson and Rimstidt 1994; Nordstrom and Alpers 1997). Nevertheless, these faster values are product of the catalytic effect of the bacteria *Thiobacillus ferrooxidans* on the oxidation of $Fe^{2+}_{(aq)}$ to $Fe^{3+}_{(aq)}$, a process not addressed in the simulations of this study. Under abiotic conditions, the oxidation rate of $Fe^{2+}_{(aq)}$ to $Fe^{3+}_{(aq)}$ happens in the order of 1.5×10^{-10} mol m^{-2} s^{-1} , which makes it the limiting step of the reaction and thus yields similar pyrite oxidation rates to those reported with oxygen (Singer and Stumm 1970; Xu et al. 2000). This constrain is added to the fact that meteoric water could not carry high loads of $Fe^{3+}_{(aq)}$ because of its instability at circumneutral pH, as is the case for the rainwater in the Westfield (Pierini et al., 2002). Once pyrite is oxidized, $Fe^{2+}_{(aq)}$ can be transformed to $Fe^{3+}_{(aq)}$ (reaction 3) to subsequently precipitate as amorphous iron hydroxide (reaction 4) within minutes (Grundl and Delwiche 1993).



For deep unsaturated zones, reactions 3 and 4 would be limited by the amount of oxygen left by pyrite oxidation. This may result in high amounts of $Fe^{2+}_{(aq)}$, $SO_4^{2-}_{(aq)}$, and $H^+_{(aq)}$ ions in solution within the porous medium. Alternatively, iron hydroxides can be converted to either Goethite, thermodynamically stable at pH 2.5 - 5.5, or schwertmannite/ferrihydrite, stable at pH >5.5, over aging periods involving months (Van Der Woud and De Bruyn 1983; Knorr and Blodau 2007). On the other hand, kaolinite dissolution may be linked as the only mechanism for pH buffering in absence of carbonate minerals in the area (Bain et al. 2001; Spiessl et al. 2007). Under acidic conditions, kaolinite dissolves according to the following reaction



Although there are some reports of mine drainage waters with elevated concentrations of dissolved silica and aluminium (e.g., Morin et al. 1988; Blowes et al. 1992; Glynn and Brown 1996), the dissolution rate of kaolinite is around 5×10^{-12} under atmospheric conditions and, therefore, may not have a significant influence (Huertas et al. 1998).

Model setup

This study employs the multiple interacting continua approach (MINC - Pruess 1983; Pruess and Narasimhan 1985) included in TOUGHREACT software to setup a reactive transport model of the unsaturated overburden of the Ibbenbüren Westfield (refer to the Supplementary Information for detailed description on the mathematical foundations of the MINC modelling used in this paper). The model is built based on the dual continuum fluid flow model developed by Bedoya-Gonzalez et al. (2022). Specifically, all the calibrated hydraulic parameters defined in the original dual model are maintained, as well as the model geometry. The MINC model, however, divides the matrix blocks of which the mesh geometry is composed into 4 nodes, assigning to each of them different pressure, temperature, saturation and concentration values. While all fractures are grouped into continuum #1 under well-defined physical and chemical properties, matrix material within a certain distance from the fractures are grouped into continuum # 2, matrix material at a greater distance become continuum #3, and so on (Fig. 3). This subdivision allows the model to account for kinetic and diffusion reaction fronts among fractures

and matrix. For the model's geochemical component, the study takes as a reference the detailed mineralogical information reported in Bedoya-Gonzalez et al. (2021a). This mineral assemblage is allowed to interact either kinetically or at equilibrium with the irreducible formation water, percolating meteoric water and rebound water over variable timespans. Furthermore, dilution and diffusion processes resulting from the interaction between these two waters and atmospheric oxygen are taken into account. The following subchapters specify the features considered in the model construction.

Geometry and grid construction

The design and dimensions of the Westfield grid follow the marginal faults and well-defined boundary conditions previously explained in the hydrogeological section (Fig. 2). The 3D system is discretized into vertical columns of $10 \times 10 \text{ m}^2$ base and variable height to represent the concave topography of the Westfield. The columns' height decreases about 5 m per column according to the average thickness of rock layers measured on core samples of the shallow overburden (Bedoya-Gonzalez et al. 2021a). The same thickness is used to subdivide the grid into blocks of 5 m vertical spacing (Fig. 3). Note that only one column per terrain height is constructed due to the symmetry of the area and vertical infiltration as the only component of the global flow to the adit.

Lithological and stratigraphic arrangement of the horizontal layers within the columns is realized maintaining the proportions and stratigraphic position described in Bedoya-Gonzalez et al. (2021a). Anthropogenic deposits, located above 140 m sea level, are considered here as weathered layers (Fig. 3). Mining induced fractures within the overburden is estimated to extend up to 45 m above the uppermost mined seam (i.e. above the Dickenberg adit). This height follows mathematical relationships based on the thickness of the mined coal seam as well as depth and composition of the overburden (Bedoya-Gonzalez et al. 2022). However, the fracture zone does not extend into the first element of each column (i.e., upper 5 m), which is assigned to a weathered layer. The resulted fractured overburden is discretized into 1 fracture continuum and 4 nested matrix blocks: the first 3 (closest to the fracture) are fixed slabs with thicknesses of 0.1, 0.4 and 1 meters, while the 4th accommodate the remaining length to the next fracture. Vertical fractures are placed equidistant, with a linear density equal to 1 fracture per 10 m-long block, and total interface area of 100 m^2 between continua. This horizontal 1-D array of nested grid blocks generates gradients for solute flow and transport within the matrix, perpendicular to the fracture.

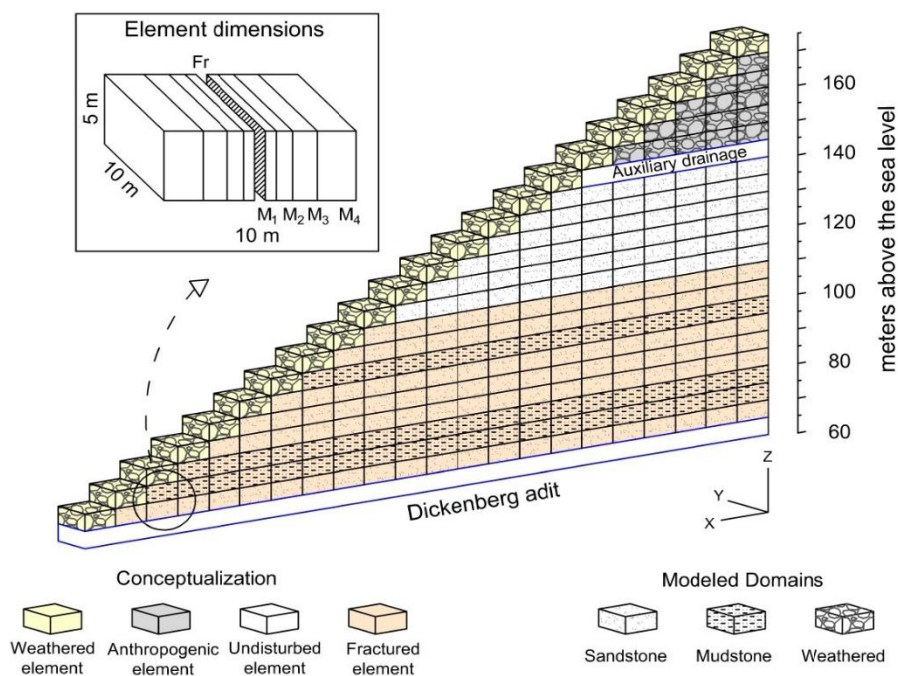


Fig. 3 Constructed grid for the shallow overburden of the Ibbenbüren Westfield. Recharge is applied directly onto the weathered blocks. For each block colored in orange, the mesh is divided into five continua with the same physical location: one for fracture (Fr) and four for the matrix media (M_n)

Hydrodynamic parameters

Different sets of permeability, porosity and van Genuchten parameters are assigned to sandstone, shale and weathered lithologies according to their actual characteristics in the field (**Table 1**). Regarding the fractured continuum, hydraulic parameters are allocated to recreate the expected hydraulic response of a highly permeable medium (e.g., gravel). These values emulate the real features of post-mining fracture zones, while meeting the software requirements for its modelling. For instance, Fractured continuum total porosity is set to 0.90 for the software to assume open fractures, as identified by Bedoya et al. 2021 in core samples of the study area. In addition, the residual water content (θ_r) is fixed at 0.05 to allow the continuum to transmit water during dry periods. If this value was zero, the relative permeability would nullify the exchange with the matrix, generating numerical insufficiencies. Note that the parameters used in both the matrix and fracture continua correspond to calibrated values for the best volumetric discharge agreement with respect to the measure data of the Dickenberg adit (Bedoya-Gonzalez et al. 2022). Therefore, disturbances of the flow component derived from changes in porosity and permeability due to mineral dissolution and precipitation are not considered in this reactive model.

Table 1 Calibrated hydraulic parameters used in the MINC model. Modified after Bedoya et al. (2022)

Lithology	Permeability (m ²)	Eff. Porosity (-)	Van Genuchten-Mualem parameters		
			θ_r (m ³ /m ³)	α (m ⁻¹)	m (-)
Sandstone	5×10^{-14}	0.10	0.30	0.07	0.35
Shale	1×10^{-17}	0.05	0.65	0.04	0.22
Weathered interval	5×10^{-13}	0.15	0.2	0.3	0.65
Fractured continuum	5×10^{-11}	0.90	0.05	0.2	0.7

Boundary conditions

No-flow boundary conditions are assigned on the left, right, front and back sides of each column, while open boundaries are set at the interfaces between the fracture and the 4 matrix continua. A flux boundary is set at the top of each column (i.e., in the weathered blocks) to account for diffuse recharge. The amount of water imposed is assumed to be either constant or daily variable depending on the modelling phase. For calculating a long-term water equilibrium, a constant recharge value of 240 mm/a is assumed, which is equivalent to the average groundwater recharge in northwest Germany (BGR 2021). Alternatively, daily precipitation values are used to evaluate the weather variability according to the recharge model of the Geological Survey of North Rhine-Westphalia (Herrmann et al. 2014). Above the weathered blocks an atmospheric boundary with a constant oxygen pressure of 0.2 bar is imposed, enabling diffusion and advection of oxygen in the gas phase.

The lower boundary (i.e. Dickenberg adit) is set to allow free drainage under gravity in most of the simulation. However, this is changed for a short period of time to a fully saturated Dirichlet-type boundary to allow capillary equilibrium with the unsaturated sequence during groundwater rebound. It is important to point out that the simulated discharge and solute concentration are calculated at this boundary by computing the fluid and solute flux of the five continua with the adit. These values are normalized for the whole area by multiplying the flux of each column by its areal representation according to the digital elevation model of the Westfield. As a result, simulated discharge and solute breakthrough curves can be compared directly to quality and quantity water measurements of the Dickenberg adit.

Hydrogeochemical conditions

All scenarios simulated in this work included isothermal conditions at 25 °C, with air and liquid as phases subject to transport. The air is composed exclusively of gaseous oxygen as it is the only relevant gas in the oxidative processes. Oxygen is treated as an ideal gas, and its interaction with the aqueous solution is assumed to be in equilibrium. The chemical composition of the liquid phase corresponds to actual formation, rebound and precipitation waters taken directly in the field or in surrounding areas (**Table 2**). Their use, however, depend on

the simulation stage of the model (see *Simulation stages* section below). Other solutes resulting from dilution and diffusion processes between these water types and atmospheric oxygen are also taken into account throughout the simulation.

Table 2 Composition of the initial and boundary waters (in mg/L) employed in the model

Composition (mg/L)	Formation water ^a	Rebound groundwater ^b	Rainwater	
	Westfield sample #1171 (depth -80 m.a.s.l)	1st year (1983)	100% ^c	30%
pH	6.8	3.2	5.5	4.4
Na ⁺	1180.0	N/A	0.73	2.43
K ⁺	33.0	N/A	0.13	0.43
Mg ⁺²	228.6	N/A	0.15	0.50
Ca ⁺²	829.7	N/A	0.50	1.67
Al ⁺³	0.03	N/A	0.005	0.02
Fe ^{+2/+3}	0.5	950	0.02	0.07
Cl ⁻	3705.3	180	3.5	11.67
HCO ₃ ⁻	207.4	N/A	0.1	0.33
SO ₄ ⁻²	226.0	4500	6.15	20.50
SiO _{2(aq)}	17.0	N/A	1	3.33
O _{2(aq)}	10.0	1.0E-70	10.0	10.0
Artificial tracer	N/A	1e-4 (mol/L)	N/A	N/A

^a Bässler (1970), ^b Klinger et al. (2019), ^c Herrmann et al. (2006)

The solid phase of the model is constructed based on detailed mineralogical information described by Bedoya-Gonzalez et al. (2021a). The Westfield overburden consists mainly of sandstone layers composed of quartz, sedimentary lithic fragments (chert and mudstones), muscovite and variable amounts of pyrite. Rocks do not present cement, but display high amounts of authigenic kaolinite in the matrix. There is neither report of carbonate minerals such as calcite or siderite. Based on this description, **Table 3** lists the abundance of primary minerals assigned to the matrix continuum along with their chemical formulas and dissociation stoichiometry. Regarding the fractured continuum, the primary mineral fraction is assumed to be zero considering its recent origin and element-free volume.

From the mineralogical composition, it is clear the dominance of interactions involving pyrite oxidation, kaolinite dissolution and dissolved oxygen (see section *Geochemical processes* for details of these reactions). Both pyrite oxidation and kaolinite dissolution are kinetically controlled reactions in the model while the formation of amorphous iron hydroxides proceeds on an equilibrium basis due its short formation time compared to the simulation periods. Further transformations of solid iron phases into goethite, ferrihydrite or schwertmannite are beyond the scope of this study and are not modelled. Although it has not been identified in the area, gypsum precipitation is introduced as a potential sulfate sink due to the high concentrations of the anion reported in the drainage. Thermodynamic and kinetic rate constants are summarized in **Table 3**. Note that in the absence of in situ kinetic measurements, representative bibliographic values of the site conditions are used here, making them neither exhaustive nor unique. Finally, the reactive surface area for the minerals is set equal to 3140 m²/m³ medium except for kaolinite and muscovite, for which it is increased by one order of magnitude due to their plate habit. This surface area is calculated using a 4-sphere cubic-closed packing arrangement of medium sand-size grains, which is a plausible simplification for tight rocks due to its packing efficiency of 74%.

Table 3 Chemical properties of the primary mineral assemblage assigned to the overburden. Thermodynamic parameters (log K) are taken from the Japan Atomic Energy Agency (JAEA).

Mineral	Initial volume fraction (%)	Reaction equation	Log K (25°C)	Rate constant (mol m ⁻² s ⁻¹)
Oxygen	0.2 (bar)	$O_{2(g)} = O_{2(aq)}$	-2.90	At equilibrium.
Pyrite	5	$FeS_2(s) + 3.5O_{2(g)} + H_2O = Fe^{2+}_{(aq)} + 2SO_4^{2-}_{(aq)} + 2H^+_{(aq)}$	217.39	1×10^{-9} (with O _(aq) mechanism = 0.5) ^a
Kaolinite	10	$Al_2Si_2O_5(OH)_4 + 6H^+_{(aq)} = 2Al^{3+}_{(aq)} + 2H_4SiO_4 + H_2O$	5.29	4.89×10^{-12} (with H ⁺ mechanism = 0.77) ^b
Muscovite	5	$KAl_3Si_3O_{10}(OH)_2 + 10H^+_{(aq)} = K^+ + 3Al^{3+}_{(aq)} + 3SiO_2(aq) + 6H_2O$	14.80	2.82×10^{-14} b
Quartz	60	$SiO_2(s) = SiO_2(aq)$	-3.74	1.02×10^{-14} b
Am. iron hydroxide (secondary)	0	$Fe(OH)_3(s) + 3H^+_{(aq)} = Fe^{3+}_{(aq)} + 3H_2O$	-4.55	At equilibrium
Gypsum (secondary)	0	$CaSO_4 \times 2H_2O = Ca^{2+}_{(aq)} + SO_4^{2-} + 2H_2O$	-4.47	At equilibrium
Porosity	10			

^a Williamson and Rimstidt (1994), ^b Palandri and Kharaka (2004)

Simulation stages

The actual geochemical signature of the Westfield drainage results from the compilation of natural and mining processes that have modified the system over time. If one considers that mining is carried out in several stages, the model would have to address variable initial and boundary conditions. This section describes the 5-stage modelling framework used to simulate long-term and seasonal changes of the groundwater chemistry, rocks saturation, and discharge volumes in the study area. At each stage, the initial time step size is set equal to 1 second and allowed to increase up to 1000 seconds. The time step sizes are automatically controlled to maintain a Courant number of less than 0.5. This stability criterion generates more accurate transport component results, which are then transferred to the reaction calculations. In addition, the criterion reduces the accumulation of errors in geochemical speciation when the results of one stage are used as initial conditions for the next one. A sketch showing the 5-stages simulation can be seen in Fig. 4.

Stage 1: saturation and composition of the formation water

Full water saturation is assigned to the entire mesh to allow each element to equilibrate by gravity and capillarity with a water table located at -80 m.a.s.l. This depth corresponds to the second exploited coal level down to which the regional water table dropped after the Dickenberg seam was mined (a process that fractured the shallow overburden). The simulation is carried out for 50 years, equivalent to the time the mine was under an intensive mining regime. Subsequently, the chemical composition of the resulting water volume is assigned equal to the water extracted at the mining faces (i.e., at -80 m.a.s.l. – see **Table 2**). However, as the residual water is localized in the unsaturated zone, it is equilibrated with an oxygen partial pressure of 0.2 bar before starting the second transport phase. Results of this stage give formation water volumes in equilibrium with the lowered water table and with compositions that are weakly influenced by meteoric water, as one would expect from a fracture-drained matrix.

Stage 2: chemistry of groundwater during mining operation

The unsaturated overburden is equilibrated with percolated water for 50 years, elapsed time between the exploitation of the Dickenberg seam (i.e., the lower boundary of the model) and the mine closure. For this

purpose, the water table is kept at -80 m.a.s.l., while a fixed injection rate of $7.5 \times 10^{-6} \text{ kg/s/m}^2$ ($\approx 240 \text{ mm/yr}$) is applied to the first element of each column. This rate corresponds to the average annual recharge of the area, equivalent to 1/3 of the precipitation. As for the injected water composition, it is calculated by applying evaporation on rainwater data reported at the French-German border (Herrmann et al. 2006) until the remaining water volume matches one third of the original volume (**Table 2**). Dissolved oxygen is included in this water with a fixed concentration of 10 mg/L. Moreover, constant diffusion and advection of gaseous oxygen from the atmospheric boundary is enabled. At the end of the stage, an equilibrium between percolate and formation waters is reached, which includes the dilution process of the latter. Results would also depict iron, sulfate and hydrogen concentrations generated by the rock-water interaction during mining time.

Stage 3: groundwater rebound

In this stage, the lower free drainage boundary is changed to fully water-saturated, with a constant pressure of 1 atmosphere. This shift allows to simulate the gravity-capillary interaction between the unsaturated sequence above the adit and the newly imposed water table during the rebound process. It also serves to evaluate the potential exchange of pollutants brought by the mine waters. The rising water tends to dissolve highly soluble efflorescent salts (solid by product of sulfide oxidation) accumulated over decades in the mine buildings, flushing them out at concentrations several times higher than those observed during operation (Younger 1997; Gzyl and Banks 2007). This process, usually referred to as first flush, results in environmentally aggressive waters, with very low pH and high metal loads. In this step, the composition of the first flush corresponds to actual measurements recorded in the decommissioning plan of the Ibbenbüren mine (**Table 2**). The average annual composition of the first year is imposed to the water-saturated lower boundary. As the water comes from the saturated zone, an oxygen partial pressure of $1 \times 10^{-70} \text{ bar}$ is assigned to it, converting it into reducing water. Finally, a conservative artificial tracer is added to the water to better quantify its movement through the overburden.

Stage 4: Post-mining water evolution

After rebound, the concentration of contaminants decreases exponentially until they reach levels close to the natural values observed in the surrounding aquifers (Younger 2000; Mugova and Wolkersdorfer 2022). Therefore, the fourth stage simulates the geochemical evolution of the water discharged from the unsaturated column after reaching capillary-gravity equilibrium. This is done by injecting the average annual recharge rate for another 35 years directly into the first weathered element and letting it percolate through the columns (**Table 2**). The lower boundary is returned to an unsaturated condition enabling free gravity drainage of percolating water into the Dickenberg adit. At the end, the simulated breakthrough curves can be compared with the real measurements recorded in the Ibbenbüren decommissioning plan (Klinger et al. 2019). The latter permits the assessment of the accuracy degree of the model.

Stage 5: Seasonal variation of the water composition

Slight fluctuations of the extracted water composition are observed in quarterly chemical measurements of the years 2016 to 2018 (data provided by RAG company). Chemical variations would be influenced by seasonal amounts of percolated water and its interactions with fractures and porous units, following what is observed in the bimodal discharge behaviour of the area. The DC flow model shows how the fractured continuum reacts quickly during the months of higher precipitation generating discharge peaks, while the recession of the signal during spring and summer months is dominated by the matrix (Bedoya-Gonzalez et al. 2022). In this step, daily recharge values from the years 2016 to 2018 are used to account for meteorological variability throughout the year. The injection rates are calculated using the monthly recharge model of the Geological Survey of North Rhine-Westphalia and average daily precipitation values measured at nearby weather stations (data provided by LANUV NRW - Table SI1 in the Supplementary Information). As for the water composition for each month, it is calculated in the same way as described in step 2, applying evaporation until the volume reaches the percentage of the reported recharge (Table SI2 in the Supplementary Information).

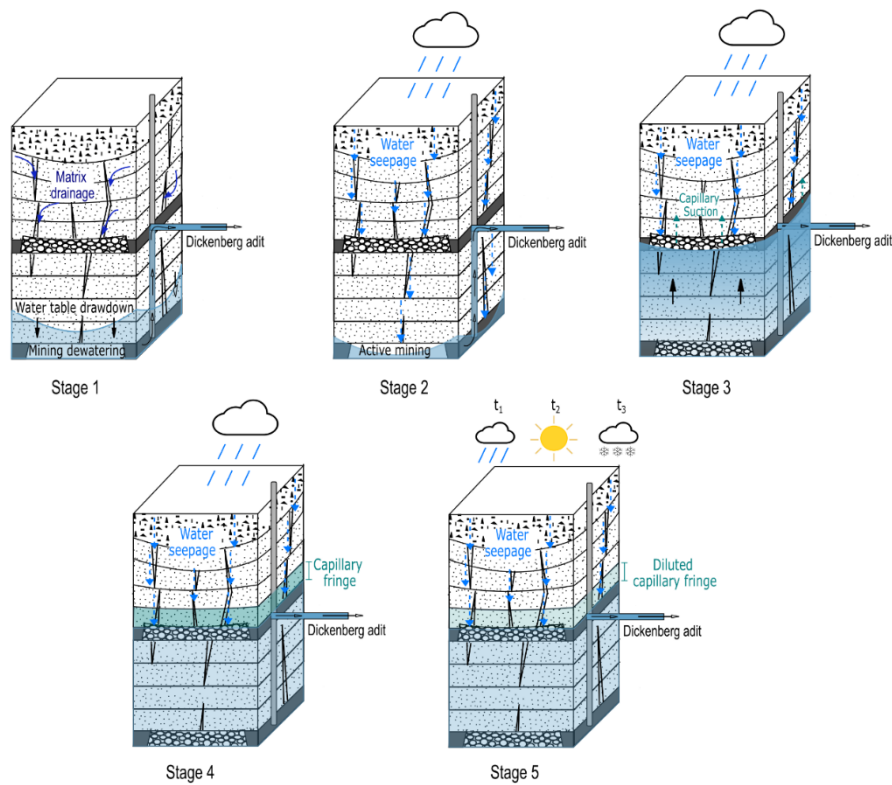


Fig. 4 Schematic representation of the 5-Stages simulation performed in this study

Results

Prior to reactive transport simulations, the flow component of the MINC model was tested independently to spot potential errors in using the parameters and configuration from the dual continuum model. Results show a large discrepancy with respect to the measured discharges for 2016 and 2017 when using the same calibrated values (Fig. 5 – green line). The recession limbs of the discharge curve indicate a higher suction and water storage in the matrix continua during winter months rather than being discharged through the fractured continuum. Therefore, it was necessary to reduce the α value of the van Genuchten -Mualem function for the fractured continuum from 0.2 to 0.1. This lower value yields higher water retentions in the fractures, counteracting the large capillary suction generated by the inclusion of a small matrix continuum next to the fracture. Once the change is made, simulations of the MINC model exhibit a good agreement with both measured and simulated drainage discharges with the DC model (Fig. 5 – orange dotted line). The latter implies that much of the discretization, parameterization and recharge values used in the DCM are still valid for simulating the flow component of a reactive transport model with several continua.

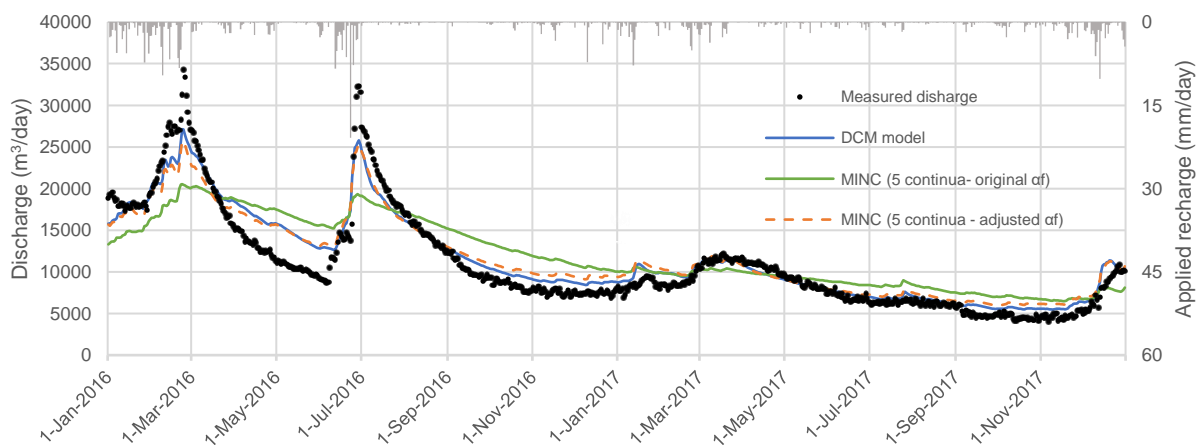


Fig. 5 Comparison of the measured and simulated discharges of the Dickenberg adit for the years 2016 and 2017. DCM: dual continuum model, MINC: Multiple Interactive Continua model, α_f = alpha parameter for the fractured continuum.

Benchmark scenario

Stage 1

Fig. 6 shows water saturations for one of the model's representative columns after 50 years of dewatering. It is seen that sandstones and shales layers remain at high saturation degree, with values ranging between 50% and 90%. Conversely, weathered elements and the fractured continuum display water saturations closer to their residual amounts (**Table 1**). These results, obtained from the equilibrium of the sequence with a lowered water table, are relevant to avoid potential over- or underestimations in the reactive and transport processes included in the model. For example, it is not the same to equilibrate pyrite with oxygen when there is an initial air saturation in the sandstones of 66% (as would be the case if the irreducible water content is taken as the initial saturation of the system) than when there is only 30%. The same sensitive problem would occur with the volume of saline formation water that has to be diluted. As mentioned above, water and gas saturations calculated in this step are used as initial conditions for the second stage.

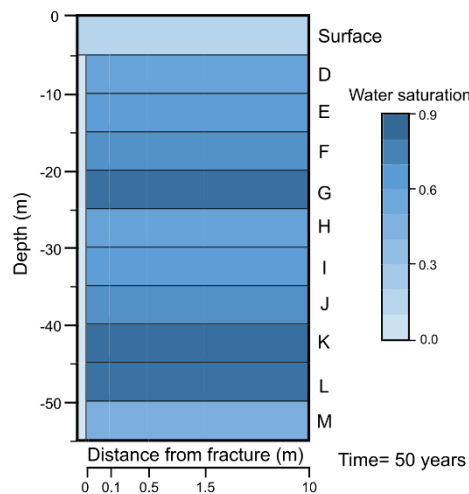


Fig. 6 Water saturation in one of the model columns (Consider for subsequent column graphs that layers G, K and L correspond to shales).

Stage 2

The conservative behaviour of chloride is used to evaluate the transport of solutes initially present in the matrix throughout mining (e.g., formation water). During the first 10 years, the initial chloride content in the sandstones (3,700 mg/L) was actively washed out, generating discharges with concentrations up to 450 mg/L (Fig. 7a). This steep increase is the result of solute exchange from the first two matrix continua closest to the fracture, as illustrated in Fig. 7b (Missing or reduction of the blue and orange bars for the 5- and 10-year periods in each layer). Beyond the tenth year of simulation, the chloride concentration in the discharge is significantly reduced due to the constant solute dilution in these two continua. However, the decrease slows down between year 15 and 20 owing to a sustained input of the anion from the third continuum. For the last 3 decades, chloride discharge concentration continues to gradually decrease as the interaction front of the meteoric water with the formation water moves towards and into the fourth matrix continuum (i.e., rock volumes further than 1.5 m from the fracture). Besides horizontal transport, the model further shows how chloride is extracted first in the layers closest to the surface, generating a vertical dilution front with the underlying layers of the same continuum (Fig. 7b). This phenomenon occurs due to vertical advection of meteoric water into the matrix, which is also facilitated by horizontal exchange with the fractured continuum. At the end of the 50-year period, the simulated chloride discharge of 180 mg/L is in good agreement with the 200 mg/L recorded in mining reports of the time (Bässler

1970). For this period, chloride dilutions of up to 90% are also observed for the first two continua of the sandstone layers and up to 30% for the fourth continuum of the upper strata (Fig. 7c).

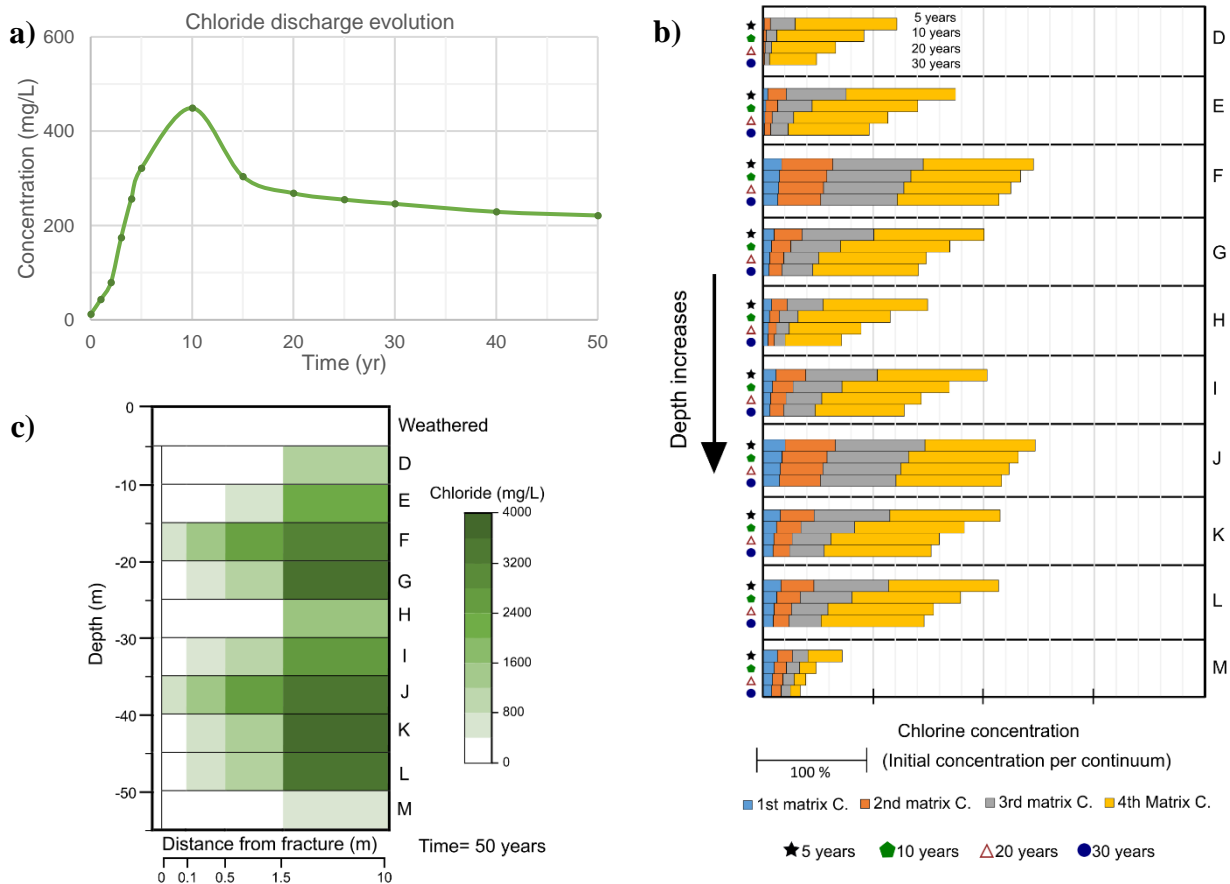


Fig. 7 Distribution of chloride ion over time. a) Discharged evolution of the ion in the Dickenberg adit. b) Evolution and c) final state of the initial imposed chloride concentration in one of the model's representative columns.

Stage 2 further returns iron and sulfate discharge concentrations consistent with historical values measured at the Ibbenbüren Westfield. Simulations of pyrite kinetic oxidation produce progressive increases of both ions in the discharge until reaching nearly steady-state levels of 1,100 mg/L for sulfate and 250 mg/L for iron in the 20th year (Fig. 8a). When plotting the pyrite distribution in the columns, it is observed that the mineral dissolves almost homogeneously over time up to 1.5 m next to the fracture continuum. This dissolution pattern is generated by the limited advection and diffusion of gaseous and dissolved oxygen into the matrix once it is exchanged from the fracture. Likewise, the rate and amount of oxygen consumed by the oxidative reaction in this interval causes pyrite dissolution to decrease by half in the fourth continuum (Fig. 8c and 8d). The latter causes the production of both ions nearly to stabilize over the last 30 years as no further amount oxygen can be introduced into the fourth continuum nor can the solute produced there be transported more rapidly back to the fractured continuum.

Oxygen distribution along the continua is, in turn, related to the development of weathering fronts on both sides of the fractures. As the amount of oxygen decreases in the horizontal direction into the matrix due to pyrite oxidation, less oxygen is available for precipitation of iron hydroxides. Fig. 8e shows that mostly the first two continua of the matrix (i.e., first 50 cm next to the fracture) ends with some amount of the solid iron phase. Most of it precipitates in the fracture continuum where the oxygen content is almost twice as high as in the second and third matrix continuum and 10 times higher than in the fourth (Fig. 8d). Under this scheme, total dissolved iron and sulfate concentrations slowly increase in the solutes of the porous medium, while amorphous iron hydroxides persist to accumulate in punctual sections of the fractured continuum. The latter seems to be, somehow, contrary to what has been reported in drill cores from the area (Bedoya-Gonzalez et al. 2021a).

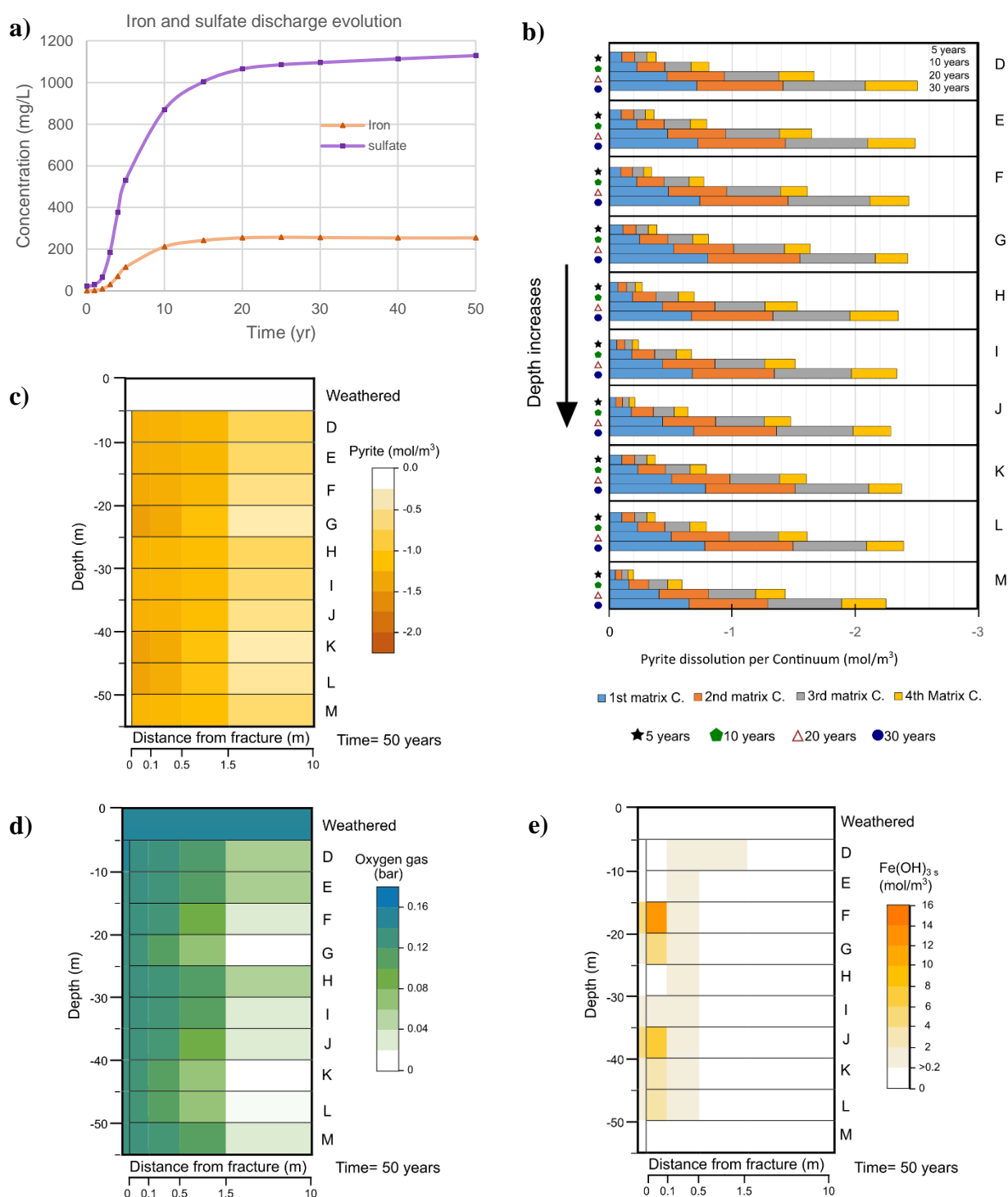


Fig. 8 Pyrite –related ions concentrations over time. a) Discharged evolution for iron and sulfate ions in the Dickenberg adit. b) Evolution and c) final state of pyrite dissolution in one of the model's columns. Distribution of d) gaseous oxygen and e) precipitated iron hydroxides for one of the model's columns after 50 years of simulation.

Finally, this stage illustrates how pyrite oxidation transforms the meteoric water feeding the Westfield into a strongly acidic solution during its seepage path. In fact, the influence of surface water on the pH of the discharge is erased before the fifth year of simulation. Thereafter, the pH achieves a steady state around 3.2 because of the weak acidity buffer capacity of the kaolinite (Fig. 9a). Dissolution of the mineral occurs in the three continua closest to the fractures, with dissolution rates much lower than those recorded for pyrite (Fig. 9b). When kaolinite

is removed in an alternative scenario, a slight increase in hydrogen concentration is observed during the first 5 years of simulation, so that low pH values are reached more quickly (Fig. 9a). It is also noted that pH continues to decrease slowly during the later years. Despite this, the difference in pH value at the end of the 50-years simulation is only 0.1 between the two scenarios.

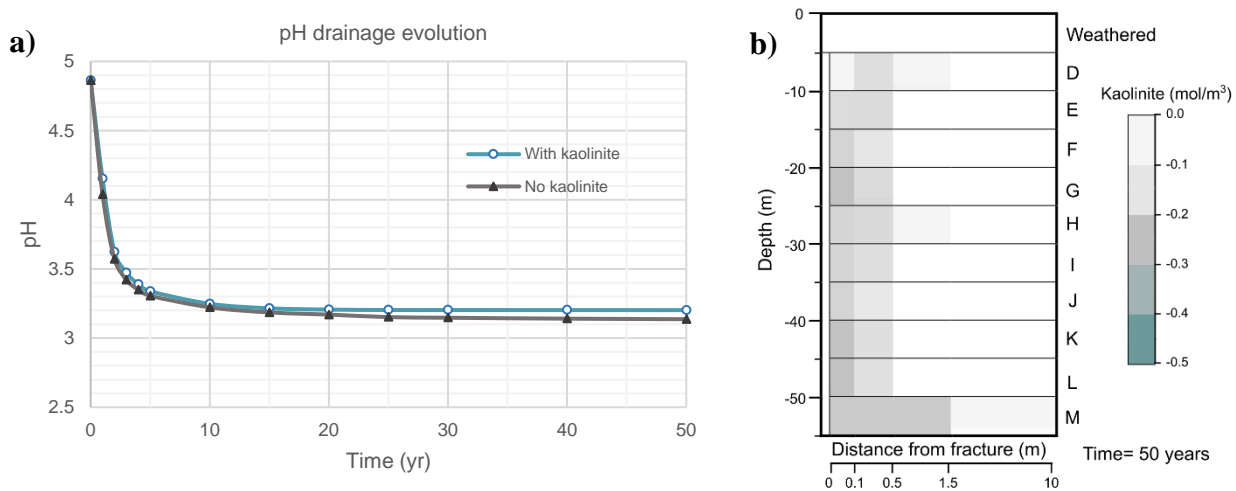


Fig. 9 Evolution and distribution of hydrogen ion in the model during the 50 years simulation. a) pH values of the discharged water and b) kaolinite dissolution patterns observed in one model's columns.

Stage 3

The influence of the mine water rebound in the unsaturated sequence above the adit was simulated with the placement of a fully water saturated Dirichlet boundary condition at the base of the domain. This boundary included a conservative tracer to quantify the advective exchange of substances from the imposed water table. Simulations reveal that the capillary action of the unsaturated sequence sucks the rebounded water during the first 840 days. For the artificial tracer this phenomenon represents a total exchange of 50 times the initial imposed amount on the lower boundary per square meter (Fig. 10a). Most of this quantity is exchanged during the first 100 days, with values of about 35% per day. However, water suction progressively decreases as the sequence becomes saturated. By day 840 the overburden reaches hydrostatic equilibrium with the air-entry pressure and the recharged water, stopping the capillary rise. As for transport, the uptaken solute moves 10 meters toward the surface within the overburden, reaching concentrations 1 to 3 orders of magnitude lower than those originally present (Fig. 10b). This thickness would correspond to the capillary fringe where solutes remain above the water table against gravity. The simulation of an alternative scenario with a homogeneous sandstone overburden, however, showed that the thickness of this fringe and the amount of exchanged tracer rely on the lithological composition. In the latter scenario, upward migration increases up to 20 meters (Fig. 10c), with tracer exchanges around 85 times the initial amount per square meter.

Similar capillary patterns to those obtained for the tracer are observed for sulfate and iron ions. Recall that concentrations of 4500 mg/L and 2000mg/L respectively were imposed on the water table boundary to emulate the large amounts measured at the mine drainage during the first flush. In this case, simulations show an enrichment of dissolved iron and sulfate for the solutes contained in the two lowermost layers of the model (Fig. 10d). In none of the simulations does the pore water reach saturation levels with respect to gypsum to precipitate, nor is there an increase in iron hydroxide precipitation that would promote the removal of any of the dissolved ions.

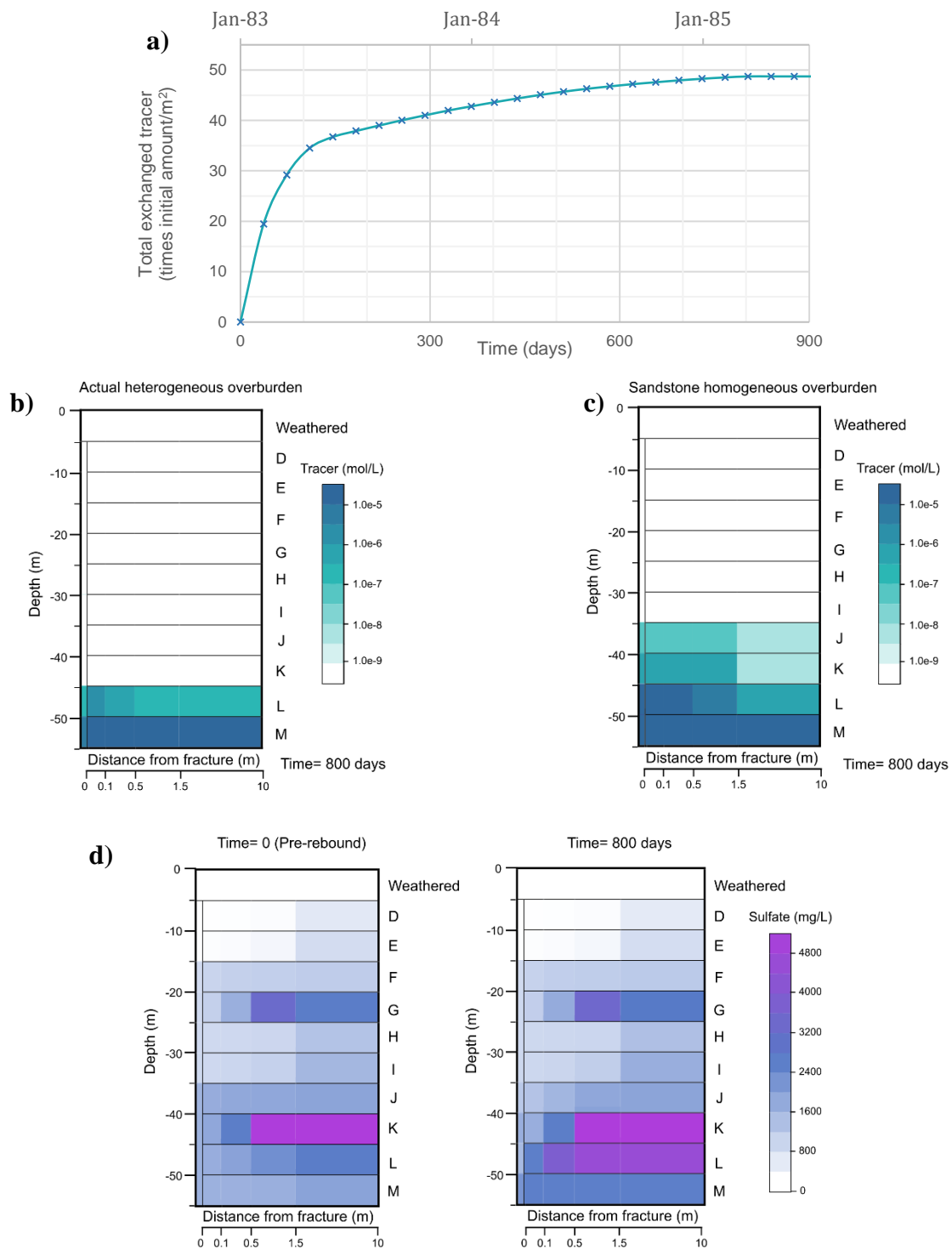


Fig. 10 Behaviour of one artificial tracer and sulfate ion during the capillary-gravity equilibrium. a) Total amount of suctioned tracer. Migration pattern of the suctioned tracer in one model’s column for b) the actual heterogeneous overburden of the Westfield and c) for an hypothetical homogeneous overburden composed of sandstones. d) Sulfate ion concentration before and after capillary suction in one model’s column for the actual heterogeneous overburden.

Stage 4

With gravity-capillary equilibrium achieved, water flow is reversed from the column to the water table. At this point, the lower boundary of the model is desaturated to simulate an open mine drainage, avoiding the re-suction of solute. Fig. 11a shows the evolution of the remaining tracer for both the current heterogeneous overburden and

the hypothetical rock sequence composed only of sandstones. In both cases, more than 70% of the tracer is released back into the adit during the first 10 years after capillary equilibration. From this point on, the release slows down as the meteoric water must travel longer distances to interact and dilute the solute of the inner matrix regions. The process is additionally counteracted by the diffusive movement of solute toward the surface. For example, Fig. 11b shows tracer signals one layer higher than it was found at the end of the capillary-gravity equilibrium for the actual heterogeneous overburden (Fig. 10b). At the end of the 35-year simulation (i.e., year 2018), 20% of the initial amount of absorbed tracer remains in the actual heterogeneous overburden, while only 10% is present in the homogeneous sandstone overburden.

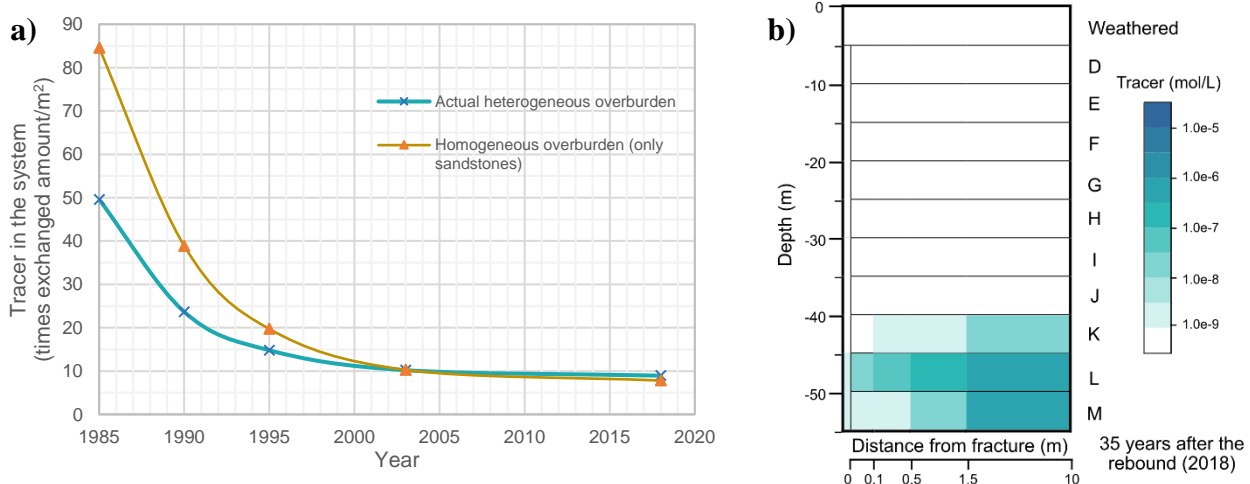


Fig. 11 Post rebound evolution of the artificial tracer within the system. a) Simulated concentration discharges in the Dickenberg adit. b) Final concentration in one of the model columns for the actual heterogeneous overburden.

For iron and sulfate, the post rebound stage is also marked by the dilution and release of the absorbed quantities. At the end of the capillary equilibrium (i.e., 1985), sulfate and iron discharge concentrations of the unsaturated sequence were of the order of 2000 mg/L and 450 mg/L respectively. During the following 4 years, concentrations of both ions decreased by 25% following the drainage of the two matrix continua next to the fracture (Fig. 12a and Fig. 12b). At this temporal point, concentrations keep decreasing, but only slightly due to the lower contribution of solute contained in the more distant continua, as it was observed for the tracer.

When comparing simulated and measured post-rebound concentrations, an equal discharge pattern is observed, although with higher measured values. Model underestimations during the first 10 years would arise from not accounting for dissolution and transport of fluorescent salts directly into the adit. Another uncertainty may correspond to higher than assumed sulfate and iron contents in the rebounded water that was brought into contact with the unsaturated sequence for its capillary equilibrium. In any case, it is observed that the external source is exhausted with time, making the simulated values progressively closer to the measured ones. After 2003, both simulated and measured sulfate signals reach a quasi-steady state close to the pre-rebound discharges, suggesting that the ion concentration again depends on the water-rock interaction above the drainage (Fig. 12a). Accordingly, the observed difference between the reference levels from this point on could be explained by underestimation of parameters already considered in the model such as pyrite amount, reactive surface area or fracture density. Iron discharge behaviour, however, is different from that of sulfate since it does not reach a stable level but further decrease with time (Fig. 12b). A similar decreasing pattern is obtained with the model by including a lower boundary with gaseous oxygen for emulating an aerated adit. This boundary condition leads to the precipitation of iron hydroxides in the sandstone layer immediately above, thus reducing the free iron discharge (Fig. 12c).

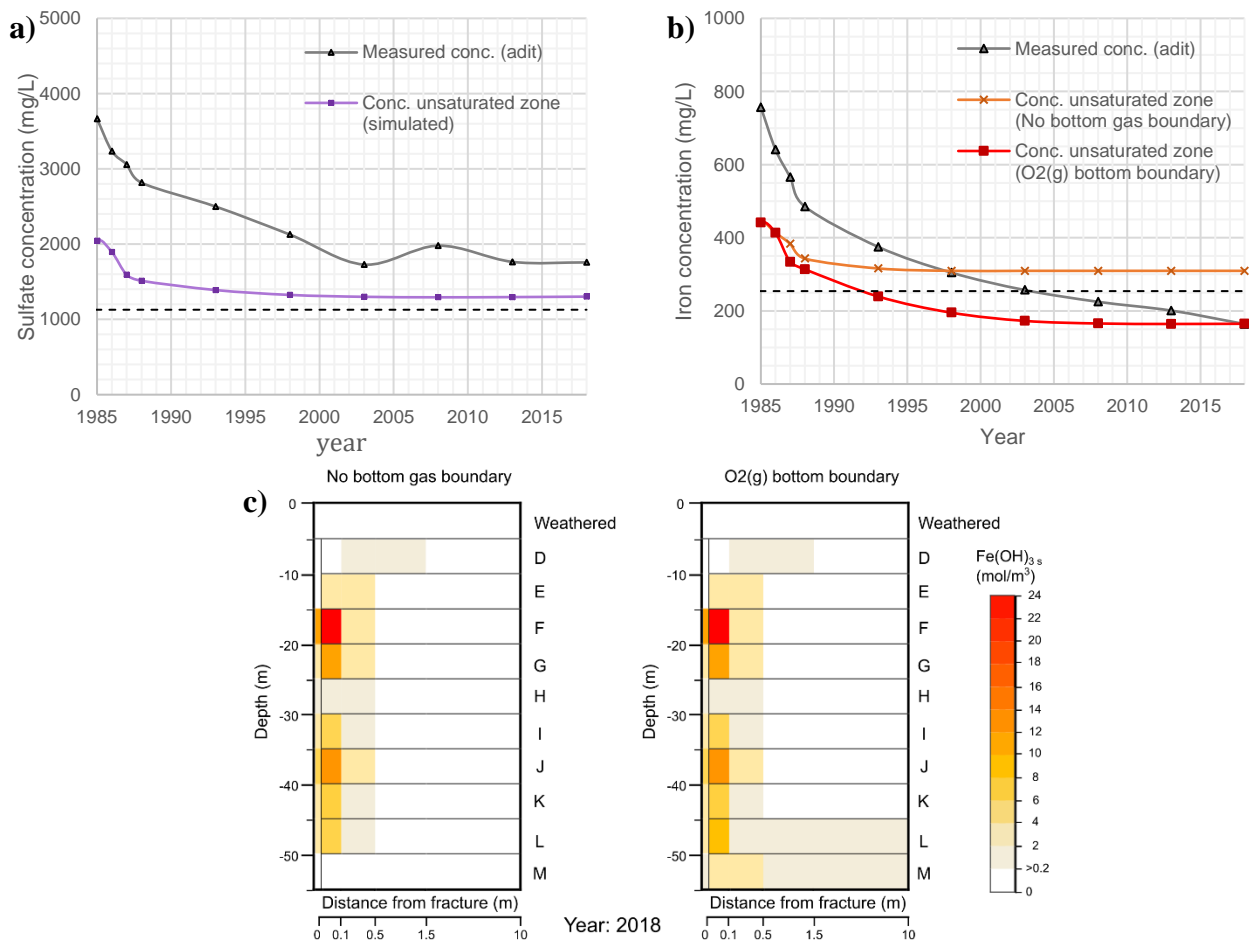


Fig. 12 Post rebound evolution of the system. Measured and simulated concentration discharges in the Dickenberg adit for a) sulfate, and b) iron. c) Comparison of the iron hydroxides precipitated in one of the model columns when including (or not) oxygen in the lower boundary.

Stage 5

The model's effectiveness in simulating seasonal discharges of sulfate, chloride and iron is evaluated by comparing quarterly measurements taken at the outflow of the Dickenberg adit. **Error! Reference source not found.a** and **Error! Reference source not found.b** show positive agreements of the anion patterns for the years 2016 and 2017, although with discrepancies in the absolute concentration values as evidenced in the post-rebound stage. Specifically, high recharge events lead to lower sulfate discharge concentrations due to a dilution effect and lower availability of gaseous oxygen to oxidize pyrite. On the other hand, periods of low infiltration lead to higher sulfate concentrations for matrix solutes, which are slowly released to fractures. For chloride, high periods of precipitation generate a slight increase in concentration as there is an increase in the amount of water exchanged between the fracture and matrix continua. This interaction causes more of the solute locked into the matrix to be pushed to the fractured continuum. In dry periods, when the recharge is minimum, the exchange is restricted, keeping chloride in the matrix. Regarding iron, simulated concentrations agrees with the measured base level, but not with the discharge pattern (**Error! Reference source not found.c**). The measured cation concentration was shown to be rather independent of the recharge events, which is contrary to the simulated signal, where peaks and valleys are similar to those observed for the anions.

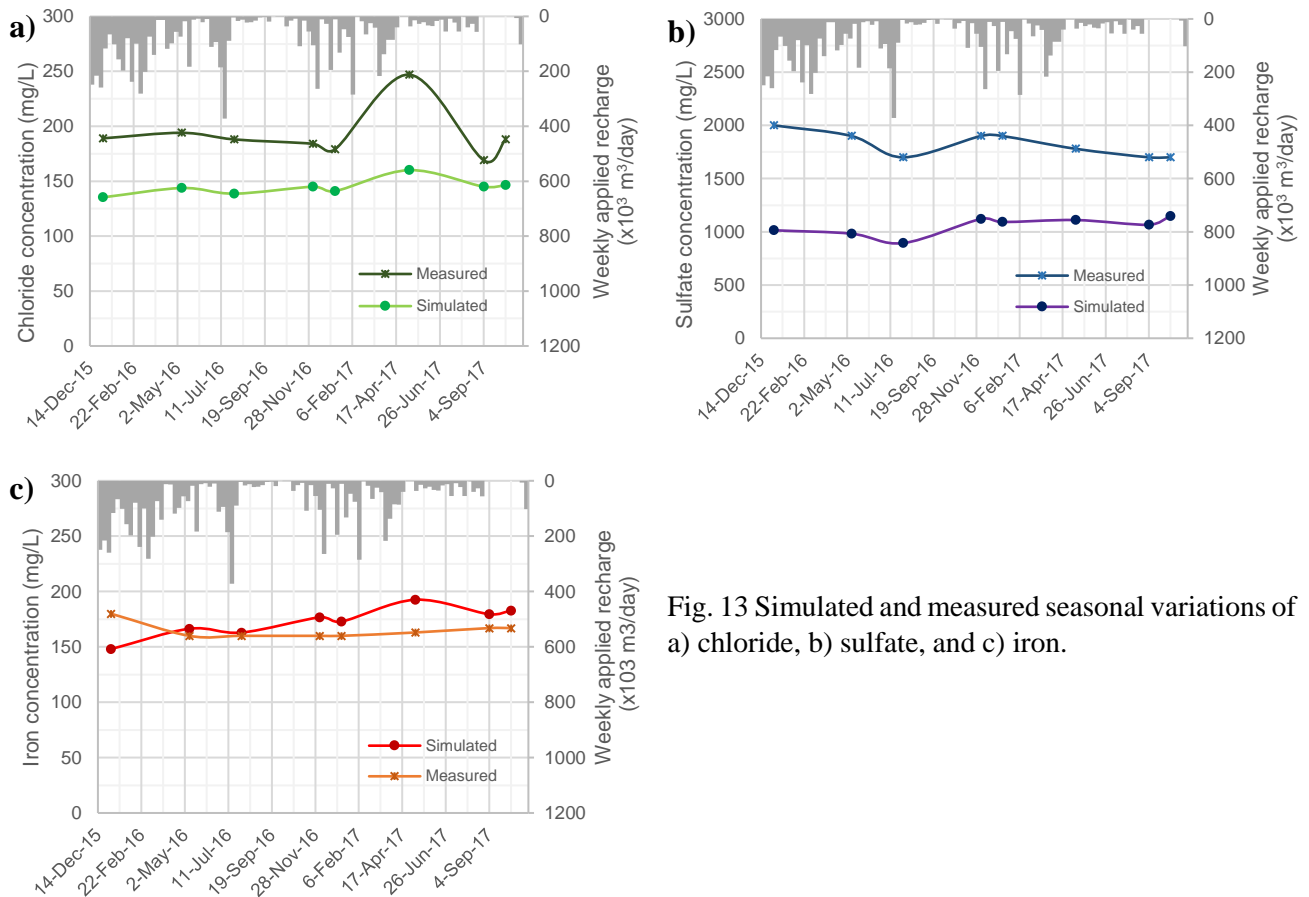


Fig. 13 Simulated and measured seasonal variations of a) chloride, b) sulfate, and c) iron.

Variations to the model setup (case scenarios)

This study simulates four additional scenarios to determine the impact of some uncertain parameters on the discrepancy between simulated and measured ion baselines. For this exercise, sulfate ion concentrations are compared due to its conservative behavior and absence of gypsum precipitation. Each scenario starts from the benchmark setting explained in the methodology and incorporates locally the variation on the parameter. All scenarios then go through steps 1 and 2 described in the simulation section in order to obtain the sulfate discharged concentration for the Dickenberg adit. Particularities of each case scenario are summarized in **Table 4**.

Table 4. Specifications of the different flow, transport and reaction parameters applied to each case scenario.

Case id.	Changed feature from the benchmark setup	Observation/reason
1	Grid simplification to 2 continua	Employment of the original grid discretization used for modeling the flow component of the Westfield (equivalent to a dual continuum model)
2	Fracture density increases to 2 and 3 fractures per 10m-length block	There is no study to the authors' knowledge on fracture density derived from coal mining
3	kinetic rate for pyrite oxidation is decreased 1 order of magnitude ($\log k = 1 \times 10^{-10} \text{ mol m}^{-2} \text{ s}^{-1}$) Reduction of the reactive surface area of the minerals base on a simple cubic packing with 8 spheres of medium sand grains ($A_s = 1600 \text{ m}^2/\text{m}^3$ of medium)	Due to lack of in-situ measurements, lower kinetic and surface area values are tested. Kinetic rate are taken from Xu et al. (2000)

4 Variable pyrite volume in sandstones and anthropogenic waste rock deposits (see **Table SI3** in the Supplementary Information)

Pyrite volume used in the benchmark scenario may be under- or over-estimated as it comes from point counts on thin sections.

There is no mineralogical characterization of the waste rock deposits.

Case scenario 1: Grid with two continua (DCM)

This scenario evaluates the dual continuum grid setup employed in Bedoya-Gonzalez et al. (2022). The comparison of the discharged sulfate between the benchmark scenario and the DCM configuration shows a strong sensitivity to the number of employed continua (Fig. 14a). When only 1 continuum is used for the matrix (i.e., the DC model) pyrite dissolution is strongly underestimated as sulfate concentration increase much slower than when the number of continua is increased to four. The higher anion production of the MINC setup at earlier times is given by the small continua spacing enough to resolve horizontal advection and diffusion gradients of gaseous and dissolved oxygen around the fracture-matrix interface. Only towards the end of the 50-year simulation does the DCM show a relatively good approximation to the benchmark baseline, when production and discharge of sulfate depend on the large volumes of rock in the innermost part of the matrix. The latter process is evident when looking at the similar amounts of average pyrite dissolution of both models (Fig. 14b).

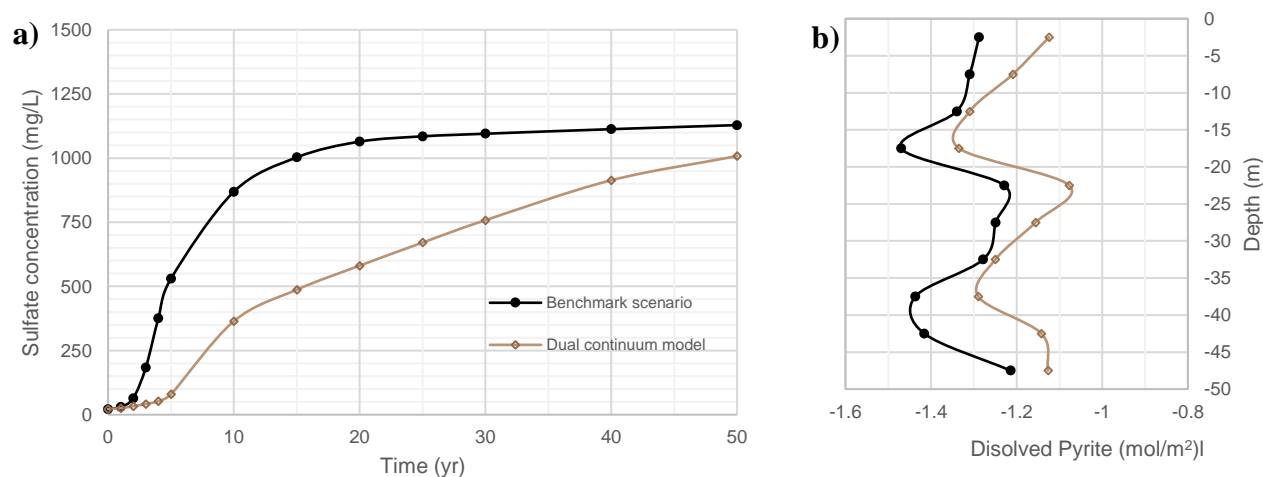


Fig. 14 Comparison between MINC and DC model setup for a) sulfate discharge evolution, and b) pyrite oxidation in one of the model's columns.

Case scenario 2: Higher fracture density

As there is no study to the authors' knowledge dealing with fracture density, continua with 2 and 3 fractures per block were arbitrarily assessed. In both cases simulations show modest variations for sulfate production, which do not exceed 15% compared to the Benchmark setup (Fig. 15a). Likewise, congruencies in pyrite dissolution are observed throughout the sequence among the 3 scenarios (Fig. 15b). The highest values are obtained with the 3-fractures/block scenario, where more matrix is in contact with oxygenated water, generating higher pyrite oxidation and sulfate discharges. Conversely, the number of fractures is found to be inversely proportional to the precipitation of iron hydroxides. Higher fracture densities makes more oxygen available to oxidize the pyrite, generating a relative depletion for precipitating the iron hydroxides. Fig. 15c shows precipitation peaks mainly in the fractured continuum above the shale layers, where less seepage water is absorbed and, therefore, more oxygen is available to carry out the precipitation process.

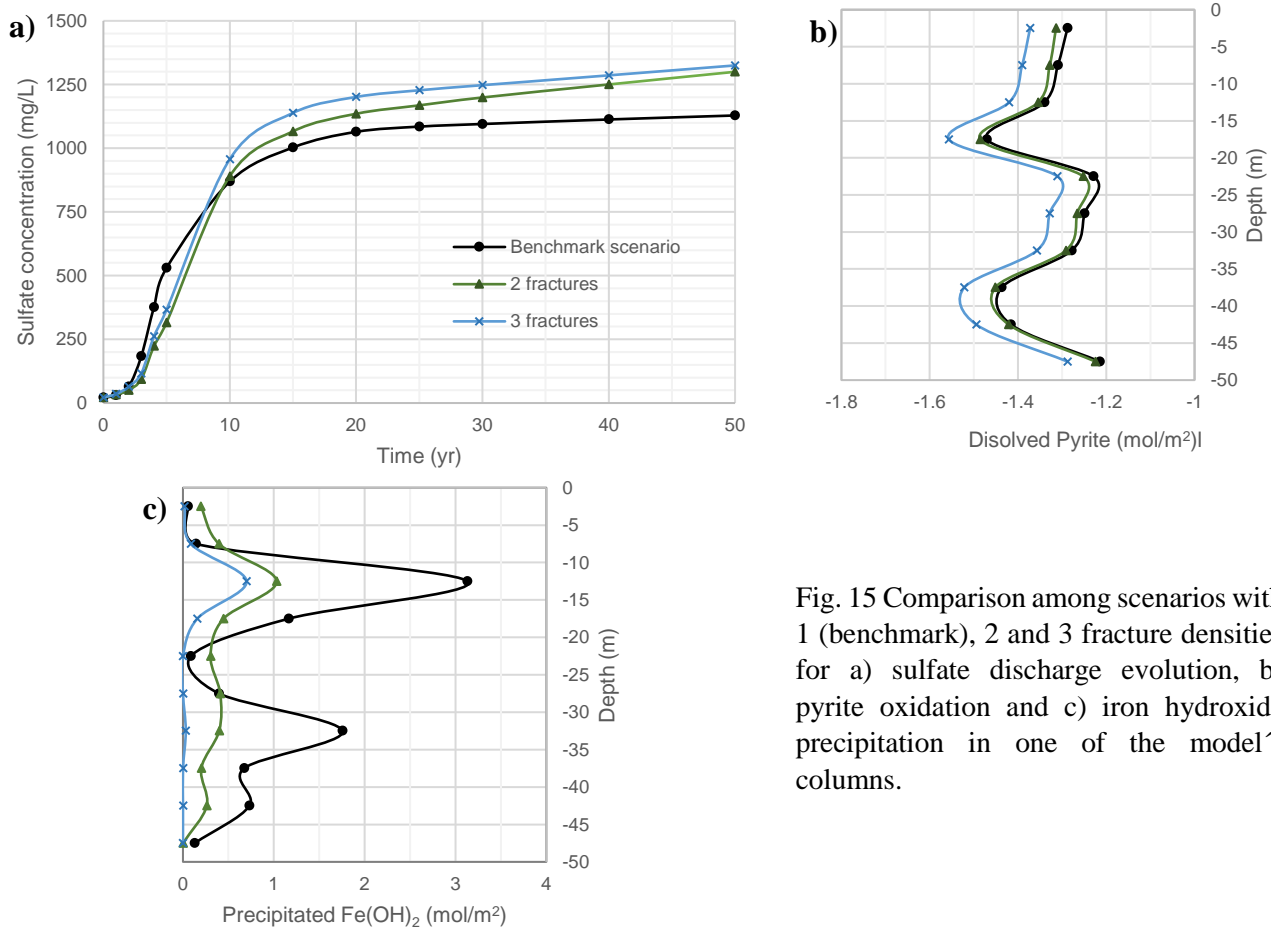


Fig. 15 Comparison among scenarios with 1 (benchmark), 2 and 3 fracture densities for a) sulfate discharge evolution, b) pyrite oxidation and c) iron hydroxide precipitation in one of the model's columns.

Case scenario 3: Pyrite oxidation kinetics and reactive surface area

Given the lower values reported in the literature (e.g., see Williamson and Rimstidt 1994; Nordstrom and Alpers 1997; Xu et al. 2000), this scenario reduce the kinetic rate constant for pyrite oxidation in one order of magnitude. The result is a notable reduction of sulfate discharges compared with the benchmark scenario (Fig. 16a). This indicates that the reaction rate is a sensible parameter in the Westfield primarily because of the constant oxygen supply from the atmospheric boundary. When the latter is turning off, sulfate concentration is almost equal to that assumed for the recharged water since little pyrite can be dissolved only with the oxygen dissolved in the recharge water.

As there is also some uncertainty about the reactive surface area to be used, the present scenario alternatively reduces the reactive surface area of the minerals to 1600 m²/m³ of material. This value was calculated using a simple cubic packing with 8 spheres formed of medium sand grains. Simulation results reveal a decrease in the amount of discharged sulfate, although not in a proportional way. While the surface area is reduced by half with respect to the benchmark, the sulfate concentration is only reduced by 25% (Fig. 16a). This disproportion may indicate a co-dependent sensitivity of the parameter probably linked to the exchange of water and oxygen between the fractured and matrix continua. The latter would be supported by the lower amount of dissolved pyrite at the end of the 50 years simulation (Fig. 16b)

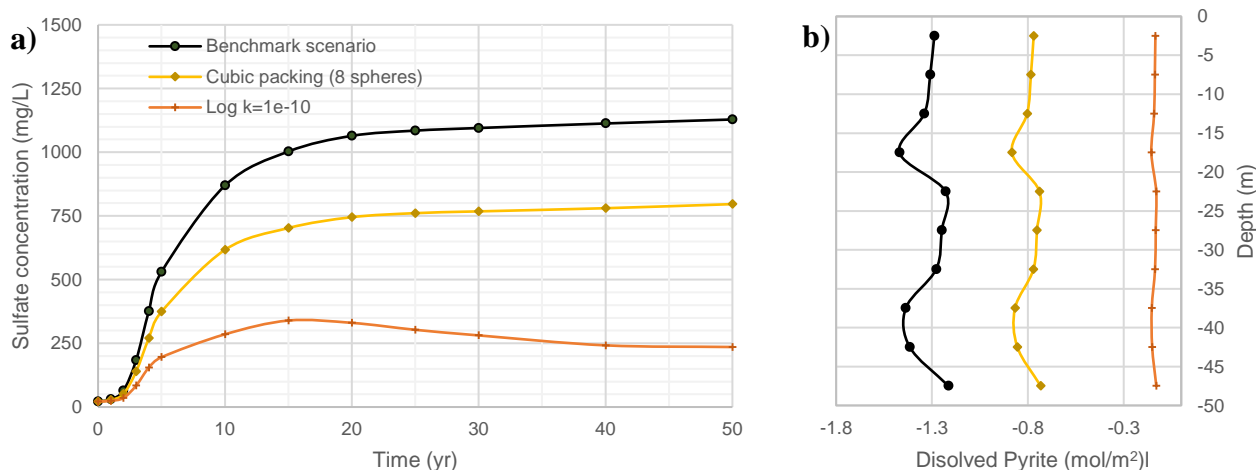


Fig. 16 Comparison between the benchmark setup and scenarios with variable mineral reactive surface area and kinetic rates for a) sulfate discharge evolution and b) pyrite oxidation in one of the model's columns. Log k in mol m⁻² s⁻¹

Case scenario 4: variable pyrite amount in waste rock deposits and sandstones

As mentioned in the setup section, this model includes materials from two different origins: 1) the Carboniferous overburden, composed of sandstones and shales layers; and 2) waste rock deposits derived from mining. In this scenario, pyrite contents in these two domains are changed independently. On the one hand, the sole discharge of the waste deposits (Fig. 17 - markers only) shows strong increases in sulfate concentrations when increasing their initial pyrite content. This would indicate that neither the amount of oxygen nor the oxidation kinetic rate are limiting factors in this zone for pyrite dissolution. The same pyrite increases, however, generate minimal variations in sulfate concentrations at the Dickenberg adit, where water from the entire area is collected (Fig. 17 - solid lines with markers). The sparse areal representation of the waste deposits in the Westfield results in a difference of less than 10% in sulfate concentrations when comparing the benchmark simulation to the scenario with 30% volumetric pyrite.

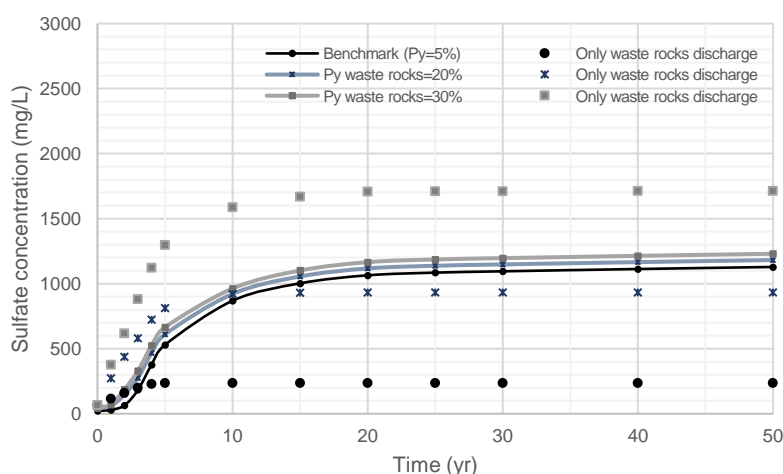


Fig. 17 Comparison of sulfate discharges for scenarios with varying amounts of pyrite in waste rock deposits. The graph shows concentrations recorded at the base of the waste rock deposits (markers only) and in the Dickenberg adit, where water from the entire area is collected (solid lines with markers).

On the other hand, the influence of pyrite variations within the Carboniferous sequence is evaluated through 3 sub-scenarios. In each of them, sandstones' pyrite content is randomly varied within ± 2 standard deviation from the counts reported in Bedoya-González et al. (2021) but maintaining the mean of 5% for the entire column. A fourth sub-scenario with 10% pyrite content per layer is also evaluated in order to include the most extreme case,

with the highest amount of pyrite recorded for the rocks. Details of the amount and distribution of pyrite per layer for each sub-scenario can be found in the **Table SI3** of the Supplementary Information. Fig. 18a shows an overall model insensitivity to heterogeneous pyrite distribution. The opposite occurs when pyrite content is homogeneously increased for the whole area. A doubling of the mineral volume generates a significant increase in sulfate discharge. As with waste rock deposits, the limiting factor for iron and sulfate production deems to be pyrite availability within the first two matrix continua rather than the amount of dissolved oxygen. In fact, oxygen surplus causes iron hydroxide to still precipitate in the sub-scenario with 10% pyrite, although its amount decreases significantly compared to the benchmark setup (Fig. 18c). Finally, Fig. 18b and Fig. 18c depict how the heterogeneous distribution of pyrite in subscenario 1 shifts the dissolution and precipitation peaks observed repeatedly in the previous simulations, although maintaining the same base values. This is also true for sub-scenarios 2 and 3, which are not included in these graphs to improve their readability.

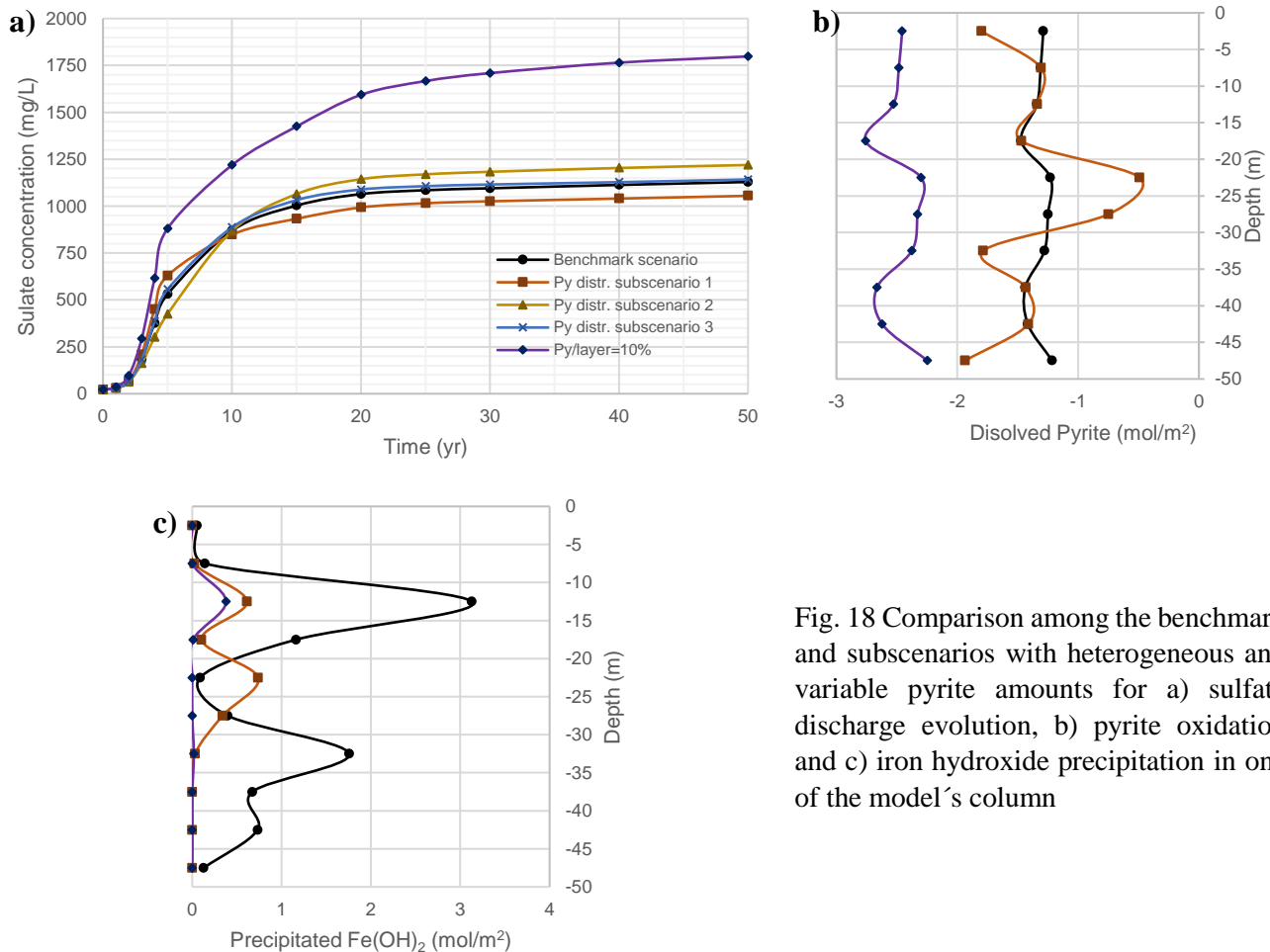


Fig. 18 Comparison among the benchmark and subscenarios with heterogeneous and variable pyrite amounts for a) sulfate discharge evolution, b) pyrite oxidation and c) iron hydroxide precipitation in one of the model's column

Discussion

The construction of a multiple continua model from a dual continuum setup, which in principle is easier to parameterize, proved to be effective for simulating solute transport in the unsaturated overburden of the Westfield. Only the α parameter of the fracture continuum had to be reduced to counteract the strong gradient that arises when shortening the mesh node distances with the new matrix elements. The latter cause an intense fluid mobilization from the fracture to the matrix, which is contrary to reality, as percolated water tend to flow mostly through the fracture network. It is important to note that van Genuchten's α parameter is inversely related to water intake suction for wetting events (Benson et al. 2014). This means that the lower the α value, the higher the water retention within the fractured continuum. Although capillary parameters for fracture networks are not well understood, the values used here are still consistent with the idea of imposing some that reflect the behaviour of a gravel-like medium, as suggested by Bedoya-Gonzalez et al. (2022).

Geochemical simulations further revealed the necessity of extending the DC model to a MINC. It was observed that a model with only two continua cannot reproduce the exchange and movement of oxygen within the matrix, greatly reducing pyrite oxidation in the overburden. Similar drawbacks when characterizing the chemical component of a fractured system using the dual continuum approach have been reported by Lichtner (2000) and Iraola et al. (2019). Both studies reveal under-representations of kinetic reactions with short equilibrium length scales, as well as numerical instabilities due to lack of chemical and flow gradients within the matrix. Thus, dividing each matrix block into a finer grid of nested elements seems to overcome the previously reported limitations. An increase in the number of continua results in greater accuracy when calculating diffusive and advective exchange for a system with two high contrast domains. Results from the benchmark scenario in this study certainly provide a realistic geochemical evolution of the system, even accounting for interaction fronts for pyrite oxidation and iron hydroxide precipitation, as described by Bedoya-González et al. (2020) on drill core samples from the Westfield.

Besides grid extension, the model required the employment of a 5-stage approach to address the limited subsurface information at the beginning of the mining period, many decades ago, and the modification of boundary conditions due to anthropogenic activities. Simulations from stages 1 and 2 yield saturations and water compositions consistent with the development of a water-conductive fracture zone within a moderately permeable overburden. Specifically, dilution fronts of geogenic solutes (chloride water for this study) were formed in both vertical and horizontal directions due to advective and diffusive exchange between the fracture and the matrix elements. This behavior would reevaluate the concept of a single depth-linked salinity gradient for this type of postmining systems. Indeed, application of transient recharge data in stage 5 of the simulation corroborated the interaction and progressive release of solutes in the horizontal component. Typically, intense recharge events in equivalent systems produce major dilution processes that decrease the ion concentration in the discharge. (Whittemore et al. 1989; Robins 1998; Lasagna et al. 2013). In the Westfield chloride concentration shows the opposite behaviour. Higher recharge events cause greater horizontal displacement of meteoric water into the matrix, drawing the locked chloride back into the fractured continuum shortly after. However, over the years, the concentration of chloride in the discharge does tend to decrease due to the depletion of the solute in the matrix.

Results from stages 1 and 2 also showed hydrogen, iron and sulfate discharges congruent with measurements taken at the Dickenberg adit. High concentrations of the 3 ions were produced from a constant pyrite oxidation in the unsaturated zone and promoted by diffusive oxygen supply from the surface (here represented with an atmospheric boundary condition). The relative thinness of the overburden led to constant flow of oxygen through the vertical fractured continuum, being exchanged horizontally with the matrix. The latter process is limited to distances of up to 1.5 m around the fractures mainly due to two factors: 1) matrix permeability restricting dissolved oxygen advection and gas diffusivity and 2) the oxidation rate of pyrite consuming the gas. Therefore, stable ion discharges achieved after 30 years of mining are mostly derived from pyrite dissolution in this rock volume. It was also seen that the amount of gaseous oxygen in this interval governs sulfate variations when time-dependent recharge is applied in the fifth stage. For instance, intense recharge events generate higher water exchanges from the fracture to the matrix, reducing the amount of oxygen to dissolve pyrite. In the case of iron, a flat concentration trend that does not react to variable recharge events is observed. This would be caused by a more complex production of hydroxide from oxygen gas at the lower boundary (i.e., at the discharge point to the adit) than the one considered in this study.

Alternatively to the geogenic interactions, the third and fourth stages of the simulation calculated the influence of the rebound process on the compositions of pore and discharge waters in the unsaturated sequence due to capillary equilibrium. In both stages, the lithological arrangement and water saturation of the overburden (obtained from stages 1 and 2 of the model) were relevant parameters in the quantification of exchanged solute and its vertical transport. For the actual heterogeneous overburden, the suction of a conservative tracer from the rebounded water table was 50 times the initially imposed concentrations per square meter, with a transport up to 15 meters upward. In the case of a homogeneous system composed exclusively of sandstones, the values increase to 80-fold and 20 m respectively. Both estimations represent worst-case scenarios, as the model does not take into account phenomena that would reduce capillary action or contaminant load, such as interruptions in the continuity of the gas phase, reduction of the porous wetting properties, thermodynamic variations or stratification

of the water column by density (e.g. see Costanza-Robinson and Brusseau 2002; Hassanizadeh et al. 2002; Boduroglu and Bashir 2022; Mugova and Wolkersdorfer 2022). Thus, the calculated transport distances correspond to the minimum margin necessary to prevent contaminants from reaching the surface or overlying aquifers. In the Westfield, about 96% of the land surface is above the 15 m. distance, while 92% would be above 20 meters. After 35 years, capillary forces maintain the thicknesses of these intervals although with concentrations of 10 to 20% of the initially exchanged amount owing to the interaction of the percolated water with the matrix continuum. The latter process, in fact, generated a vestigial enrichment of sulfate and iron discharges, which mostly dissipates within 20 years after rebound.

Throughout the 5-stage simulation, the model was able to additionally describe precipitation of iron hydroxide with some accuracy. Out of the 5 continua, the fractured and first 0.5 m of the matrix next to it (i.e., first two matrix continua) presented saturated and oxygenated conditions for their precipitation. This pattern is shown to be consistent with the weathering fronts described by Bedoya-González et al. (2020) for the Westfield sandstone layers, with the exception of fracture-filling hydroxides. The latter discrepancy is understandable considering that mineral precipitation in real open fractures is a complex process that depends on the right amount, size, and arrangement of heterogeneities within the medium to seed the particles (Jones and Detwiler 2016). It has also been found that transport limitation resulting from slow flow velocity, dead-end fractures or isolated structures favours the precipitation of solid phases (Singurindy and Berkowitz 2005; Menefee et al. 2017; Deng and Spycher 2019). Then, the extension and high permeability of mining-derived fractures in the Westfield would be an impediment to solid-phase precipitation. The amount of iron hydroxide that simulations revealed to precipitate within them may have actually been transported as suspended particles into the Dickenberg adit.

Finally, results from four alternative scenarios complemented the findings obtained with the benchmark setting. Although all four gave similar pyrite oxidation fronts in relation to the fractured continuum, iron and sulfate discharges did vary significantly according to the modified criterion. Based on actual Westfield features, equal ion discharges to those recorded in recent years (i.e., 1600 mg/L sulfate and 200 mg/L iron) could be reached by increasing pyrite oxidation rate in less than 1 order of magnitude or at a density of 3 fractures per 10 m. For the first case, the increase could be derived by the action of iron-oxidizing bacteria, as has been widely discussed in the literature (e.g., see Nordstrom 1982, 2011; Johnson 2003; Johnson and Hallberg 2005). Fracture density, on the other hand, is a more complicated parameter to evaluate since, to the authors' knowledge, there is no study that makes an approximation of it. However, Bedoya-González et al. (2022) showed that this fracture density does not significantly affect the flow behaviour of the Westfield, so both chemical and transport simulated components would be consistent with what was measured. Pyrite reactive surface area was also a sensitive parameter, but the value used for the benchmark setting is already high and consistent with the lithologic and hydraulic conditions. Moreover, the use of geometric relationships seems to be a good approximation for regional models due to uncertainties that arise when scaling measurements taken under controlled pH, temperature, and grain size conditions. Lastly, the restricted location of the waste rock deposits rendered the volume of pyrite within them insensitive. The heterogeneous distribution of the mineral in the layered overburden is neither sensitive, although the average value assigned to the entire sequence does.

Conclusions

This study has formulated and applied a multiple interactive continua (MINC) model to characterize advective and diffusive reactive transport processes in fractured post-mining coal zones. The employed approach represents a novel attempt to simulate water-rock interaction compared to commonly employed lumped or equivalent continuum models, as it simultaneously recognizes fracture and porous flow regimes. Its effectiveness was evaluated here by simulating the origin, generation and transport of acid mine drainage within the shallow and fractured overburden of the Ibbenbüren Westfield. The model was constructed by extending a dual continuum model, previously used to calculate the flow component of the zone, to a 5 continua model (1 for the fracture and 4 for the matrix) that accounts for reaction fronts and diffusion through the matrix blocks. Additionally, dissolution, precipitation and dilution processes linked to iron, sulfate and chloride bearing minerals and solutions were included using a 5-stage simulation process. The later was designed to address variations in geochemical and hydraulic conditions derived from the mining history of the area.

Simulation results produced discharges with ion concentrations close to those measured in the Westfield. The horizontal interaction between the formation water contained in the matrix continuum with the percolating water through the fractures would be responsible for the high chloride concentrations measured in the mine adit. This process also results in dilution fronts in both vertical and horizontal directions for solutes initially present in the matrix, generating quasi-stationary discharges over time. Complementary, flow of gaseous oxygen from the atmosphere through the fracture continuum proved to be of great relevance in the study area. Subsequent horizontal diffusive exchange of oxygen with the matrix continua closer to the fractures generates a constant pyrite oxidation that releases high hydrogen, sulfate and iron loads to the water. Such an oxidative process alone would produce the long-term and seasonal concentrations measured in the Westfield, if small modifications in fracture density, oxidation kinetic or mineral surface area are included, none of which affect the flow component of the model. The exception to the good fit between measured and simulated concentrations was the elevated iron and sulfate concentrations measured during the first 10 years after rebound. The difference was evaluated here by simulating the capillary suction of the rebounded mine water from the unsaturated sequence along with its subsequent release. Although the measured values did not match the simulated values, the coincidence in the decrease of the concentrations of both curves would corroborate the existence of a capillary equilibrium between the unsaturated sequence and the rebounded mine water. The latter served to establish and assessing safety levels in the unsaturated overburden by determining maximum concentrations and vertical transport distances of the rebound water during the creation of a capillary fringe. Likewise, it was useful to determine concentrations of long-lasting solutes in the capillary fringe decades after the rebound process.

Acknowledgements

The authors would like to thank Professor Dr. Christoph von Hagke, Moritz Liebl and Nicolas Villamizar at the Department of Environment & Biodiversity, University of Salzburg, for their assistance and advice with the data management and manuscript construction. We thank everybody from RAG Anthrazit Ibbenbüren for facilitating the discharge measurements and providing important insights into mine details. The Landesamt für Natur, Umwelt und Verbraucherschutz Nordrhein-Westfalen (LANUV) is thanked for supplying the precipitation data of the study area. We also thank the anonymous reviewers for their comments and suggestions to improve the manuscript.

Funding

This work was financially supported by the Forum Bergbau und Wasser—FBW.

References

- Acharya BS, Kharel G (2020) Acid mine drainage from coal mining in the United States – An overview. *J Hydrol* 588:125061. <https://doi.org/https://doi.org/10.1016/j.jhydrol.2020.125061>
- Aguilar-López JP, Bogaard T, Gerke HH (2020) Dual-Permeability Model Improvements for Representation of Preferential Flow in Fractured Clays. *Water Resour Res* 56:. <https://doi.org/10.1029/2020WR027304>
- Bain JG, Mayer KU, Blowes DW, et al (2001) Modelling the closure-related geochemical evolution of groundwater at a former uranium mine. *J Contam Hydrol* 52:109–135. [https://doi.org/10.1016/S0169-7722\(01\)00155-3](https://doi.org/10.1016/S0169-7722(01)00155-3)
- Banks D, Younger PL, Arnesen RT, et al (1997) Mine-water chemistry: The good, the bad and the ugly. *Environ Geol* 32:157–174. <https://doi.org/10.1007/s002540050204>
- Bässler R (1970) Hydrogeologische, chemische und Isotopen - Untersuchungen der Grubenwässer im Ibbenbürener Steinkohlenrevier. *Z deutsch geol Ges* 209–286. <https://doi.org/10.1127/zdgg/120/1970/209>
- Becker I, Busch B, Koehrer B, et al (2019) Reservoir Quality Evolution of Upper Carboniferous (Westphalian) Tight Gas Sandstones, Lower Saxony Basin, Nw Germany. *J Pet Geol* 42:371–392. <https://doi.org/10.1111/jpg.12742>
- Becker I, Wüstefeld P, Koehrer B, et al (2017) Porosity and permeability variations in a tight gas sandstone

reservoir analogue, Westphalian D, Lower Saxony basin, NW Germany: influence of depositional setting and diagenesis. *J Pet Geol* 40:363–389. <https://doi.org/10.1111/jpg.12685>

- Bedoya-Gonzalez D, Hilberg S, Redhammer G, Rinder T (2021a) A Petrographic Investigation of the Carboniferous Sequence from the Ibbenbüren Mine: Tracing the Origin of the Coal Mine Drainage. *Minerals* 11:1–19. <https://doi.org/10.3390/min11050483>
- Bedoya-Gonzalez D, Kessler T, Rinder T, Schafmeister M (2022) A dual - continuum model (TOUGH2) for characterizing flow and discharge in a mechanically disrupted sandstone overburden. *Hydrogeol J*. <https://doi.org/10.1007/s10040-022-02507-3>
- Bedoya-Gonzalez D, Kessler T, Schafmeister MT (2021b) Employment Of A Double Continuum Model To Characterize Groundwater Flow In Underground Post-Mining Setups: Case Study Of The Ibbenbüren Westfield. In: Stanley P, Wolkersdorfer C, Wolkersdorfer K (eds) *Mine Water Management for Future Generations*. Cardiff, Wales, United Kingdom (Natural Resources Wales, The Coal Authority, Welsh Government, Cardiff University)., pp 47 – 53
- Bedoya-González D, Rinder T, Hilberg S (2020) Evidences of water-rock interaction in a porous and fractured coalmine overburden - Towards a reactive transport model for coalmine drainage. In: *Grundwasser und Flusseinzugsgebiete : Prozesse, Daten und Modelle*. Fachsektion Hydrogeologie e.V. in der DGGV e.V., pp 193–194
- Benson CH, Chiang I, Chalermyanont T, Sawangsuriya A (2014) Estimating van Genuchten Parameters α and n for Clean Sands from Particle Size Distribution Data. 410–427. <https://doi.org/10.1061/9780784413265.033>
- BGR (2021) Groundwater resources in Germany. In: Bundesanstalt für Geowissenschaften und Rohstoffe. https://www.deutsche-rohstoffagentur.de/EN/Themen/Wasser/grundwasser_deutschland_en.html. Accessed 1 Dec 2021
- Blowes DW, Jambor JL, Appleyard EC, et al (1992) Temporal observations of the geochemistry and mineralogy of a sulfide-rich mine-tailings impoundment, Heath Steele mines, New Brunswick. *Explor Min Geol* 1:251–264
- Blowes DW, Ptacek CJ (2015) Hydrogeochemistry and microbiology of mine drainage: An update. *Appl Geochemistry* 57:3–16. <https://doi.org/10.1016/J.APGEOCHEM.2015.02.008>
- Boduroglu S, Bashir R (2022) Review of Capillary Rise Experiments for Surface-Active Solutes in the Subsurface. *Geotechnics* 2:706–730. <https://doi.org/10.3390/geotechnics2030034>
- Booth CJ (2002) The effects of longwall coal mining on overlying aquifers. *Geol Soc Spec Publ* 198:17–45. <https://doi.org/10.1144/GSL.SP.2002.198.01.02>
- Booth CJ, Bertsch LP (1999) Groundwater geochemistry in shallow aquifers above longwall mines in Illinois, USA. *Hydrogeol J* 7:561–575. <https://doi.org/10.1007/s100400050229>
- Coldewey G, Hollenbeck I, Babilinski S (2018) Abschlussbetriebsplan des Steinkohlenbergwerks Ibbenbüren Anlage 16 - Auswirkungen des Grubenwasseranstiegs im Ostfeld des Bergwerkes Ibbenbüren der RAG Anthrazit Ibbenbüren GmbH. (Final operating plan of the Ibbenbüren hard coal mine Annex 16 - Effects of the increase in mine water in the east field of the Ibbenbüren mine of RAG Anthrazit Ibbenbüren GmbH). Münster, Germany
- Costanza-Robinson MS, Brusseau ML (2002) Air-water interfacial areas in unsaturated soils: Evaluation of interfacial domains. *Water Resour Res* 38:13-1-13–17. <https://doi.org/10.1029/2001wr000738>
- Cravotta CA, Brady K (2015) Priority pollutants and associated constituents in untreated and treated discharges from coal mining or processing facilities in Pennsylvania, USA. *Appl Geochemistry* 62:108–130. <https://doi.org/10.1016/J.APGEOCHEM.2015.03.001>
- Deng H, Spycher N (2019) Modeling Reactive Transport Processes in Fractures. *Rev Mineral Geochemistry* 85:49–74. <https://doi.org/10.2138/rmg.2019.85.3>

- Doumas P, Munoz M, Banni M, et al (2018) Polymetallic pollution from abandoned mines in Mediterranean regions: a multidisciplinary approach to environmental risks. *Reg Environ Chang* 18:677–692. <https://doi.org/10.1007/s10113-016-0939-x>
- Drozdowski G, Dölling M (2018) Elemente der Osning-Störungszone (NW-Deutschland) - Leitstrukturen einer Blattverschiebungszone (Elements of the Osning Fault Zone (NW Germany) - Guiding Structures of a Foliage Displacement Zone.). Geologischer Dienst Nordrhein-Westfalen, Krefeld; Germany
- Elphick JRF, Bergh KD, Bailey HC (2011) Chronic toxicity of chloride to freshwater species: Effects of hardness and implications for water quality guidelines. *Environ Toxicol Chem* 30:239–246. <https://doi.org/10.1002/etc.365>
- Gerke HH, Dusek J, Vogel T, Khne JM (2007) Two-dimensional dual-permeability analyses of a bromide tracer experiment on a tile-drained field. *Vadose Zo J* 6:651–667. <https://doi.org/10.2136/vzj2007.0033>
- Gerke HH, van Genuchten MT (1993) Evaluation of a first-order water transfer term for variably saturated dual-porosity flow models. *Water Resour Res* 29:1225–1238. <https://doi.org/10.1029/92WR02467>
- Glynn P, Brown J (1996) Reactive transport modeling of acidic metal-contaminated ground water at a site with sparse spatial information. *Rev Mineral Geochemistry* 34:377–438
- Gombert P, Sracek O, Koukouzas N, et al (2018) An Overview of Priority Pollutants in Selected Coal Mine Discharges in Europe. *Mine Water Environ* 38:16–23. <https://doi.org/10.1007/s10230-018-0547-8>
- Grundl T, Delwiche J (1993) Kinetics of ferric oxyhydroxide precipitation. *J Contam Hydrol* 14:71–87. [https://doi.org/10.1016/0169-7722\(93\)90042-Q](https://doi.org/10.1016/0169-7722(93)90042-Q)
- Gzyl G, Banks D (2007) Verification of the “first flush” phenomenon in mine water from coal mines in the Upper Silesian Coal Basin, Poland. *J Contam Hydrol* 92:66–86. <https://doi.org/10.1016/j.jconhyd.2006.12.001>
- Hassanzadeh SM, Celia MA, Dahle HK (2002) Dynamic Effect in the Capillary Pressure-Saturation Relationship and its Impacts on Unsaturated Flow. *Vadose Zo J* 1:38–57. <https://doi.org/10.2136/vzj2002.3800>
- Herrmann F, Chen S, Kunkel R, Wendland F (2014) Auswirkungen von Klimaänderungen auf das nachhaltig bewirtschaftbare Grundwasserangebot und den Bodenwasserhaushalt in Nordrhein-Westfalen. (Effects of climate change on the sustainably manageable groundwater supply and the soil water balance in North Rhine-Westphalia.). Jülich, Deutschland
- Herrmann M, Pust J, Pott R (2006) The chemical composition of throughfall beneath oak, birch and pine canopies in Northwest Germany. *Plant Ecol* 184:273–285. <https://doi.org/10.1007/s11258-005-9072-5>
- Huertas FJ, Chou L, Wollast R (1998) Mechanism of kaolinite dissolution at room temperature and pressure : Part 1 . Surface speciation. *Geochim Cosmochim Acta* 62:417–431
- Iraola A, Trincherio P, Karra S, Molinero J (2019) Assessing dual continuum method for multicomponent reactive transport. *Comput Geosci* 130:11–19. <https://doi.org/10.1016/j.cageo.2019.05.007>
- Jankowski J, Spies B (2007) Impact of longwall mining on surface water-groundwater interactions and changes in chemical composition of creek water . XXXV Congr Int Assoc Hydrogeol Groundw Ecosyst 144–145
- Johnson DB (2003) Chemical and microbiological characteristics of mineral spoils and drainage waters at abandoned coal and metal mines. *Water, Air, Soil Pollut Focus* 3:47–66. <https://doi.org/10.1023/A>
- Johnson DB, Hallberg KB (2005) Acid mine drainage remediation options: a review. *Sci Total Environ* 338:3–14. <https://doi.org/10.1016/J.SCITOTENV.2004.09.002>
- Jones TA, Detwiler RL (2016) Fracture sealing by mineral precipitation: The role of small-scale mineral heterogeneity. *Geophys Res Lett* 43:7564–7571. <https://doi.org/10.1002/2016GL069598>
- Klinger C, Rüterkamp P, Eckart M (2019) Abschlussbetriebsplan des Steinkohlenbergwerks Ibbenbüren Anlage 17 - Prognose zur optimierten Wasserannahme nach Stilllegung des Steinkohlenbergwerkes Ibbenbüren (Ostfeld). (Final operating plan of the Ibbenbüren hard coal mine Annex 17 - Forecast for optimized water

intake after closure of the Ibbenbüren hard coal mine (Ostfeld)). Essen, Germany

- Knorr KH, Blodau C (2007) Controls on schwertmannite transformation rates and products. *Appl Geochemistry* 22:2006–2015. <https://doi.org/10.1016/j.apgeochem.2007.04.017>
- Kordilla J, Sauter M, Reimann T, Geyer T (2012) Simulation of saturated and unsaturated flow in karst systems at catchment scale using a double continuum approach. *Hydrol Earth Syst Sci* 16:3909–3923. <https://doi.org/10.5194/hess-16-3909-2012>
- Lasaga AC, Soler JM, Ganor J, et al (1994) Chemical weathering rate laws and global geochemical cycles. *Geochim Cosmochim Acta* 58:2361–2386
- Lasagna M, De Luca DA, Debernardi L, Clemente P (2013) Effect of the dilution process on the attenuation of contaminants in aquifers. *Environ Earth Sci* 70:2767–2784. <https://doi.org/10.1007/s12665-013-2336-9>
- Li L, Peters CA, Celia MA (2006) Upscaling geochemical reaction rates using pore-scale network modeling. *Adv Water Resour* 29:1351–1370. <https://doi.org/10.1016/j.advwatres.2005.10.011>
- Lichtner PC (2000) Critique of dual continuum formulations of multicomponent reactive transport in fractured porous media. In: Faybishenko B, Witherspoon PA, Benson S (eds) *Dynamics of Fluids in Fractured Rock*, Volume 122. The American Geophysical Union, pp 281–298
- Lichtner PC (1992) Time-space continuum description of fluid/rock interaction in permeable media. *Water Resour Res* 28:3135–3155. <https://doi.org/10.1029/92WR01765>
- Lichtner PC (1985) Continuum model for simultaneous chemical reactions and mass transport in hydrothermal systems. *Geochim Cosmochim Acta* 49:779–800. [https://doi.org/10.1016/0016-7037\(85\)90172-3](https://doi.org/10.1016/0016-7037(85)90172-3)
- Lotze F, Semmler W, Kötter K, Mausolf F (1962) *Hydrogeologie des Westteils der Ibbenbürener Karbonscholle (Hydrogeology of the western part of the Ibbenbüren Carboniferous floe.)*, 1st edn. Springer Fachmedien Wiesbaden GmbH., Wiesbaden, Germany
- MacCausland A, McTammany ME (2007) The impact of episodic coal mine drainage pollution on benthic macroinvertebrates in streams in the Anthracite region of Pennsylvania. *Environ Pollut* 149:216–226. <https://doi.org/10.1016/J.ENVPOL.2006.12.030>
- McKnight DM, Feder GL (1984) The ecological effect of acid conditions and precipitation of hydrous metal oxides in a Rocky Mountain stream. *Hydrobiologia* 119:129–138. <https://doi.org/10.1007/BF00011952>
- Menefee AH, Li P, Giammar DE, Ellis BR (2017) Roles of Transport Limitations and Mineral Heterogeneity in Carbonation of Fractured Basalts. *Environ Sci Technol* 51:9352–9362. <https://doi.org/10.1021/acs.est.7b00326>
- Moodley I, Sheridan CM, Kappelmeyer U, Akcil A (2018) Environmentally sustainable acid mine drainage remediation: Research developments with a focus on waste/by-products. *Miner Eng* 126:207–220. <https://doi.org/10.1016/j.mineng.2017.08.008>
- Morin KA, Cherry JA, Dave NK, et al (1988) Migration of acidic groundwater seepage from uranium-tailings impoundments, 1. Field study and conceptual hydrogeochemical model. *J Contam Hydrol* 2:271–303. [https://doi.org/10.1016/0169-7722\(88\)90008-3](https://doi.org/10.1016/0169-7722(88)90008-3)
- Mualem Y (1976) A new model for predicting the hydraulic conductivity of unsaturated porous media. *Water Resour Res* 12:513–522. <https://doi.org/10.1029/WR012i003p00513>
- Mugova E, Wolkersdorfer C (2022) Density stratification and double-diffusive convection in mine pools of flooded underground mines – A review. *Water Res* 214:118033. <https://doi.org/10.1016/j.watres.2021.118033>
- Nieto JM, Sarmiento AM, Olías M, et al (2007) Acid mine drainage pollution in the Tinto and Odiel rivers (Iberian Pyrite Belt, SW Spain) and bioavailability of the transported metals to the Huelva Estuary. *Environ Int* 33:445–455. <https://doi.org/10.1016/J.ENVINT.2006.11.010>

- Nordstrom DK (2011) Mine waters: Acidic to circumneutral. *Elements* 7:393–398. <https://doi.org/10.2113/gselements.7.6.393>
- Nordstrom DK (1982) Aqueous pyrite oxidation and the consequent formation of secondary minerals. *Acid Sulphate Weather* 10:37–56
- Nordstrom DK, Alpers CN (1997) The environmental geochemistry of mineral deposits: Part A. Processes, methods and health issues. *Rev Econ Geol Vol.* 6:325–338
- Palandri JL, Kharaka YK (2004) A Compilation of Rate Parameters of Water-Mineral Interactions Kinetics for Application to Geochemical Modeling. Menlo Park, California, USA.
- Pierini C, Mizusaki AMP, Scherer CMS, Alves DB (2002) Integrated stratigraphic and geochemical study of the Santa Maria and Caturrita formations (Triassic of the Paraná Basin), southern Brazil. *J South Am Earth Sci* 15:669–681. [https://doi.org/10.1016/S0895-9811\(02\)00114-1](https://doi.org/10.1016/S0895-9811(02)00114-1)
- Pruess K (1987) TOUGH User's Guide. 79
- Pruess K (1983) GMINC - A mesh generator for flow simulations in fractured reservoirs. Lawrence Berkeley National Laboratory, University of California, Berkeley, California. <https://doi.org/10.2172/6065621>
- Pruess K, Narasimhan TN (1985) A practical method for modeling fluid and heat flow in fractured porous media. *Soc Pet Eng J* 25:14–26. <https://doi.org/doi:10.2118/10509-PA>
- Pruess K, Oldenburg C, Moridis G (2012) TOUGH2 user's guide, version 2. Earth Sciences Division, Lawrence Berkeley National Laboratory, Berkeley, California
- Ray C, Vogel T, Dusek J (2004) Modeling depth-variant and domain-specific sorption and biodegradation in dual-permeability media. *J Contam Hydrol* 70:63–87. <https://doi.org/10.1016/j.jconhyd.2003.08.009>
- Rinder T, Dietzel M, Stammeier JA, et al (2020) Geochemistry of coal mine drainage, groundwater, and brines from the Ibbenbüren mine, Germany: A coupled elemental-isotopic approach. *Appl Geochemistry* 121:104693. <https://doi.org/10.1016/j.apgeochem.2020.104693>
- Robins NS (1998) Recharge: The key to groundwater pollution and aquifer vulnerability. *Geol Soc Spec Publ* 130:1–5. <https://doi.org/10.1144/GSL.SP.1998.130.01.01>
- Rudakov D V., Coldewey WG, Goerke-Mallet P (2014) Modeling the Inflow and Discharge from Underground Structures within the Abandoned Hardcoal Mining Area of West Field (Ibbenbüren). – In: Sui, Wanghua; Sun, Yajun; Wang C (ed) *An Interdisciplinary Response to Mine Water Challenges*. 12th International Mine Water Association Congress (IMWA 2014). Xuzhou, China, 18-22 August 2014; pp 699 – 705
- Simate GS, Ndlovu S (2014) Acid mine drainage: Challenges and opportunities. *J Environ Chem Eng* 2:1785–1803. <https://doi.org/10.1016/j.jece.2014.07.021>
- Singer PC, Stumm W (1970) Acidic Mine Drainage: The Rate - Determining Step. *Science* (80-) 167:1121–1123. <https://doi.org/10.1126/science.167.3921.1121>
- Singurindy O, Berkowitz B (2005) The role of fractures on coupled dissolution and precipitation patterns in carbonate rocks. *Adv Water Resour* 28:507–521. <https://doi.org/10.1016/j.advwatres.2005.01.002>
- Song L, Li J, Garg A, Mei G (2018) Experimental study on water exchange between crack and clay matrix. *Geomech Eng* 14:283–291. <https://doi.org/10.12989/gae.2018.14.3.283>
- Spießl SM, Prommer H, Licha T, et al (2007) A process-based reactive hybrid transport model for coupled discrete conduit-continuum systems. *J Hydrol* 347:23–34. <https://doi.org/10.1016/j.jhydrol.2007.08.026>
- Steeffel CI, DePaolo DJ, Lichtner PC (2005) Reactive transport modeling: An essential tool and a new research approach for the Earth sciences. *Earth Planet Sci Lett* 240:539–558. <https://doi.org/10.1016/j.epsl.2005.09.017>
- Timpano AJ, Schoenholtz SH, Soucek DJ, Zipper CE (2015) Salinity as a Limiting Factor for Biological Condition in Mining-Influenced Central Appalachian Headwater Streams. *JAWRA J Am Water Resour*

Assoc 51:240–250. <https://doi.org/10.1111/jawr.12247>

- Turek M (2004) Electrodialytic desalination and concentration of coal-mine brine. *Desalination* 162:355–359. [https://doi.org/10.1016/S0011-9164\(04\)00069-4](https://doi.org/10.1016/S0011-9164(04)00069-4)
- Van Der Woud JHA, De Bruyn P. (1983) Formation of Colloidal Dispersions From Supersaturated iron(III) nitrate solutions. i. precipitation of amorphous iron hydroxide. *Colloids and Surfaces* 8:55–78. [https://doi.org/https://doi.org/10.1016/0166-6622\(83\)80072-9](https://doi.org/https://doi.org/10.1016/0166-6622(83)80072-9)
- van Genuchten MT (1980) A Closed-form Equation for Predicting the Hydraulic Conductivity of Unsaturated Soils. *Soil Sci Soc Am J* 44:892–898. <https://doi.org/10.2136/sssaj1980.03615995004400050002x>
- Vöröš D, Řimnáčová D, Medvecká L, et al (2021) The impact of saline mine water on fate of mineral elements and organic matter: The case study of the Upper Silesian Coal Basin. *Chemosphere* 284:131397. <https://doi.org/https://doi.org/10.1016/j.chemosphere.2021.131397>
- Whittemore DO, McGregor KM, Marotz GA (1989) Effects of variations in recharge on groundwater quality. *J Hydrol* 106:131–145. [https://doi.org/10.1016/0022-1694\(89\)90170-4](https://doi.org/10.1016/0022-1694(89)90170-4)
- Williamson MA, Rimstidt JD (1994) The kinetics and electrochemical rate-determining step of aqueous pyrite oxidation. *Geochim Cosmochim Acta* 58:5443–5454. [https://doi.org/10.1016/0016-7037\(94\)90241-0](https://doi.org/10.1016/0016-7037(94)90241-0)
- Wolkersdorfer C, Mugova E, V. D, et al (2022a) Effects of Mining on Surface Water – Case Studies. In: Irvine K, Chapman D, Warner S (eds) *The Encyclopedia of Inland Waters Vol. 4*, 2nd edn. Oxford, UK, pp 210–224
- Wolkersdorfer C, Walter S, Mugova E (2022b) Perceptions on Mine Water and Mine Flooding – an Example from Abandoned West German Hard Coal Mining Regions. *SSRN Electron J* 79:103035. <https://doi.org/10.2139/ssrn.4166727>
- Wüstefeld P, Hilse U, Koehrer B, et al (2017) Critical evaluation of an Upper Carboniferous tight gas sandstone reservoir analog: Diagenesis and petrophysical aspects. *Mar Pet Geol* 86:689–710. <https://doi.org/10.1016/J.MARPETGEO.2017.05.034>
- Xu T, Pruess K (2001) Modeling multiphase non-isothermal fluid flow and reactive geochemical transport in variably saturated fractured rocks: 2. Applications to supergene copper enrichment and hydrothermal flows. *Am J Sci* 301:16–33. <https://doi.org/10.2475/ajs.301.1.34>
- Xu T, Sonnenthal E, Spycher N (2017) TOUGHREACT V3.32 Reference Manual: A Parallel Simulation Program for Non-Isothermal Multiphase Geochemical Reactive Transport, LBNL-DRAFT. 142
- Xu T, Spycher N, Sonnenthal E (2012) TOUGHREACT User's Guide: A Simulation Program for Non-isothermal Multiphase Reactive Transport in Variably Saturated Geologic Media, version 2.0. Lawrence Berkeley <https://doi.org/10.2172/943451>
- Xu T, White SP, Pruess K, Brimhall GH (2000) Modeling of pyrite oxidation in saturated and unsaturated subsurface flow systems. *Transp Porous Media* 39:25–56. <https://doi.org/10.1023/A:1006518725360>
- Younger PL (1997) The longevity of minewater pollution: a basis for decision-making. *Sci Total Environ* 194–195:457–466. [https://doi.org/10.1016/S0048-9697\(96\)05383-1](https://doi.org/10.1016/S0048-9697(96)05383-1)
- Younger PL (2000) Predicting temporal changes in total iron concentrations in groundwaters flowing from abandoned deep mines: A first approximation. *J Contam Hydrol* 44:47–69. [https://doi.org/10.1016/S0169-7722\(00\)00090-5](https://doi.org/10.1016/S0169-7722(00)00090-5)
- Younger PL, Wolkersdorfer C (2004) Mining Impacts on the Fresh Water Environment: Technical and Managerial Guidelines for Catchment-Focused Remediation. In: Younger PL, Wolkersdorfer C (eds). *Mine Water Environ Suppl. Iss:2*–80
- Zhang J, Chen L, Hou X, et al (2021) Multi-isotopes and hydrochemistry combined to reveal the major factors affecting Carboniferous groundwater evolution in the Huaibei coalfield, North China. *Sci Total Environ* 791:148420. <https://doi.org/https://doi.org/10.1016/j.scitotenv.2021.148420>

Supplementary Information (SI)

Mathematical fundamentals of the multiple continua modelling in this paper

Groundwater flow

The implementation of the flow component in this study closely follows that presented in Bedoya-Gonzales et al. (2022) for a dual continuum model (for a detailed description please consult the reference). The model concerns with a flow regime derived from mining-induced fractures and its relationship within porous units. Flow scenarios include isothermal flow conditions, with air and water as phase components. The fractured overburden is represented by a simplified, heterogeneous multiple continua model, with one continuum corresponding to the fracture network and the other four to the matrix. The model assumes Darcy-type fluid flow not only in the matrix but also in the fractures by assuming 2 processes: 1) laminar flow through a network of small conduits and 2) the presence of undisturbed porous layers above the fractured medium that limit the water inflow at the interface. Under these conditions, the EOS 9 module of the software TOUGHREACT simulates the unsaturated flow through 5 sets of Richards' equations (equation 6) solved at the same node. The transfer of water between continua (Γ_{ex}) is derived from their local difference in pressure as well as block size and geometry information (i.e., fracture spacing, number of sets, and shape of matrix blocks).

$$\frac{\partial}{\partial t} \Phi_c \rho S_{e-c} = \text{div} [k_{e-c} \frac{\rho}{\mu} \nabla (P_c^* + \rho g \Delta z)] + \Gamma_{ex} \quad (6)$$

Where ρ and μ are the density and viscosity of water, g is the gravity acceleration, the subscripts c indicate the continuum, Φ is the porosity and the S_e is the effective saturation defined as $S_e = (S - S_{lr}) / (1 - S_{lr})$, with S_{lr} being the residual water saturation. The effective permeability, k_e (m^2), and capillary pressure, P_c^* , are functions directly related with the water saturation of each medium as given by the van Genuchten-Mualem parametric model (Mualem 1976; van Genuchten 1980)

$$k_{e-c} = k_{a-c} S_{e-c}^{0.5} [1 - (1 - S_{e-c}^{1/m_c})^{m_c}]^2 \quad (7)$$

$$P_c^* = \frac{1}{\alpha_c} [S_{e-c}^{-1/m_c} - 1]^{1-m_c} \quad (8)$$

Where k_a is the absolute permeability, and $1/\alpha_c$ (Pa) and m_c are fitting parameters associated with the pore distribution, with $\alpha_c > 0$ and $0 < m_c < 1$. Finally, the transfer term for water (advection only) is defined as

$$\Gamma_{ex} = k_{e-a} \frac{\rho g \beta \gamma}{\mu a^2} (h_f - h_m) \quad (9)$$

Where k_{e-a} is the absolute permeability at the interface, μ_w is the water viscosity, $(h_f - h_m)$ is the head difference between the two media, β is a dimensionless geometry grid factor (3 for rectangular blocks), γ is a dimensionless scaling coefficient usually set to 0.4, and a is the distance between the center of a matrix block and the adjacent fracture (Pruess 1983; Gerke and van Genuchten 1993; Gerke et al. 2007; Kordilla et al. 2012)

Implementation of chemical and solute transport components

TOUGHREACT uses a sequential iteration approach in which the flow equations are solved first to subsequently use fluid velocities and phase saturations for chemical and transport simulations (Xu and Pruess 2001; Xu et al. 2012). Here all chemical species are only subject to transport in the liquid phase, except for oxygen that is transported in both liquid and gas phases. The system includes homogeneous aqueous phase and mineral precipitation/ dissolution reactions. The modelled chemical reactions in liquid and solid phase (equations 10 and 11 respectively) have the general form (Lichtner 1992):



Where the quantities v_{ji} and v_{js} represent the stoichiometric reaction coefficients for liquid and solid phase, A_j are the aqueous primary or basis species, A_i are the secondary aqueous species, and M_s are the minerals. These

reactions take place simultaneously in the fracture and matrix continua. Once geochemical reactions are incorporated, equation 6 can be rewritten as a mass conservation equation for each continuum in the form (Lichtner 2000):

$$\frac{\partial}{\partial t} (\epsilon_c \Phi_c \Psi_{j \rightarrow c}) + \nabla (\epsilon_c \Omega_{j \rightarrow c}) = -\epsilon_c \sum_s^n v_{js} I_{s \rightarrow c} - \Gamma_{j \rightarrow ex} \quad (12)$$

Where the subscript c indicates the respectively continuum and the quantities ϵ , Φ , Ψ , Ω and I refer to the volume fraction, porosity, total concentration of the solute j , total flux of the solute j , and kinetic reaction rate of the mineral m , respectively. Solute exchange between the two continua is defined by a coupling term as (Lichtner 2000):

$$\Gamma_{j \rightarrow ex} = A_{ex} \Omega_{j \rightarrow ex} \quad (13)$$

Unlike pure water flow, $\Gamma_{j \rightarrow ex}$ should consider solute movement due to molecular diffusion at the interface between fracture and matrix continua (A_{ex}). Thus, solute flux (Ω_j) derived from advection and molecular diffusion within and between continua is evaluated as:

$$\Omega_{j \rightarrow c} = q_c \Psi_{j \rightarrow c} - \tau_c \Phi_c D_c \nabla \Psi_{j \rightarrow c} \quad (14)$$

With q being the fluid flow velocity, τ the tortuosity, and D the diffusion coefficient, which is assumed to be the same for all species within each continuum. Under unsaturated conditions, the widely accepted Millington and Quirk model can substitute tortuosity ($\tau_c = \Phi_c^{1/3} S_{e-c}^{10/3}$), making diffusion a more straightforward value to calculate using only the porosity and effective phase saturation of the medium (Pruess et al. 2012). The total solute concentration Ψ_j can be defined relative to the chosen set of primary species with concentrations C_j as (Lichtner 1985):

$$\Psi_{j \rightarrow c} = C_{j \rightarrow c} + \sum_i^n v_{ji} C_{i \rightarrow c} \quad (15) \quad C_{i \rightarrow c} = (\gamma_{i \rightarrow c})^{-1} K_i \prod_j^n (C_{j \rightarrow c} \gamma_{j \rightarrow c})^{v_{ij}} \quad (16)$$

where C_i denotes the concentration of the i th secondary species derived from the concentration of the primary specie C_j , γ_i and γ_j are thermodynamic activity coefficients and K_i is the equilibrium constant. The mineral kinetic reaction rate (I_s) is given by (Lasaga et al. 1994):

$$I_{s \rightarrow c} = \pm k_{s \rightarrow c} A_{s \rightarrow c} |1 - Q_{s \rightarrow c}^\theta|^\eta \quad (17) \quad Q_{s \rightarrow c} = K_s^{-1} \prod_j^n (C_{j \rightarrow c} \gamma_{j \rightarrow c})^{v_{sj}} \quad (18)$$

with positive values indicating dissolution, and negative values precipitation, k_s the kinetic rate constant, A_s the specific reactive surface area of the solid phase, and Q_s the kinetic mineral saturation ratio. The parameters θ and η are experimentally determined but usually set to one. Finally, equilibrium oxygen dissolution to the liquid phase can be expressed as (Xu et al. 2017)

$$PfK = \prod_j^n (C_{j \rightarrow c} \gamma_{j \rightarrow c})^{v_{gj}} \quad (19)$$

Where P is the partial oxygen pressure and f is the gas fugacity coefficient, assumed equal to one for atmospheric pressure when the gaseous phase behave like an ideal mixture.

Grid requirements for Kinetic and Diffusion processes

There is an inherent dependence between reactive processes in heterogeneous media and the scale of discrete, DC or MINC models. The difference that exists between fracture and matrix volumes often introduces significant errors for chemical fast reactions where equilibrium occurs on the order of the pore-scale or microscale (Lichtner 2000; Li et al. 2006; Iraola et al. 2019). The short reaction length, which is generalized to the entire matrix block, leads to a steep gradient at the interface between the two continua (Steeffel et al. 2005). Therefore, regional models should be limited to systems where either the kinetic reaction rate varies smoothly over the matrix block or the characteristic chemical equilibration length scale is long compared to the matrix block size (Lichtner 2000).

Otherwise, fine grid spacing near the fracture-matrix interface is required to adequately capture geochemical gradients (i.e., reaction fronts across the matrix).

A similar space discretization problem arises in the implementation of diffusive flow under multiphase conditions. Fluid and gas exchange at the fracture-matrix interface would be governed by diffusion in the matrix rather than in the fracture due to the relatively large matrix grid size (Pruess 1987; Lichtner 2000). Since there are no documented values for the hydraulic properties at the interfaces, these are set equal to the harmonic mean between the two continua. This forces the local exchange to be dominated by the lower conductive domain (i.e., the matrix), which might be closer to reality (Ray et al. 2004; Song et al. 2018; Aguilar-López et al. 2020). As a result, conservation of diffusive flux across the interface between fracture and matrix continua can be rewritten from equation 14 as:

$$(\tau_{mf} \Phi_{mf} D_{mf})_{harm} = \frac{(d_f + d_m)(\tau_f \Phi_f D_f)(\tau_m \Phi_m D_m)}{d_m(\tau_f \Phi_f D_f) + d_f(\tau_m \Phi_m D_m)} \approx \tau_m \Phi_m D_m \quad (20)$$

The implementation of equation 20 yields a coupling term proportional to the effective matrix diffusivity, which should be independent of the matrix block size. However, large DCM matrix blocks give wrong behaviours. The area of the coupling term between two rectangular elements depends mostly on the half-length of the matrix block:

$$A_{ex} = \frac{(1-\epsilon_f)}{d_{mf}} \quad d_{mf} \approx \frac{x_m}{2} \quad (21)$$

Where d_{mf} is the distance between the nodes of two continua. Evaluating the diffusion component of the coupling term (equation 13) using the harmonic mean (equation 20) and inserting the surface term (equation 21) leads to:

$$\Gamma_{j \rightarrow ex} \approx \frac{(1-\epsilon_f)}{d_{mf}} (\tau_m \Phi_m D_m) \frac{(\Psi_{j \rightarrow f} - \Psi_{j \rightarrow m})}{d_{mf}} \quad (22)$$

From equation 22 it is inferred that the coupling term decreases by the square as the size of the matrix block increases. This behaviour is contrary to that calculated and expected for diffusive flow, so further refinement should be considered to reduce the block size dependence in fractured media models.

Table SI1

Table SI 1 Relationship between the recharge calculated by the Geological Survey of North Rhine-Westphalia and the applied recharge in this study. Daily inputs are obtained by multiplying the daily precipitation by the percentages assigned for each month. Calculated using the data from Herrmann et al. (2014)

Month	LANUV NRW recharge model		Applied recharge		
	(mm/month)	% Precipitation	2015	2016	2017
			% Precipitation		
January	60-80	0.45 - 0.62	0.55	0.50	0.45
February	20-40	0.25 - 0.55	0.40	0.40	0.35
March	20-40	0.25 – 0.56	0.42	0.40	0.40
April	10-20	0.20 – 0.45	0.35	0.35	0.20
May	10-20	0.15 – 0.30	0.25	0.25	0.15
June	10-20	0.10 – 0.40	0.32	0.30	0.15
July	0-10	0.00 – 0.12	0.09	0.09	0.06
August	0-10	0.00 – 0.10	0.08	0.05	0.00
September	5-10	0.05 – 0.16	0.12	0.10	0.00
October	10-20	0.15 – 0.30	0.22	0.20	0.20
November	20-40	0.30 – 0.60	0.50	0.45	0.22
December	40-60	0.55 – 0.85	0.80	0.65	0.50

Table S12

Table S12 Monthly chemical composition of the imposed rainwater for the year 2016 and 2017 during the stage 5. Concentrations are given in mg/L. Calculated using the data from Herrmann et al. (2006)

	Original	Avg. recharge Germany	Jan.	Feb.	Mar.	Apr.	May	Jun.	Jul.	Aug.	Sep.	Oct.	Nov.	Dec.
Recharge %	1	0.3	0.5	0.4	0.4	0.35	0.25	0.3	0.09	0.05	0.1	0.2	0.45	0.65
pH	5.5	4.4	4.6	4.5	4.5	4.5	4.3	4.4	3.9	3.7	4.0	4.2	4.6	4.7
Na ⁺	0.7	2.4	1.5	1.8	1.8	2.1	2.9	2.4	8.1	14.6	7.3	3.7	1.6	1.1
K ⁺	0.1	0.4	0.3	0.3	0.3	0.4	0.5	0.4	1.4	2.6	1.3	0.7	0.3	0.2
Mg ²⁺	0.2	0.5	0.3	0.4	0.4	0.4	0.6	0.5	1.7	3.0	1.5	0.8	0.3	0.2
Ca ²⁺	0.5	1.7	1.0	1.3	1.3	1.4	2.0	1.7	5.6	10.0	5.0	2.5	1.1	0.8
Al ³⁺	0.0	0.0	0.0	0.0	0.0	0.0	0.0	0.0	0.1	0.1	0.1	0.0	0.0	0.0
Fe ^{2+/3+}	0.0	0.1	0.0	0.1	0.1	0.1	0.1	0.1	0.2	0.4	0.2	0.1	0.0	0.0
Cl ⁻	3.5	11.7	7.0	8.8	8.8	10.0	14.0	11.7	38.9	70.0	35.0	17.5	7.8	5.4
HCO ₃ ⁻	0.1	0.3	0.2	0.3	0.3	0.3	0.4	0.3	1.1	2.0	1.0	0.5	0.2	0.2
SO ₄ ²⁻	6.2	20.5	12.3	15.4	15.4	17.6	24.6	20.5	68.3	123.0	61.5	30.8	13.7	9.5
SiO _{2(aq)}	1.0	3.3	2.0	2.5	2.5	2.9	4.0	3.3	11.1	20.0	10.0	5.0	2.2	1.5
O _{2(aq)}	10.0	10.0	10.0	10.0	10.0	10.0	10.0	10.0	10.0	10.0	10.0	10.0	10.0	10.0

Table S13

Table S13 Random distribution of pyrite per sandstone layer within the overburden in each of the 3 sub-scenarios modeled in the case scenario n°4.

Pyrite average (%)		5		
N° of sandstones layers		11		
Max limit (+2 standard deviation)		9		
Lower limit (-2 standard deviation)		2		
Sandstone #	Id layer software	Random pyrite concentrations (%)		
		Sub-scenario 1	Sub-scenario 2	Sub-scenario 3
Layer 1	8, 9	4	6	4
Layer 2	A	6	6	2
Layer 3	B	4	2	8
Layer 4	C	4	7	3
Layer 5	D	7	7	3
Layer 6	E	5	7	5
Layer 7	F	5	4	9
Layer 8	H	2	8	8
Layer 9	I	3	4	2
Layer 10	J	7	4	5
Layer 11	M	8	2	6
Shale layers	G, K, L	5	5	5

Chapter 5: Geochemistry of coal mine drainage, groundwater, and brines from the Ibbenbüren mine, Germany: a coupled elemental- isotopic approach

Rinder, T.¹, Dietzel, M.², Stammeier, J.A.^{2,3}, Leis, A.⁴, Bedoya-González, D.^{1,5}, & Hilberg, S.¹

¹ Department of Geography and Geology, University of Salzburg, Hellbrunner Str. 34, 5020 Salzburg, Austria.

² Institute of Applied Geosciences, Graz University of Technology, Rechbauerstraße 12, 8010, Graz, Austria

³ GFZ German Research Centre for Geosciences, Telegrafenberg, 14473, Potsdam, Germany

⁴ JR-AquaConSol GmbH, Steyrergasse 21, 8010, Graz, Austria

⁵ Institute for Geography and Geology, University of Greifswald, Friedrich-Ludwig-Jahn Str. 17a, 17487 Greifswald, Germany.

Published in: Applied Geochemistry Journal (2020), Vol. 121, 104693.

<https://doi.org/10.1016/j.apgeochem.2020.104693>



Geochemistry of coal mine drainage, groundwater, and brines from the Ibbenbüren mine, Germany: A coupled elemental-isotopic approach

Thomas Rinder^{a,*}, Martin Dietzel^b, Jessica A. Stammer^{b,c}, Albrecht Leis^d,
Diego Bedoya-González^{a,e}, Sylke Hilberg^a

^a University of Salzburg, Department of Geography and Geology, Hellbrunner Str. 34, 5020, Salzburg, Austria

^b Graz University of Technology, Institute of Applied Geosciences, Rechbauerstraße 12, 8010, Graz, Austria

^c GFZ German Research Centre for Geosciences, Telegrafenberg, 14473, Potsdam, Germany

^d JR-AquaConSol GmbH, Steyrergasse 21, 8010, Graz, Austria

^e University of Greifswald, Institute for Geography and Geology, Friedrich-Ludwig-Jahn Str. 17a, 17487, Greifswald, Germany

ARTICLE INFO

Editorial handling by Prof. M. Kersten

Keywords:

Coal mine drainage
Pyrite oxidation
Brine origin
Sulfur isotopic composition
Isotope proxies
Hydrogeochemistry

ABSTRACT

A coupled elemental-isotopic approach is applied to reconstruct the origin and chemical evolution of mine drainage, groundwater, and brines from the Carboniferous anthracite coal mine in Ibbenbüren, Germany. All solutions are characterized by an increase in salinity with depth, as well as by an increase in ³⁴S/³²S isotopic ratios of dissolved SO₄²⁻. Br/Cl and Na/Cl ratios in deep Na-Cl-type water indicate halite dissolution as the common source of salinity. δ³⁴S_{SO4} values increase up to +21.1‰ (VCDT), linking the salinity to the migration of groundwater from the surrounding Mesozoic sediments. ⁸⁷Sr/⁸⁶Sr ratios between 0.7108 and 0.7135 and elevated alkali concentrations indicate ongoing water-rock interaction of the evaporite-derived brines with the Carboniferous siliciclastic rocks of the mine. A positive correlation of ⁸⁷Sr/⁸⁶Sr ratios with δ²H_{H2O} and δ¹⁸O_{H2O} values suggests mixing of the brines with isotopically heavy formation water within the Carboniferous bedrock. The oxidation of pyrite is the dominant sulfate source in shallow mine drainage and groundwater with a relatively low ionic strength (I < 0.035), as indicated by δ³⁴S_{SO4} values between -8.3 and +0.3‰ (VCDT). Intermediate water compositions are the result of the dilution of brines with shallow water. In any case, modern meteoric water with δ¹⁸O_{H2O} values between -6.9 and -8.65‰ (VSMOW) is the primary water source for brines, groundwater, and mine drainage.

1. Introduction

Coal mine drainage is often characterized by poor water quality, i.e. by low pH values, high concentrations of dissolved toxic metal ions, and high salinity, posing environmental risks for the receiving streams. When groundwater has to be pumped from a mine to allow excavation, this high salinity may become an environmental issue (Banks et al., 1997; Timpano et al., 2015; Turek, 2004), as it may cause toxicity to freshwater communities (e.g. Cañedo-Argüelles et al., 2013; Elphick et al., 2011; Hart et al., 1991). Sulfide mineral weathering can lead to the formation of acid mine drainage solutions (Galán et al., 2003; Neal et al., 2005; Nieto et al., 2007). Low pH (Simate and Ndlovu, 2014) and relatively high sulfate concentrations (Wang et al., 2016) caused by sulfide mineral dissolution may have adverse toxicological effects on freshwater communities. In particular, clogging of the riverbed by the

formation of hydrous ferric oxides has a negative effect on the flora and fauna of the affected rivers (MacCausland and McTammany, 2007; McKnight and Feder, 1984; Scullion and Edwards, 1980). Toxic metal ions are an additional risk for aquatic ecosystems in the receiving water bodies. High loads of dissolved metal ions are often connected to the mining of sulfidic ores. In addition coal mine drainage in several places in Europe (Gombert et al., 2018) or the United States (Cravotta and Brady, 2015) may also carry relevant levels of toxic metals, often related to pyrite oxidation.

A number of passive and active remediation strategies are available, including microbial reduction of sulfate in constructed wetlands, and the addition of lime (Gazea et al., 1996; Johnson and Hallberg, 2005; Wolkersdorfer, 2008). Increasing attention is being devoted not only to avoiding or mitigating the negative environmental effects, but also to recovering and reusing resources deriving from the drainage (Moodley

* Corresponding author.

E-mail address: Thomas.rinder@sbg.ac.at (T. Rinder).

<https://doi.org/10.1016/j.apgeochem.2020.104693>

Received 10 March 2020; Received in revised form 9 July 2020; Accepted 13 July 2020

Available online 31 July 2020

0883-2927/© 2020 The Author(s). Published by Elsevier Ltd. This is an open access article under the CC BY license (<http://creativecommons.org/licenses/by/4.0/>).

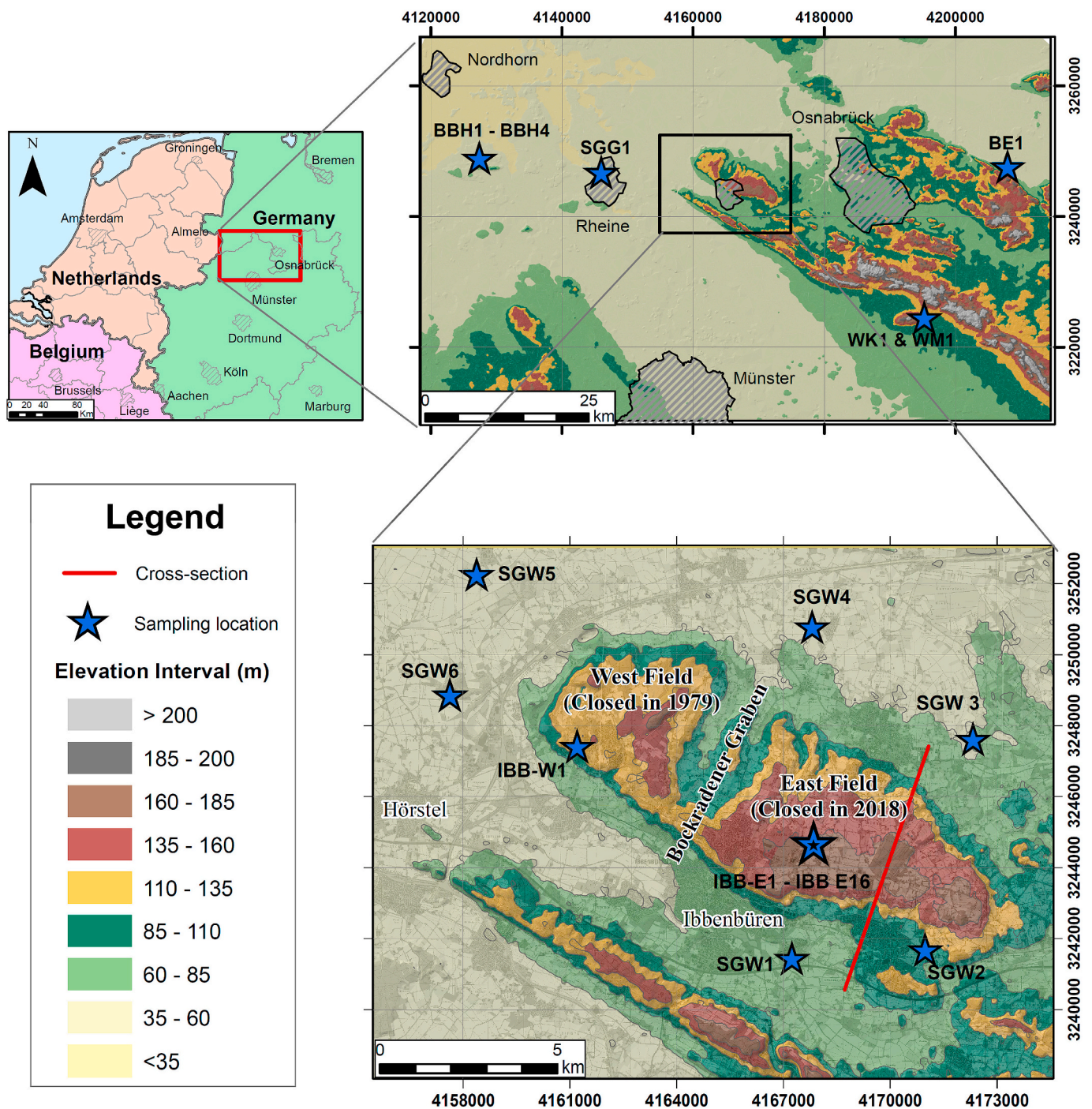


Fig. 1. Location of the Ibbenbüren coalfield. The Carboniferous blocks of the coalfield are divided by faults along the Bockradener Graben. Mining in the Westfield closed in 1979, whereas mining in the Eastfield continued until December 2018. The red line denotes the position of the cross section in Fig. 11. Modified after European Digital Elevation Model (EU-DEM), version 1.1. (For interpretation of the references to color in this figure legend, the reader is referred to the Web version of this article.)

et al., 2018; Naidu et al., 2019; Simate and Ndlovu, 2014). In any case, the design and operation of a suitable remediation process needs to be based on a solid hydrogeochemical model. However, the drainage quality is often predicted solely on the basis of a standard procedure (Dold, 2017; Parbhakar-Fox and Lottermoser, 2015).

Currently, at the anthracite mine in Ibbenbüren, an estimated volume of 15 million m³ of mine drainage enters the receiving stream each year, contributing between 61 and 80% of the total annual chloride load (MKULMV, 2016), frequently exceeding the threshold values considered harmful for freshwater ecosystems. With the mine closure in December

2018, the long-term liabilities related to the discharge of mine drainage from the abandoned mine are in public focus. Currently, the coal mine drainage causes highly saline brines, rich in iron and sulfate. The aim of this study is to examine the relevance of the individual processes of water-rock interaction for the overall chemical composition of the mine drainage solutions. This is essential in order to facilitate the prediction of the future long-term development of the water quality. Towards this goal, a sampling campaign of waters from the active mine as well as the surrounding areas was conducted. Samples were interpreted with respect to main and trace element compositions as well as to the isotope

ratios $^{34}\text{S}/^{32}\text{S}$ and $^{18}\text{O}/^{16}\text{O}$ in sulfate, $^{18}\text{O}/^{16}\text{O}$ and $^2\text{H}/^1\text{H}$ in H_2O , and $^{87}\text{Sr}/^{86}\text{Sr}$ in the dissolved Sr.

On the basis of the acquired data, the dominant reaction mechanisms are identified, and a conceptual model for the chemical evolution of the coal mine drainage solution and the groundwater of the coal mine is developed.

2. Geological setting and sampling location

The first document mentioning the mining of anthracite hard coal from the Ibbenbüren mining region dates back to 1564. In the nearby Piesberg quarry, documents reach further back, to 1461. The cumulative mass of anthracite coal extracted since the beginning of the mining operations is approximately 240 million tons. Historically, the room-and-pillar mining has been an important method. However, since the 1940s, the excavation has been carried out by longwall mining. The depth of the deepest coal seam excavated before the closure of the mine was approximately 1500 m below surface. The mine closed in December 2018 and is now being flooded.

The coalfield, known as the “Ibbenbürener Karbonscholle”, is a horst structure of Carboniferous origin, which was brought up to the surface by uplift in the Cretaceous. As a result, the coalfield is separated from the surrounding area with an offset of up to 2000 m. It consists of two hills (Schafberg and Dickenberg) divided by a NNE-SSW striking graben structure known as the Bockradener Graben (see Fig. 1). The hill chain is surrounded by Triassic, Jurassic, and, to a lesser extent, Permian rock formations in the direct vicinity of the fault structure, surrounding the block. The chain reaches a maximum height of 176 m above sea level, with a length of 14 km and a width of 4–5 km (Bässler, 1970). During mining operations, the Schafberg and Dickenberg were named “Eastfield” and “Westfield”, respectively.

The Carboniferous rocks of the Ibbenbüren coalfield represent the northwesternmost outcrops of the Paleozoic layers in Germany. These layers outcrop again in the Ruhr area, about 90 km South of Ibbenbüren. The slightly north dipping coal seams of the Ruhr area disappear under the sediments of the Münsterland Cretaceous basin to outcrop again in the Ibbenbüren area before being buried under younger sediments in the North German Basin. Although the same coal seams can be identified in both mining regions, the coal produced in Ibbenbüren is classified as anthracite coal. Therefore, it is of significantly higher quality than the hard coal of the Ruhr area. The reason for this higher coalification is still being debated, with two different hypotheses being developed. One theory connects the high coalification to an igneous intrusion in the late Cretaceous, the so-called Bramscher massif. Recently, however, an increasing number of publications suggest that a deep burial during the early Cretaceous seems more likely (Bruns et al., 2013; Bruns and Littke, 2015; Muñoz et al., 2007; Senglaub et al., 2005).

The coal seams within the deposit dip to the North with an angle of 3–25°. The main lithologies are sandstone, siltstone, claystone, and conglomerate. Kaolinite and illite have been reported as the main matrix components in the Pennsylvanian sandstone of the region, which was classified as sub-lithic arenites with low volumes of feldspar grains and muscovite (Wüstefeld et al., 2017). Upper Jurassic halite, gypsum, and anhydrite-bearing formations border with the coalfield and are associated with subsorption phenomena, e.g. the development of sinkholes in the nearby “Heiliges Feld” (Dölling and Strizke, 2009). Halite has also been detected in the Triassic sediments but not in the Permian rocks surrounding the area.

The hydrogeological situation has been discussed in detail, for instance, by Bässler (1970) and Lotze et al. (1962). In general, the Eastfield and the Westfield present different situations, due to the different mining depth as well as to differences in the Quaternary upper layer.

Mining in the Westfield was abandoned in 1979, and flooding was induced. Mining was concentrated close to the surface down to about –170 m below surface, whereas mining in the Eastfield continued to a

depth of approximately –1500 m below surface. Today, the water of the Westfield is entering the Dickenberg gallery (sample IBB-W 1), from where it is brought to a water treatment plant with settling ponds before entering the receiving stream (Ibbenbürener Aa). During active mining, the quantification of the groundwater discharge showed that infiltration from the top of the coalfield alone cannot explain the amount of mine water drainage (Lotze et al., 1962). However, after the rise of the groundwater table above the surrounding aquifers, the inflow from these aquifers can be ruled out (Rudakov et al., 2014).

In the Eastfield, mine water was still pumped at the time of sampling. The mine drainage comprises deep saline brines as well as relatively fresh meteoric waters close to the surface. Mine dewatering is carried out through a central point of discharge from where the water runs through an adit into settling ponds before entering the Ibbenbürener Aa.

Above the Eastfield and the Bockradener Graben, a Quaternary layer of up to 30 m in thickness bears groundwater. Above the Westfield, this layer is less developed; groundwater from this layer was diverted into deeper levels due to mining activities. The same is true for surface streams which are at least periodically water-bearing above the Eastfield but not above the Westfield anymore. Below the first groundwater level, the Carboniferous sandstones themselves form the most important aquifer.

Faults that are striking NNE-SSW through both parts of the coal field often reach into the Mesozoic surrounding areas. They are considered to be important for the regional hydrogeological situation, providing preferential flow paths for water entering into the coal field. The most prominent fault system – the Bockradener Graben – divides Eastfield and Westfield with an offset of up to 510 m (Bässler, 1970). The offset of the faults within the coalfields reaches values of 20–200 m. Historically, large water inflows have been related to fault systems. In general, the faults provide a flow path down to at least –600 to –700 m, where a compressive tectonic regime starts to lower the permeability. Along these faults, meteoric water can easily infiltrate into the mine. In fact, Bässler (1970) noted a temporal correlation of rainfall and discharge of mine drainage. He also noted that together with mining activities, these meteoric waters move down.

The influence of meteoric water was however limited to the upper levels of the mine, and when Bässler (1970) carried out his sampling campaign, the lowest level at that time (–900 m) did not seem to be influenced by meteoric water. With depth, the water discharge was increasingly correlated with mining activities, and was temporarily increasing when the exploitation of new areas led to the outflow of formation water. Bässler (1970) reported a porosity of the sandstones between 15 and 5% together with a permeability generally below 1 mD (millidarcy). While the low permeability of the sandstones would normally inhibit dewatering, the failure of the overburden related to longwall mining creates enough fractures to allow a temporal water-flow. The calculated age of these formation waters based on Tritium and Carbon-14 analyses was >34,000 years in some cases.

3. Methodology

Samples were taken during two different campaigns in summer 2018. Electrical conductivity, dissolved oxygen, temperature, and pH were measured *in-situ* with a WTW 350i multimeter. Redox values were measured with a Lovibond SD60. The German legislation concerning explosion protection in coal mines does not allow the use of electronic devices, so that *in-situ* measurements inside the mine were not possible (solutions IBB-E 1 to IBB-E 16). As a workaround, a gastight bottle (DURAN 150 ml) was used for sampling, and measurements were carried out within 5 h after sampling. All samples were filtered through 0.45 µm regenerated cellulose filters and stored in (i) gastight Duran glass bottles (150 ml) for alkalinity measurements, and (ii) prewashed 125 ml HDPE Nalgene bottles for chemical analyses. Samples for cation analyses were acidified down to pH ≈ 2 with concentrated HNO_3 (Merck ultrapure). The samples were placed in a cooling box and transferred to

the laboratory for measurements. Alkalinity was measured *in-situ* by colorimetry using an Aqualytic AL800 photometer. Ion chromatography and ICP-OES measurements were determined at the Graz University of Technology, Austria. The concentrations of dissolved cations (Na^+ , K^+ , Mg^{2+} , Ca^{2+}) and anions (Cl^- , NO_3^- , SO_4^{2-} and Br^-) were determined by ion chromatography with a Dionex ICS-3000. Chemical analyses of the trace elements were carried out with an ICP-OES (Perking Elmer) with analytical precision better than $\pm 5\%$ based on replicate analyses of the selected samples ($n = 2$). Strontium isotope ratios were determined at the NAWI Graz Central Lab Water, Minerals and Rocks at the Graz University of Technology, Austria. Strontium was separated using a Sr-specific extraction chromatographic resin (Sr spec (T)) using 3 mol l^{-1} HNO_3 . Isotopic ratios were determined on a Plasma 2 MC-ICP-MS (Nu instruments, Wrexham, UK). Measurements were performed with a static cup configuration in wet-plasma mode. Instrumental mass fractionation was corrected for within-run following an exponential law and assuming $^{86}\text{Sr}/^{88}\text{Sr} = 0.1194$. Krypton interferences were corrected for, using a value of $^{86}\text{Kr}/^{84}\text{Kr} = 0.30354$. The baseline was determined prior to each sample analysis for 120 s on-peak, aspirating a blank solution. The reference material NBS 987 was $^{87}\text{Sr}/^{86}\text{Sr} = 0.71026 \pm 0.00002$ (2 SD, $n = 15$). The total procedural blank was $< 0.5 \text{ ng Sr}$ and thus negligible. For analytical details see [Stammeier et al. \(2019\)](#). The isotopic composition of high saline waters was measured by classic isotopic equilibration techniques using the H_2 -water equilibration method for hydrogen ([Horita, 1988](#)) and the CO_2 -water equilibration technique for oxygen ([Epstein and Mayeda, 1953](#)). The IRMS measurements were done with a Finnigan DELTAplus Mass Spectrometer coupled to a fully automated equilibration device adapted from [Horita et al. \(1989\)](#). The isotope values of less mineralized waters were analyzed by wavelength-scanned cavity ring-down spectroscopy (WS-CRDS) using a Picarro L1102-i system. The analytical procedure of the WS-CRDS measurements is similar to that described by [Brand et al. \(2009\)](#). Typical analytical precisions (1σ) were $\pm 1\%$ for $\delta^2\text{H}_{\text{H}_2\text{O}}$ and $\pm 0.08\%$ for $\delta^{18}\text{O}_{\text{H}_2\text{O}}$, and the values were referenced relative to the Vienna Standard Mean Ocean Water (VSMOW). The analysis of $^{34}\text{S}/^{32}\text{S}$ ratios in sulfate was carried out at Imprint Analytics GmbH (Neutal, Austria) using an Eurovector elemental analyzer coupled with a NU Horizon IRMS following the method described in [Révész et al. \(2012\)](#). Measurements were carried out using an in house reference material which was calibrated against IAEA-S-2 with a mean $\delta^{34}\text{S}_{\text{SO}_4}$ of $+22.62 \pm 0.16\%$ and IAEA-S-3 with $-32.49 \pm 0.16\%$. $^{18}\text{O}/^{16}\text{O}$ ratios were determined by the same lab with a Hekatech TCEA coupled to the NU Horizon IRMS. The in house reference material was calibrated against USGS34 and IAEA-NO3 with mean $\delta^{18}\text{O}$ values of $+27.9 \pm 0.6\%$ and $+25.6 \pm 0.4\%$, respectively. The isotopic analyses of sulfur and oxygen in sulfate and hydrogen and oxygen in water were reported in the δ -notation relative to a standard (VCDT for sulfate, V-SMOW for oxygen and hydrogen). Tritium measurements were carried out by liquid scintillation after electrolytic enrichment at Hydroisotop GmbH (Schweitenkirchen, Germany). The computer code PHREEQC ([Parkhurst and Appelo, 1999](#)) with the database wateq.dat was used for hydro-geochemical modelling. For solutions with ionic strength above 1, the thermodynamic calculation was done using the Pitzer.dat database, based on recommendations from [Appelo and Postma \(2005\)](#). Pitzer.dat was also used for calculating seawater evaporation trends in [Fig. 4a to d](#). Depth data herein are given as distances to the highest point of water discharge, i.e. the reference point IBB-E-8. This is the sampling point of cumulative drainage outflow of the Eastfield just before the water reaches the surface, and lies 85 m above normal zero.

4. Results and discussion

4.1. Water types

The 31 sampled solutions cover a wide range of total dissolved solids, from values $< 1000 \text{ mg/kg}$ for the shallow groundwater surrounding the

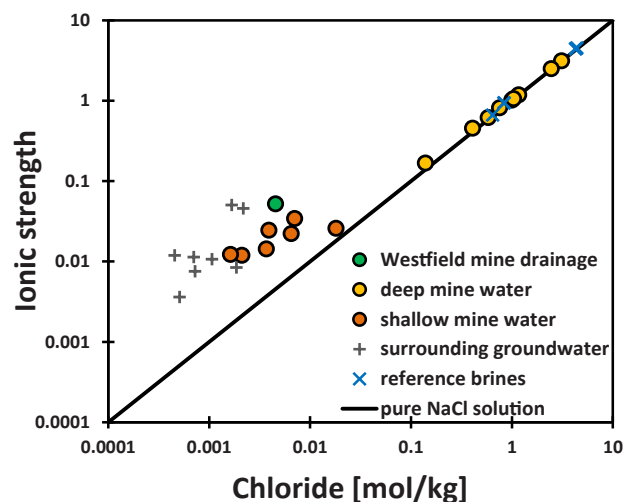


Fig. 2. Chloride concentration [mol/kg] versus ionic strength. Increasing salinity is accompanied by an increasing percentage of sodium chloride in total salinity. The black line represents a pure NaCl (1:1) solution. Solutions plotting above this line indicate a higher fraction of divalent ions contributing to total salinity.

coalfield up to a maximum of 182,000 mg/kg for a brine sample from the deepest levels of the coalfield. Based on these characteristics, the main chemical composition, and the geographical location (see [Fig. 1](#)) of the sampling points, the samples were divided into 5 different types (see [Figs. 2 and 3](#) for identification, and [Table S1](#) (Supplementary Material)). Solution IBB-W 1 (**green circle**) was sampled at the surface from the Dickenberg gallery, which gathers all groundwater from the flooded Westfield and is now the only effluent of the mine water from this part of the coalfield. The water type is classified as Ca-Mg-Na-SO₄ (see [Table S1](#) (Supplementary Material)). Additionally, the mine drainage at this point is characterized by high loads of dissolved and particulate iron. The solutions from the coalfield sampled from depths below the third level ($\approx -270 \text{ m}$) are all characterized by a relatively high ionic strength (> 0.1) and are of Na-Cl water type (IBB-E 1 to IBB-E 9; **yellow circles**). This group also includes solution IBB-E 8, whose high salinity does not correspond to the depth of the sampling point. IBB-E 8 was taken from the main drainage of the Eastfield, just before reaching the surface. It represents therefore a mixture of all the waters which are pumped from the mine, including the deep brines. Waters sampled down to the third level ($\approx -270 \text{ m}$) (IBB-E 10 to IBB-E 16; **orange circles**) are characterized by relatively low ionic strength. A water type cannot be assigned to this group, as the waters show highly variable contents of the main cations (calcium, sodium, and magnesium) with an anionic dominance of sulfate, bicarbonate, and chloride. The high fraction of divalent ions contributing to the ionic strength is shown in [Fig. 2](#). The water type plots above the black line, representing a pure NaCl solution.

For comparison, saline waters originating from other hydro-geological settings (**blue X marks**) in the wider surroundings of the coalfield were sampled and analyzed. All of them can be characterized as belonging to the Na-Cl water type. These samples include the groundwater, originating from two wells drilled into lower Triassic sediments, used for the thermal spa in Bad Bentheim (BBH 1 and BBH 2), as well as three samples from the Northern border of the Münsterland Cretaceous Basin, originating from two wells drilled into Cretaceous sediments in the city of Bad Rothenfelde (WK 1 and WM 1), and a sample from the well of the Saline Gottesgabe saltworks in the city of Rheine (SGG 1). One sample was taken from a well drilled in the North German Basin close to the city of Bad Essen (BE 1). The last group constitutes the shallow groundwater (**grey crosses**) surrounding the coalfield (SGW 1 to SGW 6), as well as two shallow groundwaters originating from an aquifer of Upper Jurassic sediments, which are used for the thermal spa

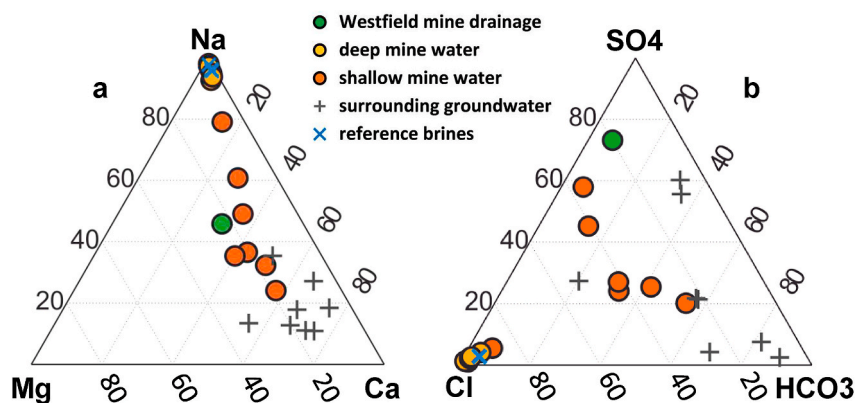


Fig. 3. Ternary plots showing the relative molar proportion of main cations (Mg^{2+} , Ca^{2+} , and Na^+) (a), and main anions (SO_4^{2-} , Cl^- , and HCO_3^-) (b).

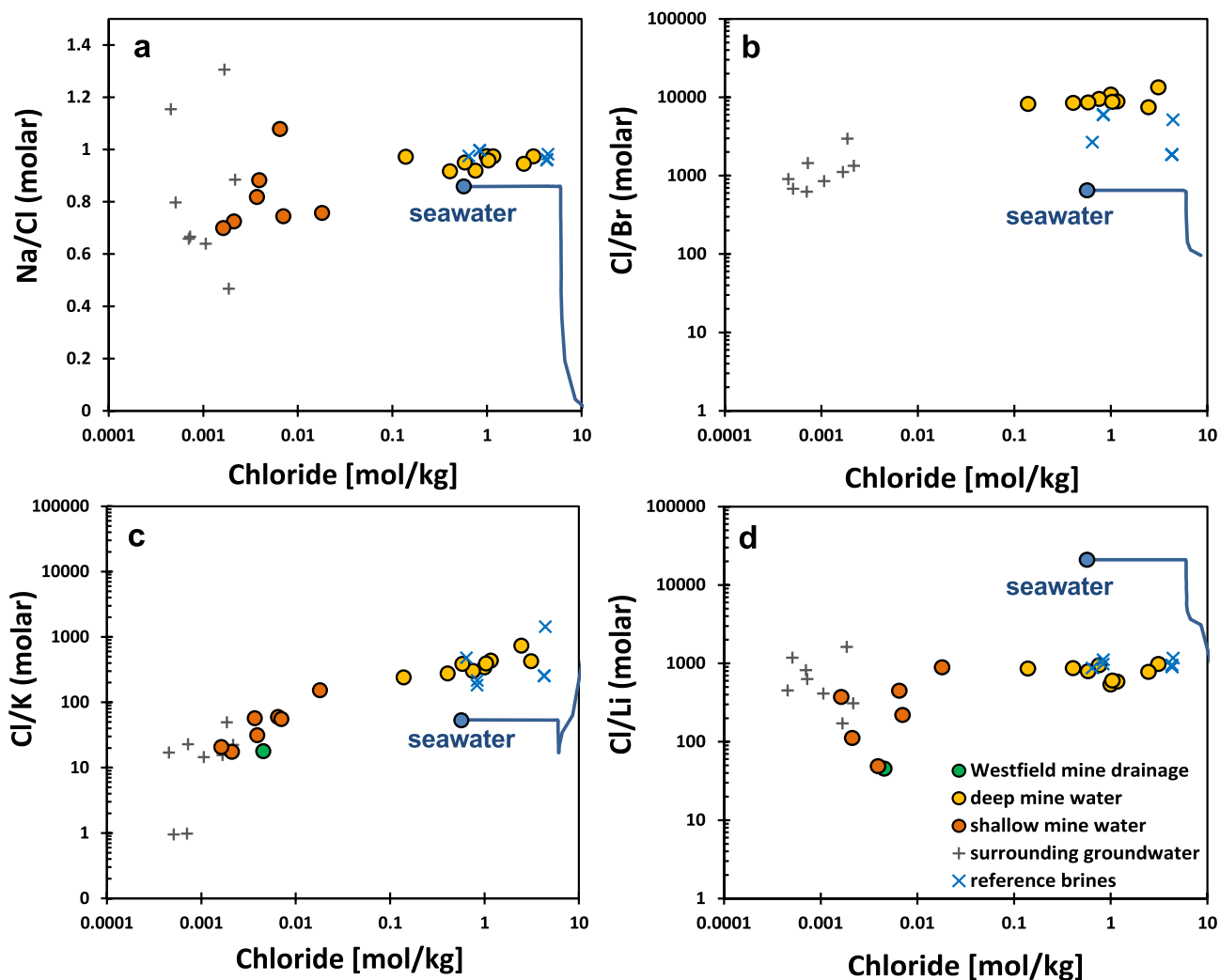


Fig. 4. Molar Na/Cl (a), Cl/Br (b), Cl/K (c), and Cl/Li (d) ratios versus Cl concentration [mol/kg]. Seawater composition after [Millero et al. \(2008\)](#); Lithium concentration taken from [Riley and Tongudai \(1964\)](#); Evolution of the respective molar ratio during seawater evaporation until saturation of carnallite is reached for comparison (blue line). (For interpretation of the references to color in this figure legend, the reader is referred to the Web version of this article.)

in Bad Bentheim (BBH 3 and BBH 4). As those waters originate from different geological units, they are characterized by diverse contents of main ions. In any case, however, Ca^{2+} is the dominant cation (see [Fig. 3](#) and [Table S1](#) (Supplementary Material)).

4.2. Geochemical evolution and reaction mechanisms

4.2.1. Dissolution of evaporites from adjacent layers

The chemical composition of the analyzed water is summarized in [Table S1](#) (Supplementary Material). The chloride concentration in the deep mine water (IBB-E 1 to IBB-E 9) is between 7.6 and 1910 times

higher than that of the corresponding shallow mine water down to the third level. The strong correlation of Na^+ versus Cl^- points to halite dissolution as the main source of salinity in these waters (see Figs. 2 and 4a). The Cl/Br ratio in the solutions from the coalfield is relatively constant (see Fig. 4b), indicating a single source of salinity for both elements. Note that the Br^- concentration in sample IBB-W 1 and in the shallow mine waters (IBB-E 10 to IBB-E 16) was below the detection limit.

The Na/Cl ratios indicate that a single source of salinity starts to influence the mine water chemistry below the third level (≈ -270 m). There is no indication of halite dissolution in the shallow waters above. Note that, while indicating halite dissolution as the main source of Na^+ , the deep mine waters show a Na^+ depletion with respect to Cl^- (see Table S1 (Supplementary Material) for Na/Cl ratios). A loose correlation between the decreasing Ca^{2+} content and the increasing Na/Cl ratio suggests a Na^+ source/ Ca^{2+} sink mechanism similar to the observations of Kloppmann et al. (2001). Cation exchange of the saline waters with clay minerals in the siliciclastic aquifer is a plausible explanation for this trend.

The observed Cl/Br ratios (between 13,457 and 7,465) are well within the expected values for halite dissolution and further corroborate the impression gained from Na/Cl ratios.

In general, Cl/Br ratios have been used to evaluate the origin of salinity in various hydrogeological settings (e.g. Alcalá and Custodio, 2008; Chowdhury et al., 2018; Davis et al., 1998; Egeberg and Aagaard, 1989; Fontes and Matray, 1993a; Katz et al., 2011; Kloppmann et al., 2001; Panno et al., 2006). Those studies took advantage of the relatively conservative behavior of Cl^- and Br^- in most aquatic environments, which allows to use those ions to trace the origin of groundwater salinity. During halite formation, bromide will co-precipitate with halite (Braitsch and Herrmann, 1963; McCaffrey et al., 1987; Siemann and Schramm, 2000). This co-precipitation can be followed using the distribution coefficient after McCaffrey et al. (1987):

$$D_{\text{Br}^-} = \frac{[\text{Br}^-]/[\text{Cl}^-]_{\text{halite}}}{[\text{Br}^-]/[\text{Cl}^-]_{\text{brine}}} \quad (1)$$

The average D_{Br^-} found by these authors is rather constant around 0.032. The molar Cl/Br of modern seawater is around 650. This ratio is suggested to have been constant throughout Earth's history (Foriel et al., 2004; Horita et al., 2002, 1991). On a local scale, upon evaporation of seawater, this ratio will decrease with the onset of halite precipitation and reach a value around 40 in the late evaporation stage at the onset of carnallite ($\text{KMgCl}_3 \cdot 6\text{H}_2\text{O}$) precipitation. Therefore, the Br^- concentration of halite formed during an early evaporation stage concentration will be lower compared to later evaporation stages, following a Rayleigh fractionation pattern as the solution gets enriched in Br^- relative to Cl^- . The Cl/Br ratio at the initial start of halite precipitation will be approximately 20,000, and will lower to about 5,500 in the halite, i.e. well within the range of 13,457 to 7,465 observed in the Ibbenbüren brines. Minerals like carnallite and sylvite incorporate Br^- into the crystal structure more readily compared to halite (Hardie and Eugster, 1971), so the influence of the respective minerals is not evident.

4.2.2. The interaction of brines with the carboniferous bedrock

The incorporation of K^+ into halite during seawater evaporation can be described by equation (2):

$$D_{\text{K}^+} = \frac{[\text{K}^+]/[\text{Na}^+]_{\text{halite}}}{[\text{K}^+]/[\text{Na}^+]_{\text{brine}}} \quad (2)$$

According to McCaffrey et al. (1987), D_{K^+} averages to 0.0008, which corresponds to a Na/K ratio in halite between 5,000 in the early evaporation stage and 2,000 at later stages. The Na/K ratio of deep mine waters is between 235 and 700. According to equation (2), if all Na^+ in the analyzed solutions is attributed to halite, the dissolution of halite may account for 19 up to a maximum of 56% of K^+ in the deep mine

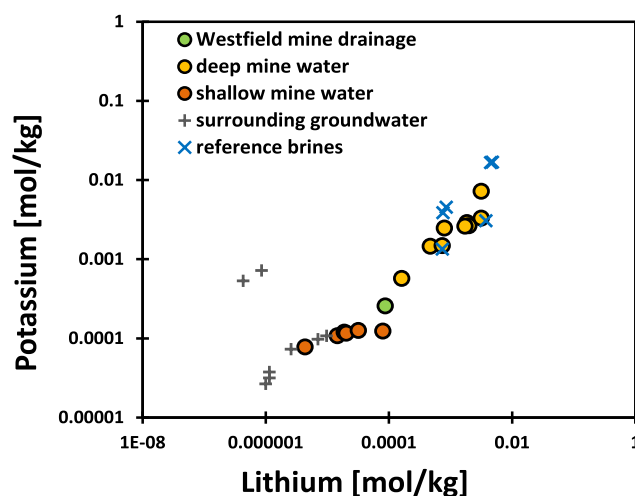


Fig. 5. Lithium concentration versus potassium concentration [mol/kg].

waters (IBB-E 1 to IBB-E 10). The K^+ concentration of the shallow mine waters is rather constant and explains at most 5% of the total K^+ concentration of deep waters. Consequently, an additional source of K^+ other than halite is needed to explain the observed values. In principle, further possible sources of K^+ in the groundwater are:

- (1) K^+ -rich evaporites like carnallite or sylvite from the surrounding area;
- (2) K-feldspar, muscovite, and clay minerals from the matrix of the Carboniferous sandstone;
- (3) fertilizers.

(1) Evaporites with high K^+ content have not been reported in the Mesozoic rocks surrounding the study area. The only sources of such minerals are the Permian sedimentary rocks of the Zechstein unit, which once covered the coalfield. The Permian Zechstein Sea is known to have reached the evaporation stage for carnallite in some areas of Germany. Therefore, the formation water, which originates from the dissolution of such Permian evaporites, might produce elevated K^+ contents. However, to our knowledge, no carnallite or sylvite has been reported in the Zechstein deposits surrounding the coalfield, and the contribution of carnallite or sylvite dissolution is not evident from the Cl/Br ratios. Additionally, $\delta^{34}\text{S}_{\text{SO}_4}$ values of the dissolved sulfate (see chapter 4.3.3) do not indicate the contribution of Permian deposits.

(2) K^+ concentrations not only show a strong correlation with chloride (see Fig. 4c), but also with Li concentrations (see Fig. 5). A strong positive correlation of K^+ and Li^+ suggests aluminosilicates as the source of these elements. The origin of Lithium from the dissolution of evaporites seems unlikely due to a very limited uptake of Li in either halite or any other minerals of the evaporation series (e.g. Fontes and Matray, 1993a; Shalev et al., 2018). Evaporation of seawater generates elevated Cl/Li ratios compared to the mine waters (see Fig. 4d). This is a frequent observation for saline brines, in which Li concentrations readily exceed the sea water composition as well as concentrations that might be reached during evaporation of such seawater (Chan et al., 2002; Stueber et al., 1993). The interaction of the mine water with aluminosilicates in the aquifer is a likely source in this case.

Fractured and porous sandstone with low volumes of feldspar and muscovite is the main aquifer of the Ibbenbüren coalfield. Illite has been reported as an important matrix component within this sandstone (Becker et al., 2017; Wüstefeld et al., 2017), with kaolinite as a minor component. From thermodynamic considerations, the dissolution of illite or feldspar at current ambient temperature conditions cannot generate the observed K^+ concentrations (Zhu, 2005). In accordance

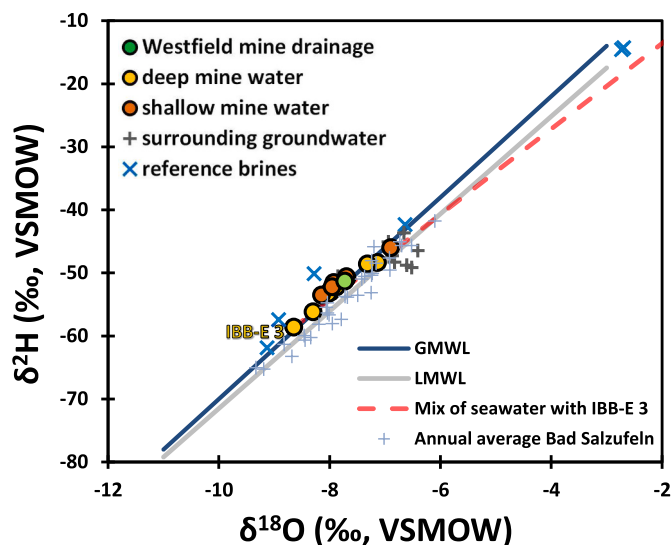
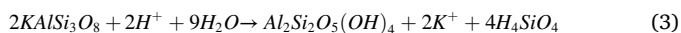


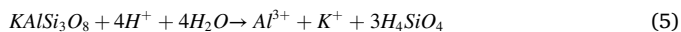
Fig. 6. $\delta^{18}\text{O}$ versus $\delta^2\text{H}$ values (‰; VSMOW). The blue line denotes the Global Meteoric Waterline (GMWL) after Craig (1961). The grey line denotes the Local Meteoric Waterline (LMWL) of the nearest station (Bad Salzufen) obtained from the IAE/WMO global network of isotopes in precipitation (GNIP) database Stumpp et al. (2014). Light grey crosses are annual average values of the station from 1978 to 2011, plotted for reference. The red dotted line shows the hypothetical trend during mixing of solution IBB-E 3 with seawater. (For interpretation of the references to color in this figure legend, the reader is referred to the Web version of this article.)

with the respective mineralogy, other processes that influence the K^+ content in solution include kaolinite formation and illitisation (Egeberg and Aagaard, 1989).

Incongruent dissolution of K-feldspar and subsequent kaolinite formation are accompanied by the liberation of K^+ ions, as represented by equation (3). The subsequent illitisation of kaolinite in equation (4) after Thyne et al. (2001) would remove K^+ from the solution again. However, the formation of illite according to equation (4) in the investigated setting occurs only in a temperature window from around 70 °C up to around 130 °C (Becker et al., 2017).



Outside this temperature window, the reaction will not be completed. A decrease in K^+ and aluminum contents due to the dissolution of k-feldspar under open system conditions has been reported in other sandstone reservoirs (Ehrenberg, 1991; Wilkinson et al., 2014), following equation (5).



It can be hypothesized that the resulting K^+ might be preserved in formation water. K^+ might also be adsorbed onto clay minerals in general, being available for ion exchange reactions at later stages (e.g. Thyne et al., 2001; Wilkinson et al., 2014). Ion exchange of K^+ from the interlayer of illite in the presence of sodium has been reported by Scott and Smith (1966). Bibi et al. (2011) reported an increasing release of K^+ with increasing salinity for experiments carried out with illite at different pH values and two different ionic strengths.

(3) The influence of agriculture seems negligible for most water samples and especially for the mine waters. The measured K^+ concentrations in the shallow mine waters are in the range of the normal background expected for groundwater in the area (Wendland et al., 2005). This holds true notwithstanding ionic strength values that are elevated with respect to the local shallow groundwater (SGW 1 to SGW 6). Other ions indicative of fertilizers such as nitrate or phosphate were

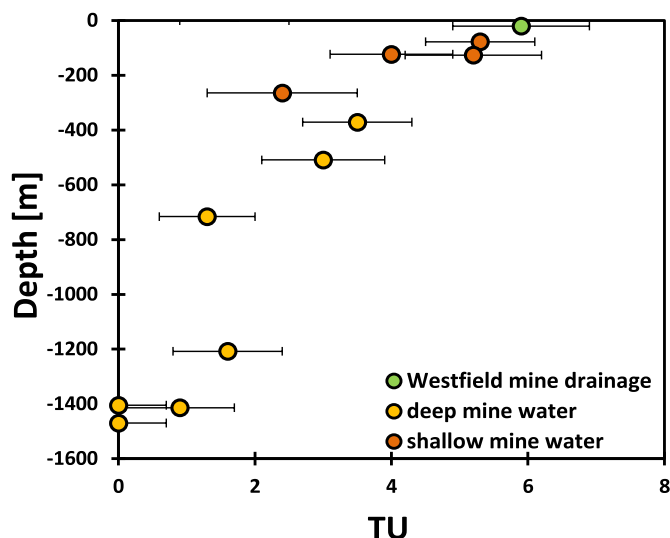


Fig. 7. Tritium units (TU) versus depth in meters. Within the uncertainty, Tritium was present down to the lowest level, indicating the presence of some modern water throughout the mine. Samples IBB-E 3 and IBB-E 4 from the lowest level show TU values below the detection limit (<0.6 TU). Tritium was not analyzed in all samples (see Table S1 (Supplementary Material)).

only found in SGW 3 and SGW 4, taken from agricultural areas surrounding the coalfield. In the latter case, the influence of manure and fertilizer might play a distinctive role in the formation of the waters, but a detailed interpretation of the underlying mechanisms is outside the scope of this article.

4.3. Isotopic signatures

4.3.1. Deuterium and oxygen

The shallow groundwater samples of the surrounding aquifers (SGW 1–SGW 6) plot in the field of the local meteoric precipitation, but with a low d-excess compared to the LMWL (local meteoric water line; see Fig. 6). The summer of 2018 was extraordinarily dry and warm compared to the average climate situation. The shallow groundwater also plots in the upper, isotopically heavy area compared to the annual composition of precipitation in the area (light grey crosses). We therefore assume that the shallow groundwater in this region shows signals of evaporation. Compared to the LMWL, the mine waters of the coalfield show a slight offset towards the GMWL. Such a relatively high d-excess compared to the LMWL might indicate a high proportion of autumn and winter rain events. The average annual precipitation in the area is rather constant through the year, with small maxima from July to September and from December to January. A high d-excess is generally related to relatively low humidity over the oceans (e.g. Pfahl and Sodemann, 2014), which is the case during autumn and winter in the North Atlantic ocean. Evapotranspiration losses above the coalfield, which is under extensive agricultural use, should result in an overrepresentation of precipitation from late autumn and winter within the aquifer.

There is no correlation of the isotopic ratios with depth. Neither influence of Pleistocene waters nor mixing of meteoric water with formation waters of oceanic origin can be deduced from these values. Isotopic evolution during mixing of meteoric water with formation water of oceanic origin is indicated in Fig. 6 (red dashed line). Pleistocene waters show signals that are isotopically light, compared to our values (e.g. Kloppmann et al., 2001). Additionally, Tritium is present in solutions from all levels of the mine down to ≈ -1500 m. Samples BBH 1 and BBH 2 show an isotopic composition typical of precipitation under warmer climate conditions, rather than a mix of meteoric water with seawater or evaporating brines (e.g. Knauth and Beeunas, 1986).

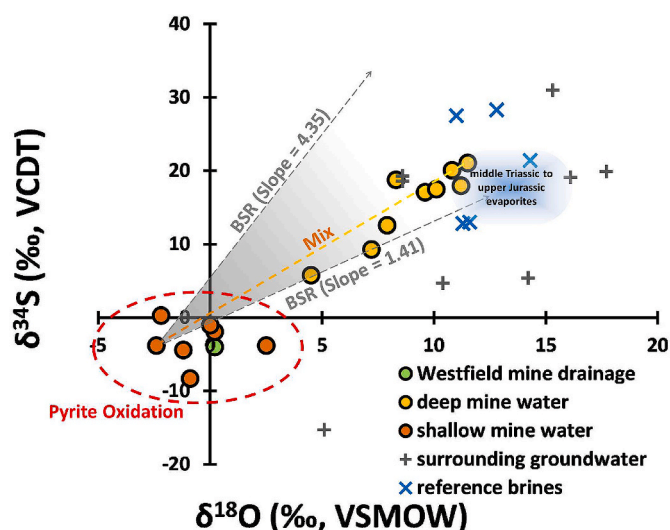


Fig. 8. $\delta^{34}\text{S}$ versus $\delta^{18}\text{O}$ (‰, VCDT) values of dissolved sulfate. The area between the dashed grey lines indicates the possible pathways of isotopic evolution during bacterial sulfate reduction (BSR), starting from sample IBB-E-14; slopes are derived from Brunner et al. (2005). The isotopic trend during conservative mixing is indicated for endmember IBB-E-3 (highest $\delta^{34}\text{S}$, highest ionic strength) with IBB-E-14 (pyrite oxidation, high sulfate). $\delta^{34}\text{S}$ range for middle Triassic to upper Jurassic evaporites from Müller et al. (1966), the range of $\delta^{18}\text{O}$ is based on Claypool et al. (1980).

4.3.2. Tritium

Tritium (^3H) is the radioactive isotope of hydrogen with a half-life of ≈ 12.4 years. It is reported in tritium units (TU), where 1 TU equals 1 ^3H atom in 10^{18} atoms of hydrogen (Kendall and Doctor, 2003). Natural background levels of Tritium are between 1 and 10, but significant amounts of Tritium have been emitted into the atmosphere during nuclear bomb tests in the '50s and '60s. The quantification of Tritium does not allow to calculate the groundwater age as the measurement of its decay product (^3He) would be needed as well (e.g. Schlosser et al., 1988). However, the presence of Tritium implies the presence of some fraction of modern (i.e. after 1950s) water. Tritium has been measured in 13 solutions from the coalfield. Tritium data indicate an increasing groundwater age with depth (Fig. 7). Tritium is present down to the lowest level, approximately 1500 m below the surface. Note that the solutions IBB-E 3 and IBB-E 4 from the lowest level are free of Tritium within uncertainty. However, $\delta^2\text{H}_{\text{H}_2\text{O}}$ and $\delta^{18}\text{O}_{\text{H}_2\text{O}}$ values do not indicate the contribution of formation water as the main mechanism determining the chemical composition of the water. On the contrary, it seems likely that ongoing water rock interaction is contributing to the formation also of the saline brines, which are influenced by meteoric water infiltration.

4.3.3. Sulfur and oxygen in sulfate

The interpretation of sulfur and oxygen isotopes in sulfate is based on the groundbreaking work carried out by Claypool et al. (1980), Holser and Kaplan (1966), and Müller et al. (1966) showing that the sulfur and oxygen isotopic composition of seawater sulfate changed through time. Since those seminal works, numerous measurements have helped to improve our knowledge about temporal and spatial patterns of the record preserved (e.g. Bernasconi et al., 2017; Kampschulte and Strauss, 2004; Strauss, 1997; Turchyn and Schrag, 2006; Utrilla et al., 1992). The role of microbes in the sulfur cycle and the traces they leave in the isotopic signal has been thoroughly investigated (e.g. Balci et al., 2007; Böttcher et al., 2001; Habicht and Canfield, 1997). The isotopic signals have proven useful to trace the origin of sulfur in various hydrogeological settings (Bottrell et al., 2008; Brenot et al., 2015, 2007; Burke et al., 2018; Dogramaci et al., 2001; Fontes and Matray, 1993b; Otero

and Soler, 2002; Tichomirowa et al., 2010), and specifically within the context of mine drainage (Gammons et al., 2013; Migaszewski et al., 2018). The sample distribution in Fig. 8 points to different sources of dissolved sulfate. Shallow mine waters (IBB-E 10 to IBB-E 16; IBB-W 1) show a $\delta^{34}\text{S}_{\text{SO}_4}$ signature between -8.3‰ and $+0.3\text{‰}$ with $\delta^{18}\text{O}_{\text{SO}_4}$ values between -2.4 and $+2.5\text{‰}$. In contrast, the deep mine waters (IBB-E 1 to IBB-E 9) are isotopically heavy with $\delta^{34}\text{S}_{\text{SO}_4}$ values between $+5.8$ and $+21.1\text{‰}$, and $\delta^{18}\text{O}_{\text{SO}_4}$ ranging from $+4.5$ to $+11.2\text{‰}$. The isotopic composition of the shallow mine waters (IBB-E 10 – IBB-E 16; IBB-W 1) is typical for sulfate derived from oxidation of pyrite (e.g. Brenot et al., 2015; Haubrich and Tichomirowa, 2002).

For sulfate derived from pyrite oxidation, the $\delta^{18}\text{O}_{\text{SO}_4}$ values can be used to decipher the oxidation mechanism (e.g. Balci et al., 2007; HeideI et al., 2013, 2011, and references therein). In principle, the oxidation of pyrite can utilize O_2 or Fe(III) as oxidant. If Fe(III) is the oxidant, then the oxygen in the newly formed sulfate will derive mainly from H_2O . Both sources will have a different isotopic fingerprint, with the H_2O -derived oxygen being relatively light compared to the O_2 -derived oxygen. $\delta^{18}\text{O}_{\text{H}_2\text{O}}$ of the Ibbenbüren groundwaters is $\approx -8\text{‰}$. The isotope enrichment factor between sulfate and water during pyrite oxidation $\epsilon_{\text{SO}_4-\text{H}_2\text{O}}$ ($\epsilon_{\text{SO}_4-\text{H}_2\text{O}} \approx \delta^{18}\text{O}_{\text{SO}_4} - \delta^{18}\text{O}_{\text{H}_2\text{O}}$) has been reported to be between 0 and 4‰. Accordingly, if H_2O is the sole source of oxygen in sulfate, then the $\delta^{18}\text{O}_{\text{SO}_4}$ should be between -4 and -8‰ . In contrast, the $\delta^{18}\text{O}_{\text{O}_2}$ of the atmospheric oxygen is $\approx +23.5\text{‰}$. The isotopic enrichment factor between sulfate and atmospheric oxygen during pyrite oxidation $\epsilon_{\text{SO}_4-\text{O}_2}$ ($\epsilon_{\text{SO}_4-\text{O}_2} \approx \delta^{18}\text{O}_{\text{SO}_4} - \delta^{18}\text{O}_{\text{O}_2}$) has been reported to be between -4.3 and -9.8‰ (Heidel and Tichomirowa, 2011). Accordingly, if O_2 is the sole source of oxygen in sulfate, then the $\delta^{18}\text{O}_{\text{SO}_4}$ should be between $+13.7$ and $+19.2\text{‰}$. In the studied waters, the $\delta^{18}\text{O}_{\text{SO}_4}$ values between -2.4 and $+2.5\text{‰}$ suggest the oxidation of pyrite through Fe(III) as the main oxidant. Finally, the denitrification of nitrate could also contribute to pyrite oxidation in an agricultural area (Böttcher et al., 1990; Zhang et al., 2009).

With the depth increasing, sulfate becomes increasingly isotopically heavy for both sulfur and oxygen. Two different mechanisms have to be considered to explain this trend of isotopic enrichment, as detailed below.

- (1) Processes that influence the isotopic composition of sulfur and oxygen in sulfate include microbial sulfate reduction and sulfur disproportionation (Antler et al., 2013; Böttcher et al., 2001; Taylor et al., 1984; Thamdrup et al., 1993). A maximum isotope fractionation between sulfate and hydrogen sulfide of $\delta^{34}\text{S}_{\text{SO}_4 - \text{H}_2\text{S}} \approx -70\text{‰}$ has been reported during bacterial sulfate reduction (e.g. Brunner et al., 2005). BäSSLer (1970) proposed bacterial sulfate reduction as the reason for the increasingly heavy $\delta^{34}\text{S}_{\text{SO}_4}$ and $\delta^{18}\text{O}_{\text{SO}_4}$ values of the remaining sulfate in the Ibbenbüren Eastfield. A closer investigation of this hypothesis is of relevance for the setup of a conceptual hydrogeological model, as for this reason the author concluded that the influence of the infiltration of water from the Mesozoic sediments outside of the coalfield is negligible.
- (2) The isotopic composition of sulfate from the dissolution of Mesozoic sediments surrounding the coalfield results in an isotopic signature as is found in the deep mine waters. Comparable $\delta^{34}\text{S}_{\text{SO}_4}$ values around $+20\text{‰}$ for upper Jurassic and middle Triassic gypsum and anhydrite have been reported by Müller et al. (1966). The apparent trend could be caused by the mixing of two endmembers: (i) meteoric water with an isotopic signature derived from pyrite oxidation, and (ii) brines with signatures derived from dissolution of evaporates from the vicinity of the coal field.

The expected isotopic evolution for both scenarios is examined in Fig. 8. The chosen endmembers for the “mixing hypothesis” are solution IBB-E 3 (highest ionic strength and highest $\delta^{34}\text{S}_{\text{SO}_4}$) for the dissolution of

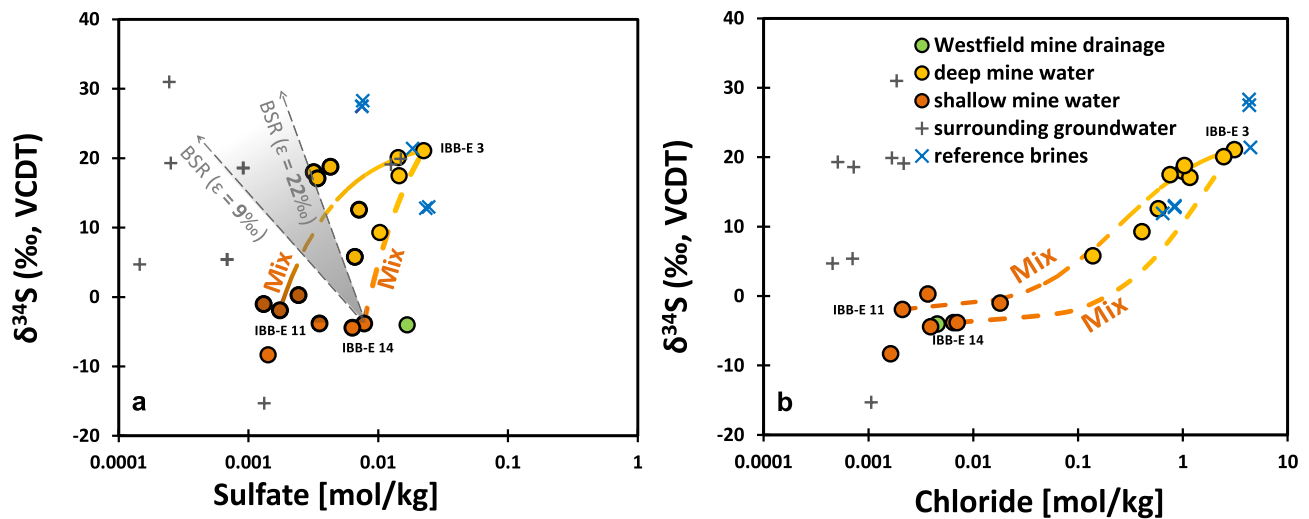


Fig. 9. $\delta^{34}\text{S}$ versus dissolved sulfate (a) and $\delta^{34}\text{S}$ versus chloride [mol/kg] (b). The area between the dashed grey lines denotes isotopic enrichment (ϵ) during bacterial sulfate reduction (BSR). The slopes are derived from Fritz et al. (1989). Endmember mixing is plotted for solution IBB-E 3 with IBB-E 14 (high sulfate), and for IBB-E 3 with IBB-E 11 (low sulfate).

Mesozoic evaporites, and IBB-E 14 as the pyrite endmember with a typical isotopic signature for pyrite oxidation. In principle, the mixing of those two endmembers delivers a plausible fit for most of the analyzed waters. However, the samples are also within the expected trend for the isotopic evolution of the pyrite endmember during bacterial sulfate reduction.

Investigating the correlation of $\delta^{34}\text{S}_{\text{SO}_4}$ against the dissolved sulfate reveals that, on average, sulfate in the deep mine waters is higher compared to the shallow mine waters (see Fig. 9a). Therefore, if bacterial sulfate reduction (BSR) or disproportionation is the dominant process leading to isotopic enrichment in the deep brines, an additional source of sulfur during infiltration is needed. Sedimentary pyrite and sulfur from the coal are possible sources of additional sulfate in this case. A source of isotopically heavy values is the coal derived sulfur, for which values from approximately -50% to $+40\%$ have been measured (Seal, 2006). High isotopic ratios of pyrite have also been reported by Drake et al. (2018), but commonly sedimentary pyrite is isotopically light with respect to the initial sulfate (Strauss, 1997), with more common values being slightly negative or circumneutral. Three pyrite samples measured from the Ibbenbüren coalfield range from $\delta^{34}\text{S}_{\text{FeS}} = -4$ to $+8\%$ (Bässler, 1970). Bernardez et al. (2013) carried out batch experiments to investigate the influence of sulfate concentration on the conversion rate of sulfate to H_2S in the presence of sulfate reducing bacteria. They found an increasing conversion rate of sulfate to H_2S with increasing sulfate content. On that account, it is doubtful whether a system can be under the influence of BSR and at the same time sulfate can be increasing with depth. However, the sample distribution in Fig. 9a would need such a process. Additionally, while sulfate reducing bacteria have been reported at very high salinities (Foti et al., 2007), the salinity of the brines IBB-E 3 and IBB-E 4 is so high that some limitations regarding the possible mechanisms of microbial sulfate reduction have to be considered (Oren, 1999).

However, solutions IBB-E 1, IBB-E 2, and IBB-E 9 are in the range of BSR starting from pyrite endmember IBB-E 14 (see Fig. 9a).

The expected isotopic fractionation of the pyrite endmember during BSR is described using the Rayleigh equation (6), for which kinetic isotope enrichment factors have been described by Fritz et al. (1989).

$$\delta^{34}\text{S}_{\text{remaining sulfate}} = \delta^{34}\text{S}_{\text{init}} - \epsilon^{34}\text{S}_{\text{BSR}} \cdot \ln f \quad (6)$$

where f is the fraction of the remaining sulfate, $\delta^{34}\text{S}_{\text{init}}$ is the $\delta^{34}\text{S}_{\text{SO}_4}$ composition of the initial sulfate, and $\epsilon^{34}\text{S}_{\text{BSR}}$ is the kinetic isotope enrichment factor expressed in ‰ (see, e.g. Hayes (2004) for details

about notation). The $\epsilon^{34}\text{S}_{\text{BSR}}$ found by these authors is between 9% and 22%. The $\delta^{34}\text{S}_{\text{init}}$ value of the “pyrite endmember” IBB-E14 is -3.8% . BSR would create solutions with lower dissolved sulfate content at the respective $\delta^{34}\text{S}_{\text{SO}_4}$ values for most solutions. Applying a large kinetic enrichment factor of 22‰ and starting from a solution rich in dissolved sulfate (IBB-E 14), the isotopic composition and amount of dissolved sulfate can be reached for solutions IBB-E 1, IBB-E 2, and IBB-E 9. The rest of the intermediate solutions can be described through mixing of the brine endmember (IBB-E 3) and pyrite-derived solutions with high (IBB-E 14) or low dissolved sulfate content (IBB-E 11). However, $\delta^{34}\text{S}_{\text{SO}_4}$ values also increase with salinity. The isotopic composition of sulfate resulting from the dissolution of Mesozoic sediments surrounding the coalfield could result in an isotopic signature as that found in the deep mine waters. This possibility is corroborated by a correlation of increasing $\delta^{34}\text{S}_{\text{SO}_4}$ with an increase in dissolved chloride (see Fig. 9b). The coevolution of $\delta^{34}\text{S}_{\text{SO}_4}$ together with increasing Cl^- concentrations can be described through endmember mixing, according to the sulfate concentration of the pyrite endmember. The mixing of IBB-E 14 (high sulfate concentration) with the brine (IBB-E 3) produces solutions that are isotopically light with respect to the observed values. Some influence of BSR is suggested in that case in accordance with the modelling result shown in Fig. 9a. However, the mixing of solution IBB-E 11 (low sulfate concentration) with the brine (IBB-E 3) generally fits well with the observed trend. Conclusively, the intermediate waters seem to be mostly influenced by the mixing of two endmembers. BSR cannot be fully excluded and might contribute to the observed isotopic evolution with depth but in any case mixing will be the governing process.

Finally, some of the reference samples were taken from defined geological systems. Therefore, BBH 1 and BBH 2 were gathered from an aquifer of Buntsandstein with $\delta^{34}\text{S}_{\text{SO}_4}$ values between $+27.5$ and $+28.3\%$. High values for lower Triassic sediments have been reported, e.g., by Kampschulte and Strauss (2004). The origin of SGG 1 is under debate, but a $\delta^{34}\text{S}_{\text{SO}_4}$ value of $+11.9\%$ is indicative of Permian origin. WM 1 and WK 1 were sampled from the sediments of the Münsterland Cretaceous basin. The origin of the salinity in these waters is not clear, but the values indicate Permian origin. From Fig. 9b, it should be considered, however, that a mixture of pyrite dissolution and evaporate in analogy to the mine waters could also be responsible for the observed $\delta^{34}\text{S}_{\text{SO}_4}$. The $\delta^{34}\text{S}_{\text{SO}_4}$ values of sulfate in atmospheric deposition in Central Europe vary between 0% and $+7\%$, whereas $\delta^{18}\text{O}_{\text{SO}_4}$ values range between $+7\%$ and $+17\%$ (Knöller et al., 2004; Novák et al., 2001), which would be indicative of the isotopic composition of samples

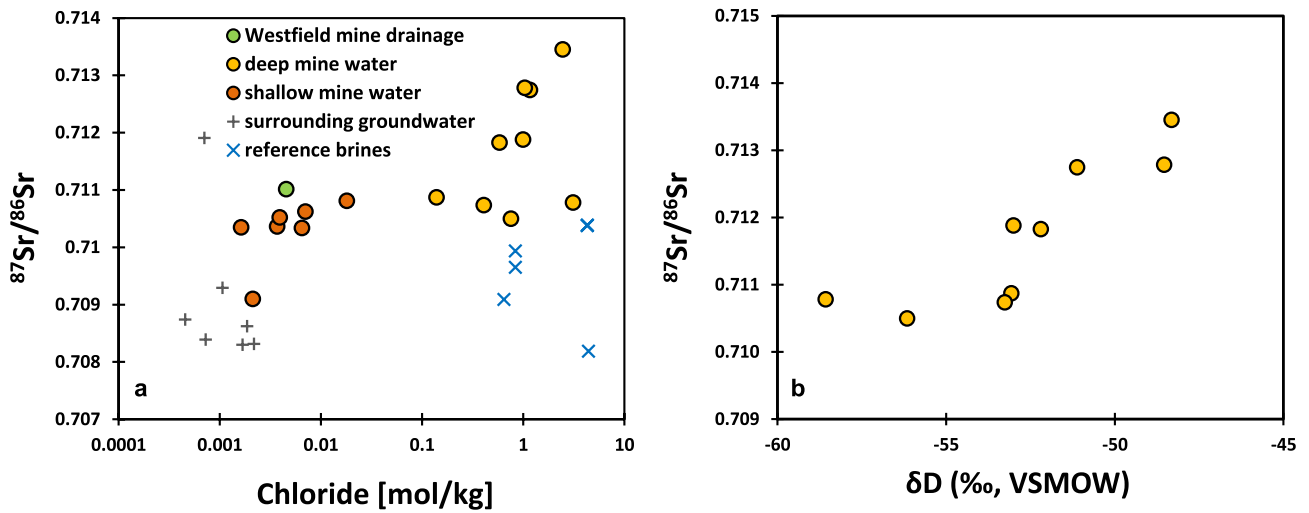


Fig. 10. $^{87}\text{Sr}/^{86}\text{Sr}$ isotope ratio versus chloride [mol/kg] (a), and $^{87}\text{Sr}/^{86}\text{Sr}$ ratio versus δD (‰, VSMOW) (b) in the deep mine water. The correlation indicates a contribution of isotopically heavy connate water to the mine water chemistry.

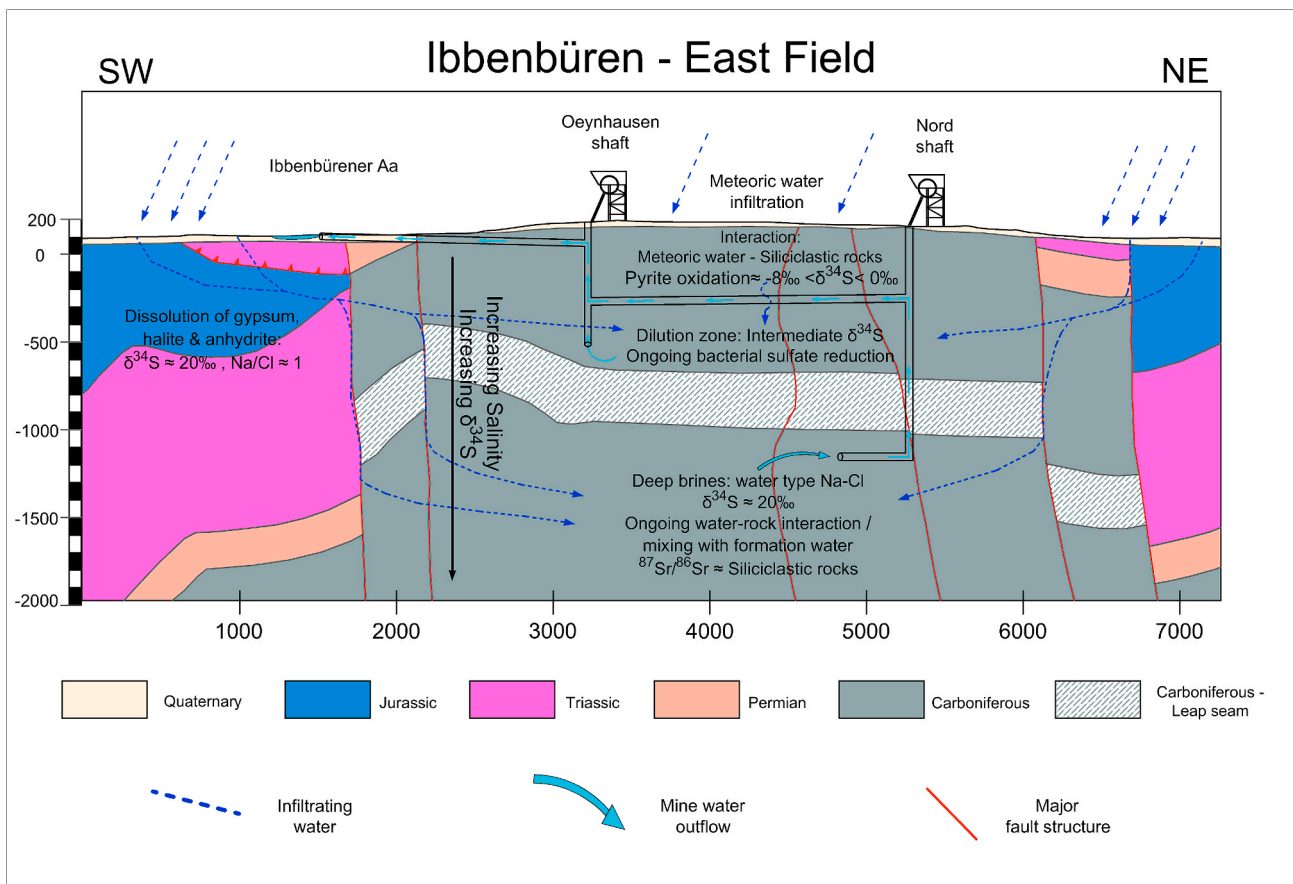


Fig. 11. Schematic cross section through the Ibbenbüren Eastfield including a conceptual hydrogeochemical model, depicting the origin and evolution of mine drainage, groundwater, and brines in the mine. Modified after Drozdewski (1985).

IBB 2 and IBB 3. However, the isotopic composition of fertilizers has also been reported in the same area (Otero et al., 2008).

4.3.4. Strontium isotopes

The $^{87}\text{Sr}/^{86}\text{Sr}$ ratio of the mine waters (IBB-W 1; IBB-E 1 to IBB-E 16) ranges from 0.7091 to 0.7135 (see Table S1 (Supplementary Material) and Fig. 10a). While most of the mine waters plot around $^{87}\text{Sr}/^{86}\text{Sr}$ ratios

from 0.710 to 0.711, the NaCl type brines show a trend towards more radiogenic values with the highest $^{87}\text{Sr}/^{86}\text{Sr}$ ratios of 0.7135 reached in those waters, sampled from the deepest level of the mine. A similar trend has been reported, for instance, by Egeberg and Aagaard (1989) for groundwater samples in the North Sea, and by Grobe and Machel (2002) for groundwater from the Münsterland Cretaceous basin. The highly mineralized reference waters have $^{87}\text{Sr}/^{86}\text{Sr}$ ratios between 0.7082 and

0.7104. Compared to the deep mine waters, these Sr isotopic compositions are closer to the range of marine carbonates, likely due to the dissolution of marine evaporites. Nonetheless, with the exception of sample BE 1, taken from a well in the north German basin, the reference brines are isotopically heavy compared to the isotopic signature of the relevant Mesozoic marine evaporites of the region (Burke et al., 1982). The shallow groundwaters (SGW 1 to SGW 6) plot around a $^{87}\text{Sr}/^{86}\text{Sr}$ ratio of 0.709, with the exception SGW 3 that exhibits a value of 0.712.

There is no correlation between strontium content and isotopic signature in the deep mine waters. Normally, the contribution of Sr^{2+} from evaporite dissolution should dominate the isotopic composition (Faure, 2001). Yet, at the Ibbenbüren mine, Sr correlates with alkaline elements. For this reason, the contribution of radiogenic ^{87}Rb from the weathering of Rb-rich minerals such as K-feldspar or muscovite has to be considered in our case, as suggested by Grobe and Machel (2002). The Rb-rich minerals within the Paleozoic rocks might have generated relevant levels of isotopically heavy Sr. Note that a correlation of an increasing $^{87}\text{Sr}/^{86}\text{Sr}$ ratio with increasing $\delta\text{D}_{\text{H}_2\text{O}}$ and $\delta^{18}\text{O}_{\text{H}_2\text{O}}$ values (Fig. 10b) suggests the presence of formation water contributing to the isotopic composition. This is in accordance with the relatively high K^+ and Li^+ concentrations (see above), which cannot be explained by water-rock-interaction at ambient temperature. Formation water, resulting from hydrothermal water-rock interaction, would have reached the necessary temperature.

5. Conclusions

A multi proxy approach including chemical and isotopic analyses was successfully used to elucidate the chemical evolution of mine drainage and groundwater from the Ibbenbüren coal mine (see Fig. 11).

The waters are a result of water-rock interaction, migration, and mixing of different fluids. Mine drainage and groundwater throughout the whole mine show influence of modern meteoric water through δD , $\delta^{18}\text{O}$, and Tritium values. Salinity and sulfur isotopic ratios generally increase with depth.

- (1) Salinity in the deep Na-Cl brines can be assigned to halite dissolution through Na/Cl and Br/Cl ratios. Within the context of the local geological situation, the origin of these brines from outside of the coalfield is corroborated by $\delta^{34}\text{S}_{\text{SO}_4}$ values typical for the dissolution of Mesozoic evaporites that surround the coalfield.
- (2) The mixing of those brines with formation water from the siliclastic rocks of the Carboniferous host rock and ongoing water-rock interaction are indicated by radiogenic strontium, K^+ and Li^+ . The enrichment in alkalis with salinity cannot be attributed to halite dissolution and therefore could result from interaction with the siliclastic rocks of the coalfield. Additionally, a positive correlation of $^{87}\text{Sr}/^{86}\text{Sr}$ with $\delta^2\text{H}_{\text{H}_2\text{O}}$ and $\delta^{18}\text{O}_{\text{H}_2\text{O}}$ values of the mine fluids suggests the presence of formation water, contributing to the water chemistry.
- (3) Shallow mine waters down to the third level ≈ -270 m below surface show a $\delta^{34}\text{S}_{\text{SO}_4}$ composition typical for the oxidation of sulfides. No influence of halite, gypsum, or anhydrite dissolution can be deduced in the shallow waters.
- (4) Intermediate water compositions are a result of mixing between the Na-Cl brines and shallow mine waters. From the co-evolution of $\delta^{34}\text{S}_{\text{SO}_4}$ values and dissolved sulfate together with salinity, only minor influence of bacterial sulfate reduction is suggested in those intermediate waters.

Declaration of competing interest

The authors declare that they have no known competing financial interests or personal relationships that could have appeared to influence the work reported in this paper.

Acknowledgements

This study was funded by Forum Bergbau Wasser. We greatly thank Johannes Wulfert, Heinz Dieter Pollmann, Norbert Schriever, Kai Oppermann, Thomas Heeger, and everybody from RAG Anthrazit Ibbenbüren for facilitating sampling and providing important insights into mine details. We thank Stefanie Eichinger, Judith Jernej and Andrea Wolf at NAWI Graz Central Lab for Water, Minerals and Rocks for the analyses. Thorsten Krämer from Fachklinik Bad Bentheim, Axel Pfeiffer from the city of Bad Rothenfelde, Jules Vleugels from Förderverein Saline Gottesgabe are thanked for allowing us to take samples from the respective brines. We also thank the two anonymous reviewers for their comments and suggestions that helped improve this manuscript.

Appendix A. Supplementary data

Supplementary data to this article can be found online at <https://doi.org/10.1016/j.apgeochem.2020.104693>.

References

- Alcalá, F.J., Custodio, E., 2008. Using the Cl/Br ratio as a tracer to identify the origin of salinity in aquifers in Spain and Portugal. *J. Hydrol.* 359, 189–207. <https://doi.org/10.1016/j.jhydrol.2008.06.028>.
- Antler, G., Turchyn, A.V., Rennie, V., Herut, B., Sivan, O., 2013. Coupled sulfur and oxygen isotope insight into bacterial sulfate reduction in the natural environment. *Geochem. Cosmochim. Acta* 118, 98–117. <https://doi.org/10.1016/j.gca.2013.05.005>.
- Appelo, C.A.J., Postma, D., 2005. *Geochemistry, Groundwater and Pollution*. Balkema.
- Balci, N., Shanks, W.C., Mayer, B., Mandernack, K.W., 2007. Oxygen and sulfur isotope systematics of sulfate produced by bacterial and abiotic oxidation of pyrite. *Geochem. Cosmochim. Acta* 71, 3796–3811. <https://doi.org/10.1016/j.gca.2007.04.017>.
- Banks, D., Burke, S.P., Gray, C.G., 1997. Hydrogeochemistry of coal mine drainage and other ferruginous waters in north Derbyshire and south Yorkshire, UK. *Q. J. Eng. Geol. Hydrogeol.* 30, 257–280. <https://doi.org/10.1144/GSL.QJEG.1997.030.P3.07>.
- Bässler, R., 1970. Hydrogeologische, chemische und Isotopen-Untersuchungen der Grubenwässer des Ibbenbürener Steinkohlenreviers. *Z. Dtsch. Geol. Ges.* 209–286.
- Becker, I., Wüstefeld, P., Koehrer, B., Felder, M., Hilgers, C., 2017. Porosity and permeability variations in a tight gas sandstone reservoir analogue, Westphalian D, Lower Saxony basin, NW Germany: influence of depositional setting and diagenesis. *J. Petrol. Geol.* 40, 363–389. <https://doi.org/10.1111/jpg.12685>.
- Bernardez, L.A., de Andrade Lima, L.R.P., de Jesus, E.B., Ramos, C.L.S., Almeida, P.F., 2013. A kinetic study on bacterial sulfate reduction. *Bioproc. Biosyst. Eng.* 36, 1861–1869. <https://doi.org/10.1007/s00449-013-0960-0>.
- Bernasconi, S.M., Meier, I., Wohlwend, S., Brack, P., Hochuli, P.A., Bläsi, H., Wortmann, U.G., Ramseyer, K., 2017. An evaporite-based high-resolution sulfur isotope record of Late Permian and Triassic seawater sulfate. *Geochem. Cosmochim. Acta* 204, 331–349. <https://doi.org/10.1016/j.gca.2017.01.047>.
- Bibi, I., Singh, B., Silvester, E., 2011. Dissolution of illite in saline-acidic solutions at 25 °C. *Geochem. Cosmochim. Acta* 75, 3237–3249. <https://doi.org/10.1016/j.gca.2011.03.022>.
- Böttcher, J., Strebel, O., Voerkelius, S., Schmidt, H.L., 1990. Using isotope fractionation of nitrate-nitrogen and nitrate-oxygen for evaluation of microbial denitrification in a sandy aquifer. *J. Hydrol.* 114, 413–424. [https://doi.org/10.1016/0022-1694\(90\)90068-9](https://doi.org/10.1016/0022-1694(90)90068-9).
- Böttcher, M.E., Thamdrup, B., Vennemann, T.W., 2001. Oxygen and sulfur isotope fractionation during anaerobic bacterial disproportionation of elemental sulfur. *Geochem. Cosmochim. Acta* 65, 1601–1609. [https://doi.org/10.1016/S0016-7037\(00\)00628-1](https://doi.org/10.1016/S0016-7037(00)00628-1).
- Bottrell, S., Tellam, J., Bartlett, R., Hughes, A., 2008. Isotopic composition of sulfate as a tracer of natural and anthropogenic influences on groundwater geochemistry in an urban sandstone aquifer, Birmingham, UK. *Appl. Geochem.* 23, 2382–2394. <https://doi.org/10.1016/j.apgeochem.2008.03.012>.
- Braitsch, O., Herrmann, A.G., 1963. Zur Geochemie des Broms in salinaren Sedimenten: Teil I: experimentelle Bestimmung der Br-Verteilung in verschiedenen natürlichen Salzsystemen. *Geochem. Cosmochim. Acta* 27, 361–391. [https://doi.org/10.1016/0016-7037\(63\)90077-2](https://doi.org/10.1016/0016-7037(63)90077-2).
- Brand, W.A., Geilmann, H., Crosson, E.R., Rella, C.W., 2009. Cavity ring-down spectroscopy versus high-temperature conversion isotope ratio mass spectrometry; a case study on $\delta^2\text{H}$ and $\delta^{18}\text{O}$ of pure water samples and. *Rapid Commun. Mass Spectrom.* <https://doi.org/10.1002/rcm.4083>.
- Brenot, A., Carignan, J., France-Lanord, C., Benoit, M., 2007. Geological and land use control on $\delta^{34}\text{S}$ and $\delta^{18}\text{O}$ of river dissolved sulfate: the Moselle river basin, France. *Chem. Geol.* 244, 25–41. <https://doi.org/10.1016/j.chemgeo.2007.06.003>.
- Brenot, A., Négrel, P., Petelet-Giraud, E., Millot, R., Malcuit, E., 2015. Insights from the salinity origins and interconnections of aquifers in a regional scale sedimentary aquifer system (Adour-Garonne district, SW France): contributions of $\delta^{34}\text{S}$ and $\delta^{18}\text{O}$

- from dissolved sulfates and the $^{87}\text{Sr}/^{86}\text{Sr}$ ratio. *Appl. Geochem.* 53, 27–41. <https://doi.org/10.1016/J.APGEOCHEM.2014.12.002>.
- Brunner, B., Bernasconi, S.M., Kleikemper, J., Schroth, M.H., 2005. A model for oxygen and sulfur isotope fractionation in sulfate during bacterial sulfate reduction processes. *Geochem. Cosmochim. Acta* 69, 4773–4785. <https://doi.org/10.1016/J.GCA.2005.04.017>.
- Bruns, B., di Primio, R., Berner, U., Littke, R., 2013. Petroleum system evolution in the inverted Lower Saxony Basin, northwest Germany: a 3D basin modeling study. *Geofluids* 13, 246–271. <https://doi.org/10.1111/gf.12016>.
- Bruns, B., Littke, R., 2015. Lithological dependency and anisotropy of vitrinite reflectance in high rank sedimentary rocks of the Ibbenbüren area, NW-Germany: implications for the tectonic and thermal evolution of the Lower Saxony Basin. *Int. J. Coal Geol.* 137, 124–135. <https://doi.org/10.1016/J.COAL.2014.11.007>.
- Burke, A., Present, T.M., Paris, G., Rae, E.C.M., Sandilands, B.H., Gaillardet, J., Peucker-Ehrenbrink, B., Fischer, W.W., McClelland, J.W., Spencer, R.G.M., Voss, B.M., Adkins, J.F., 2018. Sulfur isotopes in rivers: insights into global weathering budgets, pyrite oxidation, and the modern sulfur cycle. *Earth Planet Sci. Lett.* 496, 168–177. <https://doi.org/10.1016/J.EPSL.2018.05.022>.
- Burke, W.H., Denison, R.E., Hetherington, E.A., Koepnick, R.B., Nelson, H.F., Otto, J.B., 1982. Variation of seawater $^{87}\text{Sr}/^{86}\text{Sr}$ throughout Phanerozoic time. *Geology* 10 (516). [https://doi.org/10.1130/0091-7613\(1982\)10<516:VOSSTP>2.0.CO;2](https://doi.org/10.1130/0091-7613(1982)10<516:VOSSTP>2.0.CO;2).
- Cañedo-Argüelles, M., Kefford, B.J., Piscart, C., Prat, N., Schäfer, R.B., Schulz, C.-J., 2013. Salinisation of rivers: an urgent ecological issue. *Environ. Pollut.* 173, 157–167. <https://doi.org/10.1016/J.ENVPOL.2012.10.011>.
- Chan, L.-H., Starinsky, A., Katz, A., 2002. The behavior of lithium and its isotopes in oilfield brines: evidence from the Heletz-Kokhav field, Israel. *Geochem. Cosmochim. Acta* 66, 615–623. [https://doi.org/10.1016/S0016-7037\(01\)00800-6](https://doi.org/10.1016/S0016-7037(01)00800-6).
- Chowdhury, A.H., Scanlon, B.R., Reedy, R.C., Young, S., 2018. Fingerprinting groundwater salinity sources in the gulf coast aquifer system, USA. *Hydrogeol. J.* 26, 197–213. <https://doi.org/10.1007/s10040-017-1619-8>.
- Claypool, G.E., Holser, W.T., Kaplan, I.R., Sakai, H., Zak, I., 1980. The age curves of sulfur and oxygen isotopes in marine sulfate and their mutual interpretation. *Chem. Geol.* 28, 199–260. [https://doi.org/10.1016/0009-2541\(80\)90047-9](https://doi.org/10.1016/0009-2541(80)90047-9).
- Craig, H., 1961. Isotopic variations in meteoric waters. *Science* 133, 1702–1703. <https://doi.org/10.1126/science.133.3465.1702>.
- Cravotta, C.A., Brady, K.B.C., 2015. Priority pollutants and associated constituents in untreated and treated discharges from coal mining or processing facilities in Pennsylvania, USA. *Appl. Geochem.* 62, 108–130. <https://doi.org/10.1016/J.APGEOCHEM.2015.03.001>.
- Davis, S.N., Whittemore, D.O., Fabryka-Martin, J., 1998. Uses of chloride/bromide ratios in studies of potable water. *Ground Water* 36, 338–350. <https://doi.org/10.1111/j.1745-6584.1998.tb01099.x>.
- Dogramaci, S.S., Herczeg, A.L., Schiff, S.L., Bone, Y., 2001. Controls on $\delta^{34}\text{S}$ and $\delta^{18}\text{O}$ of dissolved sulfate in aquifers of the murray basin, Australia and their use as indicators of flow processes. *Appl. Geochem.* 16, 475–488. [https://doi.org/10.1016/S0883-2927\(00\)0052-4](https://doi.org/10.1016/S0883-2927(00)0052-4).
- Dold, B., 2017. Acid rock drainage prediction: a critical review. *J. Geochem. Explor.* 172, 120–132. <https://doi.org/10.1016/J.GEXPLO.2016.09.014>.
- Dölling, M., Strizke, R., 2009. Geowissenschaftliche Untersuchungen im Subrosionsgebiet des „Heiligen Feldes“ (nördliches Münsterland, Nordwestdeutschland). *Geol. Palaontol. Westfalen* 72, 31–69.
- Drake, H., Whitehouse, M.J., Heim, C., Reiners, P.W., Tillberg, M., Hogmalm, K.J., Dopson, M., Broman, C., Åström, M.E., 2018. Unprecedented ^{34}S -enrichment of pyrite formed following microbial sulfate reduction in fractured crystalline rocks. *Geobiology* 16, 556–574. <https://doi.org/10.1111/gbi.12297>.
- Drozdowski, G., 1985. Tiefentektonik der Ibbenbürener Karbonscholle. In: *Beiträge Zur Tiefentektonik Westdeutscher Steinkohlelagerstätten. Geologisches Landesamt Nordrhein-Westfalen*, pp. 189–216.
- Egeberg, P.K., Aagaard, P., 1989. Origin and evolution of formation waters from oil fields on the Norwegian shelf. *Appl. Geochem.* 4, 131–142. [https://doi.org/10.1016/0883-2927\(89\)90044-9](https://doi.org/10.1016/0883-2927(89)90044-9).
- Ehrenberg, S.N., 1991. Kaolinized, potassium-leached zones at the contacts of the Garn Formation, Haltenbanken, mid-Norwegian continental shelf. *Mar. Petrol. Geol.* 8, 250–269. [https://doi.org/10.1016/0264-8172\(91\)90080-K](https://doi.org/10.1016/0264-8172(91)90080-K).
- Elphick, J.R.F., Bergh, K.D., Bailey, H.C., 2011. Chronic toxicity of chloride to freshwater species: effects of hardness and implications for water quality guidelines. *Environ. Toxicol. Chem.* 30, 239–246. <https://doi.org/10.1002/etc.365>.
- Epstein, S., Mayeda, T., 1953. Variation of O^{18} content of waters from natural sources. *Geochem. Cosmochim. Acta* 4, 213–224. [https://doi.org/10.1016/0016-7037\(53\)90051-9](https://doi.org/10.1016/0016-7037(53)90051-9).
- Faure, G., 2001. *Origin of Igneous Rocks, Origin of Igneous Rocks*. Springer Berlin Heidelberg. <https://doi.org/10.1007/978-3-662-04474-2>.
- Fontes, J.C., Matray, J.M., 1993a. Geochemistry and origin of formation brines from the Paris Basin, France: 1. Brines associated with Triassic salts. *Chem. Geol.* 109, 149–175. [https://doi.org/10.1016/0009-2541\(93\)90068-T](https://doi.org/10.1016/0009-2541(93)90068-T).
- Fontes, J.C., Matray, J.M., 1993b. Geochemistry and origin of formation brines from the Paris Basin, France: 2. Saline solutions associated with oil fields. *Chem. Geol.* 109, 177–200. [https://doi.org/10.1016/0009-2541\(93\)90069-U](https://doi.org/10.1016/0009-2541(93)90069-U).
- Foriel, J., Philippot, P., Rey, P., Somogyi, A., Banks, D., Ménez, B., 2004. Biological control of Cl/Br and low sulfate concentration in a 3.5-Gyr-old seawater from North Pole, Western Australia. *Earth Planet Sci. Lett.* 228, 451–463. <https://doi.org/10.1016/J.EPSL.2004.09.034>.
- Foti, M., Sorokin, D.Y., Lomans, B., Mussman, M., Zacharova, E.E., Pimenov, N.V., Kuenen, J.G., Muyzer, G., 2007. Diversity, activity, and abundance of sulfate-reducing bacteria in saline and hypersaline soda lakes. *Appl. Environ. Microbiol.* 73, 2093–2100. <https://doi.org/10.1128/AEM.02622-06>.
- Fritz, P., Basharmal, G.M., Drimmie, R.J., Ibsen, J., Qureshi, R.M., 1989. Oxygen isotope exchange between sulphate and water during bacterial reduction of sulphate. *Chem. Geol. Isot. Geosci.* 79, 99–105. [https://doi.org/10.1016/0168-9622\(89\)90012-2](https://doi.org/10.1016/0168-9622(89)90012-2).
- Galán, E., Gómez-Ariza, J., González, I., Fernández-Caliani, J., Morales, E., Giráldez, I., 2003. Heavy metal partitioning in river sediments severely polluted by acid mine drainage in the Iberian Pyrite Belt. *Appl. Geochem.* 18, 409–421. [https://doi.org/10.1016/S0883-2927\(02\)00092-6](https://doi.org/10.1016/S0883-2927(02)00092-6).
- Gammons, C.H., Brown, A., Poulson, S.R., Henderson, T.H., 2013. Using stable isotopes (S, O) of sulfate to track local contamination of the Madison karst aquifer, Montana, from abandoned coal mine drainage. *Appl. Geochem.* 31, 228–238. <https://doi.org/10.1016/J.APGEOCHEM.2013.01.008>.
- Gazea, B., Adam, K., Kontopoulos, A., 1996. A review of passive systems for the treatment of acid mine drainage. *Miner. Eng.* 9, 23–42. [https://doi.org/10.1016/0892-6875\(95\)00129-8](https://doi.org/10.1016/0892-6875(95)00129-8).
- Gombert, P., Sracek, O., Koukouzas, N., Gzyl, G., Valladares, S.T., Frączek, R., Klinger, C., Bauerek, A., Areces, J.E.A., Chamberlain, S., Paw, K., Pierzchała, L., 2018. An overview of priority pollutants in selected coal mine discharges in Europe. *Mine Water Environ.* 1–8. <https://doi.org/10.1007/s10230-018-0547-8>.
- Grobe, M., Machel, H.G., 2002. Saline groundwater in the Münsterland Cretaceous Basin, Germany: clues to its origin and evolution. *Mar. Petrol. Geol.* 19, 307–322. [https://doi.org/10.1016/S0264-8172\(02\)00019-3](https://doi.org/10.1016/S0264-8172(02)00019-3).
- Habicht, K.S., Canfield, D.E., 1997. Sulfur isotope fractionation during bacterial sulfate reduction in organic-rich sediments. *Geochem. Cosmochim. Acta* 61, 5351–5361. [https://doi.org/10.1016/S0016-7037\(97\)00311-6](https://doi.org/10.1016/S0016-7037(97)00311-6).
- Hardie, L., Eugster, H., 1971. Evaporation of seawater: calculated mineral sequences. *Science* 173, 481–489. <https://doi.org/10.1126/science.173.3996.481>.
- Hart, B.T., Bailey, P., Edwards, R., Hortle, K., James, K., McMahon, A., Meredith, C., Swadling, K., 1991. A review of the salt sensitivity of the Australian freshwater biota. *Hydrobiologia* 210, 105–144. <https://doi.org/10.1007/BF00014327>.
- Haubrich, F., Tichomirowa, M., 2002. Sulfur and oxygen isotope geochemistry of acid mine drainage—the polymetallic sulfide deposit “Himmelfahrt Fundgrube” in Freiberg (Germany). *Isot. Environ. Health Stud.* 38, 121–138. <https://doi.org/10.1080/10256010208033319>.
- Hayes, J.M., 2004. *An Introduction to Isotopic Calculations*. Woods Hole Oceanographic Institution, Woods Hole, MA, p. 2543.
- Heidel, C., Tichomirowa, M., 2011. The isotopic composition of sulfate from anaerobic and low oxygen pyrite oxidation experiments with ferric iron - new insights into oxidation mechanisms. *Chem. Geol.* 281, 305–316. <https://doi.org/10.1016/j.chemgeo.2010.12.017>.
- Heidel, C., Tichomirowa, M., Breitkopf, C., 2011. Sphalerite oxidation pathways detected by oxygen and sulfur isotope studies. *Appl. Geochem.* 26, 2247–2259. <https://doi.org/10.1016/j.apgeochem.2011.08.007>.
- Heidel, C., Tichomirowa, M., Junghans, M., 2013. Oxygen and sulfur isotope investigations of the oxidation of sulfide mixtures containing pyrite, Galena, and sphalerite. *Chem. Geol.* 342, 29–43. <https://doi.org/10.1016/j.chemgeo.2013.01.016>.
- Holser, W.T., Kaplan, I.R., 1966. Isotope geochemistry of sedimentary sulfates. *Chem. Geol.* 1, 93–135. [https://doi.org/10.1016/0009-2541\(66\)90011-8](https://doi.org/10.1016/0009-2541(66)90011-8).
- Horita, J., 1988. Hydrogen isotope analysis of natural waters using an H_2 -water equilibration method: a special implication to brines. *Chem. Geol. Isot. Geosci.* 72, 89–94. [https://doi.org/10.1016/0168-9622\(88\)90040-1](https://doi.org/10.1016/0168-9622(88)90040-1).
- Horita, J., Friedman, T.J., Lazar, B., Holland, H.D., 1991. The composition of Permian seawater. *Geochem. Cosmochim. Acta* 55, 417–432. [https://doi.org/10.1016/0016-7037\(91\)90001-L](https://doi.org/10.1016/0016-7037(91)90001-L).
- Horita, J., Ueda, A., Mizukami, K., Takatori, I., 1989. Automatic δD and $\delta^{18}\text{O}$ analyses of multi-water samples using H_2 - and CO_2 -water equilibration methods with a common equilibration set-up. *Int. J. Radiat. Appl. Instrum. Part 40*, 801–805. [https://doi.org/10.1016/0883-2889\(89\)90100-7](https://doi.org/10.1016/0883-2889(89)90100-7).
- Horita, J., Zimmermann, H., Holland, H.D., 2002. Chemical evolution of seawater during the Phanerozoic: implications from the record of marine evaporites. *Geochem. Cosmochim. Acta* 66, 3733–3756. [https://doi.org/10.1016/S0016-7037\(01\)00884-5](https://doi.org/10.1016/S0016-7037(01)00884-5).
- Johnson, D.B., Hallberg, K.B., 2005. Acid mine drainage remediation options: a review. *Sci. Total Environ.* 338, 3–14. <https://doi.org/10.1016/J.SCITOTENV.2004.09.002>.
- Kampschulte, A., Strauss, H., 2004. The sulfur isotopic evolution of Phanerozoic seawater based on the analysis of structurally substituted sulfate in carbonates. *Chem. Geol.* 204, 255–286. <https://doi.org/10.1016/J.CHEMGEO.2003.11.013>.
- Katz, B.G., Eberts, S.M., Kauffman, L.J., 2011. Using Cl/Br ratios and other indicators to assess potential impacts on groundwater quality from septic systems: a review and examples from principal aquifers in the United States. *J. Hydrol.* 397, 151–166. <https://doi.org/10.1016/J.JHYDROL.2010.11.017>.
- Kendall, C., Doctor, D.H., 2003. Stable isotope applications in hydrologic studies. In: *Treatise on Geochemistry*, pp. 319–364. <https://doi.org/10.1016/B0-08-043751-6/05081-7>.
- Kloppmann, W., Négrel, P., Casanova, J., Klinge, H., Schelkes, K., Guerrot, C., 2001. Halite dissolution derived brines in the vicinity of a Permian salt dome (N German Basin). Evidence from boron, strontium, oxygen, and hydrogen isotopes. *Geochem. Cosmochim. Acta* 65, 4087–4101. [https://doi.org/10.1016/S0016-7037\(01\)00640-8](https://doi.org/10.1016/S0016-7037(01)00640-8).
- Knauth, L.P., Beeunas, M.A., 1986. Isotope geochemistry of fluid inclusions in Permian halite with implications for the isotopic history of ocean water and the origin of saline formation waters. *Geochem. Cosmochim. Acta* 50, 419–433. [https://doi.org/10.1016/0016-7037\(86\)90195-X](https://doi.org/10.1016/0016-7037(86)90195-X).
- Knöller, K., Fauville, A., Mayer, B., Strauch, G., Friese, K., Veizer, J., 2004. Sulfur cycling in an acid mining lake and its vicinity in Lusatia, Germany. *Chem. Geol.* 204, 303–323. <https://doi.org/10.1016/J.CHEMGEO.2003.11.009>.

- Lotze, F., Semmler, W., Kötter, K., Mausolf, F., 1962. Hydrogeologie des Westteils der Ibbenbürener Karbonscholle. Springer Fachmedien Wiesbaden GmbH. <https://doi.org/10.1007/978-3-6663-02578-8>.
- MacCausland, A., McTammany, M.E., 2007. The impact of episodic coal mine drainage pollution on benthic macroinvertebrates in streams in the Anthracite region of Pennsylvania. *Environ. Pollut.* 149, 216–226. <https://doi.org/10.1016/j.envpol.2006.12.030>.
- McCaffrey, M.A., Lazar, B., Holland, H.D., 1987. The evaporation path of seawater and the coprecipitation of Br⁻ and K⁺ with halite. *J. Sediment. Petrol.* 57, 928–938.
- McKnight, D.M., Feder, G.L., 1984. The ecological effect of acid conditions and precipitation of hydrous metal oxides in a Rocky Mountain stream. *Hydrobiologia* 119, 129–138. <https://doi.org/10.1007/BF00011952>.
- Migaszweski, Z.M., Gaiuszka, A., Dołęgowska, S., 2018. Stable isotope geochemistry of acid mine drainage from the Wiśniówka area (south-central Poland). *Appl. Geochem.* 95, 45–56. <https://doi.org/10.1016/j.apgeochem.2018.05.015>.
- Millero, F.J., Feistel, R., Wright, D.G., McDougall, T.J., 2008. The composition of standard seawater and the definition of the reference-composition salinity scale. *Deep-Sea Res. Part I Oceanogr. Res. Pap.* 55, 50–72. <https://doi.org/10.1016/j.dsr.2007.10.001>.
- MKULMV, 2016. Hintergrundpapier Steinkohle zum Bewirtschaftungsplan 2019-2021 für die nordrhein-westfälischen Anteile von Rhein, Weser, Ems und Maas. *Arnsberg*.
- Moodley, I., Sheridan, C.M., Kappelmeyer, U., Akcil, A., 2018. Environmentally sustainable acid mine drainage remediation: research developments with a focus on waste/by-products. *Miner. Eng.* 126, 207–220. <https://doi.org/10.1016/j.mineng.2017.08.008>.
- Müller, G., Nielsen, H., Ricke, W., 1966. Schwefel-Isotopen-Verhältnisse in Formationswässern und Evaporiten Nord- und Süddeutschlands. *Chem. Geol.* 1, 211–220. [https://doi.org/10.1016/0009-2541\(66\)90017-9](https://doi.org/10.1016/0009-2541(66)90017-9).
- Munoz, Y.A., Littke, R., Brix, M.R., 2007. Fluid systems and basin evolution of the western Lower Saxony Basin, Germany. *Geofluids* 7, 335–355. <https://doi.org/10.1111/j.1468-8123.2007.00186.x>.
- Naidu, G., Ryu, S., Thiruvenkatachari, R., Choi, Y., Jeong, S., Vigneswaran, S., 2019. A critical review on remediation, reuse, and resource recovery from acid mine drainage. *Environ. Pollut.* 247, 1110–1124. <https://doi.org/10.1016/j.envpol.2019.01.085>.
- Neal, C., Whitehead, P.G., Jeffery, H., Neal, M., 2005. The water quality of the river Carnon, west Cornwall, November 1992 to March 1994: the impacts of wheal Jane discharges. *Sci. Total Environ.* 338, 23–39. <https://doi.org/10.1016/j.scitotenv.2004.09.003>.
- Nieto, J.M., Sarmiento, A.M., Ollás, M., Canovas, C.R., Riba, I., Kalman, J., Delvals, T.A., 2007. Acid mine drainage pollution in the Tinto and Odiel rivers (Iberian pyrite belt, SW Spain) and bioavailability of the transported metals to the Huelva estuary. *Environ. Int.* 33, 445–455. <https://doi.org/10.1016/j.envint.2006.11.010>.
- Novák, M., Jäcková, I., Prechová, E., 2001. Temporal trends in the isotope signature of air-borne sulfur in Central Europe. *Environ. Sci. Technol.* 35, 255–260. <https://doi.org/10.1021/es0000753>.
- Oren, A., 1999. Bioenergetic aspects of halophilism. *Microbiol. Mol. Biol. Rev.* 63, 334–348. <https://doi.org/10.1128/mmb.63.2.334-348.1999>.
- Otero, N., Soler, A., 2002. Sulphur isotopes as tracers of the influence of potash mining in groundwater salinisation in the Llobregat Basin (NE Spain). *Water Res.* 36, 3989–4000. [https://doi.org/10.1016/S0043-1354\(02\)00125-2](https://doi.org/10.1016/S0043-1354(02)00125-2).
- Otero, N., Soler, A., Canals, A., 2008. Controls of $\delta^{34}\text{S}$ and $\delta^{18}\text{O}$ in dissolved sulphate: learning from a detailed survey in the Llobregat River (Spain). *Appl. Geochem.* 23, 1166–1185. <https://doi.org/10.1016/j.apgeochem.2007.11.009>.
- Panno, S.V., Hackley, K.C., Hwang, H.H., Greenberg, S.E., Krapac, I.G., Landsberger, S., O'Kelly, D.J., 2006. Characterization and identification of Na-Cl sources in ground water. *Ground Water* 44, 176–187. <https://doi.org/10.1111/j.1745-6584.2005.00127.x>.
- Parbhakar-Fox, A., Lottermoser, B.G., 2015. A critical review of acid rock drainage prediction methods and practices. *Miner. Eng.* 82, 107–124. <https://doi.org/10.1016/j.mineng.2015.03.015>.
- Parkhurst, D.L., Appelo, C.A.J., 1999. User's Guide to PHREEQC (Version 2) : a Computer Program for Speciation, Batch-Reaction, One-Dimensional Transport, and Inverse Geochemical Calculations, Water-Resources Investigations Report. <https://doi.org/10.3133/wri994259>.
- Pfahl, S., Sodemann, H., 2014. What controls deuterium excess in global precipitation? *Clim. Past* 10, 771–781. <https://doi.org/10.5194/cp-10-771-2014>.
- Révész, K., Haiping, Q., Coplen, T.B., 2012. Determination of the $\delta^{34}\text{S}$ of sulfate in water; RSL lab code 1951, chap. 10 of Stable isotope-ratio methods, sec. C. In: *Book 10, Methods of the Reston Stable Isotope Laboratory*.
- Riley, J.P., Tongudai, M., 1964. The lithium content of sea water. *Deep Sea Res. Oceanogr. Abstr.* 11, 563–568. [https://doi.org/10.1016/0011-7471\(64\)90002-6](https://doi.org/10.1016/0011-7471(64)90002-6).
- Rudakov, Dmitry V., Coldewey, Wilhelm G., Goerke-Mallet, P., 2014. Modeling the inflow and discharge from underground structures within the abandoned hardcoal mining area of west field (Ibbenbüren). In: Sui, Wanghua, Sun, Yajun, Wang, C. (Eds.), *An Interdisciplinary Response to Mine Water Challenges. 12th International Mine Water Association Congress (IMWA 2014)*. China University of Mining and Technology, Xuzhou, China, pp. 699–705.
- Schlosser, P., Stute, M., Dörr, H., Sonntag, C., Münnich, K.O., 1988. Tritium/³He dating of shallow groundwater. *Earth Planet Sci. Lett.* 89, 353–362. [https://doi.org/10.1016/0012-821X\(88\)90122-7](https://doi.org/10.1016/0012-821X(88)90122-7).
- Scott, A.D., Smith, S.J., 1966. Susceptibility of interlayer potassium in micas to exchange with sodium. *Clay Clay Miner.* 69–81. <https://doi.org/10.1016/B978-0-08-011908-3.50008-6>.
- Scullion, J., Edwards, R.W., 1980. The effect of pollutants from the coal industry on the fish fauna of a small river in the South Wales coalfield. *Environ. Pollut. Ecol. Biol.* 21, 141–153. [https://doi.org/10.1016/0143-1471\(80\)90042-2](https://doi.org/10.1016/0143-1471(80)90042-2).
- Seal, R.R., 2006. Sulfur isotope geochemistry of sulfide minerals. *Rev. Mineral. Geochem.* 61, 633–677. <https://doi.org/10.2138/rmg.2006.61.12>.
- Senglaub, Y., Brix, M.R., Adriasola, A.C., Littke, R., 2005. New information on the thermal history of the southwestern Lower Saxony Basin, northern Germany, based on fission track analysis. *Int. J. Earth Sci.* 94, 876–896. <https://doi.org/10.1007/s00531-005-0008-z>.
- Shalev, N., Lazar, B., Köbberich, M., Halicz, L., Gavrieli, I., 2018. The chemical evolution of brine and Mg-K-salts along the course of extreme evaporation of seawater – an experimental study. *Geochem. Cosmochim. Acta* 241, 164–179. <https://doi.org/10.1016/j.gca.2018.09.003>.
- Siemann, M.G., Schramm, M., 2000. Thermodynamic modelling of the Br partition between aqueous solutions and halite. *Geochem. Cosmochim. Acta* 64, 1681–1693. [https://doi.org/10.1016/S0016-7037\(99\)00385-3](https://doi.org/10.1016/S0016-7037(99)00385-3).
- Simate, G.S., Ndlovu, S., 2014. Acid mine drainage: challenges and opportunities. *J. Environ. Chem. Eng.* 2, 1785–1803. <https://doi.org/10.1016/j.jece.2014.07.021>.
- Stammeier, J.A., Hippler, D., Nebel, O., Leis, A., Grengg, C., Mittermayr, F., Kasemann, S.A., Dietzel, M., 2019. Radiogenic Sr and stable C and O isotopes across Precambrian-Cambrian transition in marine carbonatic phosphorites of Malý Karatau (Kazakhstan)—implications for Paleo-environmental change. *G-cubed* 20, 3–23. <https://doi.org/10.1029/2018GC007767>.
- Strauss, H., 1997. The isotopic composition of sedimentary sulfur through time. *Palaeogeogr. Palaeoclimatol. Palaeoecol.* 132, 97–118. [https://doi.org/10.1016/S0031-0182\(97\)00067-9](https://doi.org/10.1016/S0031-0182(97)00067-9).
- Stueber, A.M., Walter, L.M., Huston, T.J., Pushkar, P., 1993. Formation waters from Mississippian-Pennsylvanian reservoirs, Illinois basin, USA: chemical and isotopic constraints on evolution and migration. *Geochem. Cosmochim. Acta* 57, 763–784. [https://doi.org/10.1016/0016-7037\(93\)90167-U](https://doi.org/10.1016/0016-7037(93)90167-U).
- Stumpp, C., Klaus, J., Stichler, W., 2014. Analysis of long-term stable isotopic composition in German precipitation. *J. Hydrol.* 517, 351–361. <https://doi.org/10.1016/j.jhydrol.2014.05.034>.
- Taylor, B.E., Wheeler, M.C., Nordstrom, D.K., 1984. Stable isotope geochemistry of acid mine drainage: experimental oxidation of pyrite. *Geochem. Cosmochim. Acta* 48, 2669–2678. [https://doi.org/10.1016/0016-7037\(84\)90315-6](https://doi.org/10.1016/0016-7037(84)90315-6).
- Thamdrup, B., Finster, K., Hansen, J.W., Bak, F., 1993. Bacterial disproportionation of elemental sulfur coupled to chemical reduction of iron or manganese. *Appl. Environ. Microbiol.* 59, 101–108.
- Thyne, G., Boudreau, B.P., Ramm, M., Midtbø, R.E., 2001. Simulation of potassium feldspar dissolution and illitization in the Staffjord formation, North Sea. *Am. Assoc. Petrol. Geol. Bull.* 85, 621–635. <https://doi.org/10.1306/8626C965-173B-11D7-8645000102C1865D>.
- Tichomirowa, M., Heidel, C., Junghans, M., Haubrich, F., Matschullat, J., 2010. Sulfate and strontium water source identification by O, S and Sr isotopes and their temporal changes (1997–2008) in the region of Freiberg, central-eastern Germany. *Chem. Geol.* 276, 104–118. <https://doi.org/10.1016/j.chemgeo.2010.06.004>.
- Timpano, A.J., Schoenholtz, S.H., Soucek, D.J., Zipper, C.E., 2015. Salinity as a limiting factor for biological condition in mining-influenced central Appalachian headwater streams. *J. Am. Water Resour. Assoc.* 51, 240–250. <https://doi.org/10.1111/jawr.12247>.
- Turchyn, A.V., Schrag, D.P., 2006. Cenozoic evolution of the sulfur cycle: insight from oxygen isotopes in marine sulfate. *Earth Planet Sci. Lett.* 241, 763–779. <https://doi.org/10.1016/j.epsl.2005.11.007>.
- Turek, M., 2004. Electrodialytic desalination and concentration of coal-mine brine. *Desalination* 162, 355–359. [https://doi.org/10.1016/S0011-9164\(04\)00069-4](https://doi.org/10.1016/S0011-9164(04)00069-4).
- Utrilla, R., Pierre, C., Orti, F., Pueyo, J.J., 1992. Oxygen and sulphur isotope compositions as indicators of the origin of Mesozoic and Cenozoic evaporites from Spain. *Chem. Geol.* 102, 229–244. [https://doi.org/10.1016/0009-2541\(92\)90158-2](https://doi.org/10.1016/0009-2541(92)90158-2).
- Wang, N., Dorman, R.A., Ingersoll, C.G., Hardesty, D.K., Brumbaugh, W.G., Hammer, E.J., Bauer, C.R., Mount, D.R., 2016. Acute and chronic toxicity of sodium sulfate to four freshwater organisms in water-only exposures. *Environ. Toxicol. Chem.* 35, 115–127. <https://doi.org/10.1002/etc.3148>.
- Wendland, F., Hannappel, S., Kunkel, R., Schenk, R., Voigt, H.J., Wolter, R., 2005. A procedure to define natural groundwater conditions of groundwater bodies in Germany. *Water Sci. Technol.* 51, 249–257. <https://doi.org/10.2166/wst.2005.0598>.
- Wilkinson, M., Haszeldine, R.S., Morton, A., Fallick, A.E., 2014. Deep burial dissolution of K-feldspars in a fluvial sandstone, Pentland formation, UK central North Sea. *J. Geol. Soc. (Lond.)* 171, 635–647. <https://doi.org/10.1144/jgs2013-144>.
- Wolkersdorfer, C., 2008. Water Management at Abandoned Flooded Underground Mines. Springer, Berlin, Heidelberg. <https://doi.org/10.1007/978-3-540-77331-3>.
- Wüstefeld, P., Hilde, U., Koehler, B., Adelmann, D., Hilgers, C., 2017. Critical evaluation of an Upper Carboniferous tight gas sandstone reservoir analog: diagenesis and petrophysical aspects. *Mar. Petrol. Geol.* 86, 689–710. <https://doi.org/10.1016/j.marpetgeo.2017.05.034>.
- Zhang, Y.C., Slomp, C.P., Broers, H.P., Passier, H.F., Cappellen, P. Van, 2009. Denitrification coupled to pyrite oxidation and changes in groundwater quality in a shallow sandy aquifer. *Geochem. Cosmochim. Acta* 73, 6716–6726. <https://doi.org/10.1016/j.gca.2009.08.026>.
- Zhu, C., 2005. In situ feldspar dissolution rates in an aquifer. *Geochem. Cosmochim. Acta* 69, 1435–1453. <https://doi.org/10.1016/j.gca.2004.09.005>.

Chapter 6: Conclusion

The present dissertation formulates and applies a multiple continuum approach to characterize advective and diffusive reactive transport processes in post-mining coal zones. This type of numerical modeling represents a novel attempt to simulate water-rock interaction in fractured overburdens compared to commonly employed lumped or equivalent continuum models. Specifically, two different flow regimes are modelled simultaneously: a highly permeable one with low storage (fractures) and a less permeable one with high storage (porous matrix blocks). The effectiveness of the approach was evaluated here by simulating the origin, generation, transport, and discharged volume of acid mine drainage within the shallow and fractured overburden of the Ibbenbüren Westfield.

Analyses on core samples from the area show the strong influence that mining-derived fractures have on the water-rock interaction within the Carboniferous sequence. These structures, which broadly segment the rock sequence into several pieces, create weathering fronts on both sides of their planes with formation of oxidized pyrite and amorphous iron hydroxides. The distribution of both elements right in the fractured segments reveals how oxygenated water flows through the fractures, exchanging locally with the matrix, where it interacts with previously locked rock minerals. This evidence allowed me to design and build the dual continuum numerical model to simulate, at first, the flow component of the field. Simulation results, which successfully reproduce the transient discharge of the Westfield drainage, show the fractured continuum as the main responsible for the strong and short peak discharge events during the winter months, while the flow within the matrix continuum greatly influences the smooth recession limb of the dry periods. I also found that the direction and amount of water exchanged between the two continua depends on the element that dominates the flow in each season. Thus, water flows from the fracture to the matrix during the winter months due to its higher saturation and pressure in the fractured continuum. The flow reverses in the summer months when the relative potential of the matrix increases due to fracture desaturation. However, continued matrix desaturation in prolonged summers increases its capillary pressure, causing the matrix to reabsorb water infiltrating through the overburden. The latter makes the simulated discharge not easily responsive to summer precipitation events, as also shown by measured data in the area.

With the flow component calibrated, the transport and geochemical elements are included in the model. For this purpose, the two-continuum setup is extended to a multiple continua model with five nested blocks strings: one for the fractures and four for the rock matrix. The addition of continua is necessary to avoid under-representations of kinetic reactions with short equilibrium length scales and numerical instabilities due to lack of chemical and flow gradients within the matrix. Results from the 5-continua benchmark scenario provide high accuracy when calculating diffusive and advective exchange among the domains, as well as realistic long- and short-term geochemical evolution for 1) concentrations and discharges of ions measured at the drainage of the Westfield, and 2) reactive fronts of pyrite oxidation and iron hydroxide precipitation identified in core samples. Both matches required the simulation of dissolution, precipitation and dilution processes of iron, sulfate and chloride-bearing minerals and solutions, through a 5-step process that emulates the mining history of the area. Likewise, I used for the reactive transport model most of the hydraulic parameters calibrated for the dual continuum flow setup, which turned out to be easier since they are simpler to parameterize in the latter.

Finally, simulations of both flow and reactive transport components reveal two sensitive aspects that must be considered when applying the dual or multiple continuum approach. On the one hand, it is important to use an accurate water balance for the area, as the fractured continuum reacts easily to recharge events that may cause significant discrepancies. On the other hand, I found that the parameters of the capillary function for the fractured continuum (especially alpha) are highly sensitive to the simulation of fluid exchange between the two continua, which inherently affects the water-rock interaction within the matrix. A good fit of the van Genuchten capillary function for the fractured continuum is found here by setting all its parameters to values that resemble a permeable medium, with large pore diameters, similar to a gravel. Actually, treating the entire fractured continuum as a porous medium with enhanced hydraulic properties is a simplification that fits the post-mining zone quite well when compared to other dual-continuum models (e.g., Kordilla et al. 2012; Dal Soglio et al. 2020). The presence of an undisturbed overburden above the fracture zone reduces the flow velocity of water entering into the fractures, favoring the application of a Darcian porous-media numerical solution.

6.1 Future work

Subsequent research could focus on applying the multiple continuum model to similar coal mining settings. This would either corroborate the suitability of the conceptualized parameters or find those sensitive variables that require change and, thus, further investigation for the approach. The most convenient case might be the shallow overburden of the Ibbenbüren

Eastfield where almost the same flow and geochemical settings constructed for the Westfield can be employed. Similarities include mining-derived fracture zones as the main elements of meteoric water transport in the first 300 m of the overburden, as shown by isotopic analyses in Chapter 5. Furthermore, lateral water inflows in this shallow mining section can be ruled out, as there is no evidence of $\delta^{34}\text{S}$ in SO_4 linked to the dissolution of halite, gypsum, or anhydrite from the surrounding Mesozoic formations. What does need to be added, however, is a thick Quaternary aquitard at the surface that would potentially limit the inflow of rainfall water and the diffusion of gaseous oxygen. Also, this new model can employ measurements of $\delta^{34}\text{S}$ in sulfates and $\delta^{18}\text{O}$, $\delta^2\text{H}$, and Tritium in water as a calibration method. For the deeper Eastfield overburden, the multiple continuum approach is no longer applicable since mass transport has been attributed to a few regional faults. It should be noted that the approach is valid for cases where fractures densities are high enough to average their behavior in a single network of common properties (Barenblatt et al. 1960; Neuman 2005; Kovács and Sauter 2007).

Future work may also include in the proposed simulation framework geochemical and transport processes that are commonly observed in mined areas but are seldom modeled. Among them, I highlight the formation of efflorescent salts (i.e., solid hydrated sulfates) resulting from the evaporation of acid mine water in cavities of the unsaturated zone. Modeling these precipitates requires simultaneous consideration of infiltration and evaporation processes in cavities with well-defined relative humidity, temperature, and ventilation conditions. Despite its complexity, the implementation of such a boundary in the present model can be assisted with the theory and semi-physical evaporation model of nuclear repositories developed by Ghezzehei et al. (2004) in TOUGHREACT. As results, this step will predict deposition of evaporite minerals as potential metal sinkers while more accurately characterizing the interface of the fractured overburden (already a dual continuum media) with open cavities (i.e., new elements with completely different physical and hydraulic conditions).

Finally, the model would benefit greatly from the inclusion of a dynamic phreatic level that can emulate groundwater rebound after mine closure. This process requires measurements of water potentials during the mine flooding in order to validate calibrated hydraulic and physical properties of the fractured medium for its simulation. Running such a process would also account for the dissolution of hydrated sulfates proposed in the previous step, providing more accurate first flush ionic concentrations to be used in the capillary-gravitational equilibrium. In the same vein, the model could subsequently describe the stratification of highly mineralized rebounding waters as well as upward diffusive deep-water fronts if thermal data along the depth profile are included. Simulation of both processes would allow us to analyze long-term mine

water distribution in the fractured and porous media of the overburden, while comparing them with widely documented results from open shafts (e.g., see the compilation made by Coldewey et al. 1999; Nuttall and Younger 2004; Mugova and Wolkersdorfer 2022).

6.2 References

- Barenblatt GI, Zheltov IP, Kochina IN (1960) Basic concepts in the theory of seepage of homogeneous liquids in fissured rocks [strata]. *J Appl Math Mech* 24:1286–1303. [https://doi.org/10.1016/0021-8928\(60\)90107-6](https://doi.org/10.1016/0021-8928(60)90107-6)
- Coldewey WG, Hewig R, Richter R, et al (1999) Mittelfristige Entwicklung des Chemismus und der Dichteschichtungen von Grubenwässern in Bergwerken und ihre Auswirkungen auf nutzbares Grund- und Oberflächenwasser [Medium-term development of the chemism and density stratification of mine water and their impact on usable groundwater and surface water] Deutsche Montan Technologie GmbH. Essen, Germany
- Dal Soglio L, Danquigny C, Mazzilli N, et al (2020) Modeling the matrix-conduit exchanges in both the epikarst and the transmission zone of Karst systems. *Water (Switzerland)* 12:1–19. <https://doi.org/10.3390/w12113219>
- Ghezzehei TA, Trautz RC, Finsterle S, et al (2004) Modeling Coupled Evaporation and Seepage in Ventilated Cavities. *Vadose Zo J* 3:806–818. <https://doi.org/10.2113/3.3.806>
- Kordilla J, Sauter M, Reimann T, Geyer T (2012) Simulation of saturated and unsaturated flow in karst systems at catchment scale using a double continuum approach. *Hydrol Earth Syst Sci* 16:3909–3923. <https://doi.org/10.5194/hess-16-3909-2012>
- Kovács A, Sauter M (2007) Modelling karst hydrodynamics. In: Goldscheider N, Drew D (eds) *Methods in Karst Hydrogeology*. Taylor & Francis, London, pp 201–222
- Mugova E, Wolkersdorfer C (2022) Density stratification and double-diffusive convection in mine pools of flooded underground mines – A review. *Water Res* 214:118033. <https://doi.org/10.1016/j.watres.2021.118033>
- Neuman SP (2005) Trends, prospects and challenges in quantifying flow and transport through fractured rocks. *Hydrogeol J* 13:124–147. <https://doi.org/10.1007/s10040-004-0397-2>
- Nuttall CA, Younger PL (2004) Hydrochemical stratification in flooded underground mines: an overlooked pitfall. *J Contam Hydrol* 69:101–114. [https://doi.org/10.1016/S0169-7722\(03\)00152-9](https://doi.org/10.1016/S0169-7722(03)00152-9)

Eigenständigkeitserklärung

Hiermit erkläre ich, dass diese Arbeit bisher von mir weder an der Mathematisch-Naturwissenschaftlichen Fakultät der Universität Greifswald noch einer anderen wissenschaftlichen Einrichtung zum Zwecke der Promotion eingereicht wurde.

Ferner erkläre ich, dass ich diese Arbeit selbstständig verfasst und keine anderen als die darin angegebenen Hilfsmittel und Hilfen benutzt und keine Textabschnitte eines Dritten ohne Kennzeichnung übernommen habe.

Greifswald, den 16. Januar 2023

Diego Alexander Bedoya Gonzalez

Curriculum Vitae

Education

- Since May 2019 **Ph.D. candidate** in Hydrogeology / Universität Greifswald, Greifswald, Germany
- Thesis:** Reactive transport modeling in geomechanically dynamic coal mine systems - Numerical approaches to characterize subsurface mine- water interactions
- September 2016 – September 2018 **Master in Science:** Hydrogeology and Environmental Geosciences / Georg August Universität Göttingen, Göttingen, Germany
- Thesis:** Hydraulic fluid flow-back (HFF) spill patterns related to fault reactivation during unconventional reservoir development and operation
- February 2009 – April 2014 **Bachelor in Science:** Geology / Universidad Nacional de Colombia, Bogota, Colombia
- Thesis:** Seismological attenuation models for a section of the Colombian Andes foothills using coda waves.

Work Experience

- May 2019 – July 2022 **Paris Lodron University Salzburg / Research Assistant**
- Reactive transport simulation of geomechanically modified sedimentary sequences after underground mining activities:
- ▶ Investigating numerical approaches to characterize the origin and transport of contaminants in fractured and partially saturated media.
 - ▶ Setting up and implementing equivalent continuum, dual continuum, multiple interacting continua, and discrete groundwater models.
 - ▶ Development of scientific papers and presentations at international congresses.
- October 2018 – January 2019 **EIATEC SAS / Hydrogeologist**
- Environmental impact assessment (EIA) to modify the exploitation license of a coal area in Cesar, Colombia:
- ▶ Construction of the conceptual hydrogeological model for the exploitation of an unconventional methane reservoir and reinjection of fluids to deep reservoirs.
 - ▶ Developing the environmental management plan.
 - ▶ Editing the geology, geomorphology, and geotechnical chapters of the final technical report.

- July 2017 –
December 2017
- Georg-August-Universität Göttingen / Student Assistant**
- Thin section petrography using polarized light and scanning electron microscopy
- ▶ Identifying flow structures, textures, and hydrothermal alterations in thin sections belonging to sedimentary units from southwestern Germany.
- October 2015 –
June 2016
- HMV Ingenieros / Environmental Geologist**
- Environment Alternatives Assessment for the electricity grid reinforcement between La Virginia and Alférez cities, Colombia:
- ▶ Collecting and analyzing mechanical soil probes, geotechnical information, quarry database, and intrinsic geological parameters.
 - ▶ Assessing the alternatives' susceptibility to landslide processes based on lithological, morphological, climatological, seismic, hydrological, and hydrogeological features.
 - ▶ Writing and socialization of the final report for scientific peers of the environmental authority.
- July 2015 –
September 2015
- Acuiferos S.A.S. / Environmental Geologist**
- Hydrogeological study for the construction of the "Río Magdalena-2" Highway between Remedios and Alto Dolores cities, Colombia.
- ▶ Collecting and analyzing lithological, stratigraphic, and structural data, including brittle and ductile deformations.
 - ▶ Measuring water infiltration values and groundwater potentials.
 - ▶ Producing detailed geological maps at 1:10,000 scale.
 - ▶ Writing the final technical report for the environmental authority
- May 2014 –
May 2015
- Geoestudios LTDA. / Geologist**
- Geological field exploration activities focused on the analysis of potential development areas for the cement and oil & gas industries.
- ▶ Collecting rock samples, lithologic and structural data.
 - ▶ Analyzing drill core samples using optical and chemical techniques.
 - ▶ Producing geological maps, structural profiles, and stratigraphic columns at 1:1,000 and 1:10,000 scales.
 - ▶ Calculation of limestone reserves for 2 exploitation prospects.
 - ▶ Writing partial and final technical reports.

Training & skills

Training

- ▶ Geothermal-DHC Training School (20-24/09/2021)
- ▶ Reactive Transport modelling with OpenGeoSys-6 (29-30/06/2021)
- ▶ Short course in applied reactive transport modelling (10-14/06/2019)
- ▶ Introduction to Using the VIC Hydrologic Model with NASA Earth Observations (15-28/02/2018)
- ▶ Decentralized Safe Drinking Water (03/10/2016 – 24/02/2017)
- ▶ Reservoir Geomechanics (01/04/2014 – 10/06/2014)

PC skills

TOUGHREACT
MODFLOW
FEFLOW
SURFER
ARCGIS
AUTOCAD
MATLAB / R & RSTUDIO

Languages

Spanish: Native language
English: Full professional proficiency
German: Limited working proficiency

List of publications

Bedoya-Gonzalez, D., Hilberg, S., Kessler, T., Schafmeister, M.-T. & Rinder, T. (Subm.) A multiple interactive continua model (MINC) to simulate reactive mass transport in a post-mining coal zone: A case study of the Ibbenbüren Westfield. *Mine Water and the Environment Journal*

Bedoya-Gonzalez, D., Kessler, T., Rinder, T. & Schafmeister, M. T. (2022) A Dual Continuum model (TOUGH2) for characterizing flow and discharge in a mechanically disrupted sandstone overburden. *Hydrogeol J.* <https://doi.org/10.1007/s10040-022-02507-3>.

Fazio, M., Ibemesi, P., Benson P., **Bedoya-González, D.**, Sauter, M. (2021) The role of rock matrix permeability in controlling hydraulic fracturing in sandstones. *Rock Mech Rock Eng* 54:5269. <https://doi.org/10.1007/s00603-021-02580-2>

Bedoya-Gonzalez, D., Kessler, T. & Schafmeister, M.-T. (2021) Employment of A Double Continuum Model to Characterize Groundwater Flow In Underground Post-Mining Setups: Case Study Of The Ibbenbüren Westfield. In: Stanley, P., Wolkersdorfer, C., Wolkersdorfer, K.: *Mine Water Management for Future Generations*. p. 47 – 53.

Bedoya-Gonzalez, D., Hilberg, S., Redhammer, G. & Rinder, T. (2021). A Petrographic Investigation of the Carboniferous Sequence from the Ibbenbüren Mine: Tracing the Origin of the Coal Mine Drainage. *Minerals* 11:1–19. <https://doi.org/10.3390/min11050483>.

Rinder, T.; Dietzel, M.; Stammeier, J.A.; Leis, A.; **Bedoya-González, D.**; Hilberg, S. (2020) Geochemistry of coal mine drainage, groundwater, and brines from the Ibbenbüren mine, Germany: A coupled elemental-isotopic approach. *Appl. Geochem J.*, 121. <https://doi.org/10.1016/j.apgeochem.2020.104693>

Bedoya-González, D., Vargas-Jiménez, C.A., Chicangana, G. (2014) Modelos de atenuación para una zona del piedemonte llanero colombiano utilizando atenuación de ondas coda. *Boletín de Geología*, 36:91–100, ISSN 0120-0283. <https://revistas.uis.edu.co/index.php/revistaboletindegologia/article/view/4477>

Conference Contributions

Bedoya-Gonzalez, D., Hilberg, S., Kessler, T., Schafmeister, M.-T. & Rinder, T. (2022) Application of a Double Continuum model to describe reactive transport in disrupted coal mining areas: a case study of the Ibbenbüren Westfield, Germany. 28th Tagung der Fachsektion Hydrogeologie e. V.in der DGGV e.V.: Grundwasser-Klima-Gesellschaft. 23-25 March 2022 – Virtual conference (Oral presentation).

Bedoya-Gonzalez, D., Kessler, T. & Schafmeister, M.-T. (2021) Employment of A Double Continuum Model to Characterize Groundwater Flow In Underground Post-Mining Setups: Case Study Of The Ibbenbüren Westfield. 14th Mine Water and the Environment Congress: Mine Water Management for Future Generations. 12-15 July 2021 – Virtual conference (Oral presentation)

Bedoya Gonzalez, D., Rinder, T. & Hilberg, S. (2021) Signs of water-rock interaction in fractured coalmine overburdens – First steps for setting a double-continuum reactive transport model. Goldschmidt virtual Conference. 4-9 July 2021 (Poster presentation)

Bedoya Gonzalez, D., Rinder, T. & Hilberg, S. (2020) Evidences of water-rock interaction in a porous and fractured coalmine overburden - Towards a reactive transport model for coalmine drainage. 27th Tagung der Fachsektion Hydrogeologie e. V.in der DGGV e.V.: Grundwasser und Flusseinzugsgebiete. 25-28 March 2020, Leipzig (Poster presentation)

Acknowledgments

This thesis was supported by the foundation "Forum Bergbau und Wasser (FBW)".

First of all, I would like to thank Prof. Maria-Theresia Schafmeister and Assoz. Prof. Sylke Hilberg, who not only applied for the funding and supervised this thesis, but also contributed many ideas and always put me on the right track. I would also like to thank Dr. Thomas Rinder for all his help in obtaining the data from the responsible authorities, as well as for his assistance in the conceptualization and analysis of the reactive transport models. Moreover, he was always ready to provide immediate and helpful career (and moral) support. Many thanks to Dr. Timo Kessler, who was willing to listen whenever modeling problems arose, providing valuable comments, useful observations and interesting discussions. I would also like to thank the Department of Environment and Biodiversity of the University of Salzburg, its research staff and its head, Prof. Christoph von Hagke, for welcoming me and constantly being willing to help me in the completion of this dissertation. Many thanks also to my friends and graduate students Nicolas, Anne-Laure, Moritz, Ruihong, Mengyue and Fabian, with whom I spent many happy moments. Finally, I would like to give all my gratitude to my family for supporting and advising me throughout my doctoral studies; therefore, this thesis would not have been possible without their unconditional love.